ARCHIVES OF ACOUSTICS
14, 3-4, 145-160 (1989)

A-WEIGHTED SOUND PRESSURE LEVEL CALCULATION IN THE DISSIPATIVE ATMOSPHERE

KRYSTYNA BEREZOWSKA-APOLINARSKA, RUFIN MAKAREWICZ

Institute of Acoustics, A. Mickiewicz University
(60-769 Poznań, Matejki 48)

During propagation of sound in the atmosphere a certain fraction of acoustical energy is absorbed by air. Thus, acoustical pressure decreases exponentially with distance. The rate of this drop is expressed by coefficient α which depends on frequency and meteorological conditions.

Absorption coefficient $\alpha(f)$ is approximated in this study by binominal function of frequency with two coefficients depending on temperature and relative humidity. The *A*-weighted sound pressure level is expressed by the function depending on parameters which describe absorption and the distance between the source and the point of observation. Thus the integration is substituted for summation over frequency bands. Calculations are made and charts are drawn to show differences in *A*-weighted pressure level calculation which result from $\alpha(f)$ approximation by binominal function.

Podczas propagacji dźwięku w atmosferze, część energii akustycznej jest pochłaniana przez powietrze. W wyniku tego pochłaniania ciśnienie akustyczne spada wykładniczo z odległością, a prędkość tego spadku wyraża współczynnik α, który zależy od częstotliwości i warunków meteorologicznych.

W pracy przedstawiono współczynnik pochłaniania dźwięku przez powietrze $\alpha(f)$ jako jawną funkcję częstotliwości w postaci dwumianu ze współczynnikami β i γ zależnymi od temperatury i wilgotności względnej. Wyrażono poziom dźwięku mierzony w dB(A) w postaci wzoru zależnego m. in. od parametrów opisujących pochłanianie (β, γ) i odległości od źródła do punktu obserwacji. W ten sposób zastąpiono sumowanie względem pasm częstotliwości całkowaniem. Przeprowadzono rachunki i sporządzono wykresy ilustrujące różnice w obliczeniach poziomu dźwięku, które wynikają m. in. z zastosowania uproszczonej postaci funkcji $\alpha(f)$.

1. Introduction

Environmental noise depends on several basic phenomena such as reflection, diffraction, refraction, interaction with ground and air absorption.

A simplified description of the latter is the aim of the study. Dependence of the absorption coefficient on frequency, temperature and relative humidity is very complex. The accuracy of *A*-weighted sound pressure level calculations required by

planners, traffic engineers, road designers, etc. makes possible to simplify some relations.

First attempt was taken up in Ref. [4]. Critical remarks on it are given in part 4. There we have (Eq. (18)) absorption coefficient α in a form of a binominal containing coefficients which depend on temperature and relative humidity. Numerical values of these coefficients are determined for temperature range from $-$ 10°C till 40°C and relative humidities 10% $-$ 100%.

The noise control requires explicit relations among quantities describing effect of noise on people i.e. noise indices and quantities describing the process of sound generation and propagation. Noise annoyance is generally evaluated in terms of A-weighted sound pressure level expressed in dB(A). We have used continuous form of A-weighting function (Eq. (9)). A continuous form of the function describing spectral density of source power which includes a fairly large class of real noise sources was introduced as well (Eq. (2)).

Introduction of continuous forms of functions describing absorption coefficient and spectral density of source power made possible to derive an explicit form of dependence between A-weigthed sound pressure level, source $-$ point of observation distance, parameters describing absorption, and parameters characterizing a source (Eqs. (7), (19)).

2. Noise source

Spectral density of mean square sound pressure in far field of nondirectional source equals:

$$p^2(f) = \frac{P(f)\varrho c}{4\pi r^2}, \tag{1}$$

where $P(f)$ represents spectral density of source's power, $\varrho c = 414$ kg m^{-2} s^{-1} temperature 20°C for speed of sound $c = 342$ m s^{-1} and air density $\varrho = 1.21$ kg m^{-3}. Formula (1) doesn't allow for absorption.

We assume that spectral density of source power is an exponential frequency function:

$$P(f) = P^{(0)} \exp(-\mu f), \tag{2}$$

where μ is expressed in seconds. For example taking into account a passanger car one may assume $P^{(0)} = 4 \cdot 10^{-5}$, $\mu = 2 \cdot 10^{-3}$. There are many other real noise sources where formula (2) is valid. Source power in n^{th} frequency band determined by $f_n^{(1)}$ and $f_n^{(2)}$ frequencies equals:

$$P_n = \int_{f_n^{(1)}}^{f_n^{(2)}} P(f)\mathrm{d}f = \frac{P^{(0)}}{\mu}\{\exp[-\mu f_n^{(1)}] - \exp[-\mu f_n^{(2)}]\}. \tag{3}$$

Now, to show source power spectrum as a function of parameter u we introduce band sound power level, $L_{Wn} = 10 \lg(P_n/P_0)$, where $P_0 = 10^{-12}$ W. Difference

between two successive band sound power levels $\Delta L_n = L_{Wn} - L_{Wn+1}$, equals:

$$\Delta L_n = 10\lg\left\{\frac{\exp[\mu f_n^{(2)}] - \exp[\mu f_n^{(1)}]}{\exp[\mu f_{n+1}^{(2)}] - \exp[\mu f_{n+1}^{(2)}]}\exp[\mu(f_{n+1}^{(2)} - f_n^{(1)})]\right\}. \tag{4}$$

If $L_{W1} = N$ dB, then $L_{W2} = N + \Delta L_1$, $L_{W3} = N + \Delta L_1 + \Delta L_2$, etc. The results of calculations are shown in Fig. 1. Despite the fact that the spectral density of source's power is a decreasing function of frequency (Eq. 2), power spectrum expressed in

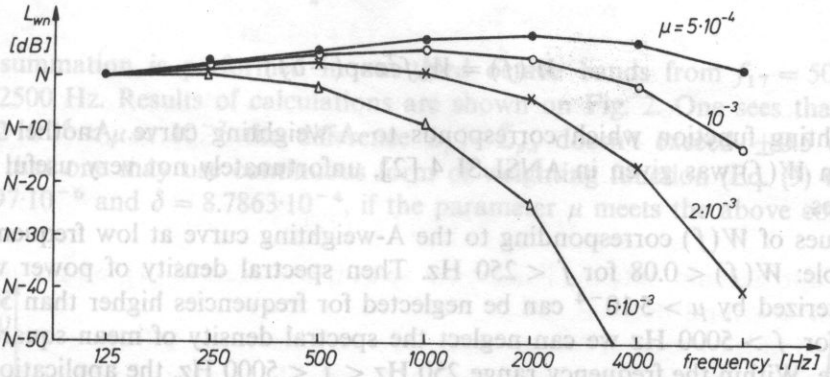

Fig. 1. Source power spectrum depending on parameter μ (Eqs (3), (4))

terms of band sound power level has a maximum. It is seen, that for increasing values of μ, L_{Wn} decreases with frequency. Then small values of μ characterize the power spectra of maximum above 5 kHz. Let f^* be the frequency which separates "low" ($f < f^*$) and "high" ($f > f^*$) parts of the spectrum. The powers P_l and P_h for the high and low sections are:

$$P_l = \int_0^{f^*} P(f)\,df \quad \text{and} \quad P_h = \int_{f^*}^{\infty} P(f)\,df. \tag{5}$$

Inserting source power spectrum (Eq. 2), we get:

$$P_l/P_h = \exp(\mu f^*) - 1. \tag{6}$$

For $\mu = 5 \cdot 10^{-4}$ and $P_l/P_h = 10$ from the above relation we get $f^* \sim 5$ kHz. It means, that for $\mu > 5 \cdot 10^{-4}$ (maximum of power spectra below 2 kHz, see Fig. 1), source's power and thus, spectral density of mean square sound pressure (Eq. (1)), may be neglected above 5 kHz. Minimal value of μ depends on $P_l \backslash P_h$ ratio. For example, $\mu \sim 3 \cdot 10^{-4}$ and $f^* \sim 5$ kHz correspond to the value of $P_l/P_h = 4$.

3. *A*-weighted sound pressure level

Sound level L_{pA} is commonly used index of noise assessment despite its weaknesses [9]. Its definition is:

$$L_{pA} = 10\lg(p_A^2/p_0^2), \tag{7}$$

where $p_0 = 2\cdot10^{-5}$ N m^{-2}. It was shown in Refs [4, 8], that *A*-weighted mean square sound pressure can be given as:

$$p_A^2 = \int_0^\infty W(f)p^2(f)df, \tag{8}$$

where

$$W(f) = W_0 f^2 \exp(-\delta f) \tag{9}$$

is weighting function which corresponds to A-weighting curve. Another form of function $W(f)$ was given in ANSI SI 4 [2], unfortunately not very useful for our purposes.

Values of $W(f)$ corresponding to the A-weighting curve at low frequencies are negligible: $W(f) < 0.08$ for $f < 250$ Hz. Then spectral density of power which is characterized by $\mu > 5\cdot10^{-4}$ can be neglected for frequencies higher than 5000 Hz. Thus, for $f > 5000$ Hz we can neglect the spectral density of mean square sound pressure. Within the frequency range 250 Hz < f < 5000 Hz, the application of the linear regression analysis yields: $W_0 = 2.5197\cdot10^{-6}$ and $\delta = 8.7863\cdot10^{-4}$ [4, 8].

From Eqs. (1), (2), (8), (9) we get [5]:

$$p_A^2 = \frac{P^{(0)}W_0\varrho c}{4\pi r^2}\int_0^\infty f^2\exp[-(\delta+\mu)f]df = \frac{P^{(0)}W_0\varrho c}{2\pi r^2(\delta+\mu)^3} \tag{10}$$

Classical method of calculation of the *A*-weighted mean square sound pressure requires summation over frequency bands:

$$\tilde{p}_A^2 = \sum_n 10^{0.1\Delta L_A(f_n)}p_n^2, \tag{11}$$

where values of ΔL_A relate to the *A*-weighted curve [2, 6], whereas p_n^2 is a mean-square sound pressure of n^{th} frequency band. Taking into account the same value of μ as in expression (10), the definition:

$$p_n^2 = \int_{f_n^{(1)}}^{f_n^{(2)}} p^2(f)df \tag{12}$$

yields (Eqs. (1), (3), (11)):

$$p_n^2 = \frac{P^{(0)}\varrho c}{4\pi r^2}\frac{\exp[\mu f_n^{(1)}]-\exp[-\mu f_n^{(2)}]}{\mu}. \tag{13}$$

We see that (Eg. 11):

$$\tilde{p}_A^2 = \frac{P^{(0)}\varrho c}{4\pi r^2} \sum_n 10^{0.1\Delta L_A(f_n)} \{\exp[-\mu f_n^{(1)}] - \exp[-\mu f_n^{(2)}]\}. \tag{14}$$

To compare $\tilde{p}_A^2$ with the value of p_A^2 we use the definition of A-weighted sound pressure level (Eq. (7)). The difference between $L_{pA} = 10\lg(p_A^2/p_0^2)$ and $\tilde{L}_{pA} = 10\lg(\tilde{p}_A^2/\tilde{p}_0^2)$ equals:

$$L_{pA} - \tilde{L}_{pA} = 10\lg\left[\frac{2W_0\mu}{(\delta+\mu)^3 \sum_n 10^{0.1\Delta L_A(f_n)} \{\exp[-\mu f_n^{(1)}] - \exp[-\mu f_n^{(2)}]\}}\right], \tag{15}$$

where summation is performed in one-third octave bands from $f_{17} = 50$ Hz to $f_{41} = 12500$ Hz. Results of calculations are shown on Fig. 2. One sees that in the range $2\cdot10^{-4} < \mu < \cdot10^{-2}$ the difference $L_{pA} - \tilde{L}_{pA}$ doesn't exceed ± 0.5 dBA. It means, that one may use continuous form of weighting function (Eq. (9) with $W_0 = 2.5197\cdot10^{-6}$ and $\delta = 8.7863\cdot10^{-4}$, if the parameter μ meets the above condition.

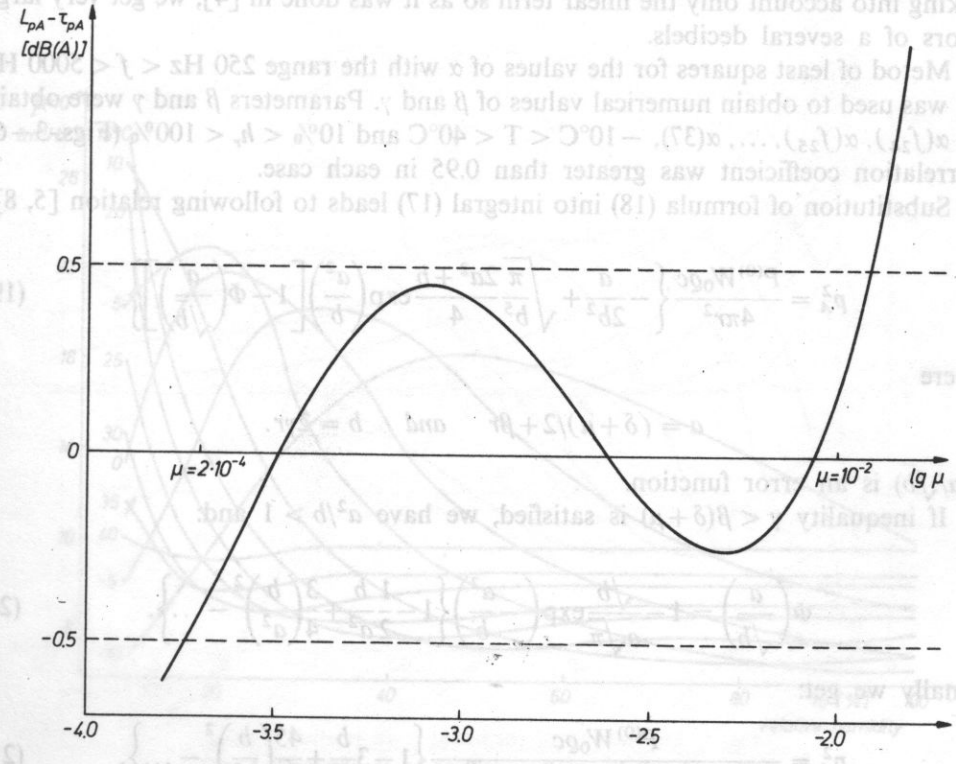

Fig. 2. Difference of A-weighted sound pressure levels $L_{pA}^{(1)} - \tilde{L}_{pA}$ (Eq. (15))

4. Air absorption of sound

The air absorption of sound is not negligible if the point of observation is in the long distance away from the source (Eq. (1)):

$$p^2(f) = \frac{P(f)\varrho c}{4\pi r^2}\exp[-2\alpha(f)r]. \tag{16}$$

Absorption coefficient α depends not only on frequency but also on temperature (T) and relative humidity (h_r).

For the spectral density of source's power determined by Eq. (2) and the weighting function (Eq. 9), we get from (Eq. (8)):

$$p_A^2 = \frac{P^{(0)}W_0\varrho c}{4\pi r^2}\int_0^\infty f^2\exp\{-[\delta+\mu+2\alpha(f)r]\}\,df. \tag{17}$$

Explicit form of the relation $\alpha(f)$ is very complex [1, 3] and the integration can not be done in closed form. The situation changes if one approximates $\alpha(f)$ by the function of a form:

$$\alpha(f) = \beta(T,h_r)f+\gamma(T,h_r)f^2. \tag{18}$$

Taking into account only the linear term so as it was done in [4], we get very large errors of a several decibels.

Metod of least squares for the values of α with the range 250 Hz $< f <$ 5000 Hz [7] was used to obtain numerical values of β and γ. Parameters β and γ were obtain for $\alpha(f_{24})$, $\alpha(f_{25})$, ..., $\alpha(37)$, $-10°\text{C} < \text{T} < 40°\text{C}$ and $10\% < h_r < 100\%$ (Figs. 3–6). Correlation coefficient was greater than 0.95 in each case.

Substitution of formula (18) into integral (17) leads to following relation [5, 8]:

$$p_A^2 = \frac{P^{(0)}W_0\varrho c}{4\pi r^2}\left\{-\frac{a}{2b^2}+\sqrt{\frac{\pi}{b^5}}\frac{2a^2+b}{4}\exp\left(\frac{a^2}{b}\right)\left[1-\Phi\left(\frac{a}{\sqrt{b}}\right)\right]\right\}, \tag{19}$$

where

$$a = (\delta+\mu)/2+\beta r \quad \text{and} \quad b = 2\gamma r.$$

$\Phi(a/\sqrt{b})$ is an error function.

If inequality $\gamma < \beta(\delta+\mu)$ is satisfied, we have $a^2/b > 1$ and:

$$\Phi\left(\frac{a}{\sqrt{b}}\right) = 1-\frac{\sqrt{b}}{a\sqrt{\pi}}\exp\left(-\frac{a^2}{b}\right)\left\{1-\frac{1}{2}\frac{b}{a^2}+\frac{3}{4}\left(\frac{b}{a^2}\right)^2-\ldots\right\}. \tag{20}$$

Finally we get:

$$p_A^2 = \frac{P^{(0)}W_0\varrho c}{2\pi r^2(\delta+\mu)^3[1+2\beta r/(\delta+\mu)]^3}\left\{1-3\frac{b}{a^2}+\frac{45}{4}\left(\frac{b}{a^2}\right)^2-\ldots\right\}. \tag{21}$$

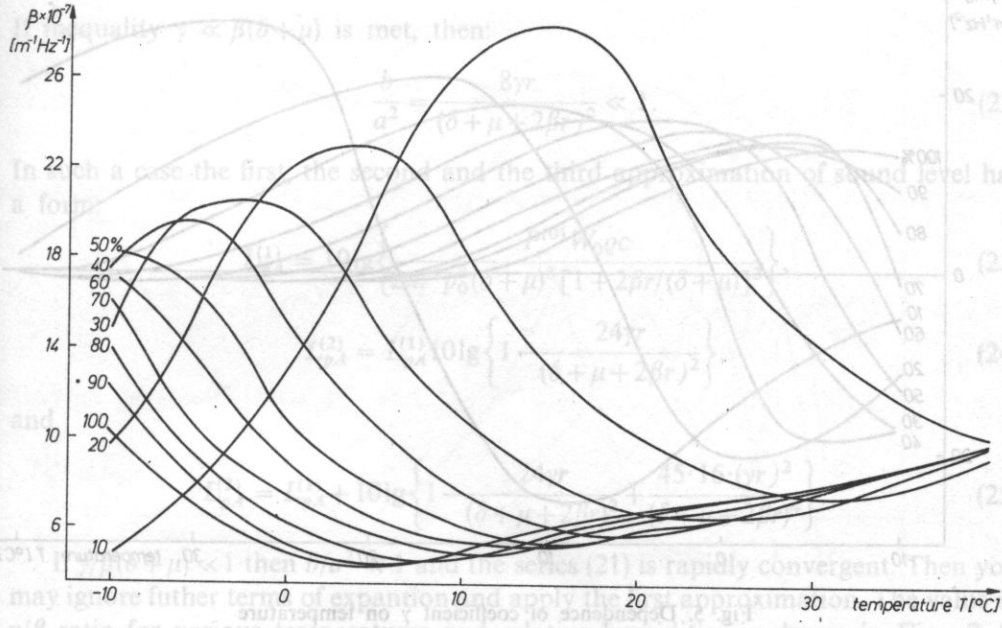

Fig. 3. Dependence of coefficient β on temperature

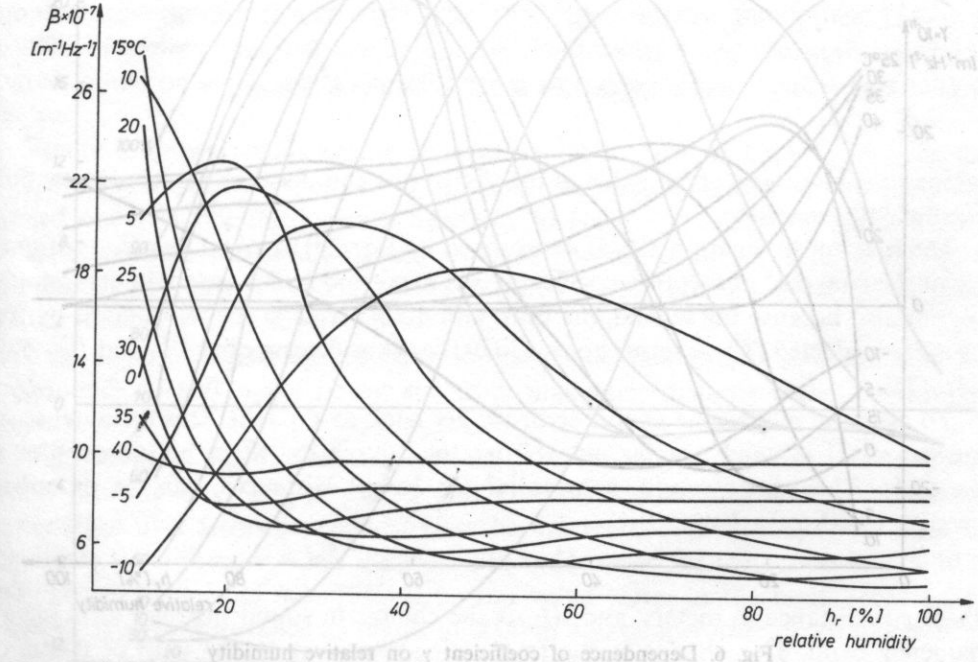

Fig. 4. Dependence of coefficient β on relative humidity

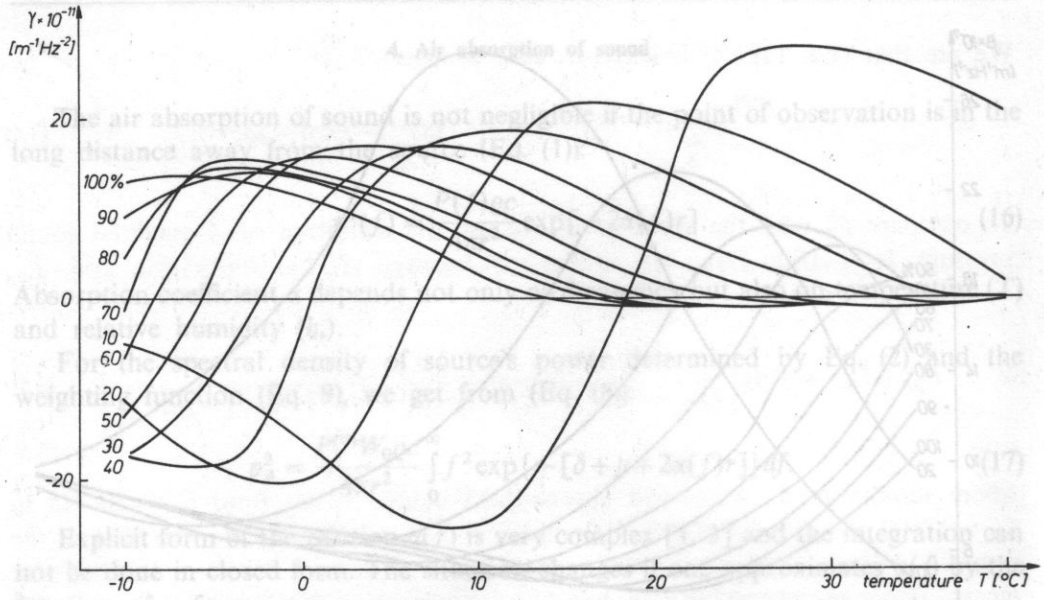

Fig. 5. Dependence of coefficient γ on temperature

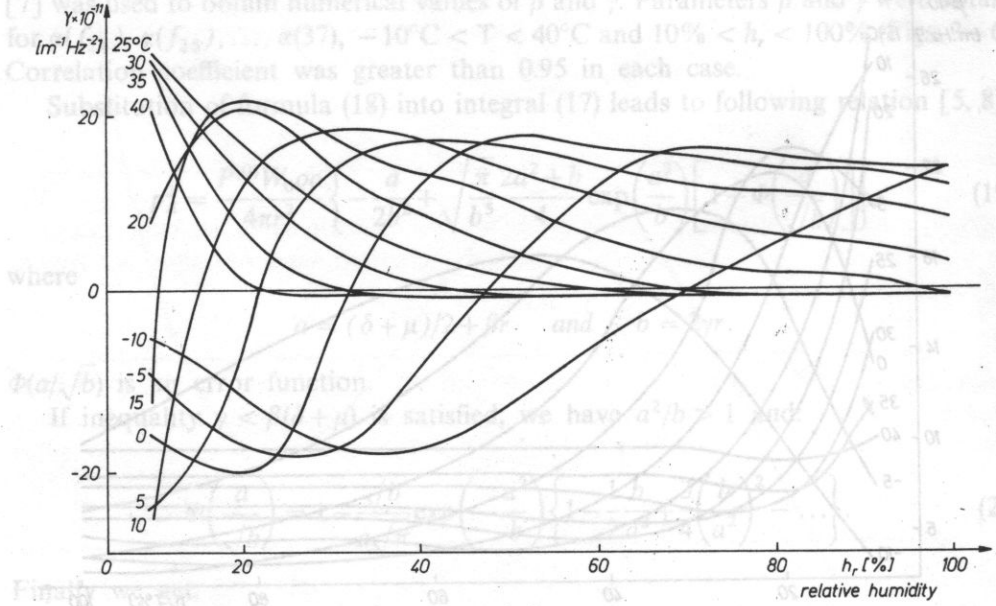

Fig. 6. Dependence of coefficient γ on relative humidity

If inequality $\gamma \ll \beta(\delta+\mu)$ is met, then:

$$\frac{b}{a^2} = \frac{8\gamma r}{(\delta+\mu+2\beta r)^2} \ll 1. \tag{22}$$

In such a case the first, the second and the third approximation of sound level has a form:

$$L_{pA}^{(1)} = 10\lg\left\{\frac{P^{(0)}W_0\varrho c}{2\pi r^2 p_0^2(\delta+\mu)^3[1+2\beta r/(\delta+\mu)]^3}\right\}, \tag{23}$$

$$L_{pA}^{(2)} = L_{pA}^{(1)}10\lg\left\{1-\frac{24\gamma r}{(\delta+\mu+2\beta r)^2}\right\}, \tag{24}$$

and

$$L_{pA}^{(3)} = L_{pA}^{(1)}+10\lg\left\{1-\frac{24\gamma r}{(\delta+\mu+2\beta r)^2}+\frac{45\cdot 16\cdot(\gamma r)^2}{(\delta+\mu+2\beta r)^4}\right\}. \tag{25}$$

If $\gamma/\beta(\delta+\mu) \ll 1$ then $b/a^2 \ll 1$ and the series (21) is rapidly convergent. Then you may ignore futher terms of expantion and apply the first approximation. The value of γ/β ratio for various temperatures and relative humidities is shown in Figs. 7, 8.

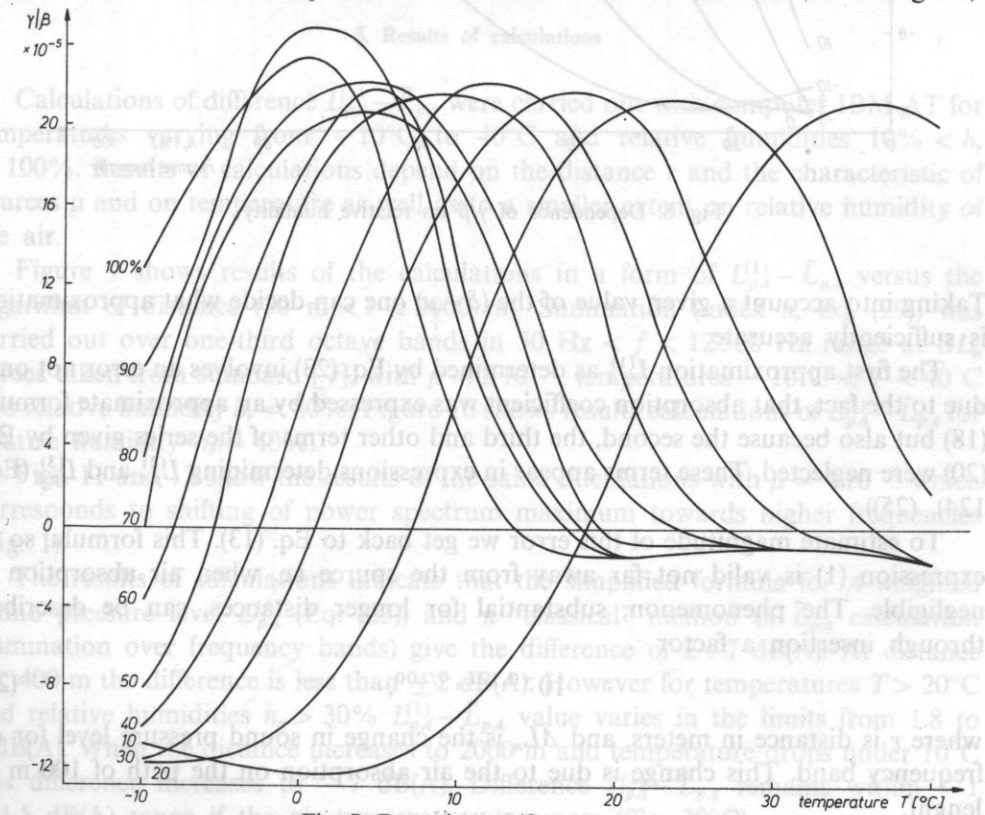

Fig. 7. Dependence γ/β on temperature

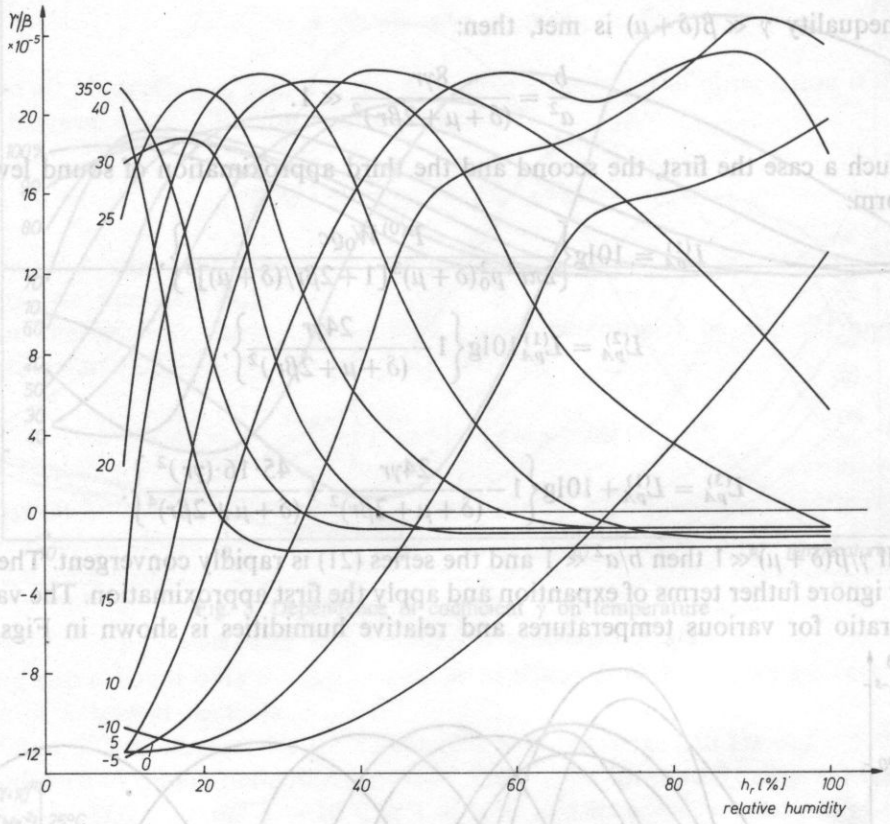

Fig. 8. Dependence of γ/β on relative humidity

Taking into account a given value of the $(\delta+\mu)$ one can decide what approximation is sufficiently accurate.

The first approximation $L_{pA}^{(1)}$ as determined by Eq. (23) involves an error not only due to the fact, that absorption coefficient was expressed by an approximate formula (18) but also because the second, the third and other terms of the series given by Eq. (20) were neglected. These terms appear in expressions determining $L_{pA}^{(2)}$ and $L_{pA}^{(3)}$ (Eqs 124), (25)).

To estimate magnitude of this error we get back to Eq. (13). This formula, so as expression (1) is valid not far away from the source i.e. when air absorption is negligible. The phenomenon, substantial for longer distances, can be described through insertion a factor

$$10^{-0,1\Delta L_n \cdot r/100}, \tag{26}$$

where r is distance in meters, and ΔL_n is the change in sound pressure level for n^{th} frequency band. This change is due to the air absorption on the path of 100 m of lenght.

Equations (13) and (26) combine into:

$$p_n^2 = \frac{P^{(0)}\varrho c}{4\pi r^2} \frac{\exp[-\mu f_n^{(1)}] - \exp[-\mu f_n^{(2)}]}{\mu} \cdot 10^{-0{\cdot}1\Delta L_n \cdot r/100}. \tag{27}$$

Summation over frequency bands yields expression for A-weighted mean square sound pressure:

$$\tilde{p}_A^2 = \frac{P^{(0)}\varrho c}{4\pi r^2 \mu} \sum_n 10^{0{\cdot}1[\Delta L_A(f_n) - \Delta L_n \cdot r/100}} \left\{ \exp[-\mu f_n^{(1)}] - \exp[-\mu f_n^{(2)}] \right\}. \tag{28}$$

Difference of sound levels $L_{pA}^{(1)}$ and $\tilde{L}_{pA} = 10\lg(\tilde{p}_A^2/p_0^2)$ (Eqs. (23), (28)) gives:

$$L_{pA}^{(1)} - \tilde{L}_{pA} = 10\lg\left[\frac{2W_0\mu}{(\delta+\mu+2\beta r)^3 \sum_n 10^{0{\cdot}1[\Delta L_A(f_n) - \Delta L_n \cdot r/100]} \{\exp[-\mu f_n^{(1)}] - \exp[-\mu f_n^{(2)}]\}} \right]. \tag{29}$$

5. Results of calculations

Calculations of difference $L_{pA}^{(1)} - \tilde{L}_{pA}$ were carried out with computer IBM AT for temperatures varying from $-10°C$ to $40°C$ and relative humidities $10\% < h_r < 100\%$. Results of calculations depend on the distance r and the characteristic of sources μ and on temperature as well as to a smaller extent on relative humidity of the air.

Figure 9 shows results of the calculations in a form of $L_{pA}^{(1)} - \tilde{L}_{pA}$ versus the logarithm of distance ($50 \text{ m} < r < 2000 \text{ m}$). Summation (index n, Eq. (29)) was carried out over one-third octave bands in $50 \text{ Hz} < f < 12\,500 \text{ Hz}$ range at ΔL_n values taken from standard [7], with $\mu = 2{\cdot}10^{-3}$, temperatures $-10°C < T < 40°C$ and relative humidity $h_r = 80\%$. Figure 10 shows results calculations of $L_{pA}^{(1)} - \tilde{L}_{pA}$ for relative humidity $h_r = 40\%$.

Figs. 11 and 12 show the results of the same calculations with $\mu = 4{\cdot}10^{-4}$ which corresponds to shifting of power spectrum maximum towards higher frequencies (Fig. 1).

The results of calculations indicate that the simplified formula for A-weighted sound pressure level $L_{pA}^{(1)}$ (Eq. (23)) and a "classical" method of $\tilde{L}_{pA}$ calculation (summation over frequency bands) give the difference of $2 \div 7$ dB(A). At distance $r < 400$ m the difference is less than ± 2 dB(A). However for temperatures $T > 20°C$ and relative humidities $h_r > 30\%$ $L_{pA}^{(1)} - \tilde{L}_{pA}$ value varies in the limits from 1.8 to 0 dB(A). When the distance increases to 2000 m and temperature drops under $10°C$ this difference increases to -7 dB(A). Difference $L_{pA}^{(1)} - \tilde{L}_{pA}$ remains within $-1 \div 1.5$ dB(A) range if the air temperature increases ($T > 20°C$).

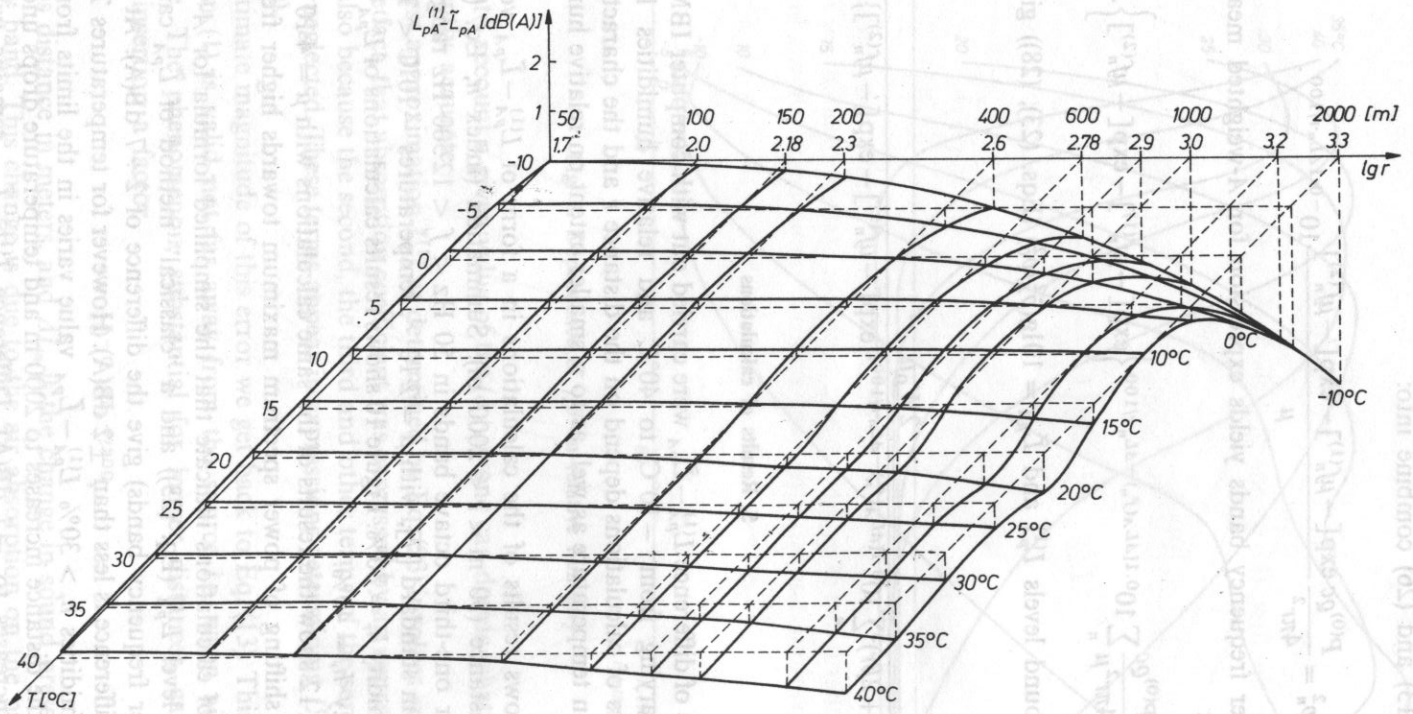

Fig. 9. Difference $L_{pA}^{(1)} - \tilde{L}_{pA}$ (Eq. (29)) versus logarithm of distance for relative humidity $h_r = 80\%$ and parameter $\mu = 2 \cdot 10^{-3}$

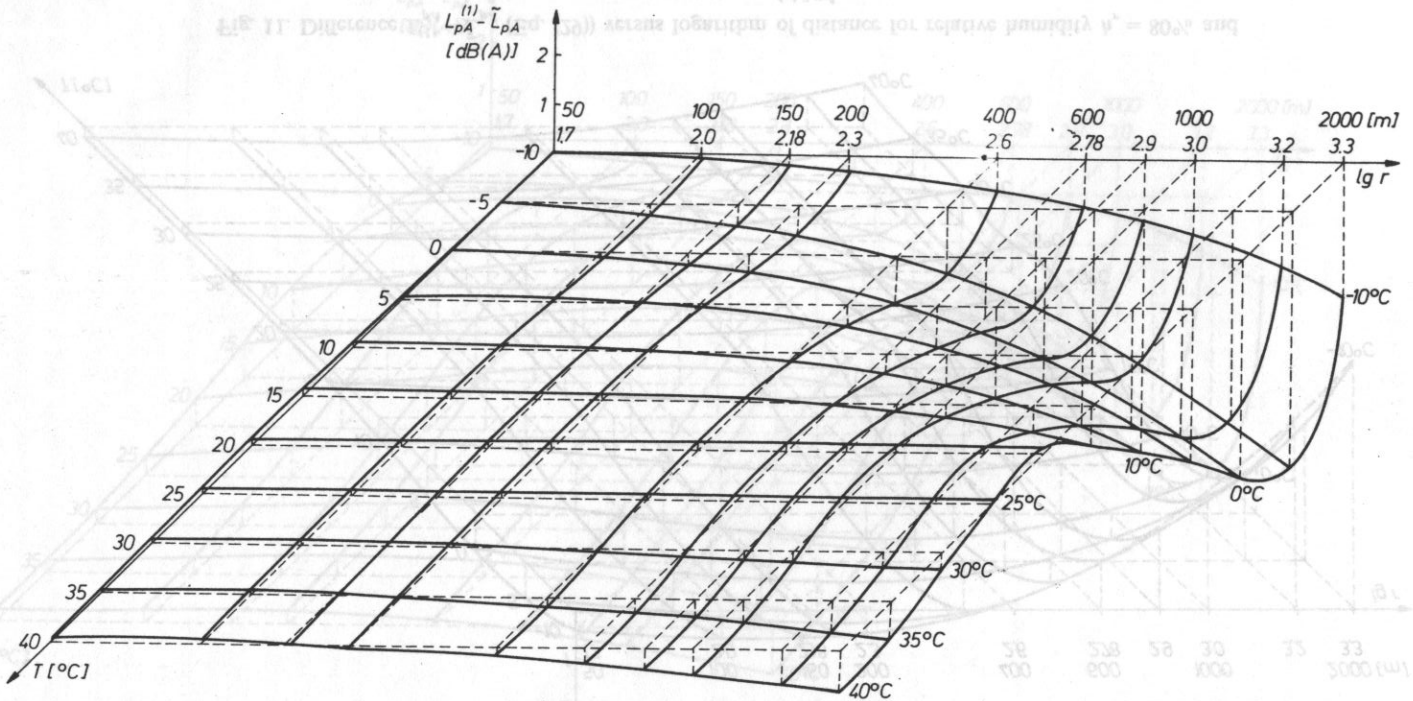

Fig. 10. Difference $L_{pA}^{(1)} - \tilde{L}_{pA}$ (Eq. (29)) versus logarithm of distance for relative humidity $h_r = 40\%$ and parameter $\mu = 2 \cdot 10^{-3}$

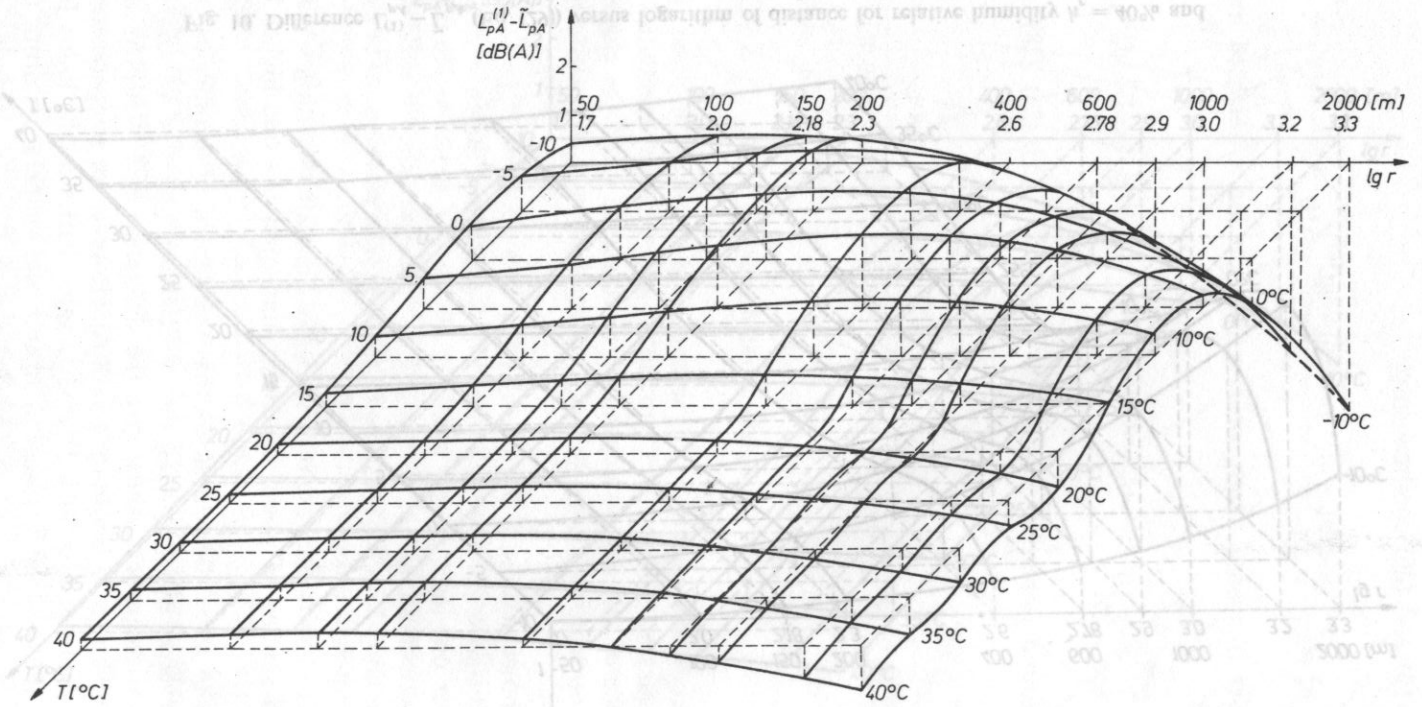

Fig. 11. Difference $L_{pA}^{(1)} - \tilde{L}_{pA}$ (Eq. (29)) versus logarithm of distance for relative humidity $h_r = 80\%$ and parameter $\mu = 4 \cdot 10^{-4}$

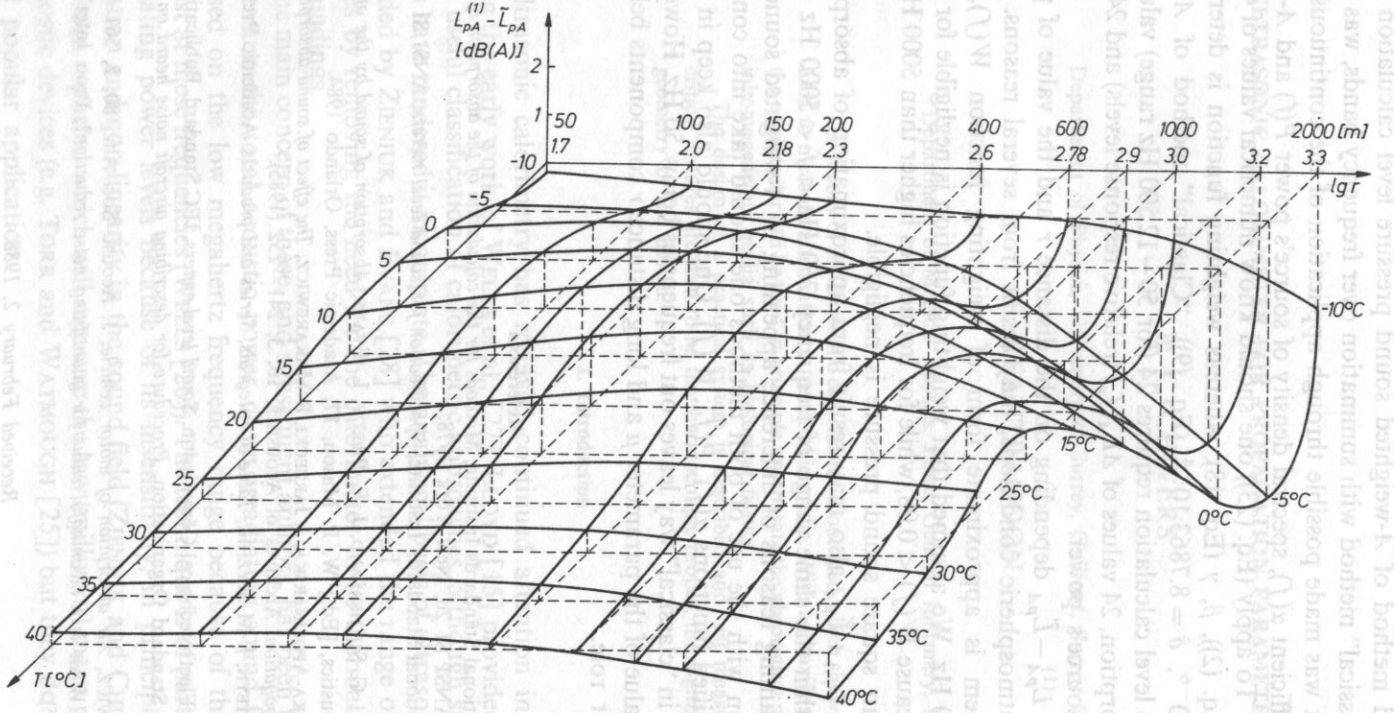

Fig. 12. Difference $L_{pA}^{(1)} - \tilde{L}_{pA}$ (Eq. (29)) versus logarithm of distance for relative humidity $h_r = 40\%$ and parameter $\mu = 4 \cdot 10^{-4}$

6. Conclusions

A simplified method of A-weighted sound pressure level calculation (Eq. (23)) instead of "classsical" method with summation over frequency bands, was presented in the paper. It was made possible through application of the continuous forms of absorption coefficient $\alpha(f)$, spectral density of source's power $P(f)$ and A-weighting function $W(f)$. To apply (Eq. (23)) one should know numerical values of 4 parameters: $P^{(0)}$, μ (Eq. (2)), β, γ (Eq. 18), whereas weighting function is determined by $W_0 = 2.5197 \cdot 10^{-6}$, $\delta = 8.7863 \cdot 10^{-4}$ (Eq. (9)). "Classical" method of A-weighted sound pressure level calculation requires 24 (for 50 – 12 500 Hz range) values of ΔL_n describing absorption, 24 values of $\Delta L_A(f_n)$ (relative response levels) and 24 values of p_n describing source's power.

Differences $L_{pA}^{(1)} - \tilde{L}_{pA}$ depending on the distance r and the value of parameter μ as well as atmospheric conditions, may result from several reasons.

One of them is approximate form of weighting function $W(f)$, for 250 Hz $< f <$ 5000 Hz. We assumed that weighting function is negligible for frequency $f <$ 250 Hz because $W(f) < 0.08$, while for frequencies higher than 5000 Hz spectral density of mean square sound pressure is negligible.

Differences $L_{pA} - \tilde{L}_{pA}$ also may result from approximation of absorption coefficient $\alpha(f)$ within the same range of frequency 250 Hz $< f <$ 5000 Hz (Eq. (18)).

When explaining reasons of difference appearing in A-weighted sound pressure level calculation with the use of both methods one should take into consideration not only simplified functions $\alpha(f)$, $P(f)$, $W(f)$. One should also keep in mind that L_{pA} calculated in "classical" way leaves out frequencies below 50 Hz. However in the case of great value of the parameter μ and long distance r components below 50 Hz play important role.

References

[1] American National Standards Institute, *Methods for the calculation of the absorption of sound by the atmosphere*, ANSI SI 26, New York 1978.

[2] American National Standards Institute, *Specification for sound level meters*, ANSI SI 4, New York 1983.

[3] H. E. BASS, L. C. SUTHERLAND, J. E. PIERCY, L. EVANS, *Absorption of sound by the atmosphere*, in: Physical Acoustics, [Ed.] W. P. Mason, **17**, Academic Press, Orlando 1984.

[4] K. BEREZOWSKA-APOLINARSKA, J. JARZECKI, R MAKAREWICZ, *The effect of sound absorption by the air on noise propagation*. Archives of Acoustics, **10**, 3, 241 – 252 (1985).

[5] I. S. GRADSHTEYN, I. M. RYZHIK, *Table of Integrals, Series and products*, Academic Press, New York 1980.

[6] International Electrotechnical Commission, *Sound level meters*, IEC Standard, Publication 651, 1979.

[7] International Standard Organization, *Procedure for describing aircraft noise heard on ground*, ISO 3891, 1978.

[8] R. MAKAREWICZ, *Air absorption of motor vehicle*, J. Acoust. Soc. Am., **80**, 2, 561 – 568 (1986).

[9] E. ZWICKER, *What is a meaningful value for guantifying noise reduction*?, Proc. Inter – Noise 85, 47 – 56 (1985).

Received February 2, 1988.

ARCHIVES OF ACOUSTICS
14, 3–4, 161–172 (1989)

AN ULTRASONIC CALORIMETER FOR PROPAGATION PARAMETER MEASUREMENT

R. C. CHIVERS

Department of Physics, University of Surrey, Guilford, Surrey GU2 5XH

S. REANTRAGOON

Department of Medical Physics, Leeds General Infirmary, Leeds

The theory of an ultrasonic calorimeter is outlined which shows that the device may be used to measure attenuation in penetrable media. With an auxiliary radiation force device the calorimeter can be used in principle to separate the absorption part of the attenuation in inhomogeneous media such as biological tissues.

The design of a practical system is described and test measurements reported. The critical features are seen to be the thermocouple probes, the digitization circuitry, and the geometry of the design.

1. Introduction

Ultrasonic calorimetry has received continued attention in the literature following the early work of WELLS et al., [27]. LLOYD [15] provided a valuable review and a useful classification of calorimetric approaches, although subsequent developments have rendered it incomplete. The analytical basis of ultrasonic calorimetry was provided by ZIENIUK and EVANS [28] who extended the range of usefulness of such devices by removing the need for the calorimeter to be thermally isolated from its surroundings.

The main concern of these, and subsequent authors, has been to construct devices to measure the total acoustic power of an irradiating sound field. Attention has focussed on the low megahertz frequency range because of the great biomedical interest at these frequencies (WELLS [26]). The technique is of particular value at high irradiating power levels because of its insensitivity, in principle, to the effects of cavitation and non-linearity in the sound field (ZIENIUK and CHIVERS [29]). Devices have been reported which will measure the low (milliwatt) mean power levels used in diagnostic devices (e.g. TORR and WATMOUGH [25]) but they do not appear to have found popular application.

The present work emerged from an idea of the late Professor Roy ELLIS of using a calorimeter to measure that component of the effective ultrasonic irradiation of a system that can correctly be compared with the concept of dose in ionising radiation. The majority of the measurement techniques that are in current use, such as miniature hydrophones (PRESTON et al, [20]; LEWIN [14]) or radiation force balances (FARMERY and WHITTINGHAM, [11]; ANSON and CHIVERS [3], measure ultrasonic field parameters in water. They are thus even one stage removed from the measurement of exposure. The calculation of the field parameters at a given site then requires knowledge of the ultrasonic propagation parameters, specifically velocity and absorption or attenuation, of the biological medium between the transducer (whose field pattern is known in water) and the site of interest, and an appropriate propagation equation. This inter-relationship between the measurement of exposure and knowledge of the ultrasonic propagation parameters of the medium will be discussed in more detail in a subsequent section.

The device described here was designed to be used to measure the propagation parameters of an inhomogeneous medium such as biological tissue, suspensions, or oceanic sediments. The interest was in measuring the absorption and the attenuation on the same specimen at the same time. (For an inhomogeneous medium the difference between them is the contribution of the scattering to the attenuation). The magnitude of the scattering contribution to the attenuation in soft tissues is a matter of some discussion. Direct measurement of scattering estimates it as 2% (CAMPBELL and WAAG [5]) or as much as 13% (NASSIRI and HILL [17]) of the attenuation. If it is significant, it may compromise the value of both attenuation and scattering measurements made with conventional plane wave measurement approaches (CHIVERS [7]). Measurements of absorption have been made directly (PARKER [18, 19]) but the lack of simultaneous attenuation measurements introduces the non-negligible factor of biological variation into the error bars, thus effectively preventing accurate assessment of the (potentially small) difference between attenuation and absorption.

The paper presents the analytical basis of the device and the design considerations that constrain the form of its experimental realisation for a given application. An example of such a device is discussed in detail both in terms of its mechanical construction and the associated electronics. Some results on a known medium – castor oil – and on beef muscle are presented, as test procedures. The device is shown to be adequate for measurement of the attenuation but the separation of the scattering component will require improved instrumentation and a full error analysis.

2. Theoretical basis

The plane wave model assumed is illustrated in Fig. 1. The calorimeter is assumed to consist of a chamber of length l. Inserted into it a distance y from each end are thermocouple detectors (they need not be symmetrically arranged but the amend-

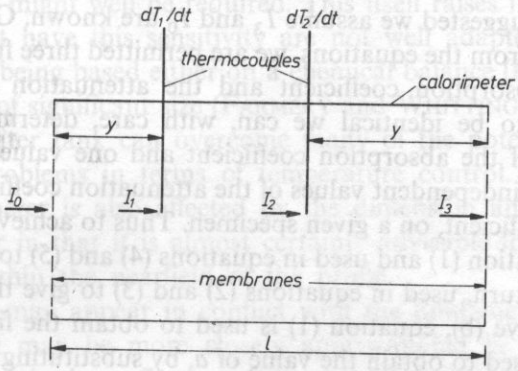

Fig. 1. Basic theoretical model

ment to the theory is trivial). The intensities of the ultrasonic waves entering the calorimeter, impinging on thermocouple 1, impinging on thermocouple 2, and leaving the calorimeter are I_0, I_1, I_2, and I_3, respectively. The temperatures registered by the thermocouples are designated by T_1 and T_2, so that:

$$\left[\frac{dT_1}{dt}\right]_0$$

represents the initial temporal gradient of temperature registered by the first thermocouple.

It is assumed that the medium inside the calorimeter is inhomogeneous but uniformly so, such that it is possible to specify a single ultrasonic absorption coefficient, a, and a single attenuation coefficient a_t which characterise the medium and are, in general, different. It is further assumed that I_0 and I_3 are known (since they can be measured either with a calibrated hydrophone (e.g. PRESTON et al., [20]) or by a radiation force device (e.g. ANSON and CHIVERS, [3]).

The equations describing the behaviour of the calorimeter are then:

$$I_3 = I_0 \exp(-a_t l), \tag{1}$$

$$\left[\frac{dT_1}{dt}\right]_0 = aI_1/\varrho C, \tag{2}$$

$$\left[\frac{dT_2}{dt}\right]_0 = aI_2/\varrho C, \tag{3}$$

$$I_i = I_0 \exp(-a_t y), \tag{4}$$

$$I_2 = I_0 \exp(-a_t(x+y)), \tag{5}$$

where the $I_i (i = 0, 1, 2, 3)$, a, a_t, x, y, T_1 and T_2 have been defined above, and ϱ and C are the density and specific heat capacity of the medium respectively. Equations (2) and (3) are from FRY and FRY [12].

In the approach suggested we assume I_3 and I_0 are known. Given that I_1 and I_2 are to be determined from the equations, we are permitted three further unknowns. If the values of the absorption coefficient and the attenuation coefficient are not considered a priori to be identical we can, with care, determine either: (a) two independent values of the absorption coefficient and one value of the attenuation coefficient, or (b) two independent values of the attenuation coefficient and one value of the absorption coefficient, on a given specimen. Thus to achieve (a), the value of a_t is obtained from equation (1) and used in equations (4) and (5) to obtain values of I_1 and I_2 which are, in turn, used in equations (2) and (3) to give the two independent values of a. To achieve (b), equation (1) is used to obtain the first value of a_t, and equation (2) (or (3)) used to obtain the value of a, by substituting a_t into equation (4) (or (5)) and obtaining I_1 (or I_2). Inserting this value of a into equation (3) (or (2)) permits I_2 (or I_1) to be obtained, which can then be used in equation (5) (or (4)) to obtain the second value of a_t.

It is interesting to consider the case in which the medium inside the calorimeter is homogeneous so that $a_t = a$. The ratio of equations (2) and (3) gives:

$$\left[\frac{dT_1}{dt}\right]_0 \Big/ \left[\frac{dT_2}{dt}\right]_0 = \frac{I_1}{I_2} = I_1 \exp(-ax) \tag{6}$$

so that if:

$$\frac{dT_1}{dt} \quad \text{or} \quad \frac{dT_2}{dt}$$

is measured we can determine I_0 from equation (4) or (5) as:

$$I_0 = \exp(ay) I_i = \left[\frac{dT_1}{dt}\right]_0 \frac{\varrho C \exp(ay)}{a} \tag{7}$$

(with a similar result using I_2), so that the calorimeter may be used to measure exposure in the conventional way. A rather fuller discussion of the significance of this has been given elsewhere (REANTRAGOON and CHIVERS [21]).

3. Numerical constraints

The practical implementation of a device based on the principles outlined in the previous section has implicit in it a number of limitations. These are essentially related to the dimensions of the calorimeter, i.e. its length and diameter, and of the positioning of the thermocouples within it. The first of these, the maximum length that is acceptable, is determined by the overall attenuation of the material in the calorimeter. The incident intensity I_0 has to be sufficiently low to avoid the complication of non-linear effects. If the output intensity is also to be measured, the overall attenuation should not place it too close to the threshold of sensitivity of the radiation force balance available. With a radiation force in water of 67mg per watt,

a sensitivity of 100μg might well be required. This itself raises important problems since the devices that have this sensitivity are not well adapted for an auxiliary measurement role – being based either on a chemical balance (ROONEY [23]) or on a self-contained unit of significant size (FARMERY and WHITTINGHAM [11]). The use of a large enough water tank can overcome many of the potential problems but introduces greater problems in terms of temperature control. The choice of the length of the calorimeter is also affected by the dimension and frequency of the irradiating transducer in that it is almost certainly advisable for the whole of the calorimeter to lie within the nearfield of the probe.

At first sight this may appear in conflict with the fundamental assumption of a plane wave, which may be more closely approximated in the far-field. It is, however, crucial, not only that reflections from the side walls of the calorimeter due to beam divergence are avoided, but also that the radiation force device at the exit of the calorimeter can intercept all the beam, without too much divergence to cause inaccuracy in the measurement. There is some pressure to reduce the size of the sample as much as is reasonably possible because of the relative difficulty in obtaining large tissue specimens. The decision to keep the calorimeter in the near field of the transducer is therefore a compromise. However, the condition of a „plane wave" given above is not the usual interpretation. Equations (1)–(5) indicate that the 'plane wave' assumption is not that of a uniform pressure amplitude and phase across the beam, but of a uniform (vector) intensity. To the authors' knowledge this is a topic which still requires calculation but, from consideration of the conservation of energy, it is likely to be a good first approximation in the near field. It is known to be invalid in the far-field. The diameter of the calorimeter is thus controlled by the diameter of the irradiating transducer.

The spacing of the thermocouples is firstly determined by the need to have them sufficiently far from the ends of the specimen for there to be no thermal anisotropy in their environment. The first thermocouple can, subject to this restriction, be close to the entry port of the calorimeter where the intensity is highest and the temporal gradient of the rise in temperature (Equation (4)) high. The position of the second thermocouple is determined by a compromise between having a high temperature gradient, and the need for the temperature rise to be very different from that of the first thermocouple. The second aspect arises from the use of the ratio of equations (4) and (5) to obtain the attenuation coefficient.

For an intensity of 100mWcm^{-2} the temperature gradient for tissue (using the values of specific heat capacity given by SHITZER [24] and a value of the absorption coefficient of 0.1 nepers/cm (WELLS, [26]) is of the order of 3 millidegrees Kelvin per second at 1MHz. The temperature gradient increases with frequency as the absorption coefficient increases. This has significance in connection with the electronics discussed in section 4.3 below.

Two further considerations are relevant. The thermocouples have to be small compared to the wavelength. This only presents problems at frequencies of several tens of megahertz and above since commercially available thermocouples are

available as small as 13μm. The last consideration is the distance between the exit port of the calorimeter and the target on the radiation force balance. Most radiation force devices use a self-centering concave conical target. It is important not only to have the whole of the ultrasonic beam impinging on the target, but the target itself must be sufficently far away to prevent energy reflected from the target reentering the calorimeter, or being reflected by the calorimeter back onto the target. It can be seen that for a calorimeter of radius R with an axial ultrasonic beam of radius r the spacing between the calorimeter and the vertex of the inverted conical target is given by

$$z > -(r+R)\cot 2\theta$$

where θ is the semi angle of the cone. θ has to be greater than 45° to prevent rays reflected from the target hitting it again. Thus 2θ is always obtuse and cot 2θ always negative.

4. Experimental arrangement

The experimental arrangement is shown in Fig. 2 (schematic) and Fig. 3. A rectangular platform of perspex (A) had fitted above its centre a collar (B) (with three pairs of screws) for holding the irradiating transducer. This platform could be raised and lowered with respect to the bottom of the immersion tank by two rods (C)

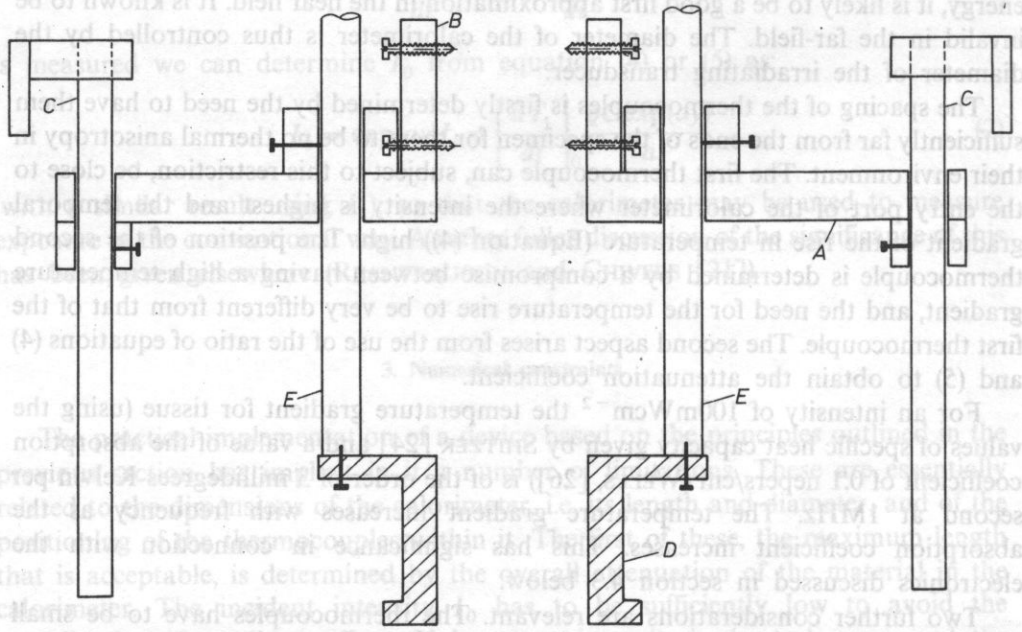

Fig. 2. Overall experimental arrangement: A – adjustable platform, B – transducer holder, C – rods for adjusting platform height, D – calorimeter, E – rods for adjustment of height of calorimeter

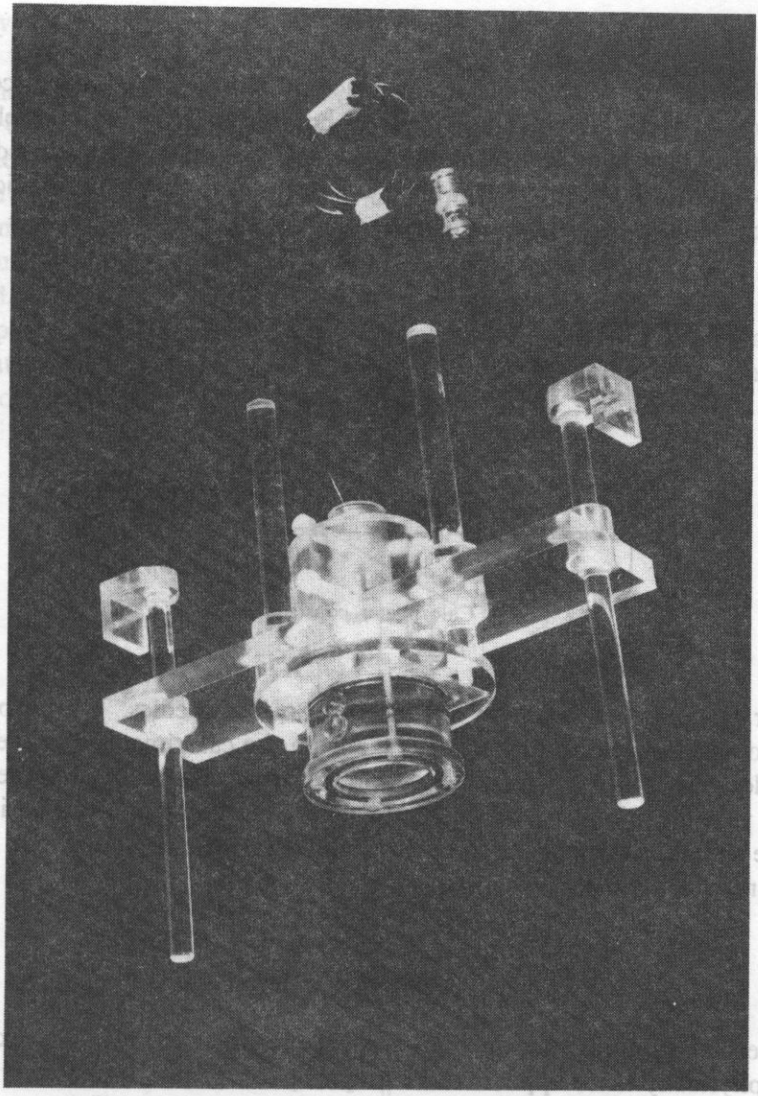

Fig. 3. Actual experimental construction

suspended from the top of the tank walls. The calorimeter (*D*) was attached to the platform by two rods (*E*) that also permitted its depth with respect to the platform to be varied. Below the calorimeter was the target of the radiation force device.

The tank in which the calorimeter and radiation force balance was immersed consisted of a thin-walled transparent tank within a larger tank (AINDOW [1]) with stirrer and thermostat control. The radiation force device was a novel design developed in the laboratory. It had a sensitivity of 40μW/mA and the inverted conical target (half angle 60°) stood about 10cm from the floor of the tank.

4.1. Calorimeter design

A detailed diagram of the calorimeter construction is shown in Fig. 4. It consists of a cylinder with two end plates. The end plates hold acoustic windows in place (5μm polythene) with 'o' rings to seal the specimen in the calorimeter. At one side are the entry ports for the thermocouples which are introduced via hypodermic needles. Each port contains a thin rubber mebrane held in place by a plug. The plug and

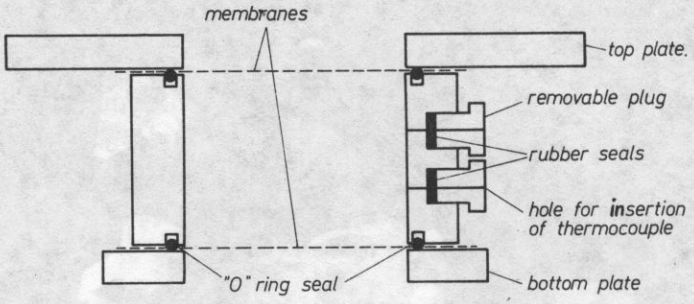

Fig. 4. Calorimeter construction

calorimeter have aligned holes for the insertion of the needles. The purpose of the rubber is to act as a seal to prevent leakage from the calorimeter specimen volume. The basic design permits the introduction of cylindrical chambers of different lengths and entry port positions to be used. For the experimental investigation of the method the chamber was chosen to be 3cm long with the entry ports 1cm from each end. The internal diameter was 4cm.

4.2. Sensors and circuitry

Chrome: constantan thermocouples were constructed for the experiments. Although physically there appears to be ample space for two insulated wires within a 31 gauge needle, the mechanical weakness of the wires is insufficient to overcome the frictional forces encountered. A local thermocouple manufacturer confirmed our inability to pass two wires down the needle. Finally one wire was taken outside and one inside – with appropriate varnish insulation. The thermocouples were tested for linearity (59μV per degree K) and inserted into the calorimeter using a 23 gauge needle.

Three types of circuitry are used in the system. The first is that for the radiation force device (which is described elsewhere; ANSON et al [2]). The second is that for the transmitter excitation which was a standard variable frequency, variable length toneburst generation system. Pulses of typically 20 cycles every ms were used. The third type of circuitry was that for logging the temporal variation of the temperature

measured by the two thermocouples. The circuitry used for this last is shown in Fig. 5. The termocouples are connected to high gain operational amplifiers and receive further amplification before being fed to a 12-bit ADC for processing by a Motorola 6809 system. Only one ADC was available so an analogue switch was used. The temperature gradients are typically higher in the initial phases and gradually flatten out. The main interest however is in the initial stages where the conflicting interests of low signal levels and high required sampling rates exist. In order to reduce the high frequency noise, a low pass (Sallen and Key) active filter was incorporated. The ADC used (ICL 7109) was an integrating ADC with an integration period of 40ms which was chosen also for its noise rejection capability. The temperature: time curves were extrapolated to obtain the initial (i.e. in the first second or so) temperature gradients.

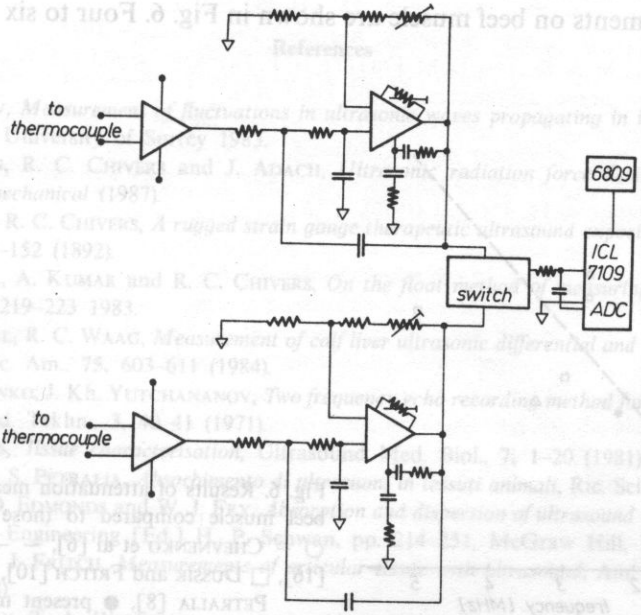

Fig. 5. Thermocouple circuitry

5. Testing the calorimeter

An extensive preliminary investigation identified the care that has to be taken with the experimental design. In addition to ensuring the correct geometry to keep the radiation force target within the near field of the transducer and to obtain high enough temperature rises on the thermocouples to provide a satisfactory signal to noise ratio, particular attention needs to be paid to the avoidance of non-linearity in the irradiating transducers as the exciting voltage is increased to improve the signal levels.

The preparation of the specimen had to ensure the removal of air-bubbles – the major reason for the use of transparent materials in the calorimeter construction. The tissues specimens used were fresh beef muscle (perpendicular to the fibres) cut to fit the calorimeter by a specially devised apparatus (REANTRAGOON and CHIVERS [22]). The thermocouples were then inserted into the tissue using hypodermic needles (see section 4.1.). Measurements were carried out on castor oil at 37° and the fresh beef muscle at 20° at mean power levels up to 500mW. The radiation force balance measurements are relatively well established so the calorimeter was tested by measuring the attenuation coefficient of the material in the holder using the two temperature gradients. On castor oil, results of 0.27 ± 0.03 dBcm^{-1} and 0.70 ± 0.20 dBcm^{-1} were obtained at 1.0 and 2.25 MHz respectively. These fit reasonably with the data of DUNN et al [9] and FYKE et al. [13]. The former authors give 0.174 dBcm^{-1} (FYKE et al., giving 0.30 dBcm^{-1}) at 1 MHz and 0.67 dBcm^{-1} at 2.25 MHz. The variation in the literature values is clearly not helpful here.

The measurements on beef muscle are shown in Fig. 6. Four to six measurements

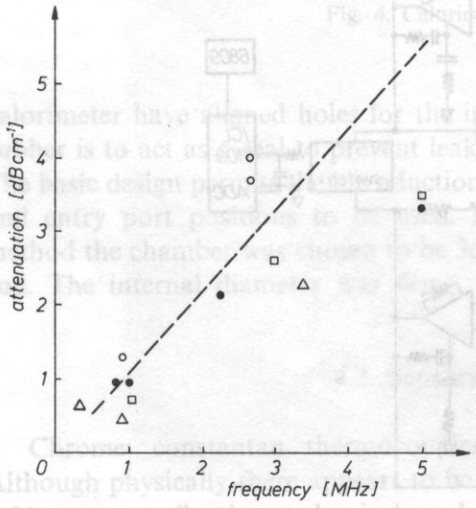

Fig. 6. Results of attenuation measurement of fresh beef muscle compared to those in the literature: ○ – CHEVNENKO et al [6], – – – NASSIRI et al, [16], □ DUSSIK and FRITCH [10], △ COLOMBATI and PETRALIA [8], ● present measurements

were taken at each frequency. It can be seen that they appear to be well within the range of data the literature displays, showing particularly close agreement with the data of DUSSIK and FRITCH [10]. Preliminary results on the contribution of absorption to attenuation place it between 0 and 20%. It is clear that before more reliable figures can be provided, careful error analysis will be needed, together with procedures refined to reduce the error bars. Being a quasi-continuous wave device, there is the chance possibility of the thermocouples hitting axial minima. One of the important parameters to vary (slightly) is thus the distance of the calorimeter from the transducer if a reliable set of results is required.

5. Conclusion

The calorimeter described has a number of potential applications ranging from the simple measurement of attenuation in penetrable media such as liquids, to the separation of the absorption contribution to the attenuation on inhomogeneous materials, and the measurement of 'dose' (albeit in a very limited sense) in biological materials. The investigations reported here were restricted by the equipment available although the device is clearly suitable for attenuation and dose rate measurement. However with attention to the manufacture of reliable thermocouple probes, to the digitization procedures and the geometrical design of the calorimeter, the device would appear to be a useful adjunct to the ultrasonic measurement techniques currently available. The separation of the scattering component of the attenuation will require much improved circuitry and a full error analysis.

References

[1] J. D. AINDOW, *Measurement of fluctuations in ultrasonic waves propagating in homogeneous media*, PhD Thesis, University of Surrey 1983.

[2] L. W. ANSON, R. C. CHIVERS and J. ADACH, *Ultrasonic radiation force devices with non-linear suspensions mechanical* (1987).

[3] L. W. ANSON, R. C. CHIVERS, *A rugged strain gauge therapeutic ultrasound exposimeter*, J. Med. Eng. Tech., **6**, 150–152 (1892).

[4] V. N. BINDAL, A. KUMAR and R. C. CHIVERS, *On the float method of measuring ultrasonic output*, Acustica **53**, 219–223 1983.

[5] J. A. CAMPBELL, R. C. WAAG, *Measurement of calf liver ultrasonic differential and total cross sections*, J. Acoust. Soc. Am., **75**, 603–611 (1984).

[6] A. A. CHEVNENKO, J. Kh. YUTCHANANOV, *Two frequency echo recording method for differential tumour diagnosis*, Med. Tekhn., **3**, 40–41 (1971).

[7] R. C. CHIVERS, *Tissue characterisation*, Ultrasound Med. Biol., **7**, 1–20 (1981).

[8] S. COLOMBATI, S. PETRALIA, *Absorbimento di ultrasuoni in tessuti animali*, Ric. Sci., **20**, 71–78 (1950).

[9] F. DUNN, P. D. EDMONDS and W. J. FRY, *Absorption and dispersion of ultrasound in biological media*, tn: Biological Engineering [Ed.] H. P. Schwan, pp. 214–251, McGraw Hill, New York 1969.

[10] K. DUSSIK, D. J. FRITCH, *Measurements of articular tissue with ultrasound*, Am. J. Phys. Med., **37**, 160–165 (1958).

[11] M. J. FARMERY, T. A. WHITTINGHAM, *A portable radiation force balance for use with diagnostic ultrasonic equipment*, Ultrasound Med. Biol., **3**, 373–379 (1978).

[12] W. J. FRY, R. B. FRY, *Determination of absolute sound levels and acoustic absorption coefficient by thermocouple probes–theory*, J. Acoust. Soc. Am., **26**, 294–310 (1954).

[13] F. E. FYKE, J. F. GREENLEAF, *Continuous wave measurements of acoustic attenuation in an oil/polymer mixture*, Ultrasound Med. Biol., **5**, 87–89 (1979).

[14] P. A. LEWIN, *Miniature piezoelectric polymer ultrasonic hydrophone probes*, Ultrasonics, **19**, 213–216 (1981).

[15] F. A. LLOYD, *Energy measurement*, in: Ultrasonic techniques in biology and medicine, [Ed.] B. Brown and D. Gordon pp. 46–86 Iliffe Books, London 1967.

[16] D. K. NASSIRI, D. NICHOLAS, C. R. HILL, *Attenuation of ultrasound in skeletal muscle*, Ultrasonics, **17**, 230–232 (1979).

[17] D. K. NASSIRI, C. R. HILL, *The differential and total bulk acoustic scattering cross sections of some human and animal tissues*, J. Acoust. Soc. Am., **79**, 2034–2047 (1986).

[18] K. J. PARKER, *The thermal pulse decay technique for measuring ultrasonic absorption coefficients*, J. Acoust. Soc. Am., **74,** 1356–1361 (1983).

[19] K. J. PARKER, *Ultrasonic attenuation and absorption in liver tissue*, Ultrasound Med. Biol., **9,** 363–369 (1983).

[20] R. C. PRESTON, D. R. BACON, A. J. LIVETT and K. RAJENDRAN, *PVDF membrane hydrophone performance properties and their relevance to the measurement of the acoustic output of medical equipment*, J. Phys., **E16,** 786–796 (1983).

[21] S. REANTRAGOON, R. C. CHIVERS, *Calorimetric assessment of propagation parameters, exposure and dose rate*, in: Physics in Medical Ultrasound, [Ed.] K. Martin and D. H. Evans IPSM, London 1987.

[22] S. REANTRAGOON, R. C. CHIVERS, *A procedure for cutting soft tissue speciments of regular shape*, Ultrasound Med. Biol., **13,** 364–367 L (1987).

[23] J. A. ROONEY, *Determination of acoustic power output in the microwatt-milliwatt range*, Ultrasound Med. Biol., **1,** 1–4 (1973).

[24] A. SHITZER, *Studies of heat transfer in animals*, in: Topics in transport phenomena, [Ed.] C. Gutfinger, Halsted Press 1975.

[25] G. R. TORR, D. J. WATMOUGH, *A constant flow calorimeter for the measurement of acoustic power at megahertz frequencies*, Phys. Med. Biol., **22,** 444–450 (1977).

[26] P. N. T. WELLS, *Biomedical ultrasonics*, Academic Press, London 1977.

[27] P. N. T. WELLS, M. A. BULLEN, D. M. FOLLETT, H. F. FREUNDLICH and J. A. JAMES, *The dosimetry of small ultrasonic beams*, Ultrasonics, **1,** 106–110 (1963).

[28] J. K. ZIENIUK, B. EVANS, *The influence of thermal parameters on making ultrasonic power measurements by a calorimeter method*, Acustica, **25,** 47–52 (1971).

[29] J. K. ZIENIUK, R. C. CHIVERS, *Measurement of ultrasonic exposure with radiation force and thermal methods*, Ultrasonics, **14,** 161–172 (1976).

Received October 27, 1987.

ARCHIVES OF ACOUSTICS
14, 3–4, 173–179 (1989)

DEVIATION OF THE ACOUSTIC PRESSURE TO PARTICLE VELOCITY RATIO FROM THE ϱc VALUE IN LIQUIDS AND SOLIDS AT HIGH PRESSURES

LESZEK FILIPCZYŃSKI, ANNA GRABOWSKA

Department of Ultrasonics, Institute of Fundamental Technological Research,
Polish Academy of Sciences
(00-049 Warszawa, Świętokrzyska 21)

Basing on fundamental equations of nonlinear acoustics the authors determined the ratio of the acoustic pressure to the particle velocity p_a/u for a travelling plane wave as a function of condensation. Nonlinear effects in the medium depend on the nonlinearity parameter B/A and on the maximum pressure. As the measure of those nonlinearities, the deviation of the p_a/u ratio from the $\varrho_0 c_0$ value was introduced and computed for water, fat tissue, steel and aluminium alloy, up to pressures of 100 MPa. The B/A value for steel and aluminium could be determined basing on acousto-elastic properties of these metals.

In this way it could be shown that the capacitance hydrophone, used for measurements in lithotripsy, does not introduce nonlinearities caused by its steel front plate when measuring nonlinear acoustic pressure fields. For, the mentioned deviation is two orders of magnitude lower for steel than for water and soft tissues.

Key words: Hydrophone, nonlinearity, lithotripsy.

Opierając się na podstawowych związkach akustyki nieliniowej autorzy wyznaczyli stosunek akustycznego ciśnienia do prędkości cząstkowej p_a/u dla płaskiej fali bieżącej jako funkcję kondensacji. Nieliniowe efekty zależą od parametru nieliniowości B/A i od maksymalnego ciśnienia akustycznego w ośrodku. Jako miarę nieliniowości autorzy wprowadzili odchylenie stosunku p_a/u od wielkości $\varrho_0 c_0$ i wyznaczyli wartość tego odchylenia dla wody, tkanki tłuszczowej, stali i stopu aluminiowego dla ciśnień dochodzących do 100 MPa. Wyznaczono wartość B/A dla stali i stopu aluminiowego w oparciu o akusto-sprężyste własności tych metali.

Autorzy wykazali, że hydrofony pojemnościowe, stosowane w pomiarach w litotrypsji, nie wnoszą nieliniowości powodowanych przez ich stalową czołową płytę podczas pomiarów nieliniowych pól o dużych ciśnieniach akustycznych. Albowiem wspomniane odchylenie jest dwa rzędy wielkości mniejsze w stali niż w wodzie i w tkance tłuszczowej.

1. Introduction

The authors proposed and described in a previous paper [6] capacitance hydrophones for measurements of high pressure shock wave pulses, occuring in lithotripsy. At the pressure values of 100 MPa ($\sim$1000 atm) there exist nonlinear effects in the medium penetrated by the shock wave. For the study of these effects the authors have developed an experimental lithotrypsy system with shock wave pressures of 40 MPa [6] and recently even higher, equal to 62 MPa [7]. In such

a situation it is necessary to use in the measurement system a perfect linear hydrophone to eliminate any additional nonlinear effects which be caused by the measurement device. The solid and plastic piezoelectric hydrophones, which are used in measurements of acoustical fields in lithotripsy, do not assure the indispensable linearity and moreover, they are quickly damaged under the action of schock waves of such high pressures.

The purpose of this paper was to investigate the linearity of the proposed capacitance hydrophones, since they promissed to be linear due to elastic properties of metals. For, the main part of the capacitance hydrophone, its front plate, which is penetrated by the wave, is made of metal. It was also intended to introduce a practical nonlinearity measure connecting both, the medium properties and the pressure value.

2. Basic relations

The dependence between pressure p and density ϱ for the adiabatic process is nonlinear. Expanding the state equation $p = p(\varrho, S)$ around the constant values of ϱ_0 and entropy S_0 (since the acoustic wave is basically an isentropic process) one can write [1]

$$p = p_0 + \left(\frac{\partial p}{\partial \varrho}\right)_{\varrho_0 S_0} (\varrho - \varrho_0) + \frac{1}{2!}\left(\frac{\partial^2 p}{\partial \varrho^2}\right)_{\varrho_0 S_0} (\varrho - \varrho_0)^2 + \ldots, \tag{1}$$

where p is the instantaneous pressure, p_0 – hydrostatic pressure. Hence the acoustic pressure can be denoted as the difference

$$p_a = p - p_0. \tag{2}$$

The acoustic pressure can be expressed in an another form

$$p_a = As + Bs^2/2! + Cs^3/3! + Ds^4/4! + \ldots \tag{3}$$

where $s = (\varrho - \varrho_0)/\varrho_0$ denotes condensation and

$$A = \varrho_0 \left(\frac{\partial p_a}{\partial \varrho}\right)_{\varrho_0 S_0} = \varrho_0 c_0^2; \quad B = \varrho_0^2 \left(\frac{\partial^2 p_a}{\partial \varrho^2}\right)_{\varrho_0 S_0};$$
$$C = \varrho_0^3 \left(\frac{\partial^3 p_a}{\partial \varrho^3}\right)_{\varrho_0 S_0}; \quad D = \varrho_0^4 \left(\frac{\partial^4 p_a}{\partial \varrho^4}\right)_{\varrho_0 S_0}. \tag{4}$$

ϱ_0 and ϱ denote mean and instantaneous density of medium. c_0 – wave velocity for small amplitudes, S_0 – constant enthropy. It was found experimentaly for water [2] $B/A = 5.2$, $C/A = 42$, $D/A = 437$. For the pressure $p_a = 100$ MPa the value of $s = 0.04$ (in water) and contributions of the terms with coefficients C and D to the series (3) are equal 1% and 0.1% only. Therefore, the ratio B/A is sufficient to be taken into consideration when calculating the acoustic pressure p_a from Eq. (3). For various soft tissues the nonlinearity parameter B/A was determined experimentally by DUNN et al. [5]. In solids it was measured for some crystals only [3].

The particle velocity u can be found as a function of s from expression [1]

$$u = \pm \frac{2c_0}{B/A}[1-(1+s)^{B/(2A)}]. \tag{5}$$

3. Acoustic impedance and the ratio p_a/u

In linear acoustic for a plane, travelling wave the ratio between the acoustic pressure and particle velocity equals $\varrho_0 c_0$. This equality is no more valid for nonlinear waves. Let us determine the ratio p_a/u. From Eqs. (3) and (5) one obtains

$$p_a/u = \pm \varrho_0 c_0 s\left[1+\frac{B}{2A}s\right]\frac{B}{2A}[1-(1+s)^{B/(2A)}]^{-1}. \tag{6}$$

Expanding Eq. (5) into the Taylor series ($s << 1$)

$$u = \mp c_0 s\left[1+\frac{s}{2}\left(\frac{B}{2A}-1\right)+\ldots\right]. \tag{7}$$

From Eqs. (3) and (7) one obtains p_a/u in a more simple form

$$p_a/u = \mp \varrho_0 c_0\left(1+\frac{B}{2A}s\right)\Big/\left[1+\frac{s}{2}\left(\frac{B}{2A}-1\right)\right] \underset{s\to 0}{\to} \varrho_0 c_0 \tag{8}$$

The last expression tends to $\varrho_0 c_0$ when s approaches 0. This case corresponds to the basic relation of linear acoustics.

The ratio p_a/u should not be considered as the acoustic impedance, bacause it depends on the wave amplitude. Since the profile of the propagating wave changes with distance, its harmonic contents and the spectrum of the p_a/u ratio changes too. Because $s = s(\omega)$ then one could determine the ratio $p_a(n\omega)/u(n\omega)$ for every harmonic n. In such a case the ratio p_a/u becomes the impedance for the given harmonic. However, these impedances are not additive [8].

The condensation s can be determined directly from Eqs. (3) and (4) as the function of acoustic pressure p_a and B/A ratio (when $C = D = 0$)

$$s = \frac{A}{B}\left[\sqrt{1+2Bp_a/(A\varrho_0 c_0^2)}-1\right]. \tag{9}$$

The ratio p_a/u, expressed by Eqs. (6) or (8), depends finally on the acoustic pressure p_a and the B/A ratio. The deviation of this ratio from the acoustic impedance $\varrho_0 c_0$ characterizes the nonlinearity of the medium for a given acoustic pressure. The relative value of this deviation equals

$$\Delta = \left|\frac{p_a/u-\varrho_0 c_0}{\varrho_0 c_0}\right| \underset{s<<1}{\approx} \frac{1}{2}\left(1+\frac{B}{2A}\right)\frac{p_a}{\varrho_0 c_0^2}, \tag{10}$$

as can be found from Eqs. (8) and (9).

Figure 1 shows the values of Δ and s calculated from Eqs. (6), (8) and (9) for water and fat tissue ($B/A = 11$) as the function of acoustic pressure. Eq. (8) gives a little higher value for the fat issue than Eq. (6) for $p > 50$ MPa (see Fig. 1). Numerical values were obtained by means of the personal computer IBM AT using double precision.

For acoustic pressures of 100 MPa, which are typical in lithotrypsy, the deviation Δ for water and fat tissue equals 7% and 12%, respectively.

It should be noticed that the calculated p_a/u value corresponds to the maximum value of s which may occur in the propagating wave as a function of time.

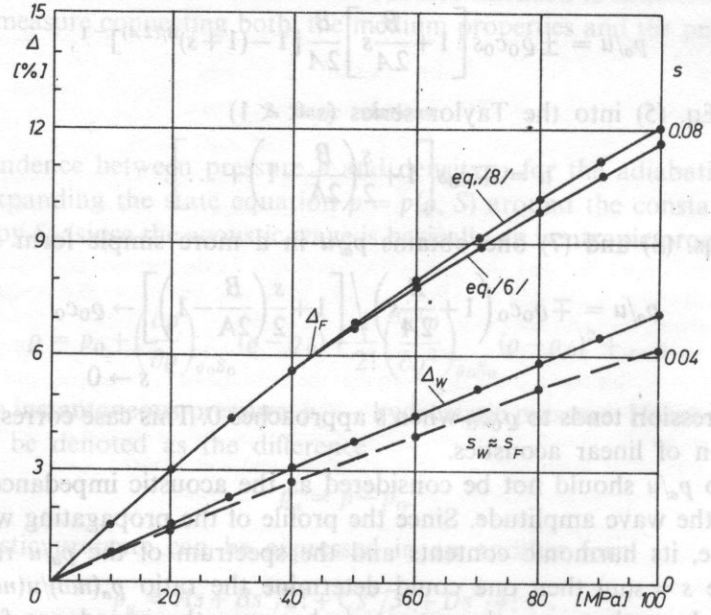

Fig. 1. The relative deviation Δ and condensation s (dashed line) versus acoustic pressure p_a, calculated for water and fat having the maximum value of B/A among soft tissues. Index W denotes water, F — fat tissue

4. Nonlinearity parameters for metals

Nonlinearity of typical metals is expressed by means of elasticity coefficients of third and higher orders. To compare the nonlinearity parameters of liquids and tissues with those of metals it was necessary to determine the B/A ratio for steel and aluminium, which are used for the construction of capacitance hydrophone.

Let us determine the ratio B/A for steel and aluminium basing on elasto-acoustic coefficients for those metals. Nonlinearity of solids causes the change of wave velocity under the action of stresses.

In such materials as steel and aluminium alloys the velocity changes can be

described by the formula [4]

$$(c-c_0)/c_0 = \beta\sigma, \tag{11}$$

for stresses σ below the yield stress [9]. Equation (11) can be found from stress–velocity measurements usualy used for determination of third order elasticity coefficients in solids.

In Eq. (11) c denotes velocity of longitudinal wave, β is the acousto-elastic constant for longitudinal waves propagating in the direction of uniaxial stress σ. For carbon steel $\beta = -12.1 \times 10^{-11}$ Pa^{-1}, and for aluminium alloy (dural) $\beta = -77.5 \times 10^{-11}$ Pa^{-1} [4].

The rate at which a particular disturbance of the wave propagates through the medium equals [1]

$$c = \mp c_0(1+s)^{((B/2A)-1)}. \tag{12}$$

Expanding this equation one obtains

$$c = c_0\left[1+\left(\frac{B}{2A}+1\right)s+\frac{B}{2A}\left(\frac{B}{2A}+1\right)s^2+\ldots\right]. \tag{13}$$

Coefficients β are determined experimentally by measuring the flight time of the maximum amplitude of the ultrasonic pulse which propagates through a metal sample for various static stresses.

Equation (13) can be transformed into the expression

$$(c-c_0)/c_0 = [B/(2A)-1]s. \tag{14}$$

Expanding the root in Eq. (9), neglecting the terms of higher orders and putting into Eq. (14) one obtains

$$(c-c_0)/c_0 = [B/(2A)-1]p_a/(\varrho_0 c_0^2). \tag{15}$$

The last expression is analogeous to Eq. (11).

It was found experimentally [9] that β is independent on static stresses below the elasticity limit. Therefore it seems to be justified to assume that the relation (11) is valid for dynamic stresses σ too. In such a case, taking into account opposite signs of stresses and pressures one obtains from Eqs. (11) and (15)

$$B/A = 2(-\beta\varrho_0 c_0^2-1). \tag{16}$$

The corresponding values for steel and aluminium alloy (dural) determined from this formula are equal to $B/A = 3.5$ for steel and 13.5 for aluminium. Now the values of condensation s and deviation Δ could be determined for these materials basing on Eqs. (9), (10), (6) and (8) (Fig. 2). For the acoustic pressure of 100 MPa for steel and aluminium Δ equals 0.05% and 0.36%, respectively. The obtained value for steel is 2 orders of magnitude lower than for water and fat tissue (see Fig. 1 and 2). Therefore, the steel front plate of the capacitance hydrophone can be considered to be linear even for pressures as high as 100 MPa.

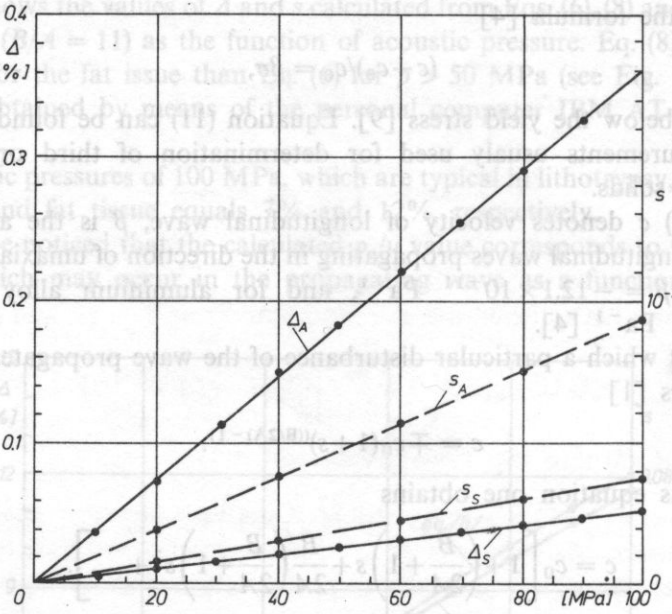

Fig. 2. The relative deviation Δ and condensation s (dashed line) versus acoustic pressure p_a, calculated for steel and for aluminium alloy. Index S denotes steel, A – aluminium alloy

For measurements of shock wave pressures used in lithotripsy the authors applied a capacitance hydrophone with the front plate made of a special steel (Polish mark 50HSA) which is characterized by a high elasticity limit of 1200 MPa. Its design and obtained measurement results were published elsewhere [6], [7].

5. Conclusions

a) Nonlinear acoustic effects occuring in various media are dependent on the ratio of nonlinearity parameters B/A and on the applied acoustic pressure. For the plane travelling wave the deviation Δ (see Eq. (10)) of the acoustic pressure to particle velocity ratio from the $\varrho_0 c_0$ value can be considered as a nonlinearity measure of these effects.

b) Basing on acousto-elastic properties of steel and aluminium alloy it was possible to determine for them B/A ratio (Eqs. (16) assuming stress to be lower than the elasticity limit.

c) It follows from deviations Δ, determined for water, fat tissue, steel and aluminium alloy, that steel is characterized by the lowest nonlinearity, 2 orders of magnitude lower than for water or fat tissue. Therefore, capacitance hydrophones do not introduce practically any additional nonlinearity caused by their front plates made of steel, into the measured nonlinear fields.

d) The calculated value of Δ makes it possible to estimate the error of pressure determination in the propagating plane wave from the approximate relation $p_a = \varrho_0 c_0 u$ when the particle velocity u was measured and vice versa.

References

[1] R. T. BEYER, *Nonlinear acoustics*, in: Physical acoustics [Ed.] W. Mason, Academic Press, New York 1965 vol. II B, 231-241.

[2] L. BJÖRNO, K. BLACK, *Higher-order acoustic nonlinearity parameters of fluids*, in: Nonlinear deformation waves [Eds.] U. Nigul, J. Engelbrecht, Springer, Berlin 1983, 355.

[3] M. BREAZEALE, *Propagation of ultrasonic waves in nonlinear solids of cubic, hexagonal and trigonal symmetry*, 11-th Intern. Congr. on Acoustics, Paris, vol. 2, 1983, 145–148.

[4] J. DEPUTAT, *Properties and utilization of the elasto-acoustic effect for measurement of residual stresses* (in Polish), Institute of Fundamental Technological Research, Report nr 28, Warsaw 1987, p. 23, 24.

[5] F. DUNN, W. LAW, L. FRIZELL, *The ultrasonic nonlinearity parameter for biological media*, Archives of Acoustics, 9, 1–2 (1984) 29–34.

[6] L. FILIPCZYŃSKI, J. ETIENNE, A. GRABOWSKA, T. WASZCZUK, R. KOWALSKI, M. GRYZIŃSKI, J. STANISŁAWSKI, *An experimental lithotripsy system for the study of shock wave effects.* Archives of Acoustics, **14**, 1–2 (1989) 11–27.

[7] L. FILIPCZYŃSKI, J. ETIENNE, *Capacitance hydrophone for pressure determination in lithotripsy*, Ultrasound in Medicine and Biology, 16 (1990).

[8] M. KWIEK, *Akustyka laboratoryjna* I. *Podstawy akustyki teoretycznej*, PWN, Poznań 1968, 127.

[9] I. MIGNOGNA, A. CLARK, B. RATH, C. VOLD, *Acoustic stress measurement in aluminium and steel considering differences in texture*, in: Proc. Review of progress in quantitative NDE [Eds.] D. Thomson, D. Chimenti, vol. 5, 201–206 Plenum Press, New York 1986.

Received December 29, 1988.

ARCHIVES OF ACOUSTICS
14, 3–4, 181–190 (1989)

ACOUSTICAL SHADOW OF A SPHERE IMMERSED IN WATER. II

LESZEK FILIPCZYŃSKI, TAMARA KUJAWSKA

Department of Ultrasonics, Institute of Fundamental Technological Research Polish Academy of Sciences
(00–049 Warszawa, ul. Świętokrzyska 21)

Assuming a continuous plane wave incident on a rigid sphere immersed in water the authors computed directivity characteristics of the acoustic pressure behind the sphere. The obtained results were converted and presented in the rectangular coordinate system in the form of acoustic isobars for *ka* values in the range between 4π and 200π.

Assuming the -6dB isobar to be the shadow boundary, the authors found an almost linear proportionality between the relative shadow range and the *ka* parameter. The proportionality coefficient was determined and hence a basic formula was given which connects the shadow range, the sphere radius with the wavelength. It can be useful in many ultrasonic problems.

Key words: acoustical shadow, sphere, water, isobar, shadow range.

Przyjmując płaską falę ciągłą padającą na sztywną kulę w wodzie, autorzy wyznaczyli charakterystyki kierunkowości ciśnienia akustycznego za kulą. Uzyskane wyniki przeniesiono w układ współrzędnych prostokątnych w postaci akustycznych izobar dla wartości *ka* w zakresie od 4π do 200π.

Przyjmując izobarę -6 dB jako granicę cienia, autorzy znaleźli liniowy związek między względnym zasięgiem cienia a parametrem *ka*. Na tej podstawie uzyskali zasadniczy wzór łączący zasięg cienia, promień kuli z długością fali. Wzór ten może być stosowany w wielu zagadnieniach ultradźwiękowych.

1. Introduction

In the previous papers [3], [2], [1] the authors determined the shadow arising behind a rigid sphere immersed in water for the case of an incident continuous plane wave. Due to axial symmetry computation results were presented in the form of directivity diagrams in two spherical coordinates (r, θ) with angular resolution equal to $\Delta\theta = 1°$ (Fig. 1). The shadow range r_{-6dB}, equal to the distance at which one observs a 6 dB drop relatively to the incident wave pressure, was determined, as well as the corresponding angles to θ_{-6dB} for some *ka* values.

The purpose of the present paper is the determination of the acoustic pressure field for a greater range of *ka* values with a higher angle resolution and hence the determination of isobar curves behind the sphere in rectangular space coordinates.

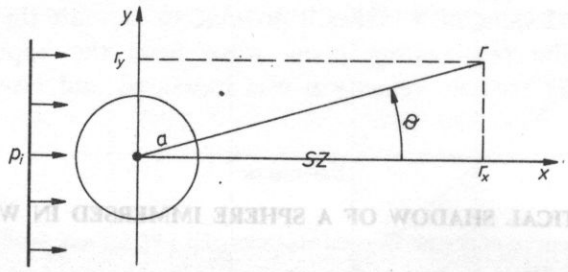

Fig. 1. The spherical coordinate system with the plane wave (p_i) incident on the sphere and the shadow zone (SZ). a – radius of the sphere, r, θ – spherical coordinates, r_x, r_y – projections of r on the symmetry axis x and on the arbitrary axis y, perpendicular to x and passing through the sphere center, respectively

Moreover, the authors intended to generalize the obtained numerical results to present them in the form of a formula enabling simple calculations of shadow range behind the rigid sphere.

2. Acoustic isobars

The acoustic shadow behind the rigid sphere was determined in the previous papers [3], [1] by calculating the acoustic pressure p_s which is equal to the sum of the incident plane wave and the reflected wave pressures. It has the form

$$p_s = \exp(-jkr\cos\theta) - \sum_{m=0}^{\infty} (-j)^{m+1}(2m+1)\sin\eta_m(ka)\exp[j\eta_m(ka)] \times P_m(\cos\theta)h_m^{(2)}(kr), \quad (1)$$

where r, θ are coordinates of the polar system, a radius of the sphere, $k = 2\pi/\lambda$, λ wavelength in the surrounding medium, $\eta_m = \text{arc tan}[-j_m'(ka)/n_m'(ka)]$, j_m, n_m' derivatives of spherical Bessel and Neumann functions, $h_m^{(2)}$ spherical Hankel function, P_m Legendre polynomial, m natural number, $j = \sqrt{-1}$.

In general p_s is a function of the following variables

$$p_s = f(k, a, r, \theta). \quad (2)$$

The dependence on the distance r and on the sphere radius a is represented in Eq (1) by dimensionless products kr and ka respectively. The parameter ka characterizes the shadow form and kr can be considered as a variable. It will be convenient to present the results of our computations in general coordinates introducing the ratio of the two products equal to

$$kr/ka = r/a \quad (3)$$

From Eq. (1) directicity diagrams $p_s = f(\theta)$ were computed for the acoustic pressure behind the sphere for various values of r/a changing the angle by steps equal to $\Delta\theta = 0.1°$. The obtained results were converted and presented in rectangular

coordinates r_x/a, r_y/a in the form of acoustic isobars. They are presented in the lower part of Figs. 2–9 with respect to the acoustic pressure level (0 dB) of the plane continuous wave incident on the rigid sphere. Its center is placed at the origin of coordinates $r_x/a = r_y/a = 0$. The plane wave travels from left to right. On the top of the Figures there are presented angles θ corresponding to the pressure drops of 3, 6 and 9 dB which were obtained from computed directivity characteristics. The r_y/a axis is many times enlarged when comparing with the r_x/a axis. The -6 dB isobars were chosen to be the boundary of the shadow according to our previous definition [3], [1].

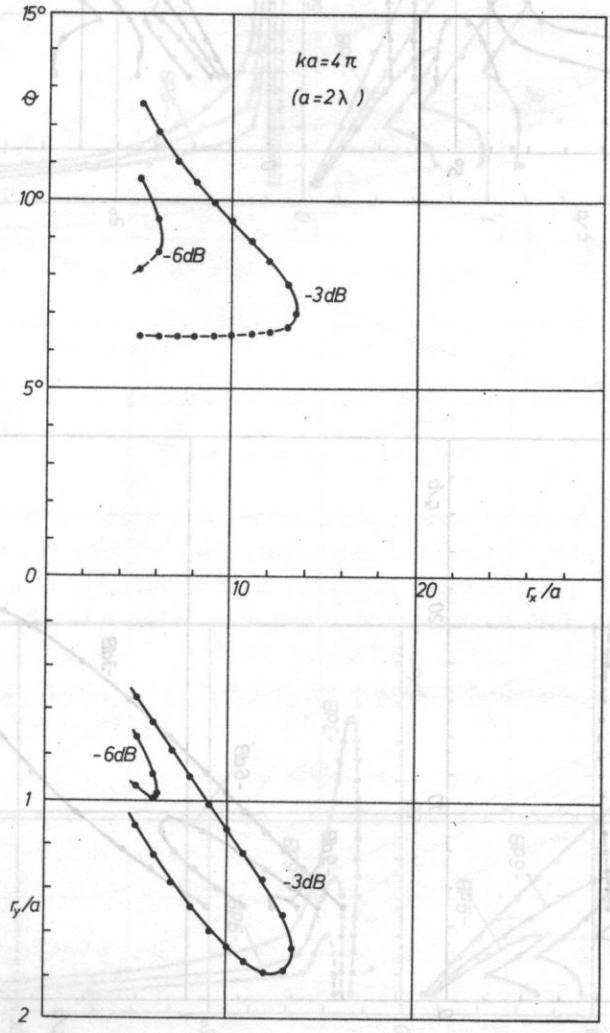

Fig. 2. Angles θ corresponding to adequate pressure drops (top) and acoustic isobars behind a rigid sphere computed for $ka = 4\pi$ (bottom)

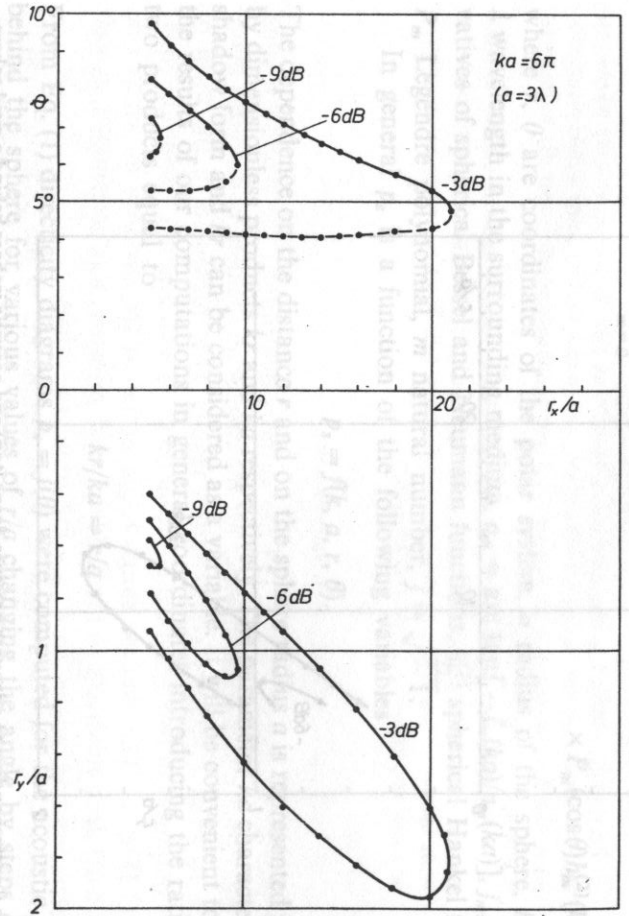

Fig. 3. As in FIG. 2, $ka = 6\pi$

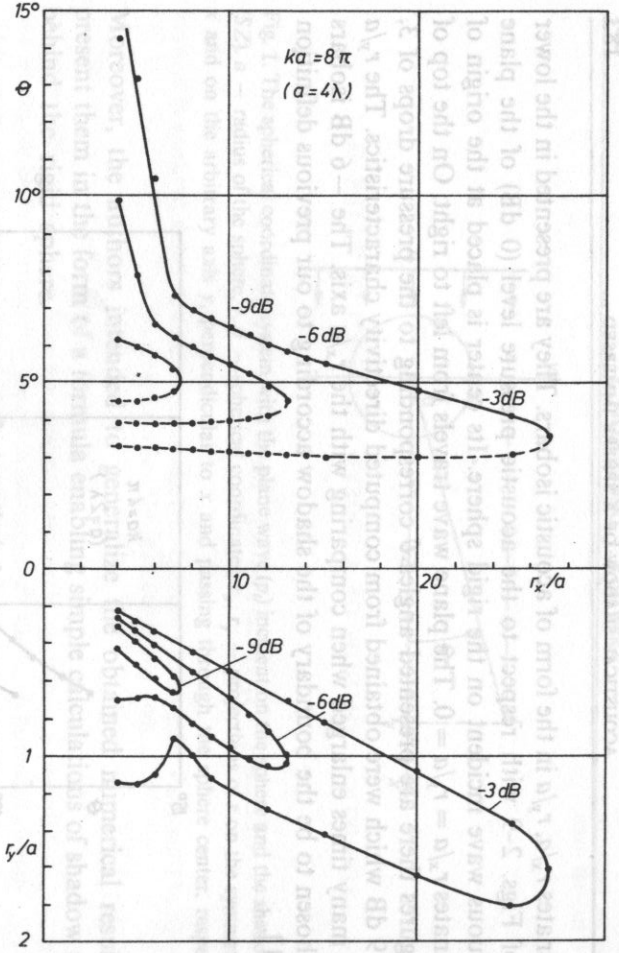

Fig. 4. As in FIG. 2, $ka = 8\pi$

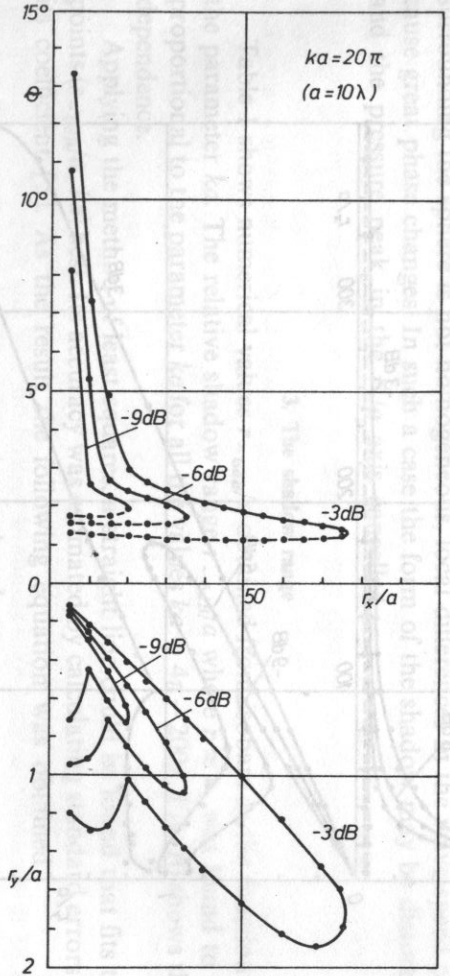

Fig. 5. As in FIG. 2, $ka = 20\pi$

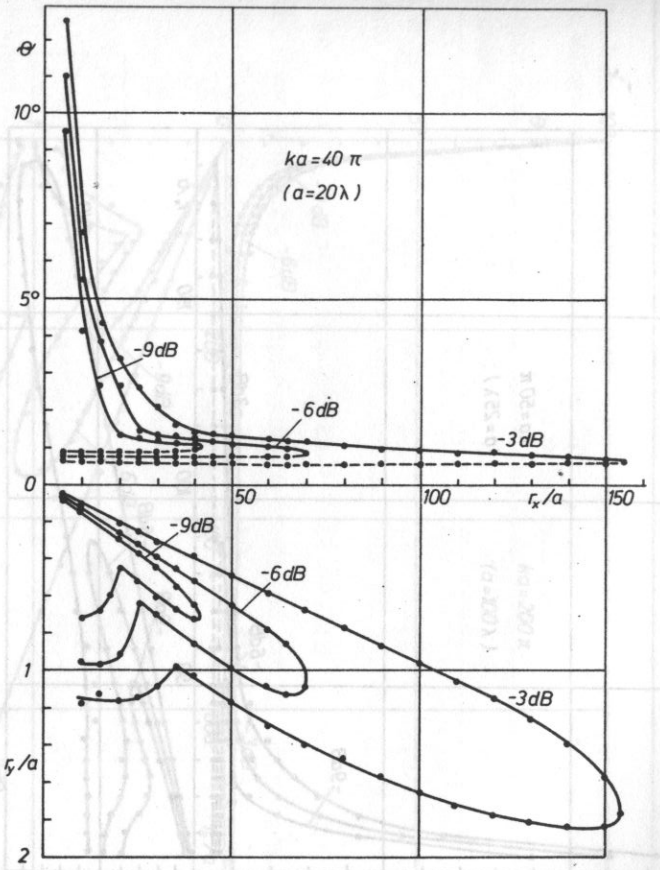

Fig. 6. As in FIG. 2, $ka = 40\pi$

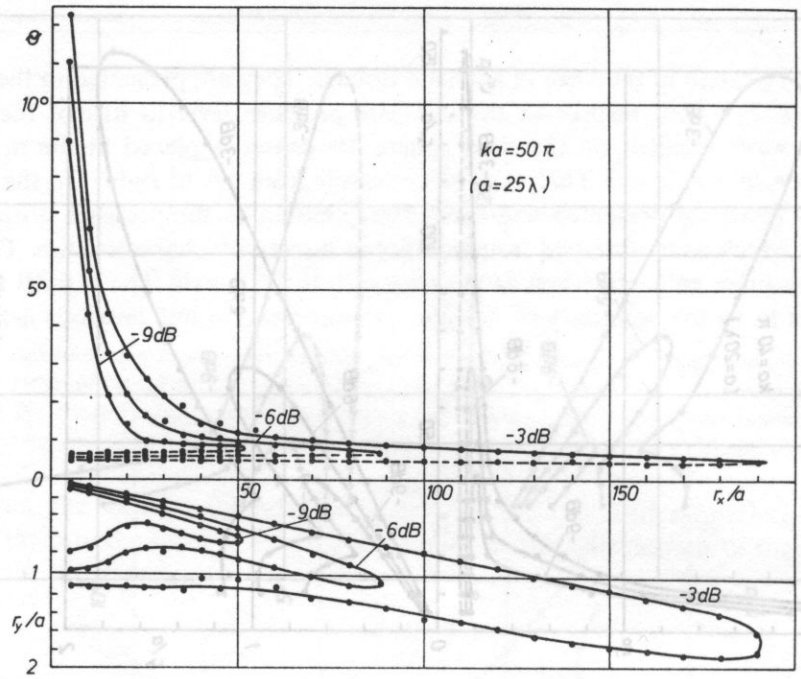

Fig. 7. As in FIG. 2, $ka = 50\pi$

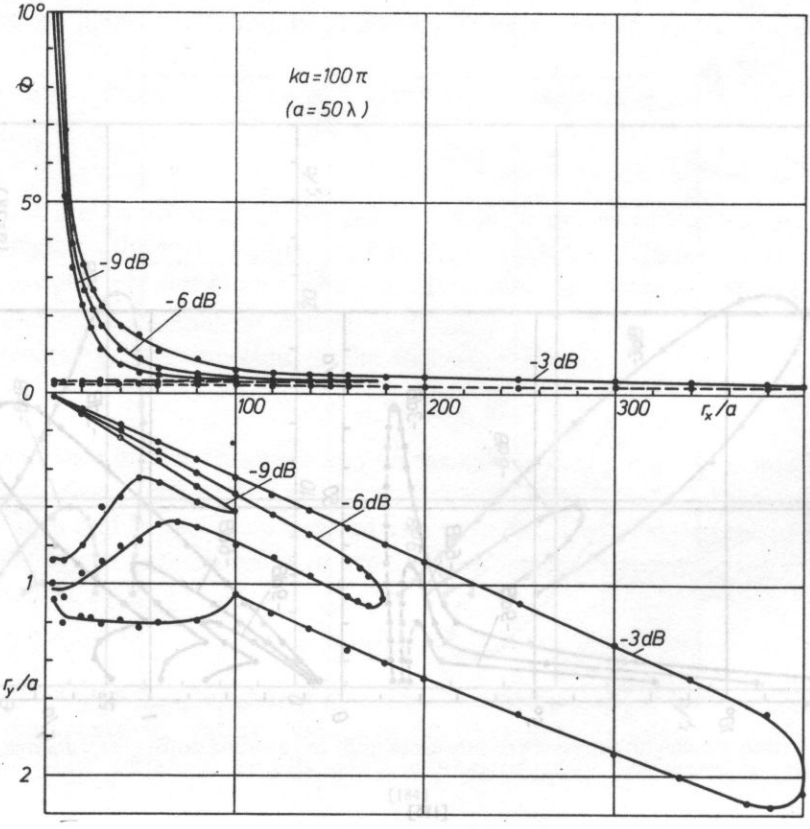

Fig. 8. As in FIG. 2, $ka = 100\pi$

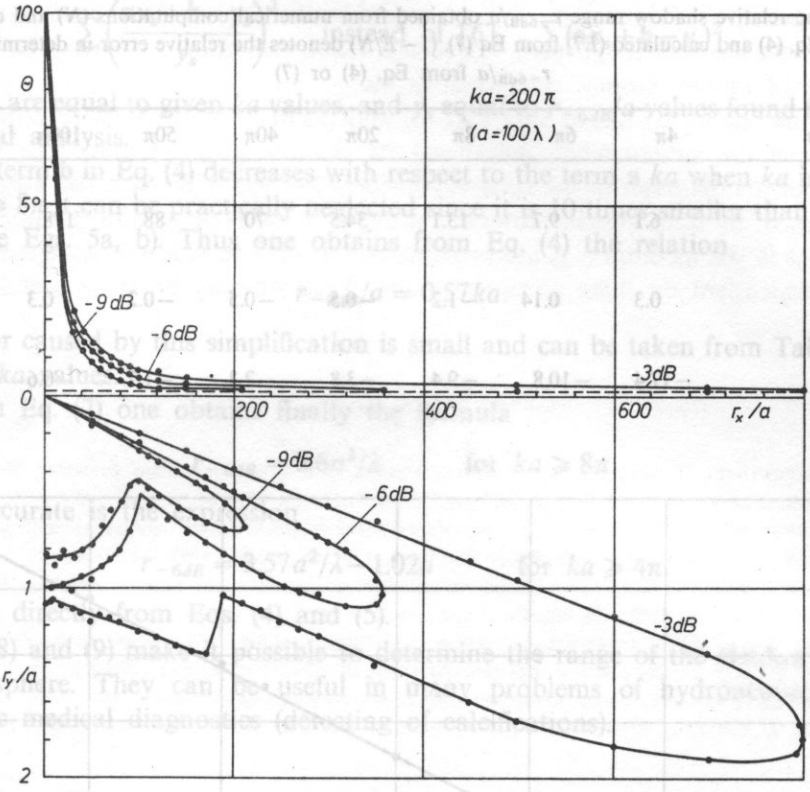

Fig. 9. As in FIG. 2, $ka = 200\pi$

It is interesting to notice that the acoustic pressure along the r_x/a axis is quite large. One does not observe there any shadow. It results from the coherency of acoustic waves, as it was discussed in details in the paper [3]. When the medium surrounding the sphere is not homogeneous, local differences in the wave speed can cause great phase changes. In such a case the form of the shadow may be distorted and the pressure peak in the r_x/a axis cancelled.

3. The shadow range

Table 1 shows numerical values r_{-6dB}/a obtained from isobars as the function of the parameter ka. The relative shadow range r_{-6dB}/a where $r \approx r_x$ was found to be proportional to the parameter ka for all the values $ka = 4\pi - 200\pi$. Fig. 10 shows this dependence.

Applying the method of least squares, a straight line could be found that fits the points $(r_{-6dB}/a, ka)$ best. Its accuracy was estimated by calculating standard errors of its coefficient [5]. As the result the following equation was obtained

$$r_{-6dB}/a = \mathbf{a} \cdot ka + \mathbf{b}, \quad (4)$$

Table 1. The relative shadow range r_{-6dB}/a obtained from numerical computations (N) and calculated ($E4$) from Eq. (4) and calculated ($E7$) from Eq (7). $(1-E/N)$ denotes the relative error in determination of r_{-6dB}/a from Eq. (4) or (7)

ka	4π	6π	8π	20π	40π	50π	100π	200π
$N=\frac{r_{-6dB}}{a}$	6.1	9.7	13.1	34.5	70	88	178	358
$\frac{N-E4}{N}\%$	0.3	0.14	−1.2	−0.5	−0.5	−0.2	0.3	0.6
$\frac{N-E7}{N}\%$	−17.4	−10.8	−9.4	−3.8	−2.3	−1.7	−0.6	−0.04

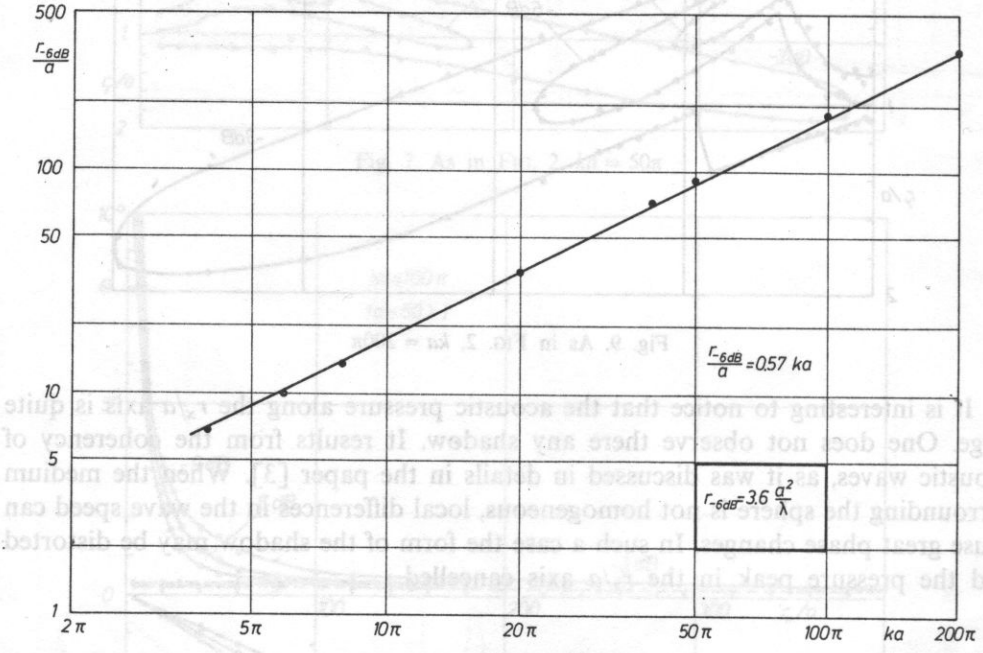

Fig. 10. The dependence of the relative shadow range r_{-6dB}/a on the ka value obtained from numerical analysis

where

$$\mathbf{a} = 0.568 \pm 0.002 \quad \text{and} \quad \mathbf{b} = -1.02 \pm 0.48. \tag{5a, b}$$

This equation was obtained by minimizing the relative error instead of the absolute one, as it is usually realized by a standard procedure. For this purpose we minimized the sum of the squares of the errors

$$\sum\left(\frac{\mathbf{a}x_s+\mathbf{b}-y_s}{y_s}\right)^2 \quad \text{instead of [6]} \quad \sum(\mathbf{a}x_s+\mathbf{b}-y_s)^2, \tag{6a, b}$$

where x_s are equal to given ka values, and y_s equal to r_{-6dB}/a values found from our numerical analysis.

The term **b** in Eq. (4) decreases with respect to the term **a** ka when ka increases. For $ka \geqslant 8\pi$ it can be practically neglected since it is 10 times smaller than the first term (see Eqs. 5a, b). Thus one obtains from Eq. (4) the relation

$$r_{-6dB}/a = 0.57ka. \tag{7}$$

The error caused by this simplification is small and can be taken from Table 1 for various ka values.

From Eq. (7) one obtains finally the formula

$$r_{-6dB} = 3.6a^2/\lambda \qquad \text{for } ka \geqslant 8\pi \tag{8}$$

More accurate is the expression

$$r_{-6dB} = 3.57a^2/\lambda - 1.02a \qquad \text{for } ka \geqslant 4\pi \tag{9}$$

obtained directly from Eqs. (4) and (5).

Eqs (8) and (9) make it possible to determine the range of the shadow behind a rigid sphere. They can be useful in many problems of hydroacoustics and ultrasonic medical diagnostics (detecting of calcifications).

4. Discussion and conclusions

Numerical results of acoustic pressure computation made it possible to present acoustic isobars behind a rigid sphere for a plane continuous wave incident on it and for various ka values in the range between 4π and 200π.

The isobars give an insight into the shadow forming behind the sphere. One should remember that they result as an approximation of calculated directivity diagrams. Fig. 8 of our previous paper [3] gives an example of exact angular distributions of the acoustic pressure behind the sphere. To obtain an adequate isobar it was necessary to draw a mean curve from pressure ondulations arising as the function of the angle θ. However, the applied approximation does not introduce any greater changes in the shape of isobars. The calculation points (Figs. 2–9) were chosen densely enought to obtain the proper shape of isobars.

It was observed that there exists an almost linear proportionality between the relative shadow range r_{-6dB}/a and the ka parameter. The proportionality coefficient could be determined and hence a basic formulae (8) and (9) were found connecting the shadow range, the sphere radius with the wavelength. Their accuracy is quite high as shown in Table 1. The basic formulae (8) and (9) were found to be valid at least for the range of $ka = 8\pi$–200π and $ka = 4\pi$–200π, respectively.

They can be useful in many ultrasonic problems especially in hydroacoustics and in ultrasonic medical diagnostic, where the shadow method is or may be used for detecting of kidney stones, calcifications etc.

It is interesting to notice that Eqs (8) and (9) make it possible to estimate the diameter of the sphere when measuring its shadow range. Up to now the only measure of the diameter of the sphere, considered as the hydroacoustic target, is the amplitude of its echo signal. However, it depends on propagation parameters and conditions in the medium (e.g. attenuation, distance). The shadow range seems to be more independent on these parameters and therefore may be more useful for this purpose.

References

[1] L. FILIPCZYŃSKI, T. KUJAWSKA, *Acoustical shadow of a sphere immersed in water*, Proc. of the V Symposium on Hydroacoustics, Gdynia 1988, 71–78 (in Polish).

[2] L. FILIPCZYŃSKI, T. KUJAWSKA, *Isobar distributions and the shadow range of spheres immersed in water*, Proc. of the VI Symposium on Hydroacoustics, Gdynia, AMW 1989, 115–120.

[3] L. FILIPCZYŃSKI, T. KUJAWSKA, *Acoustical shadow of a sphere immersed in water*. I, Archives of Acoustics, **14**, 1–2 (1989) 29–43.

[4] L. FILIPCZYŃSKI, G. ŁYPACEWICZ, *Estimation of calcification detectability in breast tissues by means of the ultrasonic echo and shadow methods*, Archives of Acoustics, **9**, 1–2 (1984).

[5] H. HÄNSEL, *Podstawy rachunku błędów*, WNT Warszawa 1968 p. 93.

[6] J. TOPPING, *Errors of observation and their treatment*, The Institute of Physics London 1956, p. 101, 105.

Received December 12, 1988.

ARCHIVES OF ACOUSTICS
14, 3–4, 191–202 (1989)

APPLICATION OF THE ELECTRIC PROBE TO THE INVESTIGATION OF SURFACE WAVE IN PIEZOELECTRICS

JERZY FILIPIAK

Instytut Fizyki, Wojskowa Akademia Techniczna (Warszawa)

A system for vizualization of the surface acoustic wave in piezoelectrics is presented. The system for surface wave front amplitude and phase measurement in weak piezoelectrics have been described. The measuring capabilities of the system have been exemplified for the bismuth-germanium oxide and quartz type substrates.

Przedstawiono układ do wizualizacji fali powierzchniowej w piezoelektrykach. Omówiono układy do pomiaru amplitudy oraz fazy frontu fali powierzchniowej w zastosowaniu do słabych piezodielektryków. Pokazano przykłady możliwości pomiarowych układów na podłożach typu tlenku bizmutowo-germanowego oraz kwarcu.

1. Introduction

Having an image of the surface acoustic wave one can estimate the parameters of this wave as well as the quality of the substarte in which it propagates. One of the methods of visualisation of the surface acoustic wave in piezoelectrics is the electric probe method. The probe made of abrasion-resistant conductor is placed on the piezoelectric surface. The electric field related to the propagating wave induces electric potential in the probe. As its magnitude is proportional to the wave amplitude, by changing the position of the probe the information on the surface wave amplitude distribution can be collected. This method was described for the first time by WILLIAMSON [1] who applied it to the piezodielectric with large electromechanic coupling coefficient, $LiNbO_3$. The condition for applying this method to investigations of all practically applied piezodielectrics, including those with small coupling coefficient (e.g. quartz), is the sufficiently large signal received by the probe. This necessitates for the analysis of the entire system in which the probe operates.

2. Analysis of the electric probe

The basic information on the surface acoustic wave distribution are the wave front amplitude and phase cross-sections made perpendicularly to the propagation direction, because of their large ammount these measurements should be carried out

automatically. Besides the signal of interest the probe receives other spurious signals. These are, the signal passing directly, the deflected signals and the signals of bulk waves propagating in the investigated substrate. As these signals usually reach the probe at different time than the measured signal, it is possible to eliminate them in the impulse-type system. The main problem that is the increase of the signal received by the probe remains. Therefore, an power flow analysis of the system is necessary. This system can be represented (Fig. 1b) as a voltage source E_g with the internal impedance R_p, loaded with the amplifier input impedance R_{in}. The magnitude of the voltage E_g depends on the surface wave power, piezodielectric substrate properties and the probe geometry.

The investigated surface wave in the piezodielectric is excited with the interdigital transducer. Its power can be equal to the acoustic power in the case of matched

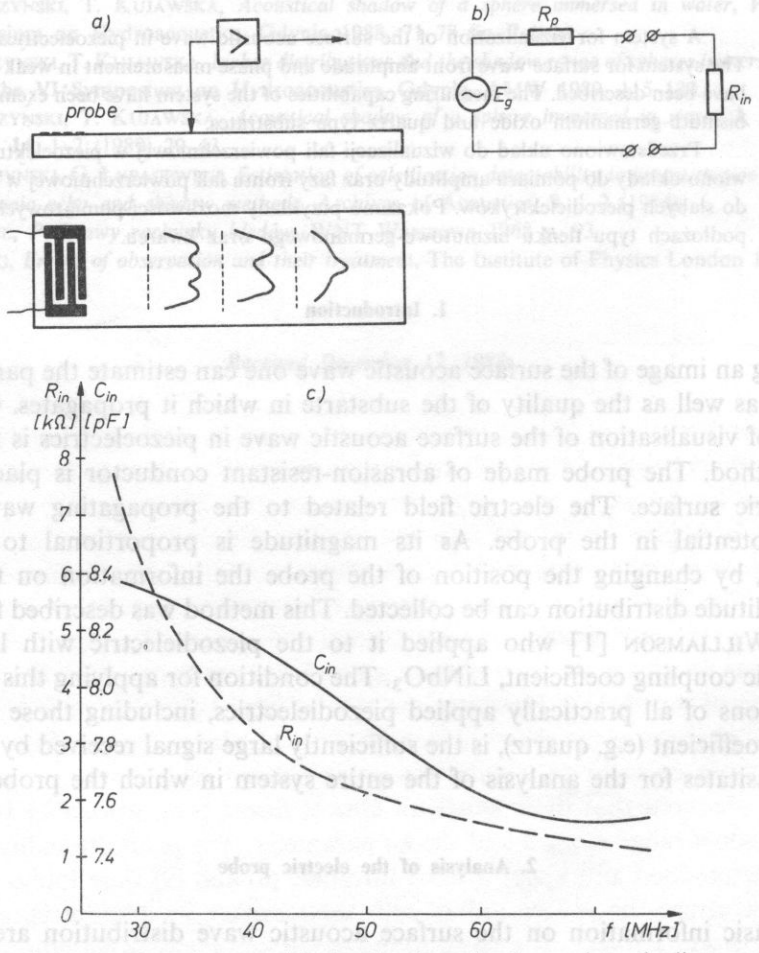

Fig. 1. a – surface wave measurement with the electric probe, b – schematic diagram of the probe, c – input parameters of the amplifier cooperating with the probe

transducer and supply generator. For a given frequency the transducers with arbitrary geometry can be matched irrespective of the piezodielectric substrate.

The power P of the amplifier cooperating with the probe (e.g. Fig. 1b) depends mainly on matching of the amplifier and the internal impedance of the source with very high resistance. Regarding this, the power increase will be proportional to the increase of the input resistance of the amplifier.

The probe geometry can be optimised for a given wave length. However for various probe geometries the received voltages differ a little [1]. As the system should work by a variety of wave lengths it is reasonable to omit the probe geometry influence, and make the probe as thin as possible.

From the above considerations it results that the increase of the signal received by the probe can be obtained in practice in the following ways:

a — by previously matching the wave exciting transducer with the supply generator;

b — by applying the amplifier with the possibly greatest input resistance.

The input parameters of the amplifier co-operating with the probe are shown in Fig. 1c. In the practically implemented system (Fig. 2) the probe output has been connected directly to the high-resistance input of the amplifier. The input capacitance of the amplifier (8 pF) and the input one of the probe (4 pF) have been eliminated with the variable-inductance coil connected with the amplifier input. Avoiding the

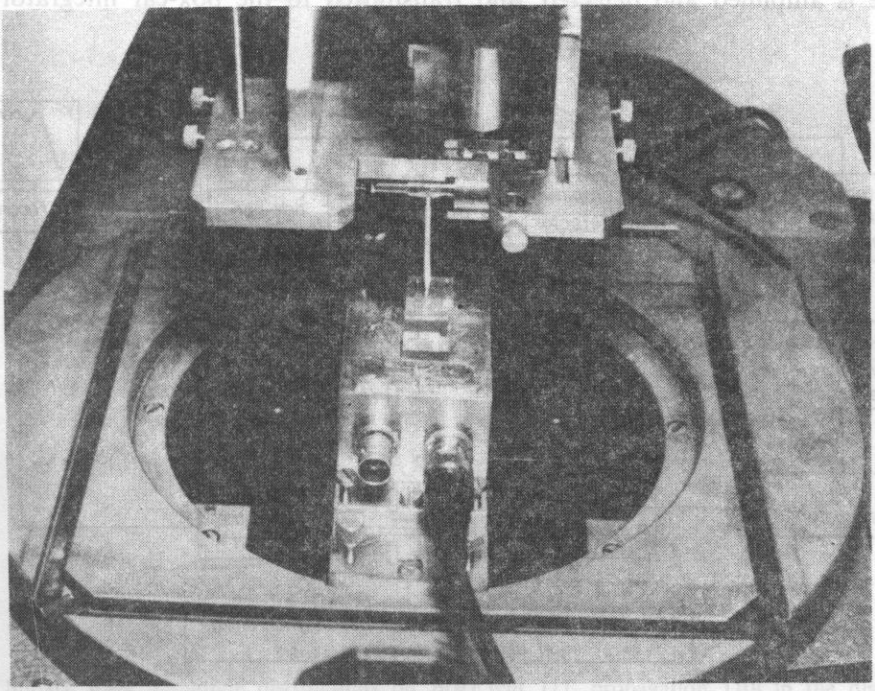

Fig. 2. The stand for surface wave measurement with the electrical probe

signal coming directly from the supply generator to the amplifier input is a problem. For this reason the whole useful signal channel has been thoroughly electricaly isolated.

The existance of backlashes, or the probe movement along the path different from the set pre-set one, can be the reason of considerable measurement errors. This is particularly important in wave front phase measurements. For example, in the case of the bismuth-silicon oxide (BGO) for the frequency equal to 30 MHz, the surface wave length is 56 μm and the 1 μm backlash limit the phase measurement accuracy to 6°.

In the system shown in Fig. 2, the probe has been mounted in two spherical holders and pressed to the tested specimen with a spring. The probe is fixed to a workshop microscope type FK 40 × 40. The specimen is placed on its table. The surface of the specimen is levelled with help of the workshopmicrometric probe. The table turn mechanism provides for precision setting of the required specimen direction.

3. System for surface wave amplitude distribution measurement

The layout of the surface wave amplitude measurement system has been shown in the Fig. 3. The surface wave is excited by the interdigital transducer supplied with a wave form of the length equal to several μs. The electric signal received by the probe is amplified and detected, and transmitted to the box-car integrator. This

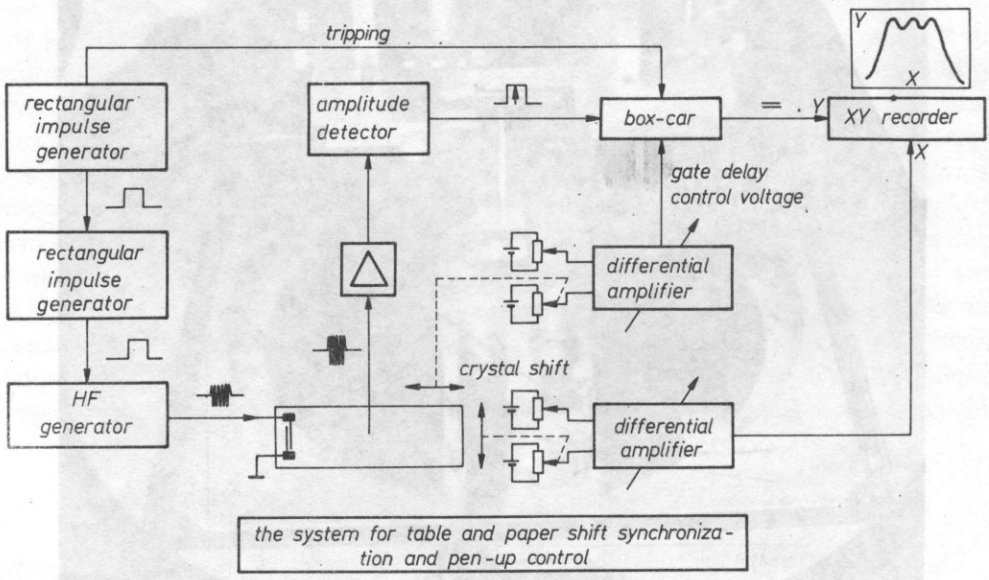

Fig. 3. The diagram of the system for surface wave amplitude distribution measurement

system transforms the received signal magnitude by the probe into the direct current signal, which is recorded in the digital or analog form. The system significantly improves the signal-to-noise ratio.

By coupling the microscope table shifts in the direction perpendicular or paralel to the wave propagation direction the sampling time before passing the signal to the box-car, should be properly changed when the probe moves allong the wave propagation direction. This way full automisation of measurements on the whole piezodielectric surface has been obtained. To ilustrate the measuring capability of the system the typical diffraction phenomenon which accompanies the surface wave propagation has been presented in Figs. 4–6. In the Fig. 4 the surface wave amplitude cross-sections perpendicular to the propagation direction is shown. They have been obtained for the bismuth-germanium oxide (*BGO* int 111, propagation 110) in

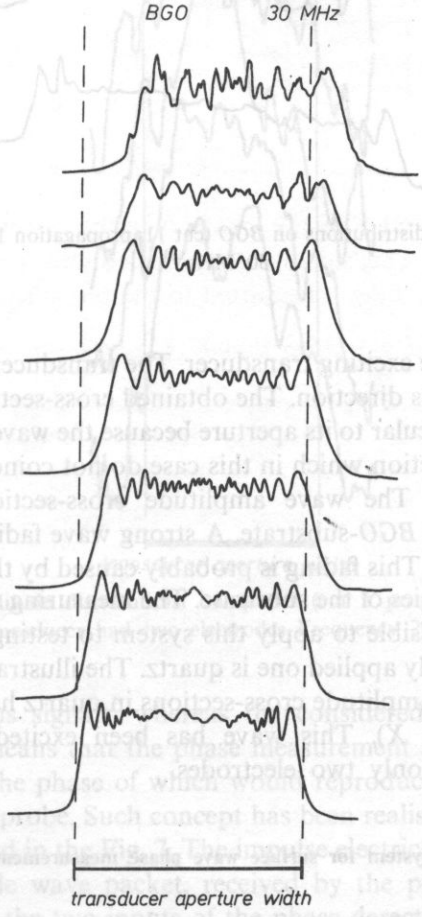

Fig. 4. Surface wave amplitude distributions on *BGO* (cut 111, propagation 110) in the distances 2, 4, 6, ... mm from the transducer. Frequency 30 MHz

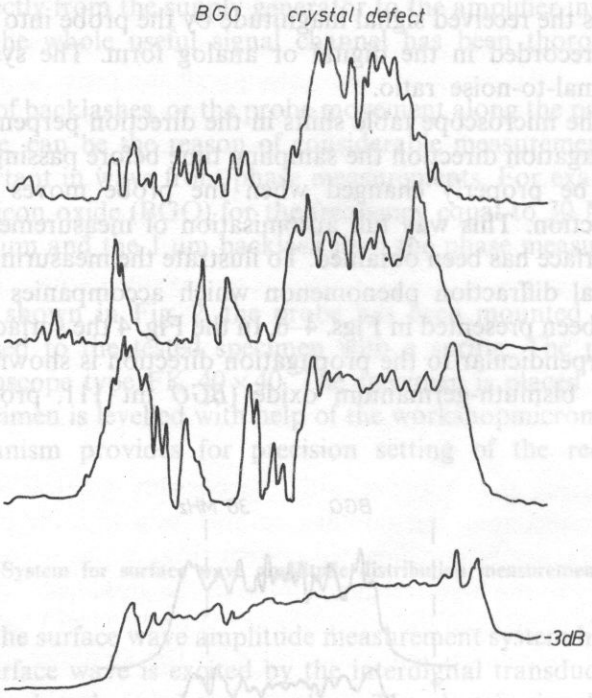

Fig. 5. Surface wave amplitude distributions on *BGO* (cut 11, propagation 110) with a defect. Frequency 30 MHz

various distances from the exciting transducer. The transducer is not placed precisely in the crystallographic axis direction. The obtained cross-sections come out from the channel which is perpendicular to its aperture because the wave propagates in near the crystallographic axis direction which in this case do not coincide with the symmetry axis on the transducer. The wave amplitude cross-sections presented in Fig. 5 illustrate a defect of the *BGO*-substrate. A strong wave fading, non-uniform in the cross-section, can be seen. This fading is probably caused by the local perturbation of the piezodielectric properties of the substrate. The measuring sensitivity of the system is high what makes it possible to apply this system to testing weak piezodielectrics. Among them the frequently applied one is quartz. The illustration of the above is the Fig. 6 in which the wave amplitude cross-sections in quartz have been presented (cut *Y*, propagation direction *X*). This wave has been excited with the interdigital transducer consisting of only two electrodes.

4. System for surface wave phase measurement

The surface wave phase measurement is much more complex than the amplitude measurement. The main problem results from the fact the available phase meters

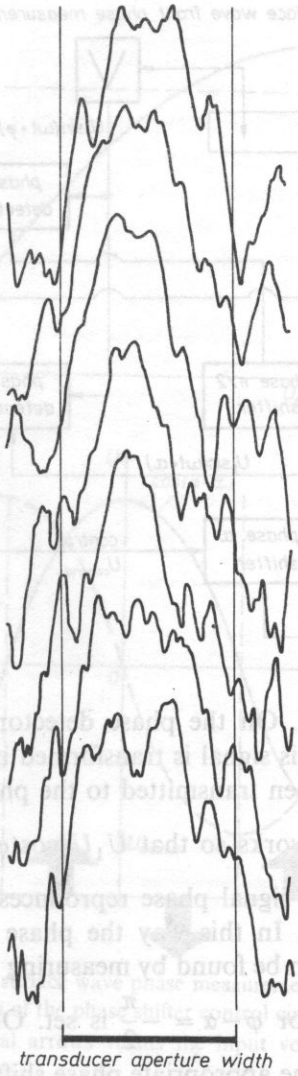

Fig. 6. Surface wave amplitude distributions on quartz (cut Y propagation X). The wave exciting transducer had two electrodes Frequency 20 MHz

operate on continuous signals, whereas the considered measuring system works impulse mode. This means that the phase measurement should be carried out with a continuous signal, the phase of which would reproduce the phase of the impulse signal received by the probe. Such concept has been realised in the measuring circuit schematically presented in the Fig. 7. The impulse electric signal $U_2 \sin(\omega t + \varphi)$ in the form of a few μs wide wave packet, received by the probe after amplification is transmitted to one of the two inputs of the phase derector. A continuous reference signal $U_1 \sin(\omega t + \alpha)$ previously transformed by the voltage controlled phase shifter is

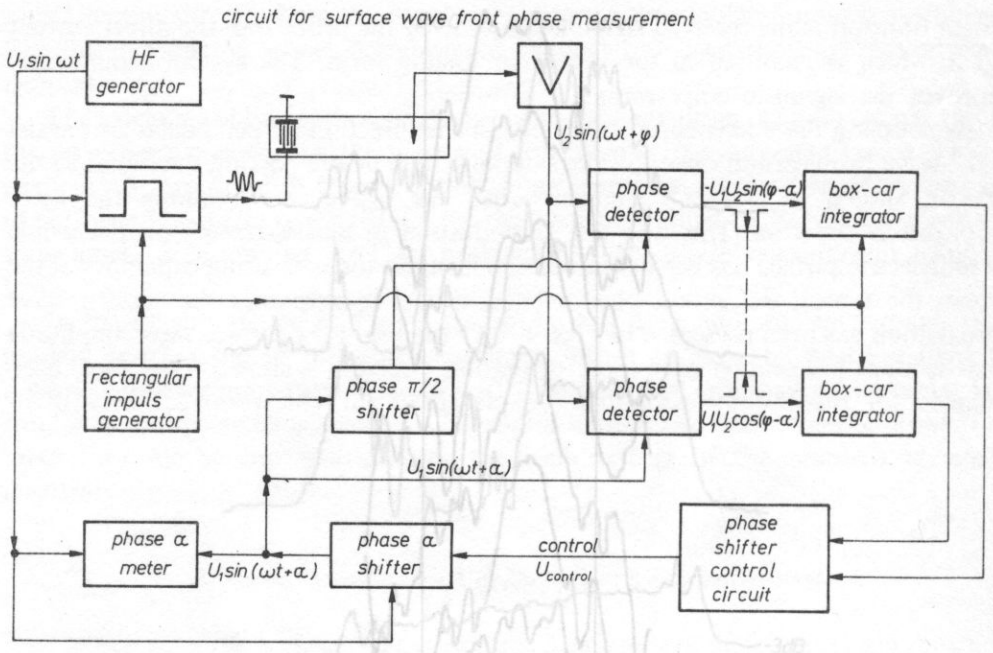

supplied to the second input. On the phase detector output the $U_1U_2\cos(\varphi-\alpha)$ impulse signal is obtained. This signal is transformed into a direct-current signal by the box-car integrator, and then transmitted to the phase shift control input. If the phase shifter control circuit works so that $U_1U_2\cos(\varphi-\alpha)=0$; hence $\varphi-\alpha=\pm\frac{\pi}{2}$ and the continuous reference signal phase reproduces the phase φ of the impulse signal received by the probe. In this way the phase φ change during the probe movement in any direction can be found by measuring the phase α, provided that an unique relation $\varphi-\alpha=+\frac{\pi}{2}$ or $\varphi-\alpha=-\frac{\pi}{2}$ is set. Obtaining the unique relation necessitates for working out the appropriate phase shift control signal in the control circuit. The phase shift control circuit characteristic has been shown in the Fig. 7b. It can be seen that the control voltage increase causes the phase shift α increase. In the Fig. 7c the arrows indicate the direction of changes with respect to the value of $\varphi-\alpha$. The up arrow indicate the control voltage increase, and the down arrow the decrease. From the Fig. 7c it is apparent that the needed character of changes of this voltage coincides with the sign of the product of $-\text{sign}(\varphi-\alpha)$ and $\cos(\varphi-\alpha)$. To obtain this product an additional voltage, proportional to $\sin(\varphi-\alpha)$ should be generated. In the diagram presented in Fig. 7 a this voltage is obtained by applying an additional loop consisting of the phase detector and the box-car integrator in which the reference voltage is shifted by the phase $\alpha+\frac{\pi}{2}$. The shift is made by a supplementary phase

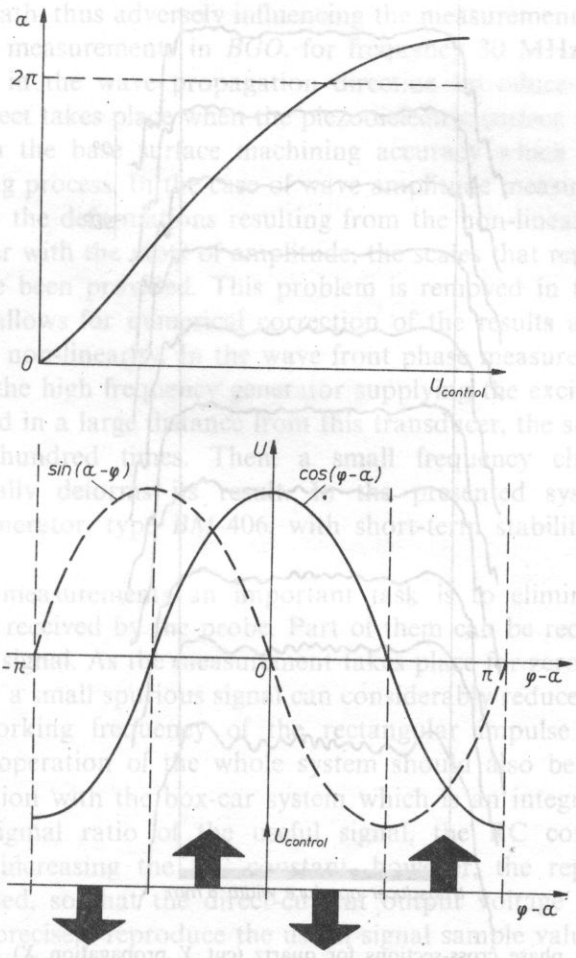

Fig. 7. a – diagram of the circuit for surface wave phase measurement, b – characteristic of the voltage driven phase shifter, c – input voltage of the phase shifter control circuit and the requires shifter control voltage change direction vertical arrows versus the input voltage phase difference range

shifter (by $\pi/2$) introduced in the reference signal circuit. The phase shift control system in the Fig. 7a generates the voltage changes dependent on the sign of the product $-\sin(\varphi-\alpha)\cdot\cos(\psi-\alpha)$. This voltage applied to the phase shifter forces the shift which allows for unique phasing on the continuous signal $U_1\sin(\omega t+\alpha)$ with the impulse signal $U_2\sin(\omega t+\varphi)$ received by the probe in the range $0\div 2\pi$. Then, the phase φ measurement is carried out by meas ring the phase α of the continuous signal with the use of a phase meter. In the system under consideration the Wiltron phase meter, model 31 OB, has been used. The surface wave front phase distribution for quartz (cut *Y*, propagation *X*) presented in the Fig. 8, illustrates the measuring capability of the discribed system.

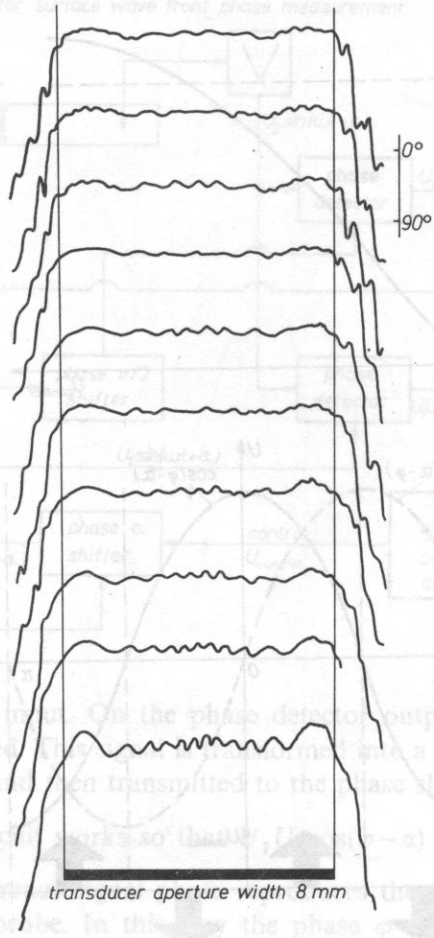

Fig. 8. Surface wave phase cross-sections for quartz (cut *Y*, propagation *X*). Frequency 30 MHz

5. Measuring technique

The probe practically does not interfere with the propagating surface wave. It receives a very small part of the wave energy, the probe diameter being of the magnitude about 20 μm, in comparison with the surface beam width usually equal to several millimeters. Therefore the measurement accuracy is concerned with accuracy of receiving and processing the signal received by the probe i.e. with the manufacturing quality and tuning of the measuring circuits, and the technique of the measurement itself.

During the measurements, particular attention should be paid to precise levelling of the tested piezodielectric. This is done with the use of screws. Levelling checking is carried out with the mechanical probe of 1 μm accuracy. Inaccurate levelling deforms

the probe travel path, thus adversely influencing the measurements. For example, in wave front phase measurements in *BGO*, for frequency 30 MHz, the 1 μm probe travel path error in the wave propagation direction introduces the 6° error.

The similar effect takes place when the piezodielectric surface is not planar. This is concerned with the base surface machining accuracy which can be estimated during the levelling process. In the case of wave amplitude measurements, attention should be paid to the deformations resulting from the non-linearity of the system. Therefore, together with the plots of amplitude, the scales that represent the system non-linearity have been provided. This problem is removed in the case of digital recording which allows for numerical correction of the results accounting for the measuring system non-linearity. In the wave front phase measurements one should be cautions with the high frequency generator supplying the exciting transducer. If the probe is placed in a large distance from this transducer, the surface wave phase changes several hundred times. Then, a small frequency change during the measurement totally deforms its result. In the presented system the TESLA programmable generator, type *BM*-406, with short-term stability 10^{-7}, has been applied.

In the phase measurements an important task is to eliminate the spurious bulk-wave signals received by the probe. Part of them can be received in the same time as the useful signal. As the measurement takes place for zeroed phase detector output signal even a small spurious signal can considerably reduce the measurement accuracy. The working frequency of the rectangular impulse generator which synchronizes the operation of the whole system should also be properly chosen. This is in connection with the box-car system which is an integrating circuit. For greater noise-to-sigmal ratio of the useful signal, the RC constant should be increased. While increasing the RC constant, however, the repeating frequency should be decrrased, so that the direct-current output voltage from the box-car integrator would precisely reproduce the useful signal sample value set to its input.

6. Conclusion

The presented method of measuring the surface wave distribution can be applied to all piezodielectrics applied in practice. It provides for simple, fully automatic measurements of the surface wave amplitude and phase. The obtained accuracy is entirely enough for piezoelectric substrate quality inspection as well as for wave parameters calculation. The impulse type operation of the system makes it possible to investigate numerous physical effects which take place in microwave acoustic systems, as e.g. wave reflection phenomenon. In comparison with the systems utilizing the wave interaction with light, the features of the described system are simplicity and better accuracy. The restriction is the applicability of the probe only to the free surfaces of the piezodielectrics, as only from such surfaces the probe is capable of receiving a signal.

Acknowledgements

The author wants to express his gratitude to Dr E. DANICKI for his encouragement and constructive discussions in the course of the presented work.

References

[1] R. C. WILLIAMSON, *Improved electrostatic probe for measurement of elastic surface waves*, IEEE Trans. Sonics Ultrasonics, vol. SU-12, 536–441, (1972).

Received June 5, 1988.

ARCHIVES OF ACOUSTICS
14, 3-4, 203-210 (1989)

APPLICATION OF DIGITAL TECHNIQUE TO THE SPECTRAL ANALYSIS OF MANDELSHTAM-BRILLOUIN SCATTERED LIGHT

TOMASZ HORNOWSKI, MIKOŁAJ ŁABOWSKI

Institute of Acoustics, A. Mickiewicz University
(60-769 Poznań, ul. Matejki 48/49)

The experimentally recorded Mandelshtam-Brillouin type light scattering function is in general a convolution of the real scattering function and the overall instrumental function, accounting for all the deformations introduced by the measuring arrangement. We propose an algorithm for the numerical deconvolution of the spectrum applicable to the correction of the latter, and the deformation of the parameters of the scattering function. Results obtained when testing the computer program determining the Rayleigh line halfwidth $\Delta\nu_R$ as well as the shift $\delta\nu_{MB}$ halfwidth $\Delta\nu_{MB}$ of the Mandelshtam-Brillouin line are given, proving high degree of the effectivity of our numerical method.

Rejestrowana eksperymentalnie funkcja rozpraszania światła typu Mandelsztama-Brillouina jest w ogólności splotem rzeczywistej funkcji rozpraszania oraz całkowitej funkcji aparaturowej opisującej wszystkie zniekształcenia wnoszone przez układ pomiarowy. W pracy przedstawiono algorytm numerycznej metody dekonwolucji widma zastosowanej do korekcji widma i wyznaczenia parametrów funkcji rozpraszania. Przedstawiono również rezultaty testowania programu komputerowego wyznaczającego szerokość połówkową linii Rayleigha $\Delta\nu_R$ oraz przesunięcie $\delta\nu_{MB}$ i szerokość połówkową $\Delta\nu_{MB}$ linii Mandelsztama-Brillouina. Wyniki testu wykazały dużą przydatność zastosowanej metody numerycznej.

1. Theoretical foundations of Mandelshtam-Brillouin light scattering

Molecular light scattering by liquid media is due to time-dependent thermodynamical fluctuations of quantities such as temperature, pressure, and concentration. Mandelshtam-Brillouin scattering is a process of this kind. The fluctuations can be said to modulate the scattered light spectrum. Thus, in accordance with the Wiener-Kinchin theorem, their variations in time reflect the underlying stochastic ocurring in the scattering media.

Classically [1], the spectral intensity distribution of the light scattered is proportional to the Fourier transform of the autocorrelation function of fluctuations in density (concentration). This quantity is termed the structural factor, and is

generally denoted by $S(\nu, q)$. Its analytical form is due to Mountain [2]:

$$S(\nu, q) = A\left\{(1-1/\gamma)\cdot\frac{\Delta\nu_R}{\nu^2+\nu_R^2}+(1/\gamma)\left[\frac{\Delta\nu_{MB}}{(\nu_0-cq)^2+\Delta\nu_{MB}^2}+\frac{\Delta\nu_{MB}}{(\nu_0-cq)^2+\Delta\nu_{MB}^2}\right]\right.$$
$$\left.+\frac{\Delta\nu_{MB}}{cq}\left[\frac{\nu+cq}{(\nu-cq)^2+\Delta\nu_{MB}^2}-\frac{\nu+cq}{(\nu-cq)^2+\Delta\nu_{MB}^2}\right]\right\}. \quad (1)$$

The first three components of the scattered light spectrum are Lorentzian in form. These are: the Rayleigh line of frequency unchanged compared to the incident frequency, and the Mandelshtam-Brillouin doublet, disposed symmetrically on either side of the central line at a distance $\delta\nu_{MB} = \pm cq$. The fourth and fifth components give a non-Lorentzian correction to the Mandelshtam-Brillouin lines shifting them slightly (towards the central line) and causing them to become asymmetric. This correction is usually very small. However, it affects the positions of the lines perceptibility and has to be taken into account when interpreting the spectrum. With the shift measured amounting to ν_p and the linewidth equal to $\Delta\nu_{MB}$, the real position of the Mandelshtam-Brillouin has to be determined from the formula

$$\nu_{MB}^2 = \nu_p^2 + 2\Delta\nu_{MB}^2. \quad (2)$$

The preceding relations are valid for media in which no relaxational processes occur. Liquids with relaxation exhibit moreover a line referred to as the Mountain line [2].

The experimentally recorded scattered light spectrum is in general the convolution of several functions [3, 4]: the line corresponding to the light source with the spectral distribution $I(\nu)$ the line of the spectral analyzer with the distribution $T(\nu, \nu')$ and the scattering line with the distrubution $S(\nu, \nu')$. The notation $X(\nu, \nu')$ is meant to signify that the function X determines the intensity of the output radiation of frequency ν which has arisen in response to input radiation of unit intensity and of frequency ν'. Since all these distributions take non-zero values only in a narrow interval about the central frequency of the incident light wave we are justified in writing

$$S(\nu, \nu') = S(\nu-\nu'), \qquad T(\nu, \nu') = S(\nu-\nu'). \quad (3)$$

In this case, the spectrum observed is given by the formula

$$0(\nu) = \int_{-\infty}^{+\infty} T(\nu-\nu')\int_{-\infty}^{+\infty} S(\nu-\nu')\cdot I(\nu'')d\nu' d\nu'' = \mathcal{F}^{-1}\{\mathcal{F}[T(\nu)]\mathcal{F}[S(\nu)]\mathcal{F}[I(\nu)]\}, \quad (4)$$

with $\mathcal{F}$ the Fourier transform, and $\mathcal{F}^{-1}$ the inverse transform.
Thus, the scattering function can be determined from the following expression

$$S(\nu) = \mathcal{F}^{-1}\{\mathcal{F}[0(\nu)]/\{\mathcal{F}[T(\nu)]\mathcal{F}[I(\nu)]\}\}. \quad (5)$$

The preceding operation is referred to as deconvolution of the spectrum. It has to be performed in order to determine the "true" scattering function contributed by the

scattering liquid and, consequently, such parameters as the shift in Mandelshtam-Brillouin line $\delta\nu_{MB}$ and its halfwidth $\Delta\nu_{MB}$.

Obviously, Eq. (5) is not accessible to strict solution, though a number of methods exist permitting approximate solutions of the problem. Here, we have in mind primarily the pseudodeconvolution method of JONES et. al. [5], as well as that of LEIDECKER and LAMACCHIA [4]. We shall discuss the former in more detail in Section 2.

2. The influence of the instrumental line on the recorded Mandelshtam-Brillouin scattered light spectrum

The deformations incurred when recording various spectra have long been the object of studies in the infrared, Raman and Mandelshtam-Brillouin spectroscopy. It has been established [3, 5, 6] that the deformation caused by the instrumental line can be neglected if the ratio of its halfwidth $\Delta\nu_I$ and that of the line investigated $\Delta\nu$ fulfils the condition $\Delta\nu_I/\Delta\nu \leqslant 0.2$. In most cases this condition is not fulfilled. Thus in order to obtain correct results, one has to have recourse to one of the methods evolved for correcting the experimentally recorded spectra.

In accordance with what has been said above, the instrumental line in the Mandelshtam–Brillouin case is the resultant of the Gaussian gas laser line [7], the Fabry-Pérot étalon line given by the Airy function [8], and the line due to the finite size of the scanning aperture described by a triangle function [4]. In practice, for the sake of simplicity, one usually makes use of the over-all instrumental function $A(\nu)$. The latter can be expressed as the product of a Gaussian and a Lorentz function:

$$A(\nu) = A_0[1+(1/\Delta\nu_L^2)(\nu-\nu_0)^2]\exp[-(1/\Delta\nu_G^2)(\nu-\nu_0)^2]. \tag{6}$$

Applying the over all instrumental function $A(\nu)$ alone, the experimentally recorded spectrum can be written in the following form:

$$O(\nu) = \int_{-\infty}^{+\infty} A(\nu-\nu')S(\nu')d\nu', \tag{7}$$

where $S(\nu)$ is the scattering function. Eq. (7) is an integral equation of the convolution type accessible to numerical solution by reduction to a set of linear equations:

$$O_i = \sum_{j=1}^{n} A_{ij}S_j, \qquad i = 1, 2, 3, \ldots, n. \tag{8}$$

O and **S** are, respectively, vectors of the experimental points measured and the scattering function, whereas **A** is the transformation matrix of the instrumental function the matrix elements of which represent the values of the symmetric instrumental function measured at the same intervals $\Delta\nu$ as the values of $O(\nu)$. The matrix **A** fulfils the normalisation condition. For deconvolution of the spectrum, i.e. for determining the scattering function $S(\nu)$ from the experimental functions $S(\nu)$ and $A(\nu)$, we used one of the available methods of deconvolution (referred to as ψ-deconvolutions), namely that of JONES et. al. [4]. According to Jones, the

transformation matrix of the instrumental function is constructed in the following form:

$$\begin{bmatrix} a_{11} & a_{12} & \dots & a_{1m} & 0 & 0 & 0 & \dots & 0 \\ 0 & a_{21} & a_{22} & \dots & a_{2m} & 0 & 0 & \dots & 0 \\ \dots & \dots & \dots & \dots & \dots & \dots & \dots & \dots & \dots \\ 0 & 0 & \dots & 0 & a_{m1} & a_{m2} & \dots & \dots & a_{mn} \end{bmatrix}.$$

The matrix is obtained as follows; having available n values of the scattering function $S(\nu_i)$ and n values of the instrumental function $A(\nu_i)$ we assume that the $2l$ values of the function $A(\nu_i)$ lying on the wings of the line are zero. Thus, the matrix **A** has $m = n-2l$ rows. In practice, the values of the matrix elements a_{ij} are determined by recording light scattering from a statistically homogeneous medium.

Jones' is an iterative method. As the zeroth approximation, one assumes the experimentally observed values of the scattering function

$$S_i^{(0)} = S_i, \quad i = 1, 2, \dots, n. \tag{9}$$

The k-th step of the iteration procedure consists of 4 stages. In the first, one determines the vector $\mathbf{B}(B_1, B_2, \dots, B_m)$ from the formula

$$\mathbf{B}^{(k)} = \mathbf{A} \cdot \mathbf{S}^{(k-1)}. \tag{10}$$

In the second – the vector $\mathbf{R}(R_1, R_2, \dots, R_m)$

$$R_i = S_{1+i}/B_i, \quad i = 1, 2, \dots, m. \tag{11}$$

In the third stage, one finds the next $(k+1)$-st approximation of the vector **S**:

$$S_i^{(k+1)} = S_i^{(k)} \cdot R_1, \quad i = 1, 2, \dots, l \tag{12}$$

$$S_i^{(k+1)} = S_i^{(k)} \cdot R_{i-1}, \quad i = l+1, l+2, \dots, l+m \tag{13}$$

$$S_i^{(k+1)} = S_i^{(k)} \cdot R_m, \quad i = l+m+1, l+m+2, \dots, n \tag{14}$$

The equations (12) and (14) describe the wings of the line. In the fourth stage we determine the value of

$$\delta^{(k)} = \sum_{i=1}^{n} |S_i^{(k)} - S_i^{(k-1)}|. \tag{15}$$

One continues the iterative procedure until the following condition is fulfilled

$$|\delta^{(k)} - \delta^{(k-1)}| \leqslant \varepsilon, \tag{16}$$

where the parameter ε is a prescribed number. For practical purposes a sufficient approximation is achieved after some 10–20 iterations.

On having determined the function $S(\nu)$ by deconvolution, one can proceed to determine the parameters of the spectrum: the halfwidth of the Rayleigh line $\Delta\nu_R$, that of the Mandelshtam-Brillouin line $\Delta\nu_{MB}$, and the Mandelshtam-Brillouin shift

$\delta\nu_{MB}$. To this aim, we made use of the procedure consisting in fitting the theoretical curve of eq. (1) to the „experimentally" determined points of the function $S(\nu)$ by the least squares method.

3. Testing the numerical procedure. The design of a measuring stand for the digital recording of Mandelshtam-Brillouin scattered light spectra

On the basis of the preceding Jones' algorithm we wrote in PASCAL language a program for deconvolution of the spectrum and the determination of the parameters of the Mandelshtam-Brillouin scattering spectrum recorded. The functioning of the fitting procedure was checked on data generated on the basis of Eqs. (1) and (6). Fig. 1 shows the instrumental line of Eq. (6). Its parameters amount to:

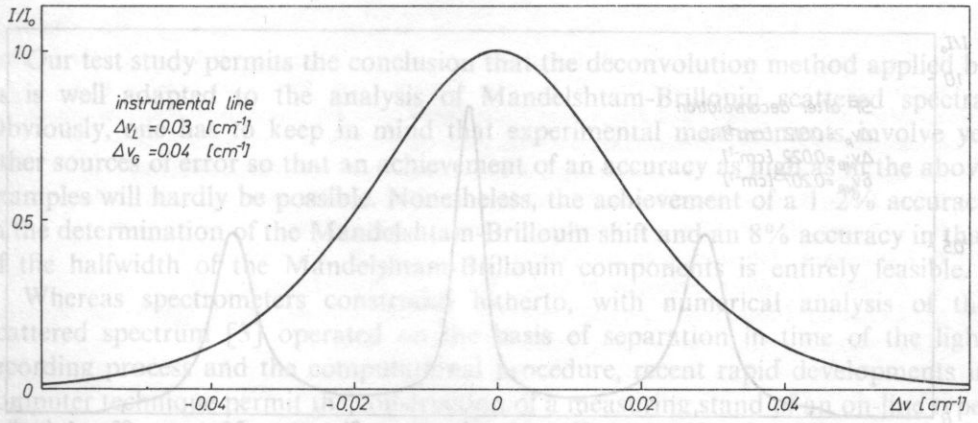

Fig. 1. Instrumental line as determined from Eq. (6)

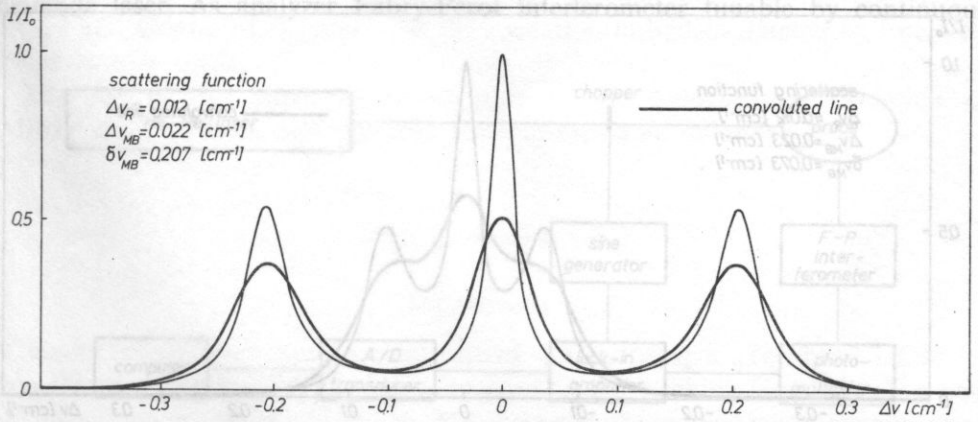

Fig. 2. Convolution of the instrumental line of Fig. 1 and the scattering function

$\Delta\nu_L = 0.03\ cm^{-1}$, and $\Delta\nu_G = 0.04\ cm^{-1}$. Its convolution with the scattering function, of parameters equal to $\Delta\nu_R = 0.012\ cm^{-1}$, $\Delta\nu_{MB} = 0.022\ cm^{-1}$ and $\delta\nu_{MB} = 0.207\ cm^{-1}$, is shown in Fig. 2, where one notes a lowering of the maxima and a broadening of all the lines. The result of the deconvolution and fitting procedure is shown in Fig. 3. Obviously, agreement between the parameters assumed and those obtained is very good.

A case of greater interest is shown in Fig. 4. Here convolution of the instrumental line of Fig. 1 and a scattering function with the parameters $\Delta\nu_R = 0.012\ cm^{-1}$, $\Delta\nu_{MB} = 0.023\ cm^{-1}$ and $\delta\nu_{MB} = 0.073\ cm^{-1}$ led to complete obliteration of the hyperfine structure, so that an analysis of the spectrum by traditional methods was not possible. However, the result of deconvolution of this spectrum is illustrated in Fig. 5 where, quite obviously, the hyperfine structure is reconstituted and the values of the parameters are in excellent agreement with those assumed.

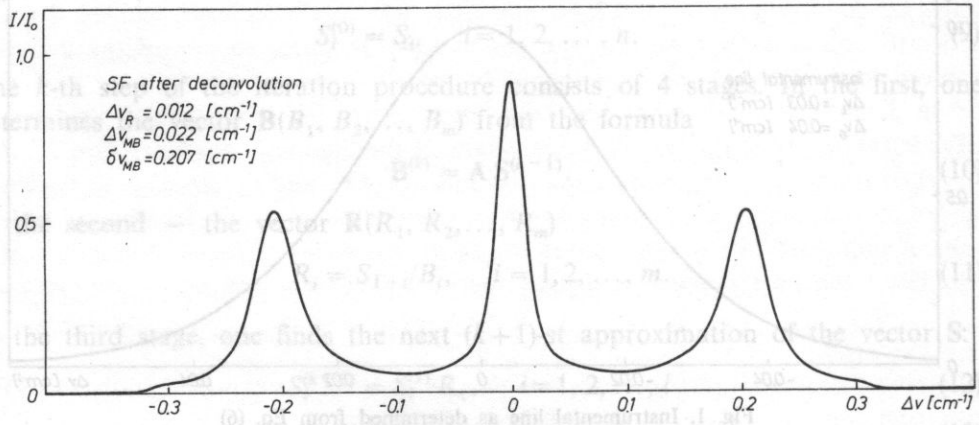

Fig. 3. The scattering function of Fig. 2 after deconvolution

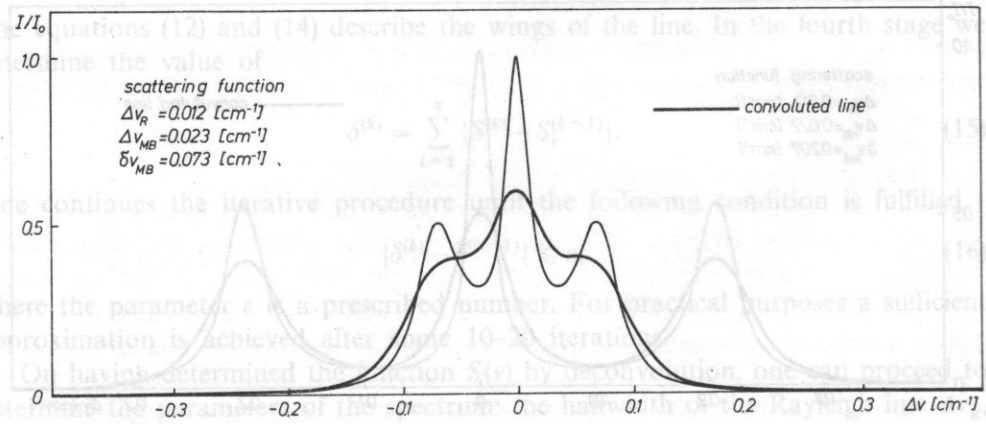

Fig. 4. Convolution of the instrumental line of Fig. 1 and the scattering function

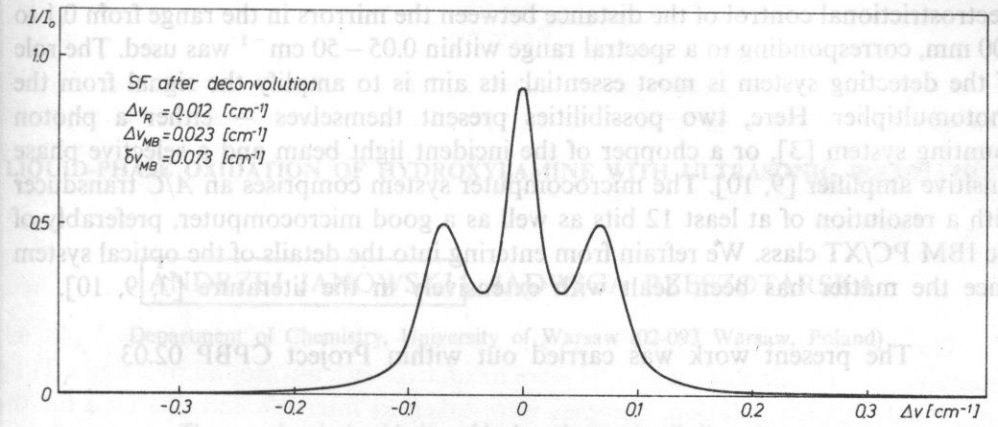

Fig. 5. The scattering function of Fig. 4 after deconvolution

Our test study permits the conclusion that the deconvolution method applied by us is well adapted to the analysis of Mandelshtam-Brillouin scattered spectra. Obviously, one has to keep in mind that experimental measurements involve yet other sources of error so that an achievement of an accuracy as high as in the above examples will hardly be possible. Nonetheless, the achievement of a 1–2% accuracy in the determination of the Mandelshtam-Brillouin shift and an 8% accuracy in that of the halfwidth of the Mandelshtam-Brillouin components is entirely feasible.

Whereas spectrometers construced hitherto, with numerical analysis of the acattered spectrum [3] operated on the basis of separation in time of the light recording process and the computational procedure, recent rapid developments in computer technique permit the construction of a measuring stand of an on-line type.

The arrangement designed by us designed (see Fig. 6) consists of the following four elements: a light source, an analyzer of the scattered light spectrum, an electronic system of detection, and a computer system. As light source we use a 50 mW He–Ne one-mode laser. As analyzer Fabry-Pérot interferometer tunable by continuous

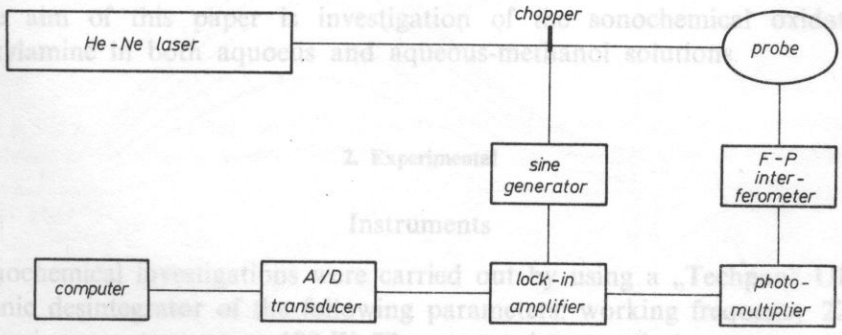

Fig. 6. Measuring stand for the digital recording of Mandelshtam–Brillouin light scattering spectra

electrostrictional control of the distance between the mirrors in the range from 0.1 to 100 mm, corresponding to a spectral range within $0.05-50\ cm^{-1}$ was used. The role of the detecting system is most essential: its aim is to amplify the signal from the photomultiplier. Here, two possibilities present themselves — either a photon counting system [3], or a chopper of the incident light beam and a selective phase sensitive amplifier [9, 10]. The microcomputer system comprises an A/C transducer with a resolution of at least 12 bits as well as a good microcomputer, preferably of the IBM PC/XT class. We refrain from entering into the details of the optical system since the matter has been dealt with extensively in the literature [3, 9, 10].

The present work was carried out within Project CPBP 02.03

References

[1] L. Landau, E. M. Lifszyc, *Electrodynamics of continuous media*, PWN, Warszawa 1960 (in Polish).
[2] P. Lallemand, *Light scattering in liquids and gases*, in: *Photon correlation and light beating spectroscopy*, red. H. Z. Cummins, E. R. Pike, Plenum Press, New York-London 1974.
[3] W. Mischke, *Mandelshtam-Brillouin light scattering in some benzene-derived molecular liquids*, A. Mickiewicz University Publications, Poznań 1982. (in Polish)
[4] H. W. Leidecker jr., J. T. LaMacchia, Journ. Acoust. Soc. Am., **43**, 143 (1968).
[5] R. N. Jones, R. Venkatanghaven, J. W. Hopkins, Spectrochim. Acta, **23A**, 941 (1967).
[6] R. A. Russel, H. W. Hopkins, Spectrochim. Acta, **9**, 133 (1957).
[7] F. Kaczmarek, *Introduction to the Physics of lasers*, PWN, Warszawa 1978.
[8] M. A. Born, E. Wolf, *Principles of optics*, Pergamon Press, London 1964.
[9] M. Łabowski *Ultra- and hypersonic properties of some selected critical liquids and mixtures.* Mickiewicz University Publications, Poznań 1980 (in Polish).
[10] G. I. A. Stegeman, W. S. Gornall, V. Volterra, B. P. Stoicheff, Journ. Acoust. Soc. Am., **49**, 979 (1971).

Received April 6, 1988.

ARCHIVES OF ACOUSTICS
14, 3-4, 211-216 (1989)

LIQUID-PHASE OXIDATION OF HYDROXYLAMINE WITH ULTRASONIC IRRADIATION

ANDRZEJ JANOWSKI, JADWIGA RZESZOTARSKA

Department of Chemistry, University of Warsaw (02-093 Warsaw, Poland)

The sonochemical oxidation of hydroxylamine in alkaline aqueous, aqueous-methanol and methanol solutions yielded peroxonitrite ion as a main product. A little nitrite and nitrate were also formed. The oxidation yield increased with methanol concentration in the solution. The mechanism of oxidation both in aqueous solution and in the presence of alcohol is discussed.

Badano sonochemiczne utlenianie hydroksylaminy w alkalicznym roztworze wodnym oraz w roztworach wodno-metanolowych. Głównym produktem utleniania był jon ONO_2^- oraz niewielkie ilości azotynów i azotanów. Stwierdzono, że wydajność utleniania wzrasta ze wzrostem stężenia metanolu w roztworze. Przedyskutowano mechanizm utleniania w roztworze wodnym oraz w obecności metanolu.

1. Introduction

The raction of hydroxylamine with various oxidizing agents has been a subject of many papers. HUGHES and NICKLIN [1] studied oxidation of hydroxylamine in alkaline solutions by saturations with gaseous oxygen. The oxidation products were peroxonitrite, nitrite and nitrate. The reaction was catalyzed by traces of Cu (II), Co (II) and Fe (II) unavoidably introduced with the reagents. On the other hand, BUTLER and GORDON [2] found that the oxidation of hydroxylamine by iron (III) yielded nitrous oxide.

The aim of this paper is investigation of the sonochemical oxidation of hydroxylamine in both aquoeus and aqueous-methanol solutions.

2. Experimental

Instruments

Sonochemical investigations were carried out by using a „Techpan" UDM-10 ultrasonic desintegrator of the following parameters: working frequency 22 ± 1.65 kHz, maximum output power 180 W. The spectrophotometrical measurements were performed on a C. Zeiss Jena „Specord UV-VIS" spectrometer.

Reagents

All chemicals (analytical grade purity hydroxylamine, hydrochloride, NaOH, $CuSO_4 \cdot 5H_2O$) were used without further purification. The solutions were prepared using twice distilled water or methanol pure for spectroscopy. EDTA solutions were prepared by dissolving a weighted amount of disodium salt of ethylenediaminetetraacetic acid.

Procedures

The $NH_2OH.HCL$ solutions of the concentration of 0.01 mole/dm^3 (40 ml) containing 0–1 mole/dm^3 of NaOH were irradiated with ultrasound by using a Ti tip immersed into the solution. Samples were taken at intervals and analyzed for the different products. The concentration of peroxonitrite was estimated from the absorbance at 302 nm, molar absorptivity being 1670 cm^{-1} mole^{-1} dm^3 [3]. Other oxidation products, nitrate and H_2O_2 also absorb in this range but with negligible intensity (molar absorptivities = 7 and 40, respectively).

Nitrate was determined by the UV spectrometric method [4]. Nitrite was determined by the standard colorimetric method involving diazotization of sulfanilic acid and coupling with α-naphthylamine.

3. Results and discussion

In both aqueous and methanol solutions sonochemical oxidation produces peroxonitrite as a main initial product, similary as in the case of O_2 oxidation (Fig. 1 and 2). Also, small amounts of NO_2^- and NO_3^- are formed (Table 1). The concentration of peroxonitrite increases almost linearly with time. The peroxonitrite yield increases

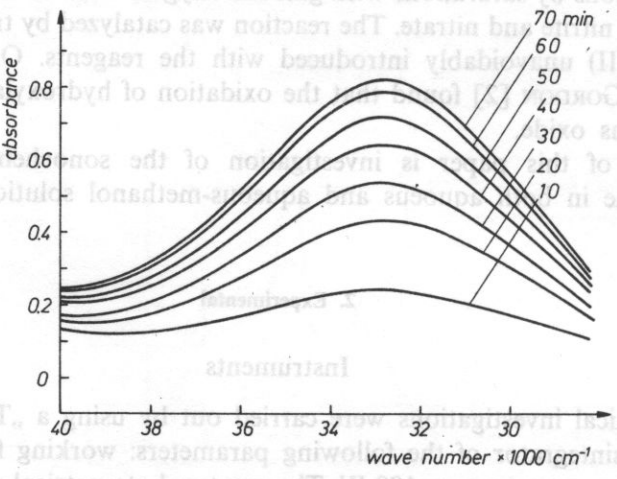

Fig. 1. Electronic spectra of 0.01 mole/dm^3 aqueous hydroxylamine solutions containing 0.5 mole/dm^3 NaOH after sonification for different time. The optical path 1 cm

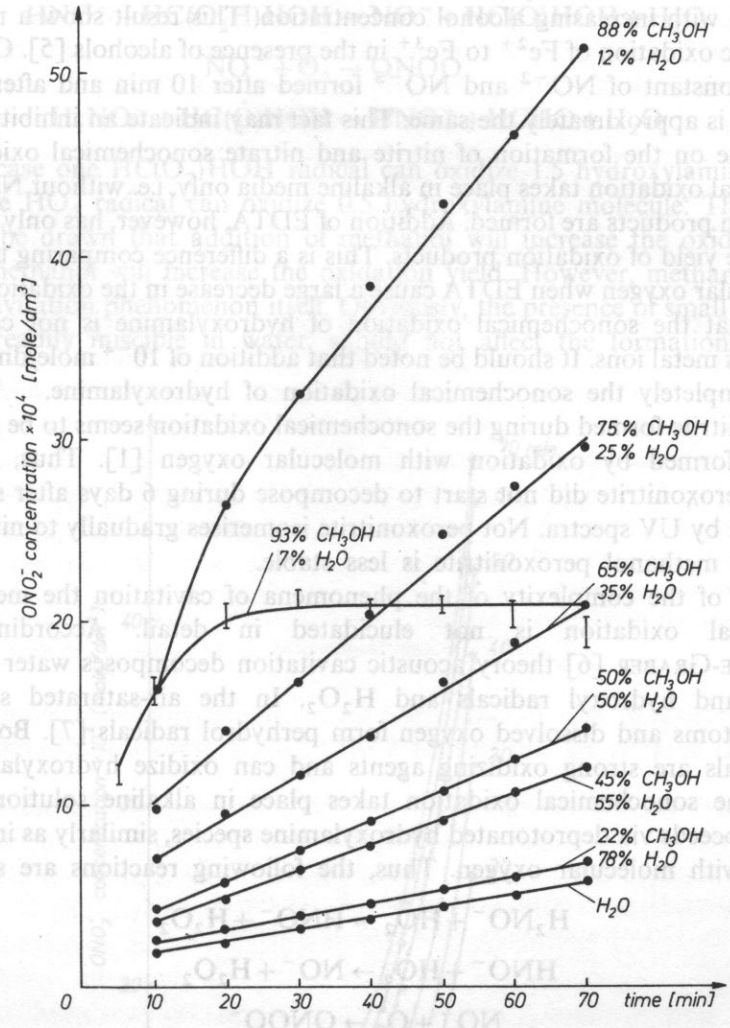

Fig. 2. The sonochemical oxidation of 0.01 mole/dm^3 hydroxylamine containing 0.5 mole/dm^3 NaOH in aqueous and aqueous-methanol solutions (in vol. %).

Table 1. Products of sonochemical oxidation of 40 ml of 0.01 mole/dm^3 aqueous, aqueous-methanol and methanol hydroxylamine solution with 0.5 mole/dm^3 NaOH added after 70 min. of sonification

vol. % H_2O / vol. % CH_3OH	100 / –	78 / 22	55 / 45	35 / 65	12 / 88	7 / 93
ONO_2^- × 10^4 mol/dm^3	5.9	6.7	12.0	20.4	49.0	20.0
NO_3^- × 10^4 mol/dm^3	1.5	1.2	1.8	2.0	5.5	0.6
NO_2^- × 10^5 mol/dm^3	2.0	2.0	3.0	3.5	5.0	7.0

significantly with increasing alcohol concentration. This result show a resemblance to ultrasonic oxidation of Fe^{2+} to Fe^{3+} in the presence of alcohols [5]. On the other hand, the constant of NO^{-2} and NO^{-3} formed after 10 min and after 70 min of sonification is approximately the same. This fact may indicate an inhibiting affect of peroxonitrite on the formation of nitrite and nitrate sonochemical oxidation. The sonochemical oxidation takes place in alkaline media only, i.e. without NaOH added no oxidation products are formed. Addition of EDTA, however, has only a negligible effect on the yield of oxidation products. This is a difference comparing to oxidation with molecular oxygen when EDTA cause a large decrease in the oxidation rate. This indicates that the sonochemical oxidation of hydroxylamine is not catalysed by adventitious metal ions. It should be noted that addition of 10^{-4} mole/dm^3 of Cu (II) inhibits completely the sonochemical oxidation of hydroxylamine.

Peroxonitrite formed during the sonochemical oxidation seems to be more stable than that formed by oxidation with molecular oxygen [1]. Thus, in aquaeus solutions peroxonitrite did not start to decompose during 6 days after sonification, as indicated by UV spectra. Not peroxonitrite isomerises gradually to nitrate. In the presence of methanol peroxonitrite is less stable.

In view of the complexity of the phenomena of cavitation the mechanism of sonochemical oxidation is not elucidated in detail. According to the PRUDHOMME-GRABER [6] theory acoustic cavitation decomposes water to produce hydrogen and hydroxyl radicals and H_2O_2. In the air-saturated solution the hydrogen atoms and dissolved oxygen form perhydrol radicals [7]. Both $\cdot OH$ and $H\dot{O}_2$ radicals are strong oxidizing agents and can oxidize hydroxylamine.

Since the sonochemical oxidation takes place in alkaline solutions only the reaction proceeds via deprotonated hydroxylamine species, similarly as in the case of oxidation with molecular oxygen. Thus, the following reactions are suggested:

$$H_2NO^- + H\dot{O}_2 \rightarrow HNO^- + H_2O_2$$

$$HNO^- + H\dot{O}_2 \rightarrow NO^- + H_2O_2$$

$$NO^- + \dot{O}_2 \rightarrow ONOO^-$$

A large increase of the oxidation yield in the presence of methanol is not unexpected because the alcohol scavanges the radicals $H\dot{O}_2$ and $\cdot OH$ to produce $R\dot{C}HOH$ [5, 8] which further reacts with O_2 to give $Rc(\dot{O}_2)HOH$. These organic peroxide radicals of strong oxidizing properties are formed during both γ-rays and sonochemical irradiation. The mechanism proposed for both radiation and ultrasonic studies [5] can be applied to sonochemical oxidation of hydroxylamine and is represented by the following reactions:

$$2HCH_2OH \xrightarrow{\cdot OH,\ H\dot{O}_2} 2H\dot{C}HOH + H_2O + H_2O_2$$

$$H\dot{C}HOH \xrightarrow{O_2} HC(\dot{O}_2)HOH$$

$$H_2NO^- + HC(\dot{O}_2)HOH \rightarrow HNO^- + HC(O_2H)HOH$$

$$HNO^- + HC(O_2H)HOH \rightarrow NO^- + HC(\dot{O})HOH + H_2O$$

$$NO^- + O_2 \rightarrow ONOO^-$$

$$H_2NO^- + HC(\dot{O})HOH \rightarrow HNO^- + HCHO + H_2O$$

In this case one $HC(\dot{O}_2)HOH$ radical can oxidize 1.5 hydroxylamine molecule whereas one HO_2 radical can oxidize 0.5 hydroxylamine molecule. Thus, a conclusion can be drawn that addition of methanol will increase the oxidation yield. However, methanol will increase the oxidation yield. However, methanol can also affect the cavitation phenomenon itself. Obviously, the presence of small amounts of methanol, readily miscible in water, should not affect the formation of cavities

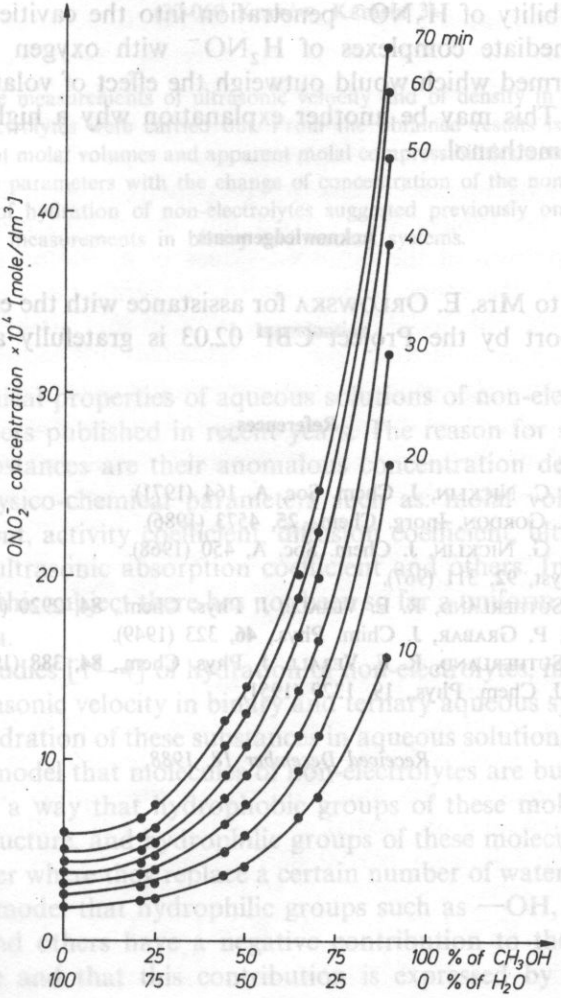

Fig. 3. Plot of ONO_2^- concentration vs. vol. concentration of methanol after sonification for different time. The solutions contain 0.01 mole /dm^3 hydroxylamine and 0.5 mole/dm^3 NaOH

significantly. However, as SEGHAL et al [5] pointed out, at higher concentrations because of its high vapor pressure alcohol can preferentially penetrate into the cavities and suppress cavitation. The authors anticipated, therefore, that in the case of Fe^{2+} sonochemical oxidation at higher alcohol concentrations the cavitational effect would overpower the chemical effects and thereby reduce the oxidation of Fe^{2+} (their experimental studies finished at concentration of 20% of alcohol in water). In the case of hydroxylamine oxidation, however, no levelling of the $ONOO^-$ concentration vs. alcohol concentration is observed (Fig. 3) even in 88% CH_3OH. The sonochemical oxidation rate increases throughout the whole concentration range of methanol. This may be explained probably by the fact that the reaction occurs in three different phases, i.e. in the gaseous phase (the cavities), the interphase that separates the cavity from the surrounding medium and the liquid medium. The possibility of H_2NO^- penetration into the cavities is not excluded. Thus, some intermediate complexes of H_2NO^- with oxygen of relatively high pressure may be formed which would outweigh the effect of volatile alcohol on the cavitation process. This may be another explanation why a high reaction yield is preserved even in methanol.

Acknowledgements

We are grateful to Mrs. E. ORŁOWSKA for assistance with the experimental work. The financial support by the Project CBP 02.03 is gratefully acknowledged.

References

[1] M. N. HUGHES, H. C. NICKLIN, J. Chem. Soc. A, 164 (1971).
[2] J. H. BUTLER, L. I. GORDON, Inorg. Chem., **25**, 4573 (1986).
[3] M. N. HUGHES, H. G. NICKLIN, J. Chem. Soc. A, 450 (1968).
[4] P. A. CAWSE, Analyst, **92**, 311 (967).
[5] C. SEGHAL, R. G. SUTHERLAND, R. E. VERALL, J. Phys. Chem., **84**, 2920 (1980).
[6] R. O. PRUDHOMME, P. GRABAR, J. Chim. Phys., **46**, 323 (1949).
[7] C. SEGHAL, R. G. SUTHERLAND, R. E. VERALL, J. Phys. Chem., **84**, 388 (1980).
[8] A. H. DEWHURST, J. Chem. Phys., 19, 1329 (1951).

Received December 18, 1988.

ARCHIVES OF ACOUSTICS
14, 3–4, 217-229 (1989)

MOLAL VOLUME AND COMPRESSIBILITY OF AQUEOUS NON-ELECTROLYTE SOLUTIONS

ADAM JUSZKIEWICZ

Faculty of Chemistry, Jagiellonian University
(30-060 Kraków, Karasia 3)

The measurements of ultrasonic velocity and of density in aqueous solutions of 20 non-electrolytes were carried out. From the obtained results isentropic compressibility, apparent molal volumes and apparent molal compressibilities were calculated. The changes of these parameters with the change of concentration of the non-electrolytes confirm the model of hydration of non-electrolytes suggested previously on the basis of ultrasonic velocity measurements in binary and ternary systems.

1. Introduction

Physico-chemical properties of aqueous solutions of non-electrolytes are subject of numerous papers published in recent years. The reason for such great interes in this group of substances are their anomalous concentration dependent changes of a number of physico-chemical parameters such as: molal volume, heat capacity, viscosity coefficient, activity coefficient, diffusion coefficient, ultrasonic velocity and compressibility, ultrasonic absorption coefficient and others. In spite of very many data collected in this subject there has not been so far a uniform theory describing all these phenomena.

In previous studies [1–4] of hydration of non-electrolytes, in which the measurements of the ultrasonic velocity in binary and ternary aqueous systems were applied, a model of the hydration of these substances in aqueous solutions was presented. It is assumed in this model that molecules of non-electrolytes are built into the structure of water in such a way that hydrophobic groups of these molecules occupy cages (voids) of this structure, and hydrophilic groups of these molecules occupy nodes of the lattice of water where they replace a certain number of water molecules. It is also assumed in this model that hydrophilic groups such as —OH, —NH_2, —$CONH_2$, =CO, —O— and others have a negative contribution to the total hydration of a non-electrolyte and that this contribution is expressed by a number of water

This work was partially financed by the Polish Academy of Sciences Problem CBBP.02.03.

molecules replaced by these groups at nodes of the lattice. Hydrophobic groups (alkyl groups), on the other hand, have a positive contribution to the total hydration and this contribution is expressed by a number of water molecules that surround an alkyl group. The total hydration is an algebraic sum of the both contributions.

The results obtained with other techniques such as: volumetric, calorimetric, viscosimetric, dielectric, NMR, IR and Raman spectroscopy confirm the above described model. On the basis of these results it may be concluded that with the hydrophobic (positive) hydration of alkyl groups of alcohols, ketones, amines, amides and their N-alkyl derivatives are connected the following effects: egzothermic effect of dissolving of a non-electrolyte, negative excess of partial molal volume, positive excess of partial molal heat capacity, positive excess of viscosity coefficient, positive excess of activity coefficients of a non-electrolyte and water, negative excess of diffusion coefficients, and others. Negatively hydrated molecules e.g. molecules of urea and formamide show the effects opposite to the above listed ones i.e. endothermic effect of dissolving, positive excess of partial molal volume of a non-electrolyte, negative excess of heat capacity and the others. In many cases the concentrations of non-electrolytes at extrema are comparable with those obtained from ultrasonic velocity measurements. In the paper [4] a qualitative analysis of literature data on this subject was carried out, for it was impossible to make a quantitative comparison of the obtained values of hydration numbers with the values obtained with the other techniques i.e. to verify the suggested model of hydration, because of the lack of numerical data for some of the examined substances.

This paper is one of the attempts undertaken to verify the suggested model of hydration of molecules of electrolytes, non-electrolytes as well as macromolecules. It presents the results of measurements of apparent molal volumes and compressibilities of 20 non-electrolytes showing either positive or negative hydration.

2. Relations between density and/or ultrasonic velocity and partial molal thermodynamic parameters of solute

Any partial molal quantity is expressed with:

$$\mathbf{F}_1 = \left(\frac{\partial F}{\partial n_i}\right)_{p,T,n_1,\ldots,n_k} \tag{1}$$

In the case of a binary solution, partial molal quantities of a solute and of a solvent are expressed by the following partial derivatives:

$$\mathbf{F}_2 = \left(\frac{\partial F}{\partial n_2}\right)_{T,p,n_1} ; \quad \mathbf{F}_1 = \left(\frac{\partial F}{\partial n_1}\right)_{T,p,n_2} \tag{2.3}$$

In order to determine partial molal quantities it is necessary to know apparent molal quantities, and these can be obtained experimentally.

In generally any apparent molal quantity of a solute is defined by the following equation:

$$\Phi F_2 = (F - n_1 \mathbf{F}_1^0)/n_2 \tag{4}$$

where F is an extensive quantity for a solution, $\mathbf{F}_1^0$ is a respective molal quantity for a solvent, n_1 and n_2 are numbers of moles of a solvent and of a solute, respectively. The relation between ΦF_2 and F_2 can be obtained by differentiating eq. (4) with respect to n_2:

$$\mathbf{F}_2 = \Phi F_2 + \left(\frac{\partial F_2}{\partial \ln n_2}\right)_{n_1} = F_2 + \left(\frac{\partial F_2}{\partial \ln m}\right) \tag{5}$$

where m is a molality (m/kG solvent).

For dilute solutions molal concentration can be replaced by molar concentration, c, and then eq. (5) changes into:

$$\mathbf{F}_2 = \Phi F_2 + \left(\frac{\partial F_2}{\partial \ln c}\right). \tag{6}$$

At the limiting concentration, when $c \to 0$

$$\mathbf{F}_2^0 = \Phi F_2^0. \tag{7}$$

Some researchers are of the opinion that no physical sense can be ascribed to the partial molal quantities and that these are only mathematical quantities because for example negative partial molal volume has no physical sense. According to the author it is not the right opinion. Physical sense can be ascribed to these quantities when molecules of a solute are considered together with molecules of a solvent solvated with a solute. Then, for example negative partial molal volume is a measure of a decrease in the volume of solvent molecules in solvation sheath as compared to the volume of solvent molecules which are not influenced on by solute molecules.

Apparent molal volume of the solute ΦV_2 is defined by:

$$\Phi V_2 = (V - n_1 \mathbf{V}_1^0)/n_2, \tag{8}$$

where V is a volume of the solution containing n_1 moles of the solvent and n_2 moles of the solute. $\mathbf{V}_1^0$ is a partial molal volume of the solvent.

Apparent molal compressibility of the solute ΦK_2 is expressed by:

$$\Phi K_2 = \left(\frac{\partial \Phi V_2}{\partial p}\right)_s = (\beta_s V - n_1 \beta_{s0} V_1^0)/n_2, \tag{9}$$

where β_s and β_{s0} are isentropic compressibilities of a solution and of solute, respectively.

Using experimental results, ΦV_2 and ΦK_2 can be calculated from the following

relations:

$$\Phi V_2 = \frac{1000}{mdd_0}(d_0 - d) + \frac{M_2}{d}, \tag{10}$$

$$\Phi K_2 = \frac{1000}{md_0}(\beta_s - \beta_{s0}) + \beta_s \Phi V_2, \tag{11}$$

$$\beta_s = \frac{1}{du^2}, \tag{12}$$

where d and d_0 are densities of the solution and of the solvent, respectively, u is the velocity of ultrasound, m is the molality (m/kG solvent), and M_2 is the molecular weight of the solute.

In liquid binary systems the principle of additivity of the above parameters is not always fulfilled: the expression $(\Phi F_2 - \Phi F_2^0)$ is a measure of the deviation from this principle.

3. Experiment

All the examined substances: methanol, ethanol, n-propanol, tert.-butanol, ethylene glycol, 1,2-propylene glycol, 1,3-butylene glycol, 2,3-butylene glycol, glycerol, acetone, 1,4-dioxane, etylene glycol monoacetate, methoxyethanol, formamide, hydrazine, N-methylformamide, acetamide, dimethylformamide, dimethylsulphoxide and urea were of analar grade. Triple-distilled water was used throughout.

Density measurements were carried out with use of a pycnometer and of a vibrating tube densimeter [5, 6]. Ultrasonic velocity measurements were carried out by the pulse-phase method [7] and by the "sing around" method [8–10]. The temperature of measurements was 25°C. For the density measurements with the vibrating tube densimeter as well as for ultrasonic velocity measurements with the "sing around" gauge the solutions were thermostated to an accuracy of ± 0.001°C, for the other measurements to ± 0.02°C.

The results of the measurements are presented in Fig. 1–13 and in Table 1.

4. Discussion

The results of the density measurements of the examined substances in solutions of the water are presented in Fig. 1–4 in the form of dependences of $(\Phi V_2 - \Phi V_2^0)$ on molar fractions of the non-electrolytes.

For the majority of the examined non-electrolytes typical curves with minima were obtained. Only for urea, formamide, hydrazine and glycerol these dependences have no minima and within the studied concentration range the values of $(\Phi V_2 - \Phi V_2^0)$ are positive. The measured densities and the calculated values of $(\Phi V_2 - \Phi V_2^0)$ at different

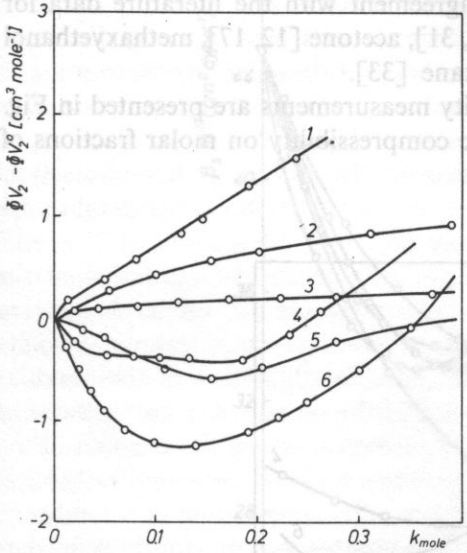

Fig. 1. Dependence of excess of the apparent molal volume of non-electrolytes ΦV_2–ΦV_2^0 on the molal fraction of solute: *1* – urea, *2* – formamide, *3* – hydrazine, *4* – *N*-methylformamide, *5* – acetamide, *6* – dimethylformamide

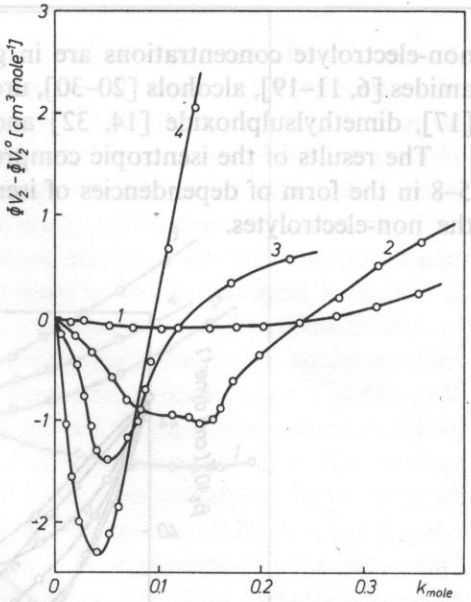

Fig. 2. Dependence of excess of the apparent molal volume of non-electrolytes ΦV_2–ΦV_2^0 on the molal fraction of solute: *1* – methanol, *2* – ethanol, *3* – *n*-propanol, *4* – *t*-butanol

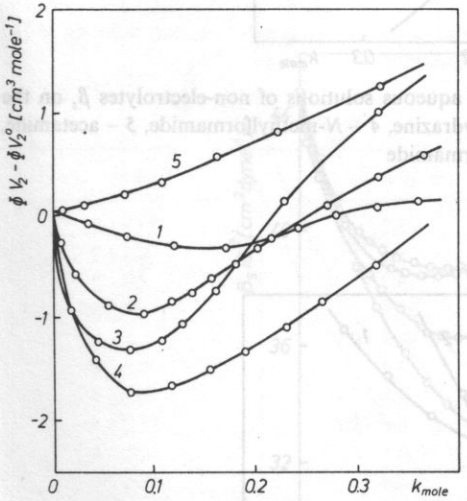

Fig. 3. Dependence of excess of the apparent molal volume of non-electrolytes ΦV_2–ΦV_2^0 on the molal fraction of solute: *1* – ethylene glycol, *2* – 1,2-propylene glycol, *3* – 2,3-butylene glycol, *4* – 1,3-butylene glycol, *5* – glycerol

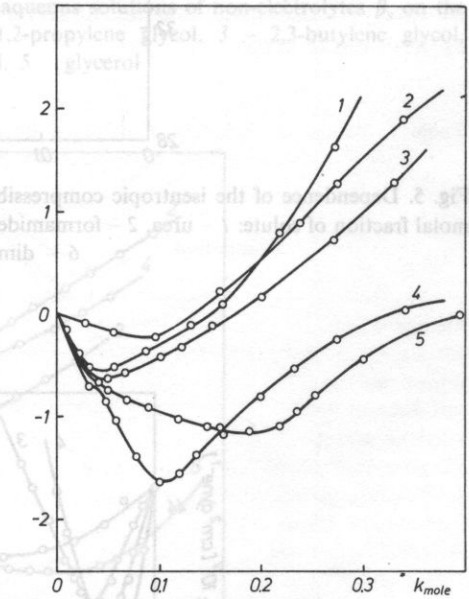

Fig. 4. Dependence of excess of the apparent molal volume of non-electrolytes ΦV_2–ΦV_2^0 on the molal fraction of solute: *1* – acetone, *2* – 1,4-dioxane, *3* – methoxyethanol, *4* – etylene glycol monoacetate, *5* – dimethylsulphoxide

non-electrolyte concentrations are in good agreement with the literature data for amides [6, 11–19], alcohols [20–30], urea [15, 31], acetone [12, 17], methaxyethanol [17], dimethylsulphoxide [14, 32] and dioxane [33].

The results of the isentropic compressibility measurements are presented in Fig. 5–8 in the form of dependencies of isentropic compressibility on molar fractions of the non-electrolytes.

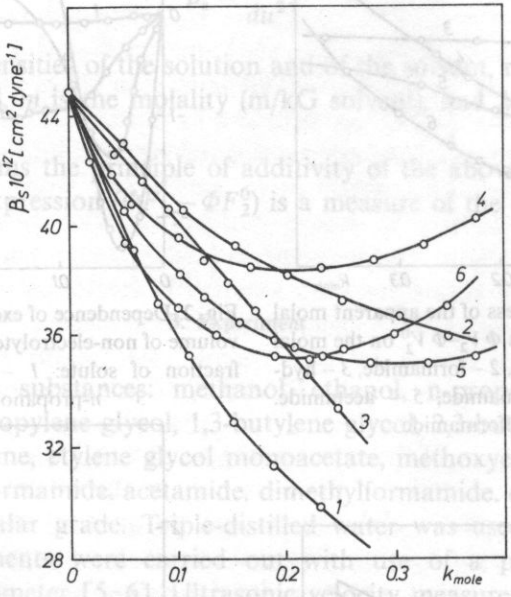

Fig. 5. Dependence of the isentropic compressibility of aqueous solutions of non-electrolytes β_s on the molal fraction of solute: *1* – urea, *2* – formamide, *3* – hydrazine, *4* – *N*-methylformamide, *5* – acetamide, *6* – dimethylformamide

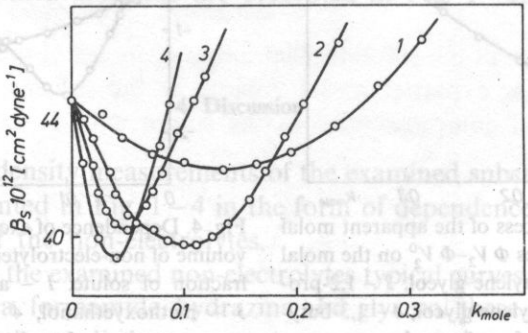

Fig. 6. Dependence of the isentropic compressibility of aqueous solutions of non-electrolytes β_s on the molal fraction of solute: *1* – methanol, *2* – ethanol, *3* – *n*-propanol, *4* – *t*-butanol

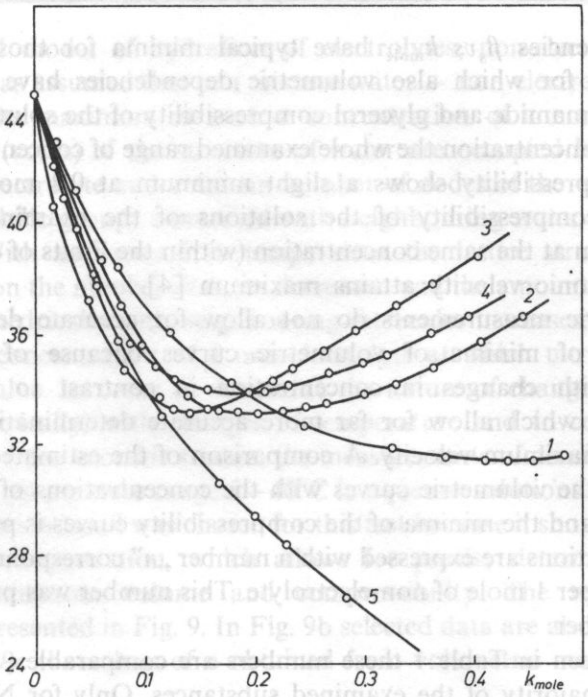

Fig. 7. Dependence of the isentropic compressibility of aqueous solutions of non-electrolytes β_s on the molal fraction of solute: *1* – ethylene glycol, *2* – 1,2-propylene glycol, *3* – 2,3-butylene glycol, *4* – 1,3-butylene glycol, *5* – glycerol

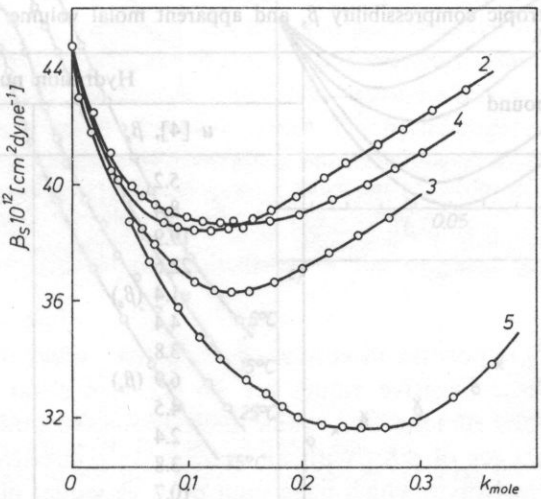

Fig. 8. Dependence of the isentropic compressibility of aqueous solutions of non-electrolytes β_s on the molal fraction of solute: *2* – 1,4-dioxane, *3* – methoxyethanol, *4* – ethylene glycol monoacetate, *5* – dimethylsulphoxide

The dependencies $\beta_s vs\ k_{mole}$ have typical minima for those of the examined non-electrolytes for which also volumetric dependencies have minima. For hydrazine, urea, formamide and glycerol compressibility of the solutions decreases with an increase in concentration the whole examined range of concentration; for ethylene glycol the compressibility shows a slight minimum at 0.4 molar fraction.

Isentropic compressibility of the solutions of the examined non-electrolytes attains minimum at the same concentration (within the limits of experimental error), at which ultrasonic velocity attains maximum [4].

Densitometric measurements do not allow for accurate determination of the concentrations of minima of volumetric curves bacause of small changes in $(\Phi V_2 - \Phi V_2^0)$ with changes in concentration in contrast to ultrasonic velocity measurements , which allow for far more accurate determination of the concentrations of the maximum velocity. A comparison of the estimated concentrations of the minima of the volumetric curves with the concentrations of the maxima of the velocity curves and the minima of the compressibility curves is presented in Table 1. These concentrations are expressed with a number „*n*" corresponding to a number of moles of water per 1 mole of non-electrolyte. This number was previously defined as hydration number.

As can be seen in Table 1 these numbers are comparable (within experimental error) for the majority of the examined substances. Only for N-methylformamide, methoxyethanol and acetone the difference between the numbers are higher than the experimental error.

Table 1. Values of hydration numbers n obtained from measurements of ultrasonic velocity u [4], isentropic compressibility β_s and apparent molal volume ΦV_2

Compound	Hydration number n	
	u [4], β_s	ΦV_2
methanol	5.2	5±2
ethanol	8.4	8.5±2
n-propanol	19.9	19±2
tert-butanol	22.6	24±2
ethylene glycol	1.4 (β_s)	4±2
1,2-propylene glycol	4.4	9.5±4
1,3-butylene glycol	3.8	9.5±4
2,3-butylene glycol	6.9 (β_s)	11.5±4
N-methylformamide	4.5	13±4
acetamide	2.4	5.5±2
N,*N*-dimethylformamide	3.8	6.5±2
acetone	10.7	17±4
methoxyethanol	6.5	25±4
1,4-dioxane	8.7	7±2
ethylene glycol monoacetate	10.5	10±2
dimethylsulphoxide	3.4	4±2

In the presented model of hydration of electrolytes, non-electrolytes and of macromolecules it was assumed that in a mixture water – non-electrolyte velocity of ultrasound attains its maximum at such a concentration of a non-electrolyte at which all the cages (voids) of the structure of water are occupied by hydrophobic groups of the non-electrolyte and a certain number of nodes of the water lattice are occupied by hydrophilic groups connected with neighbouring water molecules with hydrogen bonds. With an increase in temperature the lattice structure of water undergoes destruction the number of cages decreases, and the amount of "free" water not connected tetrahedrically with neighbouring molecules increases. This results in an decrease of the concentration of a non-electrolyte at which ultrasonic velocity attains maximum value. In order to determine the nature of changes of parameter n (obtained volumetrically) with changes of temperature and to compare it with values of n obtained from acoustic studies, the measurements of density and velocity of ultrasound in the temperature range 5–40°C in aqueous solutions of tert.-butanol were carried out. Tert.-butanol was chosen for this test because it shows considerably big changes in its concentration, which allows for precise determination of the concentration of minimum volume and compressibility. The results of these measurements are presented in Fig. 9. In Fig. 9b selected data are also given [23]. As can be seen in Fig. 9c the values of n obtained from volumetric measurements are

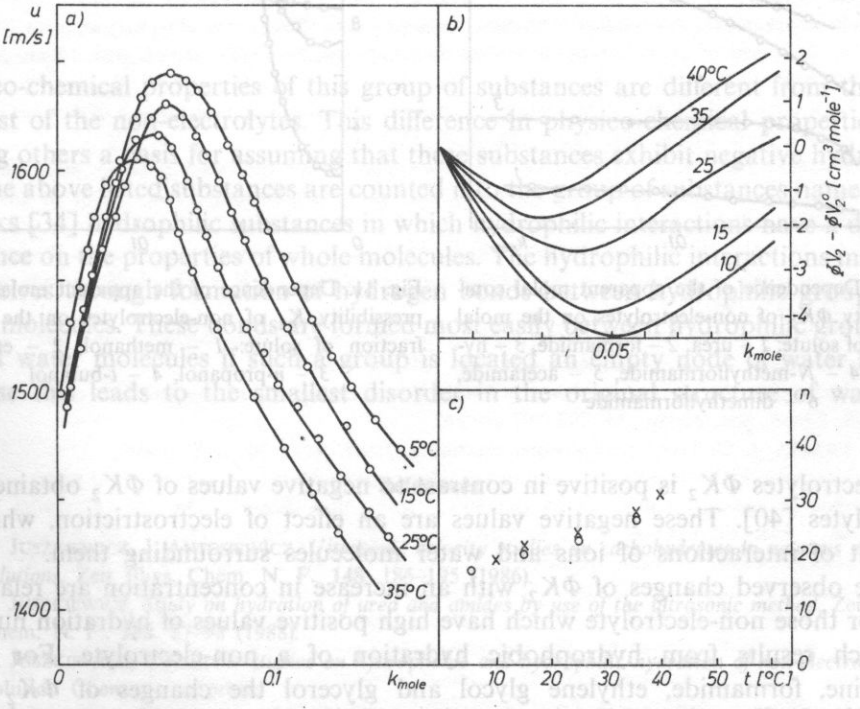

Fig. 9. Temperature dependence of ultrasonic velocity a) excess of the apparent molal volume $\Phi V_2 - \Phi V_2^0$ b) and hydration number c) from the aqueous solution of t-butanol

similar to those obtained from acoustic measurements. Also the nature of the changes with temperature is similar. This constitues a very good confirmation of the assumed model of hydration since there is no other interpretation of the effect that the non-electrolyte concentration at which certain physical parameters attain extrema decrease in temperature. Similar values of n at different temperarures obtained with two different techniques also confirm that the assumptions are correct. A similar opinion on the interpretation of this effect can be found in many other papers [16, 21, 34–39].

In Fig. 10–13 the dependences of apparent molal compressibility of solute on molar fraction of a non-electrolyte are presented. For all the examined

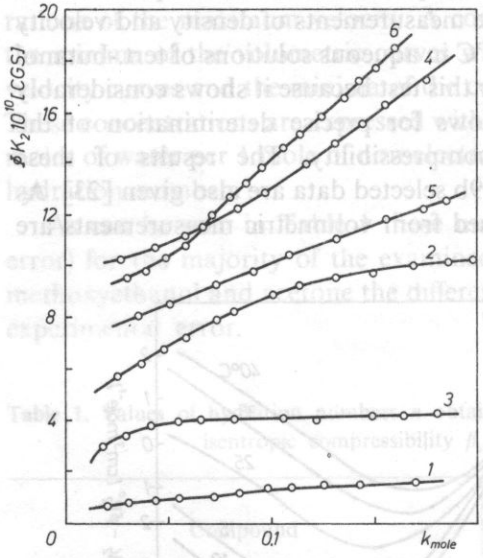

Fig. 10. Dependence of the apparent molal compressibility ΦK_2 of non-electrolytes on the molal fraction of solute: *1* – urea, *2* – formamide, *3* – hydrazine, *4* – *N*-methylformamide, *5* – acetamide, *6* – dimethylformamide

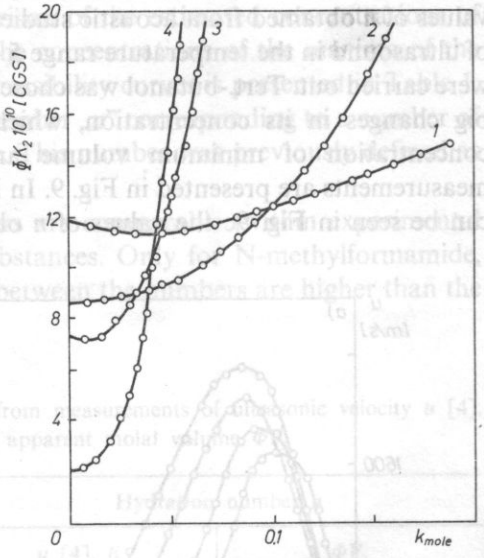

Fig. 11. Dependence of the apparent molal compressibility K_2 of non-electrolytes on the molal fraction of solute: *1* – methanol, *2* – ethanol, *3* – *n*-propanol, *4* – *t*-butanol

non-electrolytes ΦK_2 is positive in contrast to negative values of ΦK_2 obtained for electrolytes [40]. These negative values are an effect of electrostriction, which is a result of interactions of ions and water molecules surrounding them.

The observed changes of ΦK_2 with an increase in concentration are relatively high for those non-electrolyte which have high positive values of hydration number n, which results from hydrophobic hydration of a non-electrolyte. For urea, hydrazine, formamide, ethylene glycol and glycerol the changes of ΦK_2 with concentration are considerably lower, and at higher concentrations ΦK_2 for urea, hydrazine and formamide are practically constant. This prove once more that

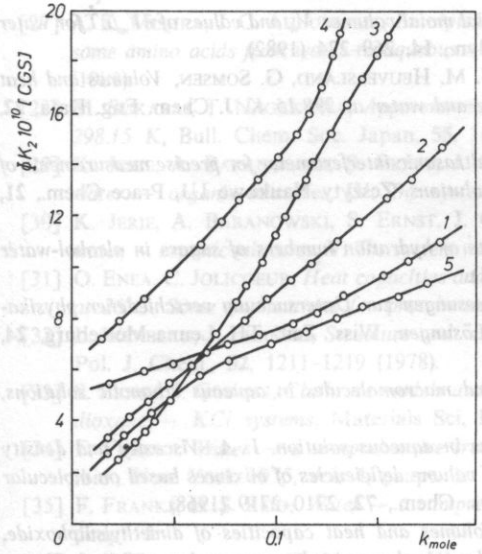

Fig. 12. Dependence of the apparent molal compressibility K_2 of non-electrolytes on the molal fraction of solute: *1* – ethylene glycol, *2* – 1,2-propylene glycol, *3* – 2,3-butylene glycol, *4* – 1,3-butylene glycol, *5* – glycerol

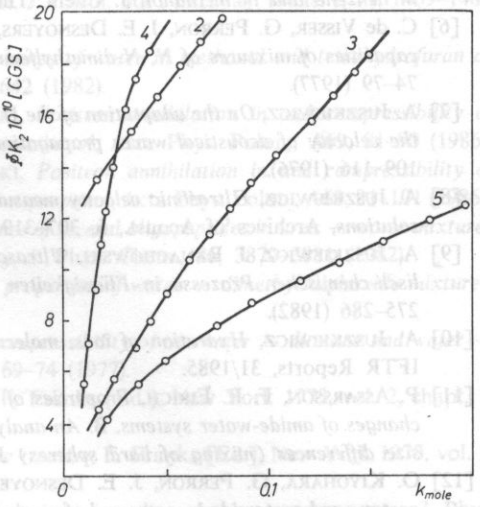

Fig. 13. Dependence of the apparent molal compressibility K_2 of non-electrolytes on the molal fraction of solute: *2* – 1,4-dioxane, *3* – methoxyethanol, *4* – ethylene glycol monoacetate, *5* – dimethylsulphoxide

physico-chemical properties of this group of substances are different from those of the rest of the non-electrolytes. This difference in physico-chemical properties was among others a basis for assuming that these substances exhibit negative hydration.

The above listed substances are counted into the group of substances named after FRANKS [34] hydrophilic substances in which hydrophilic interactions have a decisive influence on the properties of whole molecules. The hydrophilic interactions manifest themselves through formation of hydrogen bonds between hydrophilic groups and water molecules. These bonds are formed most easily between hydrophilic group and closest water molecules if such a group is located an empty node of water lattice, because this leads to the smallest disorder in the original structure of water.

References

[1] A. JUSZKIEWICZ, J. ANTOSIEWICZ, *Ultrasonic velocity studies on carbohydrates in aqueous ethanolic solutions*, Zeit Phys. Chem. N. F., **148**, 185–195 (1986).

[2] A. JUSZKIEWICZ, *Study on hydration of urea and amides by use of the ultrasonic method*, Zeit. Phys. Chem. N. F., **158**, 87–98 (1988).

[3] A. JUSZKIEWICZ, *Ultrasonic studies on hydrophobic and hydrophilic hydration of non-electrolytes*, J. Solution Chem. – in press.

[4] A. JUSZKIEWICZ, *Ultrasonic studies of hydration of non-electrolytes*, Ultrasonics – **27**, 131–139 (1989).

[5] M. SAKURAI, T. NAGAKAWA, *Densities of dilute solutions of water in benzene and in methanol at*

278.15, 288.15, 298.15, 308.15 and 318.15 K. *Partial molal volumes V_w and values of $\partial V_w/\partial T$ for water in benzene and in methanol*, J. Chem. Thermodyn., **14**, 269–274 (1982).

[6] C. de VISSER, G. PERRON, J. E. DESNOYERS, W. J. M. HEUVELSLAND, G. SOMSEN, *Volumes and heat capacities of mixtures of N, N-dimethylformamide and water at 298.15 K*. J. Chem. Eng. Data, **22**, 74–79 (1977).

[7] A. JUSZKIEWICZ, *On the adaptation of the UI–11 ultrasonic interferometer for precise measurements of the velocity of acoustical waves propagation in solutions*. Zeszyty Naukowe UJ, Prace Chem., **21**, 109–116 (1976).

[8] A. JUSZKIEWICZ, *Ultrasonic velocity measurements of hydration numbers of sugars in alcohol-water solutions*, Archives of Acoust., **6**, 307–319 (1981).

[9] A. JUSZKIEWICZ, J. RANACHOWSKI, *Ultraschallmessungen zur Untersuchung verschiedener physikalisch-chemischer Prozesse in Flüssigkeiten und Lösungen*, Wiss. Zeit. TH Leuna-Merseburg, **24**, 275–286 (1982).

[10] A. JUSZKIEWICZ, *Hydration of ions, molecules and macromolecules in aqueous ethanolic solutions*, IFTR Reports, 31/1985.

[11] P. ASSARSSON, F. R. EIRICH, *Properties of amides in aqueous solution. I. A. Viscosity and density changes of amide-water systems. B. An analysis of volume deficiencies of mixtures based on molecular size differences (mixing of hard spheres)* J. Phys. Chem., **72**, 2710–2719 (1968).

[12] O. KIYOHARA, G. PERRON, J. E. DESNOYERS, *Volumes and heat capacities of dimethylsulphoxide, acetone and acetamide in water and of some electrolytes in these mixed aqueous solvents* Can. J. Chem., **53**, 3263–3268 (1975).

[13] C. de VISSER, P. PEL, G. SOMSEN, *Volumes and heat capacities of water and N-methylformamide in mixtures of these solvents*, J. Solution Chem., **6**, 571–580 (1977).

[14] C. de VISSER, W. J. M. HEUVELSLAND, L. A. DUNN, G. SOMSEN, *Some properties of binary aqueous liquid mixtures*, J. Chem. Soc., Faraday Trans. I, **74**, 1159–1169 (1978).

[15] C. de VISSER, G. PERRON, J. E. DESNOYERS, *Volumes and heat capacities of ternary aqueous systems at 25°C. Mixtures of urea, tert.-butyl alcohol dimethylformamide and water* J. Am. Chem. Soc., **99**, 5894–5898 (1977).

[16] F. KAWAIZUMI, M. OHNO, Y. MIYAHARA, *Ultrasonic and volumetric investigation of aqueous solutions of amides*, Bull. Chem. Soc. Japan, **50**, 2229–2233 (1977).

[17] G. ROUX, G. PERRON, J. E. DESNOYERS, *The heat capacities and volumes of some low molecular weight amides, ketones, esters and ethers in water over the whole solubility range*, Can. J. Chem., **56**, 2808–2814 (1978).

[18] N. M. MURTHY, K. V. SIVAKUMAR, E. RAJAGOPAL, S. V. SUBRAHMANYAM, *Excess thermodynamic functions of the systems water + N-methylformamide and water + N,N,-dimethylformamide*, Acustica, **48**, 341–345 (1981).

[19] K. SUBBARANGAIAH, N. M. MURTHY, S. V. SUBRAHMANYAM, *Excess thermodynamic functions of the system: water + formamide*, Acoustica, **58**, 105–108 (1985).

[20] K. NAKANISHI, *Partial molal volumes of butyl alcohols and of related compounds in aqueous solution*, Bull. Chem. Soc. Japan, **33**, 793–797 (1960).

[21] F. FRANKS, J. G. IVES, *Alcohol-water mixtures*, Quart. Rev., **20**, 1–50 (1966).

[22] H. HOILAND, E. VIKINGSTAD, *Partial molal volumes and additivity of group partial molal volumes of alcohols in aqueous solution* at 25 and 35°C, Acta Chem. Scand., **A30**, 182–186 (1976).

[23] C. de VISSER, G. PERRON, J. E. DESNOYERS, *The heat capacities, volumes and expansibilities of tert.-butyl alcohol — water mixtures from 6 to 65°C*, Can. J. Chem., **55**, 856–862 (1977).

[24] A. HVIDT, R. MOSS, G. NIELSEN, *Volume properties of aqueous solutions of tert.-butyl alcohol at temperatures between 5 an 25°C*, Acta Chem. Scand., **B32**, 274–280 (1978).

[25] G. C. BENSON, O. KIYOHARA, *Thermodynamics of aqueous mixtures of non-electrolytes. I. Excess volumes of water — n-alcohol mixtures at several temperatures*, J. Solution Chem., **9**, 791–804 (1980).

[26] R. V. JASRA, J. C. AHLUWALIA, *Entalpies of solution, partial molal heat capacities and apparent molal volumes of sugars and polyols in water*, J. Solution Chem., **11**, 325–338 (1982).

[27] A. K. MISHRA, J. C. AHLUWALIA, *Entalpies, heat capacities and apparent molal volumes of transfer of some amino acids from water to aqueous t-butanol*, J. Chem. Soc., Faraday Trans. I, **77**, 1469–1483 (1981).

[28] M. SUKARAI, T. NAGAKAWA, *Apparent molar volumes of water in methanol and tetrahydrofuran at 298.15 K*, Bull. Chem. Soc. Japan, **55**, 1641–1642 (1982).

[29] K. JERIE, A. BARANOWSKI, S. ERNST, J. GLIŃSKI, *Positron annihilation in and compressibility of water – organic mixtures. IV. The system water-ethanol*, Acta Phys. Polon., **A69**, 81–90 (1986).

[30] K. JERIE, A. BARANOWSKI, S. ERNST, J. GLIŃSKI, *Positron annihilation in and compressibility of water – organic mixtures. V. The system water – n-propanol*, Acta Phys. Polon., **A69**, 91–101 (1986).

[31] O. ENEA, C. JOLICOEUR, *Heat capacities and volumes of several oligopeptides in urea – water mixtures at 25°C. Some implications for protein unfolding*, J. Phys. Chem., **86**, 3870–3881 (1982).

[32] L. WERBLAN, J. LESIŃSKI, *Structure and selected properties of water – dimethylsulphoxide mixtures*, Pol. J. Chem., **52**, 1211–1219 (1978).

[33] S. ERNST, J. GLIŃSKI, *Clathrate models and the compressibility of the water – dioxane and water – dioxane – KCl systems*, Materials Sci, III/3, 69–74 (1977).

[34] F. FRANKS, *Water – a comprehensive treatise*, F. Franks [Ed.], New York 1973, vol. 2, chapt. 1; ibid., New York 1975, vol. 4, chapt. 1.

[35] F. FRANKS, D. S. REID, *Water – a comprehensive treatise*, F. Franks [Ed.], New York 1973, vol. 2, chapt. 5.

[36] E. K. BAUMGARTNER, G. ATKINSON, *Ultrasonic velocity in nonelectrolyte – water mixtures*, J. Phys. Chem., **75**, 2336–2340 (1971).

[37] J. LARA, J. E. DESNOYERS, *Isentropic Compressibilities of alcohol – water mixtures at 25°C*, J. Solution Chem., **10**, 465–478 (1981).

[38] G. D'ARRIGO, O. CONDE, *Acoustic properties of water – ethanol mixtures at low temperatures*, J. Phys., Colloque **C7**, 185–193 (1984).

[39] G. D'ARRIGO, A. PAPARELLI, *Sound propagation in water – ethanol mixtures at low temperatures. I. Ultrasonic velocity*, J. Chem. Phys., **88**, 405–415 (1988).

[40] J. STUEHR, E. YEAGER, *Physical Acoustics*, vol. II, part A, New York-London 1965.

Received November 7, 1988.

ARCHIVES OF ACOUSTICS
14, 3-4, 231-240 (1989)

THE EFFECT OF IMPURITIES ON ACOUSTIC PROPERTIES OF GALLIUM PHOSPHIDE

ZYGMUNT KLESZCZEWSKI

Institute of Physics, Silesian Technical University
(44-100 Gliwice)

This paper presents results of measurements of propagation velocity and attenuation coefficient of an acoustic wave, and phonon-phonon coupling constant in pure GaP crystals and with impurities. Measurements were carried out with the utilization of Bragg type diffraction of laser light on an acoustic wave in frequency range from 0.2 to 1.5 GHz.

The elastic constants versus impurity concentration dependence was determined from measurements of propagation velocity of an acoustic wave. It was found that the c_{11} constant changes most of all, while the c_{12} and c_{44} change less. c_{11} and c_{44} constants decrease with the increase of impurity concentration and the c_{12} constant increases slightly. Assuming, that intervalley electron transitions are the main cause for changes of the elastic constants the deformation potential constant was calculated.

From investigations of the relationship between the attenuation coefficient and impurity concentration it was stated that attenuation in crystals with impurities exceeds attenuation in pure crystals and that the difference increases with frequency. The relaxation time, which is characteristic for intervalley electron transitions, was determined on the basis of measurements of the attenuation coefficient.

The influence of impurities on the phonon-phonon coupling constant was not stated.

W pracy przedstawiono wyniki pomiarów prędkości propagacji i współczynników tłumienia fali akustycznej oraz stałych sprzężenia fonon-fonon w czystych i domieszkowanych kryształach GaP. Pomiary przeprowadzono wykorzystując dyfrakcję Bragga światła laserowego na fali akustycznej w przedziale częstotliwości od 0.2 do 1.5 GHz.

Z pomiarów prędkości propagacji fali akustycznej wyznaczono zależność stałych sprężystych od koncentracji domieszek. Stwierdzono, że najbardziej zmienia się stała c_{11}, w mniejszym stopniu stała c_{12} i c_{44}. Stałe c_{11} i c_{44} maleją ze wzrostem koncentracji domieszek, a stała c_{12} nieznacznie wzrasta. Zakładając, że główną przyczyną zmian stałych sprężystych są międzydolinowe przejścia elektronów, wyliczono stałą potencjału deformacyjnego.

Badając zależność współczynnika tłumienia od koncentracji domieszek stwierdzono, że w kryształach domieszkowanych tłumienie jest większe niż w kryształach czystych, przy czym różnica ta wzrasta ze wzrostem częstotliwości. Pomiary współczynnika tłumienia pozwoliły wyznaczyć czas relaksacji charakteryzujący międzydolinowe przejścia elektronów.

Nie stwierdzono eksperymentalnie wpływu domieszek na stałe sprzężenia fonon-fonon.

1. Introduction

Research was aimed at the determination of the effect of impurities an acoustic properties of semiconductors. Pure and with impurities crystals of gallium phosphide GaP with three concentrations of sulfur impurities: $7.7 \cdot 10^{22}$ m^{-3}, $6.5 \cdot 10^{23}$ m^{-3} and $1.9 \cdot 10^{24}$ m^{-3}, were chosen. Crystals were obtained from the Institute of Technology of Electronic Materials in Warsaw, where also impurity concentration, carrier mobility and electric resistance of samples were determined.

At room temperature, at which measurements were performed, all impurities are ionized and investigated crystals are *n*-type semiconductors.

Lattice impurities, as well as free carriers cause changes of elastic constants of the second and third order. This, in turn, causes a change of propagation velocity and acoustic wave attenuation coefficient. Also values of phonon-phonon coupling constants change.

Within the framework of this work values of mentioned material constants were measured.

Gallium phosphide crystallizes in the cubic system, point group 43 m. Due to a relatively high value of the energy gap 2.20 eV, these crystals can be investigated with acoustooptic methods with the utilization of laser light in the visible range.

2. Experimental system

Measurements were performed with the utilization of Bragg type diffraction of laser light on a volume acoustic wave. The diagram of the set-up for measurements in shown in Fig. 1.

Investigated GaP crystals were rectangular prisms with dimensions $5 \times 5 \times 20$

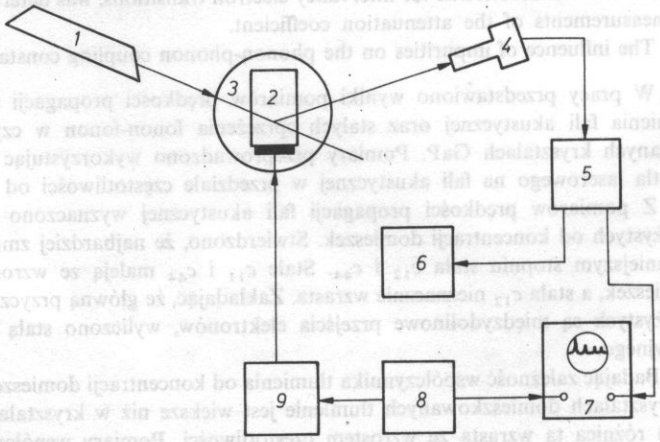

Fig.1. Diagram of measuring system *1* – laser, *2* – investigated crystal, *3* – goniometric table, *4* – multiplier phototube, *5* – selective amplifier, *6* – recorder, *7* – oscilloscope, *8* – modulating generator, *9* – high-frequency generator

mm. The parallelism of frontal planes was not worse than 5″, while the orientation accuracy was equal about 30′. Longitudinal and transverse acoustic waves were generated with $LiNbO_3$ transducers with 36° Y and X cutting, respectively. Transducers with fundamental frequency of 150–200 MHz were connected with tested crystals with an indium layer or due to adhesion. Surfacest of transducers were equal to from 2 to 5 mm^2 depending on applied frequency. High-frequency generators had the electric power of 1 W.

The propagation velocity of an acoustic wave was determined from measurements of the acoustic pulse transition time in the investigated crystal, as well as from measurements of the Bragg angle. Accuracy of velocity measurements amounted to about 0.2%.

The acoustic wave attenuation coefficient was determined with the utilization of interference of a series of waves reflected from frontal planes of the crystal at a small frequency change of these waves. This method is described in detail in paper [1]. Measurements were made in frequency range 0.2–1.5 GHz. The measurement accuracy of the attenuation coefficient equals about 10%.

Phonon-phonon coupling constants were determined from intensity measurements of light diffracted on harmonics of acoustic wave.

3. Results of measurement

Results of measurements of acoustic wave's propagation velocity in pure and with impurities GaP crystals are presented in Table 1. Values of c_{ij} constants were

Table 1. Propagation velocity of a longitudinal and transverse acoustic wave in GaP ($T = 293$ K, $f = 500$ MHz)

Impurity concentration	Direction of propagation polarization	Velocity ms^{-1}
pure	[100], [100]	5864
	[100], [001]	4156
	[110], [110]	6480
	[111], [111]	6675
$7.7 \cdot 10^{22}$	[100], [100]	5858
	[100], [001]	4150
	[110], [110]	6475
	[111], [111]	6670
$6.5 \cdot 10^{23}$	[100], [100]	5862
	[100], [001]	5150
	[110], [110]	6475
	[111], [111]	6670
$1.9 \cdot 10^{24}$	[100], [100]	5835
	[100], [001]	4145
	[110], [110]	6468
	[111], [111]	6665

determined (Table 2). On the basis of known relationships between acoustic wave's propagation velocity and elastic constants:

$$V_{[100],[100]} = \sqrt{\frac{c_{11}}{\varrho}},$$

$$V_{[110],[110]} = \sqrt{\frac{c_{11}+c_{12}+2c_{44}}{2\varrho}}, \tag{1}$$

$$V_{[111],[111]} = \sqrt{\frac{c_{11}+2c_{12}+4c_{44}}{3\varrho}},$$

$$V_{[100],[001]} = \sqrt{\frac{c_{44}}{\varrho}}.$$

Table 2. Values of elastic constants of GaP

Impurity concentration m^{-3}	c_{11} 10^{10} Nm^{-2}	c_{12} 10^{10} Nm^{-2}	c_{44} 10^{10} Nm^{-2}
pure	14.195	6.231	7.132
$7.7 \cdot 10^{20}$	14.190	6.252	7.110
$6.5 \cdot 10^{23}$	14.140	6.260	7.110
$1.9 \cdot 10^{24}$	14.058	6.280	7.094

And then angular distributions of velocities can be determined with the help of elastic constants. Figure 2 presents an exemplary velocity distribution of an acoustic wave in the XY plane in pure GaP. This distribution was calculated on the basis of determined elastic constants, and theoretical relationships between wave's velocity of propagation in an arbitrary direction and elastic constants.

Preformed measurements prove that the acoustic wave's propagation velocity is smaller in crystals with impurities than in pure crystals. Greatest differences were observed for a longitudinal wave in direction [100]. Whereas, in the case of a transverse wave in direction [100] and longitudinal waves in directions [110] and [111] much smaller differences were observed. This means that impurities cause the c_{11} constant to change the most, while elastic constant c_{44} and combination of constants $c_{11}+2c_{12}+4c_{44}$ change insignificantly. Table 3 presents changes of elastic constants: c_{11}, c_{12}, c_{44}; calculated on the basis of velocity measurements of an acoustic wave.

Performed calculations prove that the c_{11} elastic constant changes the most and the value of this constant decreases with an impurity concentration increase. The value of the c_{44} constant decreases much less while the c_{12} constant is slightly greater in crystals with impurities.

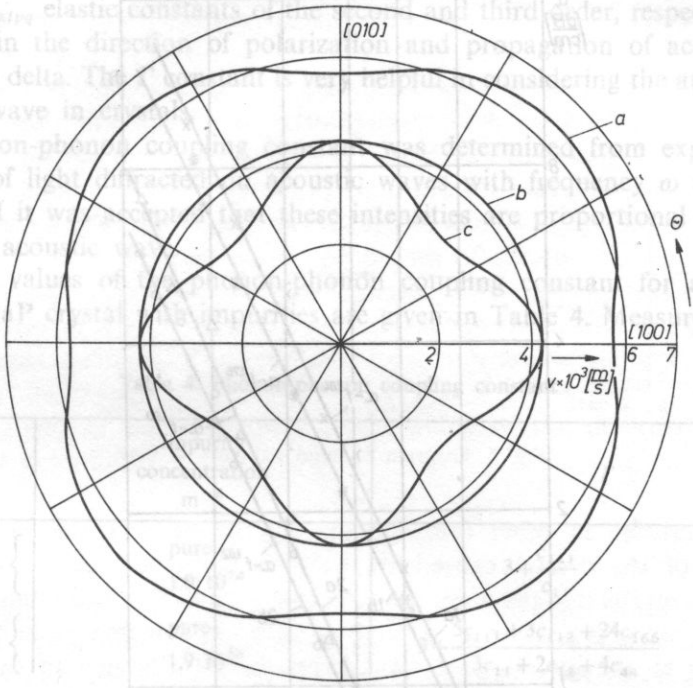

Fig. 2. Angular characteristic of propagation velocity of a longitudinal wave a and transverse waves b, c in the XY-plane in a pure GaP crystal

Table 3. Changes of elastic constants of GaP ($\Delta c_{ij} = c_{ij}(0) - c_{ij}(n)$)

Impurity concentrations m^{-3}	Δc_{11} 10^{10} Nm^{-2}	Δc_{12} 10^{10} Nm^{-2}	Δc_{44} 10^{10} Nm^{-2}
$7.7 \cdot 10^{22}$	0.005	−0.021	0.022
$6.5 \cdot 10^{23}$	0.055	−0.029	0.022
$1.9 \cdot 10^{24}$	0.132	−0.049	0.038

Figure 3 shows results of measurements of the attenuation coefficient for a longitudinal and transverse acoustic wave in direction [100] in a pure crystal and crystal with 1.9×10^{24} m^{-3} impurity concentration. Next to approximating lines — determined with the method of least squares — relationships between the attenuation coefficient and frequency are given. Measurements prove that the acoustic wave effect of damping is greater in crystals with impurities than in pure crystals, and the difference incereases with a frequency increase.

Also the phonon-phonon coupling constant was determined for two crystallographic directions with the application of Bragg type diffraction of laser light on an acoustic wave.

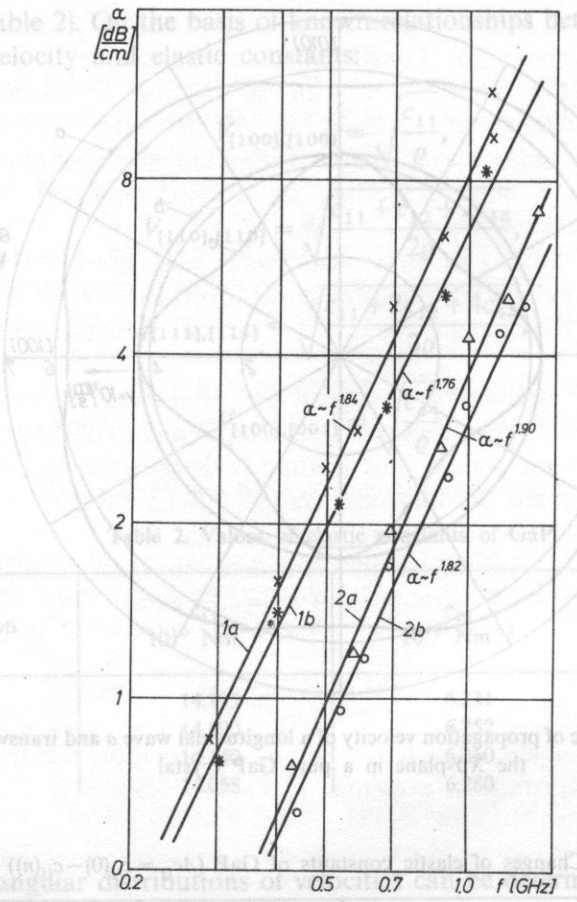

Fig. 3. Wave attenuation coefficient versus frequency, direction of propagation – [100], *1* – longitudinal wave, *2* – transverse wave with polarization [001] *a* – pure crystal, *b* – crystal with impurity concentration $\cdot 1.9 \cdot 10^{24}$ m^{-3}

If an acoustic wave with frequency propagates in a crystal, then a wave with frequency 2ω is generated due to the anharmonicity of interatomic forces. The intensity of this wave is expressed by [2]:

$$I_2(x) = \frac{\Gamma^2 q^2 I_1^2(0)}{8\varrho v^3}\left(\frac{e^{-2\alpha_1 x} - e^{-\alpha_2 x}}{\alpha_2 - 2\alpha_1}\right)^2 \tag{2a}$$

where $I_2(x)$ intensity of acoustic wave with frequency 2ω at distance x from the transducer, $I_1(0)$ intensity of acoustic wave with frequency ω; q wave number of acoustic wave with frequency ω; α_1, α_2 attenuation coefficients of acoustic waves with frequency ω and 2ω respectively; Γ phonon-phonon coupling constant. This constant is expressed by elastic constants of the second and third order

$$\Gamma = (c_{jlpq}\delta_{ik} + c_{ijql}\delta_{kp} + c_{jkqp}\delta_{ip} + c_{ijklpq})\frac{\varkappa_j \varkappa_l \varkappa_q \gamma_i \gamma_k \gamma_p}{c_{ijkl}\varkappa_j \varkappa_l \gamma_k \gamma_l}, \tag{2b}$$

where c_{ijkl}, c_{ijklpq} elastic constants of the second and third order, respectively, γ_i, $\varkappa_j$ unit vectors in the direction of polarization and propagation of acoustic wave, δ_{ik} Kronecker delta. The Γ constant is very helpful in considering the attenuation of an acoustic wave in crystals.

The phonon-phonon coupling constant was determined from expression (2a) – intensity of light diffracted on acoustic waves with frequency ω and 2ω was measured and it was accepted that these intensities are proportional to adequate intensities of acoustic wave.

Measured values of the phonon-phonon coupling constant for a pure GaP crystal and GaP crystal with impurities are given in Table 4. Measurements were

Table 4. Phonon-phonon coupling constant

Direction	Impurity concentration m^{-3}	Γ	
[100]	pure	$3+\frac{c_{111}}{c_{11}}$	6 ± 2
	$1.9\cdot10^{24}$		7 ± 3
[110]	pure	$3+\frac{5c_{111}+3c_{112}+24c_{166}}{3c_{11}+2c_{12}+4c_{44}}$	4 ± 2
	$1.9\cdot10^{24}$		4 ± 2

carried out for a longitudinal wave in directions [100] and [110] at frequency of about 0.5 GHz. Also actual expressions for the phonon-phonon coupling constant in cubical crystals are given for these directions.

Hence, in the cause of experiments the influence of impurities on the phonon-phonon coupling constant was not stated. However, it should be added that the accuracy of determination of this constant was not very high about 50% and possible changes can be within the limit of error.

4. Interpretation of achieved results. Summary

The theoretical interpretation of achieved results is a rather complicated task and requires the consideration of the effect of electron gas, as well as of ions of impurities, on elastic properties of crystals. We will discuss the influence of electron gas on crystals elastic constants only and, hence, on propagation velocity and attenuation coefficient of an acoustic wave.

Figure 4 presents the band structure of GaP [4]. The energetic minimum in the conduction band is found in the direction [100] and its is achieved on the boundary of the Brillouin zone. Bacause there are six equivalent directions [100] then there six equivalent energetic minima. All energetic minima in a not deformed crystal are filled equally with electrons. Due to stress acting along one of the directions [100], the energy in two minima, which are parallel to this direction, increases by the value

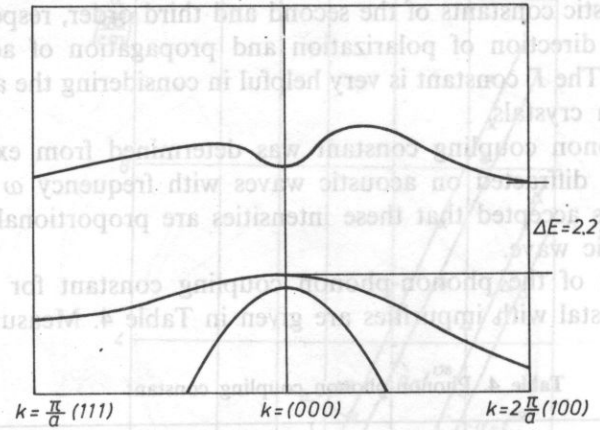

Fig. 4. Diagram of band structure of GaP

$2/3\phi$ and decreases in other four minima by the value $1/3s\phi$, where s is the deformation of the crystal caused by acoustic wave, ϕ deformation potential constant. This means that the number of electron decreases in two minima parallel to the direction of propagation and at the same time increases in four minima perpendicular to the direction of wave propagation. Changes of the number of electrons in individual minima lead to a decrease of their total energy. It can be proved [5] that the change of energy in the case under consideration is equal to

$$E = \frac{2}{9} n \frac{(\phi s)^2}{kT}, \tag{3}$$

where n — electron density, k — Boltzmann constant, T — temperature.

From a comparison of this expression with elastic strain energy $\frac{1}{2}\Delta c_{11} s^2$, we have a relationship between impurity concentration and change of adequate elastic constant c_{11} in this case

$$\Delta c_{11} = \frac{4n\phi^2}{9\,kT}. \tag{4}$$

Due to the arrangement of energetic minima in GaP, the energy of electrons during wave propagation in direction [111] changes equally in all directions, what results in

$$c_{44} = 0, \tag{5a}$$

$$c_{11} + 2c_{12} + 4c_{44} = 0, \tag{5b}$$

and correspondingly

$$c_{12} = -\frac{\Delta c_{11}}{2}. \tag{5c}$$

Measurements of propagation velocity of acoustic waves do not confirm above considerations fully.

Propagation velocity changes of an acoustic wave in direction [100] are indeed greatest, but also the velocity of a transverse wave in this direction undergoes changes. This proves that the constant c_{44} changes to be sure. These changes are smaller than changes of the constant c_{11} and occur in crystals with high concentration of impurities. Similar results were achieved in paper [6] from investigations of the influence of impurities on elastic properties of silicon.

While constant c_{12} slightly increases with the increase of impurity concentration.

It seems that the presence of ions of impurites in the crystal lattice is the main reason for mentioned divergences. These ions change interaction and, hence, elastic properties of the crystal.

From changes of the constant c_{11}, the value of the deformation potential constant was determined

$$\phi = \sqrt{\frac{9kT\Delta c_{11}}{4n}}. \tag{6}$$

When we substitute calculated values Δc_{11} for adequate values of impurity concentration, we obtain the following values of the deformation potential constant ϕ: 15.3 eV, 17.5 eV and 15.9 eV. The average is approximately 16 eV. It is a value of the same order as in other semiconductor materials.

Also intervalley transitions of electrons cause additional damping of the acoustic wave in crystals with impurities.

It appears [5] that wave damping due to intervalley transitions of electrons is expressed by

$$\Delta\alpha = \frac{\omega^2 \Delta c_{ij} \tau}{2\varrho v^3}, \tag{7}$$

where ω frequency of acoustic wave, Δc_{ij} change of elastic constants in direction under consideration, ϱ density τ relaxation time which characterizes intervalley transitions of electrons. Calculating the relaxation time from equation (7) we have

$$\tau = \frac{2\varrho v^3}{\omega^2 \Delta c_{ij}} \Delta\alpha. \tag{8}$$

Substituting achieved experimental results in the expression for a longitudinal wave in direction [100]: $\Delta\alpha = 2\text{dB/cm} = 23$ 1/m for $f = 10^9$ Hz, $\Delta c_{11} = 0.132 \cdot 10^{10}$ N/m^2, we have $\tau = 7.3 \cdot 10^{-13}$ s.

For other frequencies results of calculations are similar. Achieved values of relaxation times are too great in comparison with actual values, because attenuation increase in crystals with impurities is also caused by ions from impurities. Yet, an accurate analysis of this effect requires measurements at low temperatures when thermal ionization of impurities does not occur.

Summing up, we can say that a significant influence of impurities on acoustic

properties was stated in investigated crystals. The applied measurement method was accurate enough to determine changes of propagation velocity and acoustic wave attenuation coefficient in the considered range of impurity concentration. A full theoretical interpretation will be carried out when results of measurements in helium temperatures will be available.

References

[1] D. Mc Machen, IEEE Trans. Sonics Ultrasonics, **SU-14**, 103 (1967).
[2] W. W. Lemanow, G. A. Smoleński, Ak. Żurnał, **20**, 426 (1974).
[3] W. W. Lemanow, N. K. Juszin, FTT, **13**, 3070 (1973).
[4] I. M. Cydlikowski, *Electrons and holes in semiconductors*, (in Polish), PWN, Warszawa 1976.
[5] W. P. Mason, *Physical acoustics*, IV a Academic Press 1966.
[6] L. Opilska, A. Klimasek, J. Zabawa, *Effect of electron gas on elastic constants of n-type silicon*, (in Polish), Akustyka molekularna i kwantowa, **4**, 33–48 (1983).

Received August 21, 1987, revised version March 25, 1988.

ARCHIVES OF ACOUSTICS
14, 3–4, 241–251 (1989)

COMMENTS ON THE MOLECULAR MECHANISM OF ACOUSTIC WAVE PROPAGATION IN SIMPLE LIQUIDS

FRANCISZEK KUCZERA, JOACHIM GMYREK

Institute of Physics, Technical University of Silesia Gliwice

When seeking an explanation for the molecular mechanism of acoustic wave propagation in liquids it was stated that theoretical considerations applying the Lennard–Jones type expression for energy can not serve this purpose. A certain molecular interpretation of the ABL principle is proposed as a solution. On this path we obtain an expression for propagation velocity of an acoustic wave in terms of space filling a relationship between sound velocity and coefficient of viscosity and an expression for intermolecular compressibility.

Poszukując wyjaśnienia molekularnego mechanizmu propagacji fal akustycznych w cieczach stwierdzono, że takie rozważania teoretyczne, w których stosuje się wyrażenia na energię typu Lennarda–Jonesa nie mogą prowadzić do celu. Jako próbę wyjścia z tej sytuacji proponuje się pewną molekularną interpretację reguły ABL. Uzyskuje się w taki sposób wyrażenie na prędkość propagacji fali akustycznej w funkcji wypełnienia przestrzeni, zależność prędkości dźwięku od współczynnika lepkości oraz wyrażenie na ściśliwość międzymolekularną.

1. Considerations of an elementary, i.e. molecular mechanism of acoustic wave propagation in definite liquids require detailed information about the structure and internal interactions in these liquids. But even in a case of simple liquids, such informations are extremely scant. For example, data concerning free volume achieved by Kittel and Eyring differ by an order of magnitude [1]. Table 1 contains some values of free volume for several liquids at the temperature of 15°C, calculated by Kittel and Eyring and presented in the mentioned paper. Considerable differences between values of free volume determined by various authors with various methods have been also pointed out by SOCZKIEWICZ [9].

It should be further mentioned that conclusions of considerations applying an expression for intermolecular interaction potential energy of Lennard–Jones or similar (e.g in a statistical integral) type can not be applied in considerations of the elementary act of propagation of an acoustic wave. This act consists of effects taking place between molecules and of effects occurring in the molecule itself. It this case the compressibility of the molecule should be distinguished from intermolecular compressibility which is of kinetic as well as potential character anyway. The so-called compressibility of liquid – compressibility measured in macroscale – is a certain

Table 1. Values of free volume for chosen liquids at temperature of 15°C according to [1]

Type of liquid	$V_s\left[\frac{m^3}{mol}\right] \times 10^6$	
	according to EYRING	according to KITTEL
Benzene	0.217	0.0509
Toluene	0.209	0.0454
Chlorobenzene	0.181	0.0357
Bromobenzene	0.155	0.0296
Carbon tetrachloride	0.251	0.0566
Chloroform	0.271	0.0591

resultant of mentioned compressibilities. If we include molecules' own volume then we find that the potential field in which molecules move has nothing to do with the Lennard–Jones potential. Molecules as point sources of forces introduce an idealization which falsifies these details of the liquid's molecular structure which are necessary in considerations of the elementary process of acoustic wave propagation. However, sometimes certain segments on the diagram illustrating potential energy of molecule interaction in terms of distance r, described with the Lennard–Jones formula,

$$\varphi(r) = -\frac{a}{r^m} + \frac{b}{r^n} \tag{1}$$

are accepted as corresponding with the diameter of molecules; but this is logically delayed reasoning. This is so, because first of all conclusions are drawn at an assumption that molecules are point sources of forces then the diameter of molecules is defined as if the regard of the molecule's own volume did not change anything significant.

It results from the above that we should give up Lennard–Jones type expressions and models based on such expressions when seeking a relationships between propagation velocity of acoustic wave and quantities which characterize the actual structure of the liquid.

So all we can do in this situation is consider empirical data expressed in adequate principles and try to explain these principles in molecular terms. The theory requires information resulting from this procedure, not the other way round. It is natural that these informations can not be influenced by such side effects like molecule association or relaxation. Therefore, we will be concerned with simple liquids and with frequency range much below relaxation frequency in these liquids.

2. In the course of research on acoustic properties of liquids many empirical formulae have been formulated and later it became evident that they are not so accurate or not so universal as it seemed at the beginning (e.g. RAO rule, WADA

principle). To us it seems that the AZIZ, BOWMAN and LIM principle [2] proved itself most accurate. Further on we will use the notation – ABL principle, for short.

According to this principle propagation velocity of an acoustic wave (w) is directly proportional to density (ϱ) independently of the fact whether density changes are caused by temperature changes at constant pressure or pressure changes at constant temperature. In other words, expressions $(\partial w/\partial \varrho)_p$ and $(\partial w/\partial \varrho)_T$ are constant quantities.

Let us consider expression $(\partial w/\partial \varrho)_p = \text{const}$, which can be expressed in the following form

$$w = \frac{A}{V} + B, \tag{2}$$

where V is the specific volume of the liquid, A and B are constants dependent on kind of liquid.

Let us extrapolate in our minds and imagine that volume V decteases to a possibly smallest value V_D when molecules touch each other. We have

$$\lim w = \lim_{V \to V_D} \left(\frac{A}{V} + B \right)$$

or

$$w_D = \frac{A}{V_D} + B. \tag{3}$$

Quantities w_D and V_D can not be physically reached, but they are a result of formal extrapolation.

Now we can note

$$w - w_D = \frac{A}{V} - \frac{A}{V_D},$$

so the propagation velocity of an acoustic wave in liquids can be written in the following form

$$w = w_D - \frac{A}{V} \cdot \frac{V - V_D}{V_D}. \tag{4}$$

This expression shows how the wave's propagation velocity depends on "space filling". Coefficient A can be eliminated due to logarithmic differentiation of formula (4). Then we have

$$\frac{1}{w - w_D} \left(\frac{\partial w}{\partial T} \right)_p = \frac{1}{V - V_D} \left(\frac{\partial V}{\partial T} \right)_p - \frac{1}{V} \left(\frac{\partial V}{\partial T} \right)_p,$$

or

$$w = w_D + \frac{\left(\frac{\partial w}{\partial T} \right)_p}{\frac{1}{V} \left(\frac{\partial V}{\partial T} \right)_p} \cdot \frac{V - V_D}{V_D}. \tag{4a}$$

Quantities A and B in expression (3) or $\left(\frac{\partial w}{\partial T}\right)_p$ and $\frac{1}{V}\left(\frac{\partial V}{\partial T}\right)_p$ in expression (4a) should be determined from experiments and in this case these expressions are equivalent. Still, volume V_D remains unknown.

We will take advantage of liquids viscosity isochores in order to determine V_D. It results that liquids viscosity depends only on volume for a definite mass; it is not effected by temperature or pressure [3]. Such behaviour is a certain analog of the ABL principle for sound velocity.

The relationship between viscosity η and specific volume V(or molar V^m) at constant atmospheric pressure is, as we know, expressed by the BACZYŃSKI principle [4]

$$\eta = \frac{C}{V - V_D'}, \tag{5}$$

where C and V_D' are constant quantities for a given liquid.

BACZYŃSKI stated good conformity of this rule with experiment for 68 liquids which do not associate. The average value V_D' was determined by him at 0.307 V_k (V_k – critical volume); it is close to the value of constant $b = \frac{1}{3} V_k$ in the van der Walls equation.

In further considerations we will call quantity $V_s = V - V_D'$ from expression (5) – free volume. We are aware of the fact that the term-free volume has different meaning in various papers. This does not cause problems when the term used in a definite paper is explicitly defined. The above can be an explanation for great differences between values of free volume achieved by various authors.

If we notice the boundary value of the rearranged ABL expression

$$w_D = \frac{A}{V_D} + B,$$

then an assumption can be made that the given V_D value is a quantity corresponding with the highest possible density of the liquid and that it corresponds with quantity V_D in BACZYŃSKI's formula, because for $V = V_D$ we have $\eta = \infty$. Now, we will check again the rightness of this assumption. We will calculate V_D from (3) and V_D' from (5) and compare these values with each other. So we have a relationship $w(\eta)$

$$w_D = \frac{A}{V_D} + B = \frac{A}{V - \frac{C}{\eta}} + B. \tag{6}$$

While expression (4) assumes the following form

$$w = w_D - \frac{A}{V} \cdot \frac{V - V_D}{V_D} = w_D - \frac{A}{V} \cdot \frac{C}{\eta V_D},$$

what means that the propagation velocity of an acoustic wave (w) depends on the coefficient of viscosity (η) as

$$w = a + b \cdot \frac{1}{\eta V}, \tag{7}$$

where coefficients a and b can be easily determined from the ABL principle or BACZYŃSKI's principle.

Or course relationships (4) and (7) can be applied in the range of application of mentioned above principles.

Values of the w_D quantity for certain simple liquids at the temperature of 20°C are given in Table 2; while values of w_D for the same liquids at different temperatures can be found in Table 3.

We can notice that the w_D quantity was found constant for tested liquids and independent of temperature (the difference between maximal and minimal value of w_D does not exceed 0.2÷0.5% of the average value); while the ratio of w_D and

Table 2. Values of w_D for some simple liquids at temperature of 20°C

Type of liquids	$C \cdot 10^8$ $\left[\frac{m^2}{s}\right]$	A $\left[\frac{m^4}{kg\ s}\right]$	B $\left[\frac{m}{s}\right]$	w $\left[\frac{m}{s}\right]$	w_D $\left[\frac{m}{s}\right]$	$\frac{w_D}{w}$
n-heksane	6.484	4.950	−2163	1099.9	1605	1.459
n-heptane	6.658	5.032	−2286	1152.7	1582	1.372
n-oktane	7.145	5.107	−2392	1193.1	1561	1.308
n-nonane	7.810	5.060	−2403	1227.0	1538	1.254
benzene	5.764	4.272	−2427	1327.0	1646	1.240
toluene	5.594	4.473	−2542	1330.0	1678	1.261
carbon tetrachloride	4.752	1.591	−1597	1937.8	1153	1.229
chloroform	4.695	1.785	−1654	1001.0	1380	1.379
methyl ethyl ketone	5.989	4.086	−2069	1217.0	1642	1.348

Caution: values of w for the first four liquids come from paper [7], while for other liquids from paper [8].

Table 3. Values of w_D for some simple liquids at various temperatures

Type of liquids	t[°C]							$\frac{\Delta w_D}{w_D}$[%]
	0	10	20	30	40	50	60	
n-heksane	1605	1606	1605	1605	1606	1606	1605	0.03
n-heptane	1587	1584	1582	1581	1582	1584	1587	0.41
n-oktane	1567	1563	1561	1561	1563	1564	1571	0.40
n-nonane	1541	1538	1538	1537	1538	1538	1540	0.25
benzene	–	1648	1646	1645	1644	1645	1647	0.22
toluene	1684	1680	1678	1676	1675	1675	1675	0.53
carbon tetrachloride	1159	1155	1153	1153	1153	1154	1156	0.55
chloroform	1382	1381	1380	1380	1381	1381	1381	0.10
methyl ethyl ketone	1645	1643	1642	1642	1642	1643	1644	0.18

experimentally measured value of sound velocity w decreases from liquids with small ratio of space filling (e.g. n-hexane) to liquids with high ratio of space filling (e.g. n-octane or carbon tetrachloride).

We calculated values of sound velocity for several chosen simple liquids from formula (7) using previously found values of constants: A, C, V_D and compared them with experimental values. This confrontation is presented in Table 4.

In our calculations we used values of coefficients of viscosity for these liquids from THORPE's and RODGER's paper [5] and specific volumes were determined from international tables of physical data [6]. Values of sound velocity in presented liquids have been taken from BOELHOUWER's paper [7] and LAGEMANN's and WOOLF's paper [8].

Data presented in Table 4 proves that expression (7) gives values of sound velocity consistent with experimental values; the standard error in the range $0 \div 60°C$ is equal to approximately 1% for all tested liquids.

It is sometimes more convenient to determine characteristic quantities V_D and $V_s = V - V_D$, omitting the constant parameter C in Baczyński's formula. Logarithmic differentiation immediately changes Baczyński's expression into

$$\frac{1}{V_s}\left(\frac{\partial V}{\partial T}\right)_p = -\frac{1}{\eta}\left(\frac{\partial \eta}{\partial T}\right)_p. \tag{8}$$

Hence

$$V_s = -V \cdot \frac{\frac{1}{V}\left(\frac{\partial V}{\partial T}\right)_p}{\frac{1}{\eta}\left(\frac{\partial \eta}{\partial T}\right)_p}, \tag{9a}$$

and

$$V_D = V - V_s = V\left[1 + \frac{\frac{1}{V}\left(\frac{\partial V}{\partial T}\right)_p}{\frac{1}{\eta}\left(\frac{\partial \eta}{\partial T}\right)_p}\right], \tag{9b}$$

or from expression (4a)

$$w_D = w\left[1 + \frac{\frac{1}{w}\left(\frac{\partial w}{\partial T}\right)_p}{\frac{1}{V}\left(\frac{\partial V}{\partial T}\right)_p + \frac{1}{\eta}\left(\frac{\partial \eta}{\partial T}\right)_p}\right]. \tag{10}$$

Table 4. Values of sound velocity in some simple liquids, calculated from expression [7]

Type of liquids	$w\left[\frac{m}{s}\right]$	t[°C]							Standard error [m/s]
		0	10	20	30	40	50	60	
n-heksane	w_{cal}	1188.2	114.58	1102.2	1057.3	1022.4	964.6	917.1	
	w_{exp}	1191.9	1145.7	1099.9	1054.5	1009.5	964.7	920.2	0.9
	Δw	−3.7	+0.1	+2.3	+1.8	+1.9	−0.1	3.1	
n-heptane	w_{cal}	1235.5	1196.5	1155.8	1113.5	1069.8	1024.7	978.2	
	w_{exp}	1240.7	1196.5	1152.9	1109.7	1066.9	1024.6	982.8	1.3
	Δw	−5.2	−0.1	+2.9	+2.8	+2.9	+0.1	−4.6	
n-oktane	w_{cal}	1274.3	1236.3	1196.4	1154.8	1111.5	1066.8	1025.2	
	w_{exp}	1278.0	1235.6	1193.5	1151.9	1110.8	1070.1	1029.9	1.2
	Δw	−3.7	+0.7	+2.9	+2.9	+0.7	−3.3	−4.7	
carbon tetrachloride	w_{cal}	996.5	969.1	940.3	910.4	879.4	874.4	814.6	
	w_{exp}	1001.9	969.8	938.1	906.8	875.9	845.4	815.3	1.3
	Δw	−5.4	−0.7	+2.2	+3.6	+4.5	+2.0	−0.7	
chloroform	w_{cal}	1069.6	1037.2	1004.0	970.0	935.4	900.1	864.5	
	w_{exp}	1072.9	1037.2	1002.0	967.4	933.5	900.2	867.6	0.9
	Δw	−3.3	0.0	+2.0	+2.6	+1.9	−0.1	−3.1	
benzene	w_{cal}	−	1369.3	1326.4	1282.0	1236.2	1189.1	1141.1	
	w_{exp}	−	1374.0	1326.9	1280.2	1233.9	1188.1	1143.0	1.1
	Δw	−	−4.3	−0.5	+1.8	+3.3	+1.0	−1.9	
toluene	w_{cal}	1406.1	1368.5	1329.5	1289.5	1248.3	1206.3	1163.5	
	w_{exp}	1413.1	1371.0	1329.1	1287.4	1245.7	1204.1	1162.4	1.3
	Δw	−7.0	−2.5	+0.4	+2.1	+2.6	+2.2	+1.1	

A decision should be made in every separate case whether it is more convenient to use parameters A, B, C in discussed principles, or relative thermal coefficients in accordance with formulae (9a), (9b) and (10). These coefficients not always can be determined with desirable accuracy for example. This is in case when there is few measuring points. Let us also notice that the relative temperature coefficient of the relative thermal coefficient can be considerable. Because for an arbitrary physical quantity x we have

$$\frac{\frac{\partial}{\partial T}\left(\frac{1}{x}\cdot\frac{\partial x}{\partial T}\right)}{\frac{1}{x}\left(\frac{\partial x}{\partial T}\right)} = -\frac{1}{x}\cdot\frac{\partial x}{\partial T}+\frac{\frac{\partial^2 x}{\partial T^2}}{\frac{\partial x}{\partial T}}. \tag{11}$$

Also for this reason the possible error of determination of coefficient $\frac{1}{x}\left(\frac{\partial x}{\partial t}\right)$ can lead to a not too accurate temperature dependence.

Values of molar volumes V_s^m and V_D^m calculated from formulae (9a) and (9b), and w_D determined according to formula (10) for a group of chosen simple liquids at the temperature of 20°C are given in Table 5. Table 6 presents the V_D/V_s ratio which is a certain measure of space filling. Calculation results presented in Table 5 and 6 prove that very similar w_D values are achieved from formulae (6) and (10), and that the factor of space filling defined by the V_D/V_s ratio rapidly decreases with a temperature increase.

Table 5. Values of V_s^m, V_D^m and w_D for some simple liquids at temperature of 20°C

Type of liquids	$V_s^m \cdot 10^6$ $\left[\frac{m^3}{mol}\right]$	$V_D^m \cdot 10^6$ $\left[\frac{m^3}{mol}\right]$	$\frac{V_D^m}{V_s^m}$	w_D $\left[\frac{m}{s}\right]$	w_D/w	
					Eq. (10)	Eq. (6)
n-heksane	17.40	113.26	6.51	1618	1.471	1.459
n-heptane	16.60	129.99	7.83	1601	1.389	1.372
n-oktane	15.35	147.33	9.60	1570	1.316	1.308
n-nonane	14.03	164.69	11.74	1554	1.258	1.253
benzene	7.22	81.65	11.31	1670	1.258	1.240
toluene	9.16	97.27	10.62	1197	1.277	1.262
carbon tetrachloride	7.91	88.57	11.20	1170	1.247	1.230
chloroform	9.91	70.27	7.03	1393	1.390	1.378
methyl ethyl ketone	8.59	66.08	7.69	1652	1.356	1.348

Table 6. Values of V_D/V_s ratio in terms of temperature for some simple liquids

Type of liquids	t[°C]						
	0	10	20	30	40	50	60
n-heksane	7.95	7.19	6.51	5.90	5.36	4.87	4.43
n-heptane	9.04	8.42	7.83	7.32	6.73	6.21	5.72
n-oktane	11.16	10.35	9.60	8.89	8.22	7.89	6.99
n-nonane	14.59	13.28	11.74	10.34	9.51	8.51	7.69
benzene	–	12.74	11.31	10.09	9.05	8.14	7.34
toluene	13.01	11.74	10.62	9.63	8.75	7.95	7.22
carbon tetrachloride	16.23	12.83	11.20	9.71	8.64	7.89	7.39
chloroform	8.41	7.69	7.04	6.43	5.87	5.34	4.86
methyl ethyl ketone	9.37	8.47	7.67	7.00	6.39	5.84	5.36

3. We can also determine the compressibility of intermolecular space β_s. If we neglect changes of molecule's volume with respect to changes of intermolecular distances during deformation of liquid, then, because $V = V_D + V_s$ and $V_D = \text{const}$, we have

$$\left(\frac{\partial V}{\partial p}\right)_T = \left(\frac{\partial V_s}{\partial p}\right)_T$$

or

$$-\frac{1}{V}\left(\frac{\partial V}{\partial p}\right)_T = -\frac{1}{V}\left(\frac{\partial V_s}{\partial p}\right)_T = -\frac{V_s}{V}\cdot\frac{1}{V_s}\left(\frac{\partial V_s}{\partial p}\right)_T.$$

Hence, we have

$$\beta = \beta_s \cdot \frac{V_s}{V}. \tag{12}$$

Taking advantage of expression (9a) we achieve a formula for intermolecular compressibility

$$\beta_s = \beta\frac{V}{V_s} = -\beta\frac{\frac{1}{\eta}\left(\frac{\partial \eta}{\partial T}\right)_p}{\frac{1}{V}\left(\frac{\partial V}{\partial T}\right)_p}, \tag{13}$$

β denotes effective compressibility of liquid determined from acoustic measurements here.

The temperature dependence β_s can be determined through logarithmic differentiation

$$\frac{1}{\beta_s}\left(\frac{\partial \beta_s}{\partial T}\right)_p = \frac{1}{V}\left(\frac{\partial V}{\partial T}\right)_p + \frac{1}{\beta}\left(\frac{\partial \beta}{\partial T}\right)_p - \frac{1}{V_s}\left(\frac{\partial V}{\partial T}\right)_p. \tag{14}$$

Taking into consideration that

$$\beta_s = \frac{V^2}{Mw^2}, \quad \text{so} \quad \beta_s = \frac{V^2}{Mw^2} \cdot \frac{1}{V_s}$$

and applying expression (8) we reach

$$\frac{1}{\beta_s}\left(\frac{\partial \beta_s}{\partial T}\right)_p = 2\left[\frac{1}{V}\left(\frac{\partial V}{\partial T}\right)_p - \frac{1}{w}\left(\frac{\partial w}{\partial T}\right)_p\right] + \frac{1}{\eta}\left(\frac{\partial \eta}{\partial T}\right)_p. \tag{15}$$

Absolute values of β_s and temperature dependence of β_s for chosen simple liquids are given in Table 7.

Table 7. Values of intermolecular compressibility for some liquids at temperature of 20°C

Type of liquids	$\beta \times 10^{10}$ $\left[\frac{m^2}{n}\right]$	$\beta_s \times 10^{10}$ $\left[\frac{m^2}{n}\right]$	$\frac{\beta_s}{\beta}$	$\frac{\partial \beta_s}{\partial T} \times 10^{12}$ $\left[\frac{m^2}{n \cdot k}\right]$	$\frac{1}{\beta_s}\left(\frac{\partial \beta_s}{\partial T}\right) \times$ $\times 10^4 \left[\frac{1}{k}\right]$
n-pentane	14.98	89.72	5.99	+31.45	+35.06
n-heksane	12.53	94.11	7.51	+7.89	+8.38
n-heptane	11.01	97.20	8.83	−8.96	−9.22
n-oktane	10.00	105.94	10.60	−31.14	−29.39
n-nonane	9.25	117.86	12.74	−60.23	−51.10
benzene	6.46	79.54	12.31	−43.02	−54.09
toluene	5.54	75.99	11.62	−30.36	−39.95
carbon tetrachloride	7.13	86.92	12.20	−49.35	−56.78
chloroform	6.69	53.76	8.04	−3.71	−6.90
methyl ethyl ketone	8.38	72.78	8.69	−11.39	−15.65

Among 20 investigated simple liquids only lighter aliphatic hydrocarbons (*n*-pentane, *n*-hexane) had a positive temperature coefficient of intermolecular compressibility. The compressibility of all other liquids decreases with temperature at constant pressure. To us it seems that this can be explained by the fact that the lightest hydrocarbons have much smaller space filling than higher homologues compare with results obtained by SOCZKIEWICZ [9]. It this case intermolecular compressibility will be mainly of kinetic character, because the actual potential well is much more flat than in a case of high degree of space filling, when the compressibility will have potential nature. Such a conclusion finds confirmation also in KRZAK's research [10]. Yet, it will be possible to draw more detailed conclusions when the temperature and pressure dependence of intermolecular compressibility will be investigated for a much greater number of simple liquids. We plan to continue our research.

We consider investigations of above mentioned dependencies particularily important in understanding thermal motions of liquids molecules and of the method of transmission of an acoustic pulse in liquids. Also, we consider the application of

a model of an ideal solid body (sphere-spring type) or perfect gas model to these problems groundless, because we accept that the liquids intermolecular compressibility has kinetic character as well as potential even in such a case when we accept the bottom of the potential of intermolecular interactions is flat.

References

[1] F. C. COLLINS, M. H. NAVIDI, *The calculations of the free volumes of liquids from measurements of sonic velocity*, J. Chem. Phys., **22**, 1254–1255 (1954).

[2] R. A. AZIZ, D. H. BOWMAN, C. C. LIM, *An examination of the relationship between sound velocity and density in liquide*, Canadian Journal of Physics **50**, 646–654 (1972).

[3] K. JELLINEK, *Lehrbuch der physikalischen Chemie*, Ferdinand Enke Verlag, Stuttgart t. 1, 497, 1928.

[4] A. J. BATSCHINSKI, *Untersuchungen über die innere Reibung der Flüssigkeiten*, Z. phys. Chem. **84**, 643–706 (1913).

[5] S. THORPE and RODGER, Phill. Trans. **185A**, 397, (1895) and **189A**, 71, (1897) and also International Critical Tables t. 7, 212–222. McGraw-Hill Book Company Inc. New York 1933.

[6] *International Critical Tables of Numerical Data Physics, Chemistry and Technology*, McGraw-Hill Book Company Inc., New York 1933 3, 28–30.

[7] J. W. M. BOELHOUWER, *Sound velocities in an adiabatic compressibilities of liquid alkanes at various temperatures and pressures*, Physica **34**, 484–492 (1967).

[8] R. T. LAGEMANN, D. R. MCMILLAN, W. E. WOOLF, *Temperature variation of ultrasonic velocity in liquids*, J. Chem. Phys. **17**, 369–373 (1949) and Landolt–Börnstein, Band 5, Molekular-akustik, Springer Verlag, Berlin 1982.

[9] K. SOCZKIEWICZ, *The new acoustical method of evaluation of free volumes of liquids*, Materiały XX Otwartego Seminarium z Akustyki, Poznań 1973, t. 2, 104–108.

[10] J. KRZAK, *Comments on the potential of intermolecular interactions in liquids* (in Polish), Zeszyty Naukowe Politechniki Śląskiej, s. Matematyka–Fizyka, Gliwice, z. 30, 145–151 (1978).

Received November 21, 1987.

ARCHIVES OF ACOUSTICS
14, 3-4, 253-260 (1989)

INVESTIGATIONS CONCERNING FAST SURFACE STATES OF SEMICONDUCTORS BY MEANS OF ACOUSTIC METHODS

ALEKSANDER OPILSKI, TADEUSZ PUSTELNY

Institute of Physics, Technical University of Silesia
Gliwice, ul. Krzywoustego 2

The paper deals with the results of investigations an n-Si surfaces, obtained by determining acoustically the parameters of fast surface states in semiconductors. This new method is theoretically based on the analyses of the influence of surface states in a semiconductor on the propagation of a Rayleigh surface wave in a layer system of piezoelectric and semiconducting layers. It is possible to determine the effective life time τ of the charge carrier of fast surface states, as well as the velocity of recombination, g, of the carriers in these states.

Praca przedstawia doświadczalną weryfikację metody (zaproponowanej wcześniej przez autorów) pomiaru czasu życia oraz prędkości rekombinacji nośników. Pomiary przeprowadzono wykorzystując różne podłoża piezoelektryczne i różne warunki pomiaru próżnia, gaz obojętny. Otrzymane wyniki potwierdzają przydatność zaproponowanej przez autorów metody.

1. Introduction

The papers deals with the results of investigations on n-Si surfaces, obtained by determining acoustically the parameters of fast surface states in semiconductors. This new method is theoretically based on the results presented in [3], where the author analyses the influence of surface states in a semiconductor on the acoustic propagation of the Rayleigh's surface wave in a layer system of piezoelectric and semiconducting layers. Making use of the effect on the interaction of a surface wave and the charge carrier in the semiconductor, to which a longitudinal electric drift field is applied, it is possible to determine the effective life time τ of the charge carrier at fast surface states, as well as the velocity of recombination g of the carriers by these states.

The idea of determining the parameters τ and g consists in the determination of the frequency characteristics of relative changes of the critical drift field [3]:

$$\frac{E_{dcr}-E_{dcr}^0}{E_{dcr}^0}=\frac{\Delta E_{dcr}}{E_{dcr}^0}=\frac{g}{V_f}\cdot\frac{\omega\tau}{1+\omega^2\tau^2}, \tag{1}$$

where E_{dcr} is so-called critical field (the value of the electric field applied to the semiconductor in the direction of propagation of the surface wave, at which the electronic attenuation coefficient of the surface wave is equal to zero), $E^0_{dcr} = V_f/\mu_0$; μ_0 – volumetric mobility of the carriers in the semiconductor, V_f, ω – velocity and frequency of the acoustic surface wave; g – velocity of recombination of the charge carriers at the surface states in the semiconductor; τ – life time of the carriers in surface states.

Basing on the position of the maximum $(E_{dcr}/E^0_{dcr})_{max}$, on the frequency axis in the characteristics $(E_{dcr}/E^0_{dcr}) = f(\omega)$ we determine the value of τ:

$$\tau = \frac{1}{\omega_m} \tag{2}$$

where ω_m corresponds to $(E_{dcr}/E^0_{dcr})_{max}$.
The velocity of recombination g is determined by means of the relation

$$g = 2V_f \left(\frac{\Delta E_{dcr}}{E^0_{dcr}} \right)_{max}. \tag{3}$$

Paper [4] discusses in more detail the theoretical principles of this method the measuring position, as well as the measurement results of the parameters τ and g of surface states in n-Si obtained in atmospheric air.

The present paper deals with the results of investigations on n-Si, previously subjected to a change of the energetic structure of the surface. As the investigated parameters τ and g are affected by external conditions [1, 6], measurements were made taken in vacuum, in various atmospheres surrounding the semiconductor, at various pressures and various temperatures. For this purpose a special vacuum system was constructed, from which it was possible to remove various gases, and in which the silicon sample could be heated up to a temperature of about 1000 K [5].

The procedure of measurements was the same as that described in [4]. The measurements were carried out on the same measuring stand, supplemented by a vacuum system.

For the sake of comparison, the results of the present paper and those presented in [4] concern the same silicon sample, wave-guide substrates BGO, $LiNbO_3$, frequencies of the surface wave (within the range of 2+200 MHz) and values of electric conductivity ($\sigma_1 = 3[\Omega m]^{-1}$, $\sigma_2 = 5[\Omega m]^{-1}$, $\sigma_3 = 10[\Omega m]^{-1}$ of the n-Si sample.

Changes of the electric conductivity of the n-Si sample were achieved by illuminating it with a halogen lamp.

2. Measurements of the parameters of surface staten in silicon in vacuum

Both, the electronic attenuation coefficient α_e of a surface wave and the critical drift field E_{dcr} have been measured in the piezoelectric silicon system situated in vacuum the pressure in the measuring chamber amounting to $5 \cdot 10^{-4}$ hPa.

Figure 1 provides exemplary characteristics of the electron attenuation coefficient α_e as a function of the electric drift field E_d in a semiconductor.

Figure 2 demonstrates the frequency characteristics of relative changes of the critical drift field (characteristics No. 1). The numerically determined parameters τ and g are equal

$$\tau = (7.70 \pm 0.6) \cdot 10^{-8} \text{ s},$$
$$g = 900 \pm 70 \text{ m/s}.$$

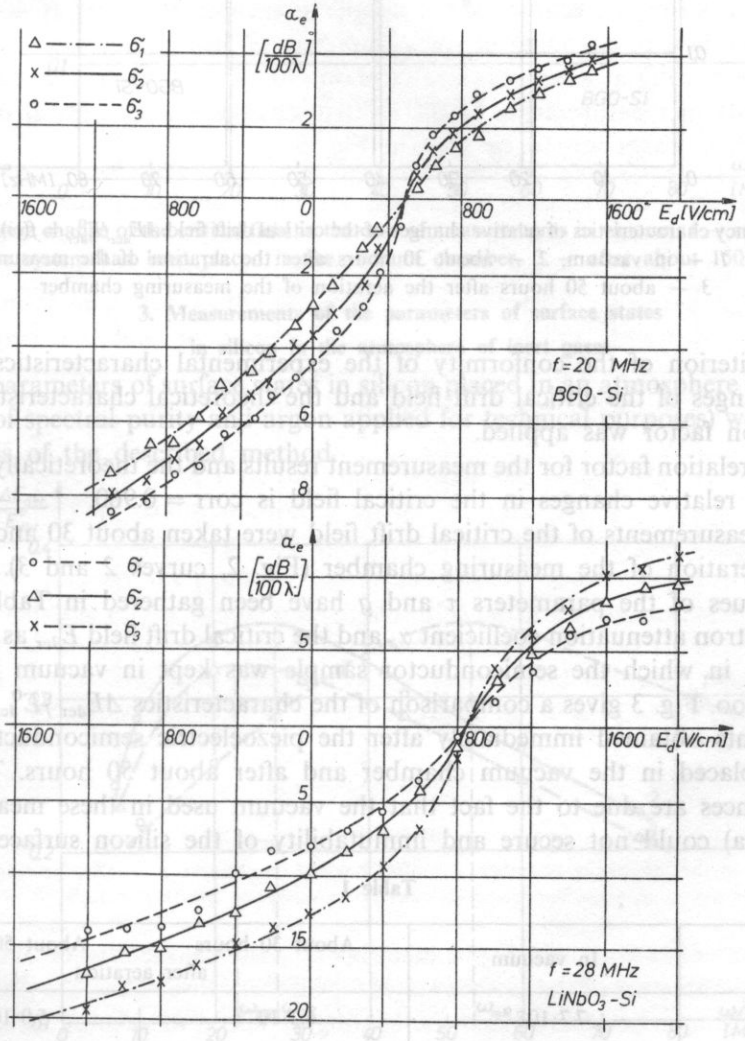

Fig. 1. Exemplary characteristics of the electron attenuation coefficient α_e for various photoconductivities of Si these measurements were made in vacuum

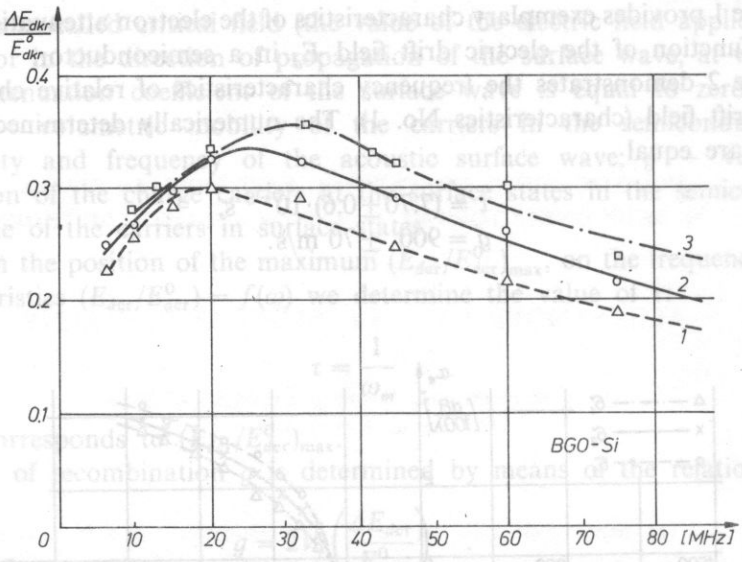

Fig. 2. Frequency characteristics of relative changes of the critical drift field $\Delta E_{dcr}/E^0_{dcr} = f(\omega)$ in the case of measurements: *1* – in vacuum, *2* – about 30 hours after the aeration of the measuring chamber, *3* – about 50 hours after the aeration of the measuring chamber

As a criterion of the conformity of the experimental characteristics with the relative changes of the critical drift field and the theoretical characteristics (Eq. 1) a correlation factor was applied.

The correlation factor for the measurement results and the theoretically predicted function of relative changes in the critical field is corr = 0.960.

Such measurements of the critical drift field were taken about 30 and 50 hours after the aeration of the measuring chamber (Fig. 2, curves *2* and *3*).

The values of the parameters τ and g have been gathered in Table 1.

The electron attenuation coefficient α_e and the critical drift field E_{dcr} as a function of the time in which the semiconductor sample was kept in vacuum have been measured, too. Fig. 3 gives a comparison of the characteristics $\Delta E_{dcr}/E^0_{dcr} = f(\omega)$ of measurements obtained immediately after the piezoelectric semiconductor system had been placed in the vacuum chamber and after about 50 hours. The apparent differences are due to the fact that the vacuum used in these measurements ($5 \cdot 10^{-4}$ hPa) could not secure and immutability of the silicon surface.

Table 1

	In vacuum	About 30 hours after aeration	About 50 hours after aeration
τ [s]	$7.7 \cdot 10^{-9}$	$6.3 \cdot 10^{-9}$	$5.0 \cdot 10^{-9}$
g $[\frac{m}{s}]$	900	1100	1200

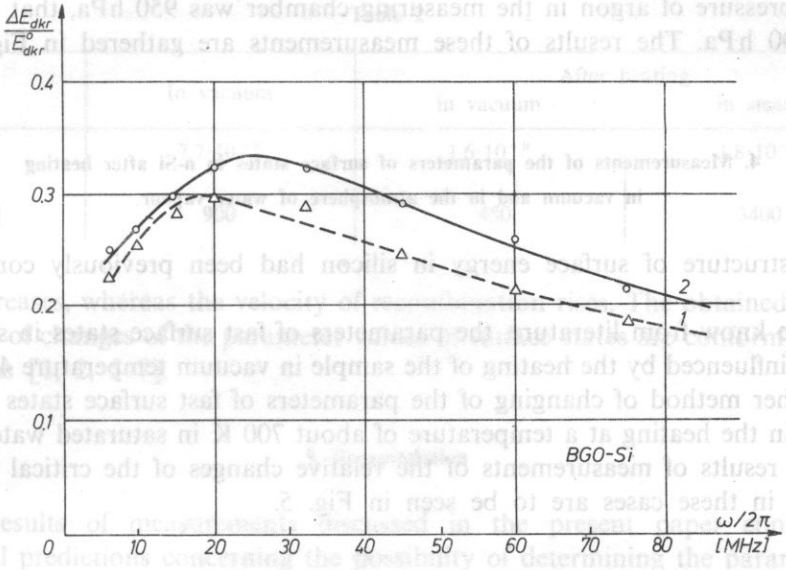

Fig. 3. Relative change of the critical field in the case of measurements in vacuum: *1* — immediately after the system had been placed in the vacuum chamber, *2* — after about 150 hours

3. Measurements of the parameters of surface states in silicon in the atmosphere of inert gases

The parameters of surface states in silicon placed in an atmosphere of inert gases (helium of spectral purity and argon applied for technical purposes) were measured by means of the described method.

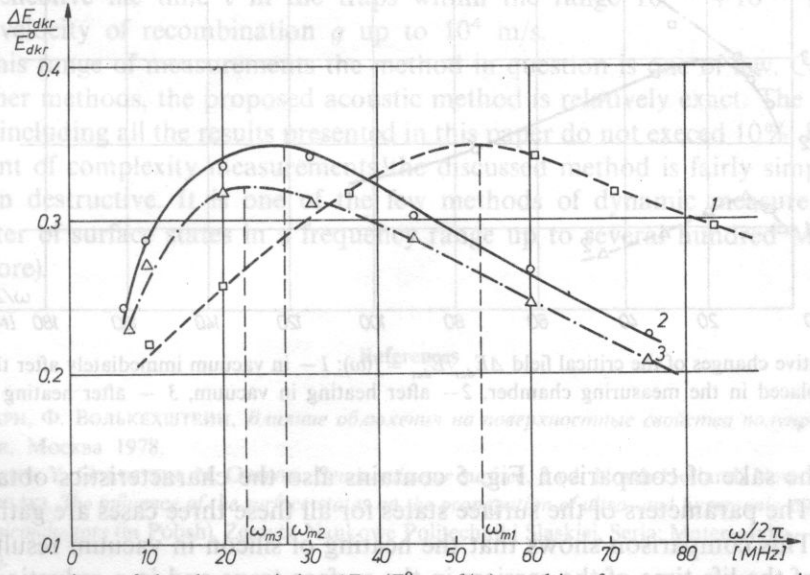

Fig. 4. A comparison of the characteristics $\Delta E_{dcr}/E^0_{dcr} = f(\omega)$ resulting from measurements in: *1* — air, *2* — argon, *3* — helium

The pressure of argon in the measuring chamber was 950 hPa, that of helium about 200 hPa. The results of these measurements are gathered in Fig. 4.

4. Measurements of the parameters of surface states in n-Si after heating in vacuum and in the atmosphere of water vapour

The structure of surface energy in silicon had been previously considecably changed.

As we know from literature, the parameters of fast surface states in silicon are strongly influenced by the heating of the sample in vacuum temperature 400 K [7].

Another method of changing of the parameters of fast surface states in silicon consists in the heating at a temperature of about 700 K in saturated water vapour [2]. The results of measurements of the relative changes of the critical drift field obtained in these cases are to be seen in Fig. 5.

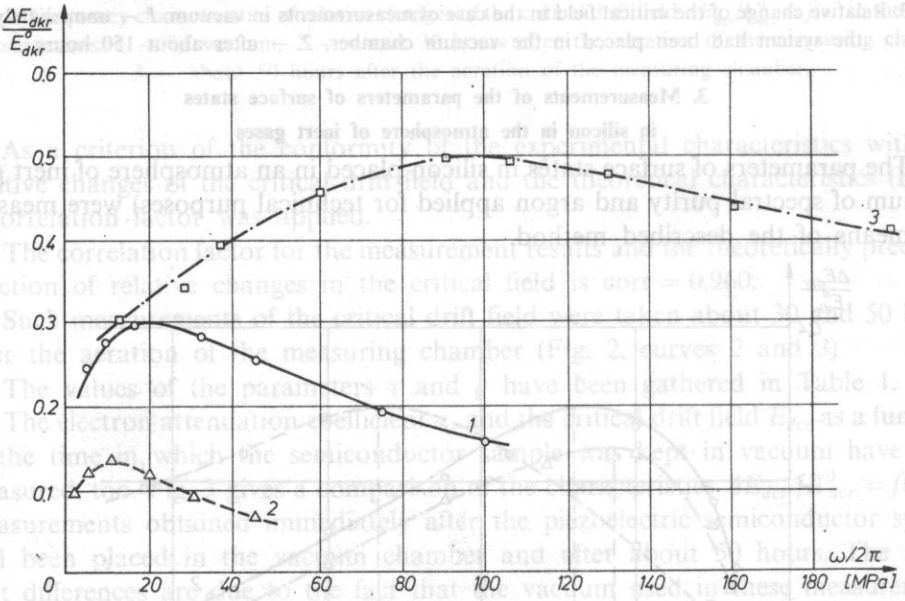

Fig. 5. Relative changes of the critical field $\Delta E_{dcr}/E^0_{dcr} = f(\omega)$: *1* — in vacuum immediately after the system had been placed in the measuring chamber, *2* — after heating in vacuum, *3* — after heating in steam

For the sake of comparison Fig. 5 contains also the characteristics obtained in vacuum. The parameters of the surface states for all these three cases are gathered in Table 2. This comparison shows that the heating of silicon in vacuum results in an increase of the life time of the carriers in the surface traps and in a reduction of the velocity of recombination g at the surface. After heating in steam the life time in the

Table 2

		In vacuum	After heating in vacuum	After heating in steam
τ	[s]	$7.7 \cdot 10^{-9}$	$1.6 \cdot 10^{-8}$	$1.8 \cdot 10^{-9}$
g	$[\frac{m}{s}]$	900	450	3400

trape decreases, whereas the velocity of recombination rises. The obtained changes directions of changes of the parameter values of surface states are conform with the predictions [1, 2, 5–7].

5. Recapitulation

The results of measurements discussed in the present paper confirm the theoretical predictions concerning the possibility of determining the parameters of fast surface states in semiconductor by means of acoustic measurements. The values for the life time of charge carriers in fast surface states obtained by means of the acoustic method as well as the velocities of recombination g of the carriers by these states agree with the predictions.

The acoustic method has made it possible – and this is of great significance – to measure simultaneously two important parameters of fast surface states in a wide range:

– the effective life time τ in the traps within the range $10^{-10}+10^{-6}$ s,
– the velocity of recombination g up to 10^4 m/s.

In this range of measurements the method in question is one of few. Compared with other methods, the proposed acoustic method is relatively exact. The errors of τ and g including all the results presented in this paper do not execed 10%. From the viewpoint of complexity measurements the discussed method is fairly simple being also non destructive. It is one of the few methods of dynamic measurements of parameter of surface states in a frequency range up to several hundred MHz (and even more).

References

[1] В. Барн, Ф. Волькехштеин, *Влияние облюхения на поверхностные свойства полупроводников*, Наука, Москва 1978.

[2] A. Many, Y. Goldstein, N. Grover, *Semiconductor surface*, 2 ed. North-Holland, New York 1971.

[3] A. Opilski, *The influence of the surface states on the propagation of ultra- and hypersonic surface waves in semiconductors* (in Polish), Zeszyty Naukowe Politechniki Śląskiej, Seria: Matematyka – Fizyka, **17** (1976).

[4] A. Opilski, T. Pustelny, *The new acoustic method of determination of the fast surface states parameters in semiconductors*, Archives of Acoustics, **10**, 2 (1985).

[5] T. PUSTELNY, *The acoustic method of determination of the surface states parameters in semiconductor*, Ph.D. thesis, IPPT PAN, Warszawa 1981.

[6] А. Рзханов, *Проблемы физической химии поверхности полупроводников* Наука, Новосибирск, 1978.

[7] А. Рзханов, *Електронные процессы на поверхности полупроводников* Наука, Москва 1982.

Received September 12, 1988.

ARCHIVES OF ACOUSTICS
14, 3–4, 261–281 (1989)

ACOUSTIC ACTIVITY OF SOME METALS DETERMINED BY THE ACOUSTIC EMISSION METHOD

S. PILECKI* and J. SIEDLACZEK**

*Institute of Fundamental Technological Research, Polish Academy of Sciences, 00-049 Warsaw, Świętokrzyska 21 (Poland)

**High Pressure Research Center, Polish Academy of Sciences, 01-142 Warsaw, Sokołowska 29 (Poland)

Measurements of the acoustic emission (*AE*) count rate or count sum as well as the *RMS* value have been carried out by the use of the different *AE* analysers and the testing machines. Specimens of the Armco iron, 45 steel, 45 HNMFA steel, bearing steel ŁH15, beryllium bronze BB2 and the alloy of the maraging type N18K9M5T and PA2N alloy have been tested. Two kinds of specimens of St90PA carbon-manganese steel have been tested, too: from new railway rails and from the 10-th year long exploited rails. *AE* characteristics and the results of the Kaiser and Bauschinger effect measurements have been presented.

Pomiary gęstości lub sumy zliczeń emisji akustycznej (*EA*) oraz wartości skutecznej *RMS* zostały wykonane za pomocą różnych analizatorów *EA* i maszyn wytrzymałościowych. Zbadane zostały próbki z żelaza Armco, stali węglowej 45, stali 45HNMFA, stali łożyskowej ŁH15, brązu berylowego BB2, stopu typu maraging N18K9M5T, stopu aluminium PA2N oraz stali węglowo-manganowej St90PA w dwóch odmianach: wykonanych z szyn kolejowych nowych i z szyn wyjętych z toru po 10 latach eksploatacji. Przedstawionio charakterystyki *EA* wszystkich tych materiałów oraz wyniki pomiarów efektu Kaisera i efektu Bauschingera stali St90Pa.

1. Introduction

Acoustic emission (*AE*) results in the propagation of the elastic waves in deformed material due to the release of its locally accumulated elastic energy [1]. *AE* sources can be concerned in three scales, that is: macro, micro and submicro scale. Bibliography of the problem distinguishes several sources of the *AE*, such as: motion of dislocations [1, 2], internal friction, initiation and propagation of crack [3–9], stress corrosion [1] or phase transitions [10]. Motion of dislocations seems to be the most important source of *AE*. It happens because the rest of the above mentioned sources are triggered, in direct as well as in indirect sense, by dislocations. Particularly, the unsteady motion of dislocations is accompanied by acoustic effects. Acoustic activity of the specimen significantly grows with decreasing velocity of dislocations due to the presence of obstacles on their way [1].

Quantitative results of *AE* measurement depend on the kind of tested material, its internal structure, kind and intensity of loading, value of self stresses, state of the interface and on many external factors. Variety of the mechanisms generating the acoustic signal and the influence of many factors causes that every kind of the material as well as the materials of the same chemical composition but of the different grain size or different internal structure, have their individual acoustic characteristics. These characteristics must be recognized before the investigations leading to the formulation of the opinion on the structure and to the estimation ot the structure deformations due to the crack growth, are initiated. In this way before the beginning of the investigations of applicable value concerning structures and machines, *AE* characteristics of their material should be obtained first. These characteristics are next used as the reference base in further tests.

The present paper is the continuation of previous work [1]. Possible differences in *AE* characteristics obtained for different materials are discussed. Possible applications of the *AE* method in determining some properties of the normalized carbon-manganese St90PA steel are also discussed. *AE* measurements for the materials in different state have been conducted during static strength tests. In this number exploited materials of the different age have been tested. In the St90PA steel tests the influence of the experiment conditions on the *AE* results have been verified. Three different test stands existing in two different laboratories have been applied in these works. The significant influence of disturbances both on the experimental results and on the necessity of verification of test apparatuses and conditions is connected with this fact.

2. Test apparatuses

Tests of the *AE* of all investigated materials except of the St90PA steel and the PA2N alloy have been done at the Zentralinstitut fuer Festkoerperphysik und Werkstofforschung of the German Democratic Republic Academy of Sciences in Dresden. Tests have been carried out for the test apparatus composed of the Trodyne *AE* analyser and the Zwick 10T testing machine of the strength power of 100 kN. The *SIMS* (Structural Integrity Monitoring System) module has been the basic element of the apparatus for *AE* measurements. This module contains systems for analog and digital processing of the acoustic signal (Fig. 1). Polish and German piezoelectric resonance transducers, *PP*, have been used in the measurements. Their resonance frequency has been equal to 200 kHz. The *EA* head has been connected with the first preamplifier *PA*1, by a doubly shielded cable of the length of 20 cm. Preamplifier has amplified the input electric signal by 40 dB. The low frequencies of the signal have been eliminated by virtue of the high-pass filter *HPF*. Frequencies lower than 100 kHz have been eliminated. Two independent cables leaded out the signal from the *HPF* filter. Two additional preamplifiers *PA*2 and *PA*3 have been used in secondary amplification of the signal. The *SIMS* system has contained, among the others, the

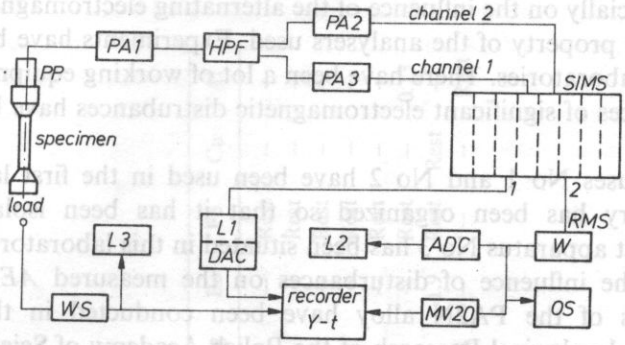

Fig. 1. Block diagram of the *AE* analyser

following equipment: high-pass filters, discriminators and system of the signal processing. These systems have produced classical parameters measured by the *AE* method, such as count rate and count sum, event rate and event sum and the *RMS*, that is root mean square of the acoustic signal. The output No 1 of the *SIMS* system has been giving the signal of the count rate in the digital form. Its value have been visible by use of the *L*1 counter. Next the signal has been passing through the digital-analog converter *DAC*. The converter has been integrated with the *L*1 counter. Then the signal has been registered by a multimanual *y–t* recorder. The averaged acoustic signal has been obtained from the second output channel of the *SIMS* system. This signal has been next amplified by the amplifier *W* and directed to the oscilloscope *OS*, digital-analog converter *DAC*, counter *L*2 and the milivoltmeter MV20 and *y–t* recorder.

Tests of the St90PA carbon-manganese steel have been carried out in Warsaw. The following three test apparatus have been used:

1. Set for *AE* measurements (*AE* analyser) type *E*1 manufactured by Institute of Nuclear Research, Poland, together with the DZM 180 printer and the Instron 1251 testing machine of a hydro drive.

2. Set for *AE* measurements the same as for set-up 1, the mechanical drive testing machine manufactured by Schoper company, German Democratic Republic. Tensile force of this machine has been equal to 100 kN.

3. Set for *AE* measurements type *DEMA*-10 manufactured by ZD Techpan, PAS, Poland, and the hydraulic press of the load 1500 kN colaborating with the reverser manufactured by the High Pressure Center, Unipress, Warsaw.

Acoustic investigations of the St90PA steel have been carried out by using these three test stands. Analogous experimental program has been used every time. Basic *AE* parameters such as count rate, and sum and event rate and events sum (excluding *RMS*) have been determined by employing of the four-channel *AE* analyser type *E*1 and one-channel analyser *DEMA*-10. High sensitivity and the low level of the self-noices are the characteristic properties of these analysers. Their sensitivity is comparable with the sensitivity of the *SIMS* set. Low resistance on the external

disturbances, specially on the influence of the alternating electromagnetic field is also the characteristic property of the analysers used. Experiments have been conducted in two different laboratories. There have been a lot of working equipment in the first laboratory. Sources of significant electromagnetic distrubances have been present in this laboratory.

Test apparatuses No· 1 and No 2 have been used in the first laboratory. The second laboratory has been organized so that it has been isolated from any disturbances. Test apparatus No 3 has been situated in this laboratory what allowed us to estimate the influence of disturbances on the measured *AE* parameters.

Investigations of the PA2N alloy have been conducted in the Institute of Fundamental Technological Research of the Polish Academy of Sciences by the use of the testing machine Instron 1251 and the *AE* analyser manufactured by the French company Audimat P. Because of the worse quality of the Audimat P analyser, manifested mainly in the high level of its self-noices, results obtained by the use of such an analyser cannot be quantitatively compared with other results.

3. Material and testing technique

The following materials have been used in experiments: Armco iron, carbon steel 45, 45HNMFA structural steel, ŁH15 bearing steel, BB2 beryllium bronze, type N18K9M5T maraging dispersion hardening alloy, PA2N aluminium alloy and St90PA carbon-manganese steel of two varieties: new and exploited within 10 years railway rails. Table 1 shows the chemical composition of these materials and Table 2 shows some of their mechanical properties.

Ten or five-times cylindrical specimens as well as flat specimens have been used for tests. The main dimensions of the specimens and way of their attachment in testing machine are shown in Fig. 2a. St90PA steel has been tested for the 10-times specimens on three test stands (see Chapter 2) and the PA2N alloy for flat specimens (Fig. 2b) on the Instron 1251 testing machine. Five-times specimens of the 45HNMFA, ŁH15, BB2 bronze and N18K9M5T alloy have been tensed by the use of Zwick mechanical testing machine. Value of the tensile load has been registered by the pen of the testing machine and together with the *AE* results on the *y–t* plotter. The force signal has been intensified by the *WS* amplifier, Fig. 1, and registered by *y–t* plotter and *L*3 counter. Use of the *L*3 counter allowed the on-line control of tensile force value. *L*3 counter has been used mainly in establishing the initial tension of the specimen after it has been attached to the handles of testing machine. It has been also used to reduce the axial clearance in handles.

Specimens have been stretched in testing machine by the use of the special handles, Fig. 2a, endowed with washers damping mechanical disturbances from mechanical and hydraulic elements of the drive. Stretching rate of the 5-times specimens has been equal 0.5 mm/min and the approximate rate for 10-times specimens was 1 mm/min what corresponds to $2.78 \cdot 10^{-4}\ s^{-1}$ in the relative measure when the active length of the specimen is taken into account.

Table 1. Chemical composition of tested materials

Material	C	Mn	Si	Cr	Ni	Mo	V	S	P	Co	Ti	Mg	Be	Fe	Cu	Al
Armco	0.02	–	–	–	–	–	–	–	–	–	–	–	–	Rest	–	–
45	0.45	0.50	0.30	–	–	–	–	–	–	–	–	–	–	Rest	–	–
St90PA	0.68	1.11	0.24	0.01	0.01	0.10	0.02	0.027	0.026	–	–	–	–	Rest	–	–
45HNMFA	0.45	0.50	0.30	1.00	1.70	0.25	0.15	0.025	0.025	–	–	–	–	Rest	–	–
ŁH15	1.10	0.40	0.30	1.50	0.30	–	–	0.020	0.027	–	–	–	–	Rest	–	–
N18K9M5T	0.012	–	–	–	18.20	4.87	–	–	–	9.0	0.72	–	–	Rest	–	0.13
BB2	–	–	–	–	–	–	–	–	–	0.25	–	–	1.9	Rest	Rest	–
PA2N	–	–	–	–	–	–	–	–	–	–	–	2.8	–	–	–	Rest

Table 2. Mechanical properties of tested materials

Material	σ_{ys} MPa	σ_u MPa	A_5 %	Necking %	Hardness HRC
Armco	155	230	26	65	–
45	327	500	24	60	–
St90PA new	600	1010	10	19	30
St90PA expl.	525	985	10	19	30
45HNMFA	1530	2040	10	32	52
	1375	1500	12	34	42
ŁH15	1780	2470	0.5	–	60
N18K9M5T	1730	1910	10	36	50
BB2	890	1160	2	–	36
PA2N	180	270	–	–	

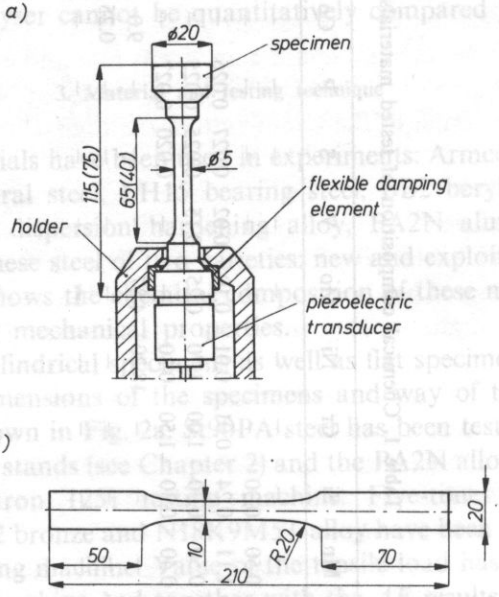

Fig. 2. Specimens for tensile testing: a) Cylindrical specimen in special holder; b) Flat specimen from PA2N alloy

Beam specimens have been used for establishing the characteristics of the St90PA steel in bending. The same specimens have been used in Bauschinger effect investigations. Their dimensions were $20 \times 30 \times 240$ mm^3. Bended specimens have been strained with the velocity of the testing machine traverse shifting equal to 2 mm/min.

In the *AE* analysers type *E*1 and *DEMA*-10, transducers type 0.5LR17B manufactured by Unipan have been used. The amplification of the preamplifier was 40 dB and the transmitted frequency band was 60...250 kHz. Discrimination

level and amplification of the main amplifier were different for each set. Their values are shown in the diagrams presenting the results of the measurements. These parameters have been related to the conditions of external disturbances and to the possibilities of the adaptation to the parameters of the cooperation with another equipment. The *AE* converter and transmitted frequency band have been calibrated experimentally by use of the equipment for *AE* simulation.

4. Acoustic emission characteristics of tested materials

The *AE* characteristics have been obtained for 8 different materials. Taking into account tests of two materials (45 HNMFA and St90PA) with two variations and remembering that one of them has been tested on three apparatus, the total amount of 14 different characteristics has been obtained. At least 5 specimens have been tested for each testing group. Good repeatability of the results obtained for each group has been found. Representative characteristics of all the tested material are presented below.

For most materials the following characteristics have been obtained: tension curve, count rate and *RMS*. In many cases the nature of changes of all the *AE* parameters obtained for the given material is similar. These parameters are count rate and count sum, event rate and event sum and *RMS*. Usually, the parameters like count rate and event rate can be used interchangeably and we can notice that when one of them is known, then the information about the acoustic features of the material is sufficient. On the other hand, there are materials for which differences between characteristics presented in the form of the count rate and *RMS* are appreciable. Results of the *AE* measurements are presented together with loading curves. Both curves have been registered simultaneously and should be interpreted as the inseparable pair when the *AE* characteristics of the materials as well as the Kaiser effect are considered. Certain differences between the obtained loading curves and the ideal curves must be noticed. Ideal curves are obtained when the tensile force and the specimens elongation are registered simultaneous by the tensometer attached to the specimen. These differences can be observed in spite of the fact that in both cases the specimen's loading takes place with the constant velocity of the testing machine traverse shifting. In acoustic tests, specimens are wrestled in the testing machine handles by means of the flexible elements damping external interferences (Fig. 2). It results from this fact that the stiffness of the loading system in tension test is changed and differences in the rate of specimen straining occurs. In the beginning of the loading process mainly more flexible washers are subjected to strain. It reflects at the initial point of the graph as the progressively growing curve. Further, flexibility of the washers decreases and the increase of their strain is transient. Corresponding point of the tension curve is imperceptibly deformed but its accuracy is good enough when the conducted experiments are of the comparative nature. All described process can be pointed out as the source of the differences mentioned above.

Deformation of the flexible washers is sometimes accompanied by a inconspicuous acoustic effect. The *AE* image of the tested materials is not deformed by this effect because it appears only initially for low level of the load, when the proper *AE* phenomenon does not appear. Only part of the stretched specimens has been loaded to the final break oft. It happened because the specimen's break oft is accompanied by a strong shock which, in turn, can lead to destruction of the piezoelectric transducer.

1. Armco iron. *AE* characteristic of the annealed Armco iron consists of two parts differing from each other (Fig. 3). The first part corresponds to the Lüders platform, whereas the second one – to the hardening range. According to the *RMS* curve, very intensive acoustic activity together with the characteristic minima and maxima is observed in the range of the plastic flow. In all the range of the Lüders platform usually 4 maxima and 4 minima can be observed. Beginning of the acoustic activity appears in the range of the elastic deformation and the last minimum always corresponds to the end of the Lüders platform. This end is marked on the tension curve also as the characteristic minimum. The mean increment of the specimen

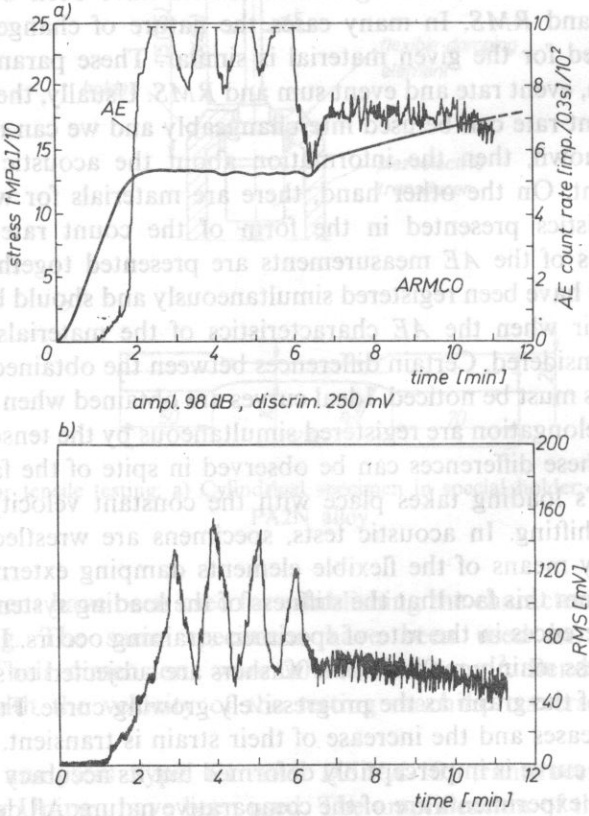

Fig. 3. *AE* characteristic of ARMCO iron: a) loading curve and *AE* count rate; b) *RMS*

elongation measured within the range of the plastic flow of the material has been equal to 3%.

Within the hardening range of the material, acoustic activity initially slightly grows, next monotonically decreases and disappears in the vicinity of the beginning of the specimen necking. The nature of the *AE* count rate curve is similar within the tension range. The average total elongation of the Armco iron specimens measured to their final rupture has been 26% whereas the average reduction of the area of the specimen measured in the fracture mane has been 65%.

2. 45 carbon steel. General character of the results obtained for the 45 steel (Fig. 4) is similar to those of the Armco iron (Fig. 3). Average increment of the specimen elongation for the plastic flow range has been about 1%. Beginning of the acoustic activity has been also observed in the elastic range of the specimen's deformation, like for the Armco iron. The only difference is that comparing to the lower bound of the yield limit, acoustic activity of the 45 carbon steel appears for higher stress than the approriate stress registered for the Armco iron. Greater number of the maximum and minimum points on the *RMS* curve has been observed within the Lüders platform and faster decrease of the acoustic activity within the hardening range has been noticed.

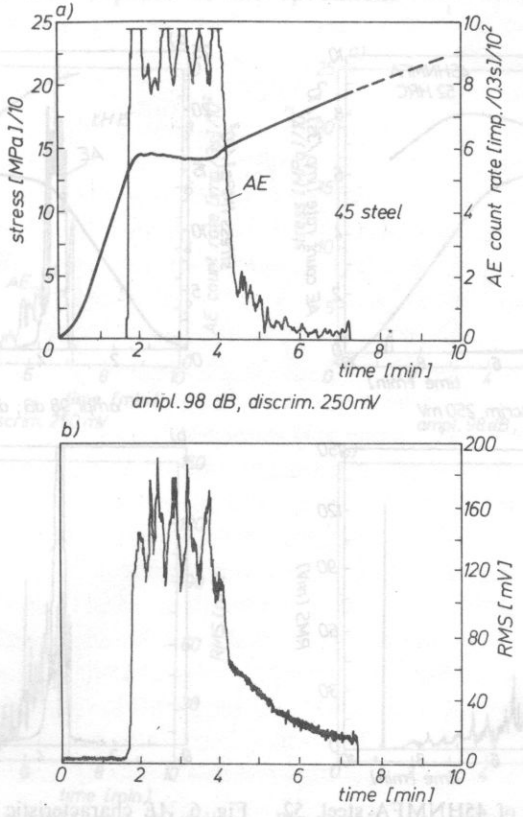

Fig. 4. *AE* characteristic of carbon steel 45

The lower bound of the yeld limit of the annealed 45 steel is approximately 2 times greater than the same bound of the Armco iron. The total elongation of the 45 steel specimens has been about 10% whereas the average reduction of the specimens area has been about 32%. Analogically as in the case of the Armco iron, the nature of the *AE* count rate is similar to the nature of the *RMS*. Initiation of the acoustic activity within the elastic deformation range and the cyclic change of this activity within the Lüders platform are the significant features of the 45 steel as well as Armco iron *AE* characteristic. The first feature gives evidence, that the range of the elastic deformation as estimated from the tension curve is elastic only in the conventional meaning. As a matter of fact, the irreversible changes of the material structure takes place even for this deformation. It leads to the energy release of the stressed specimen. Initiation of the plastic deformation registered by the *AE* method appears in the lower bound of yield limit.

3. 45HNMFA structural steel with the heat treatment on different hardness (52 and 42 HRC) has the characteristic typical for many policrystalline metals and alloys (Figs 5, 6). Acoustic activity of this steel contains in a narrow range of strain (except of the *RMS* curve of the 52 HRC hardness steel) and comes for the early beginning of

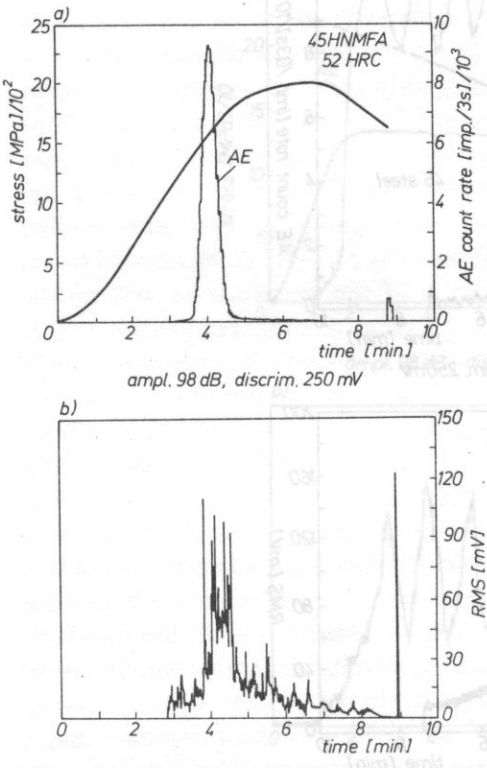

Fig. 5. *AE* characteristic of 45HNMFA steel, 52 HRC: a) loading curve and *AE* count rate: b) *RMS*

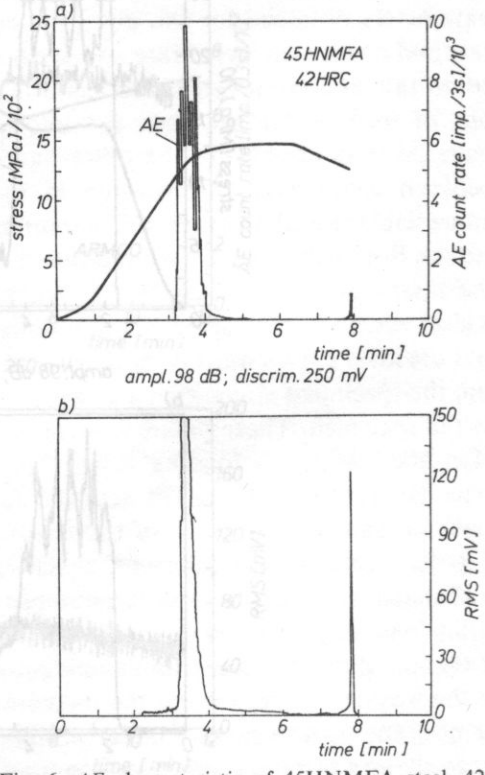

Fig. 6. *AE* characteristic of 45HNMFA steel, 42 HRC: a) loading curve and *AE* count rate; b) *RMS*

the hardening range. This steel does not exhibit the physical yield point. Significant differences of the count and event rate as well as *RMS* can be seen in *AE* characteristics of the 52 and 42 HRC hardness specimens. These differences give evidence of a different course of the plastic deformation process in the vicinity of the offset yield stress.

The *AE* count rate of the 52 HRC hardness steel grows and decreases monotonically and a curve appears in a triangular form. In the case of the 42 HRC hardness steel, significant fluctuations of the *AE* counts density is observed. Situation is just opposite if the *RMS* curves of the two varieties of this steel is taken into account (Figs 5 and 6). The acoustic activity level of the 45 HNMFA steel is lower than annealed Armco iron or 45 carbon steel.

4. ŁH15 bearing steel in the thermally treated and low-temperature tempering state exhibits different shape of the tension curve (lack of necking) as well as different character of the acoustic effect (Fig. 7). Immediate strength of this steel is very high (about 2500 MPa) whereas its irreversible elongation and cross area reduction measured in a plane of fracture are transiently small. Count rate and *RMS* appear in the vicinity of the offset yield point. Their growth is initially slow and grows with the load increase to the final repture of the specimen.

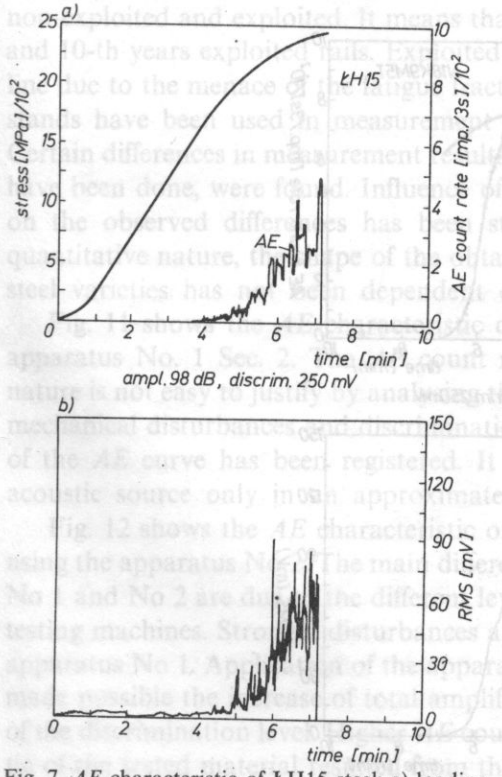

Fig. 7. *AE* characteristic of ŁH15 steel: a) loading curve and *AE* count rate; b) *RMS*

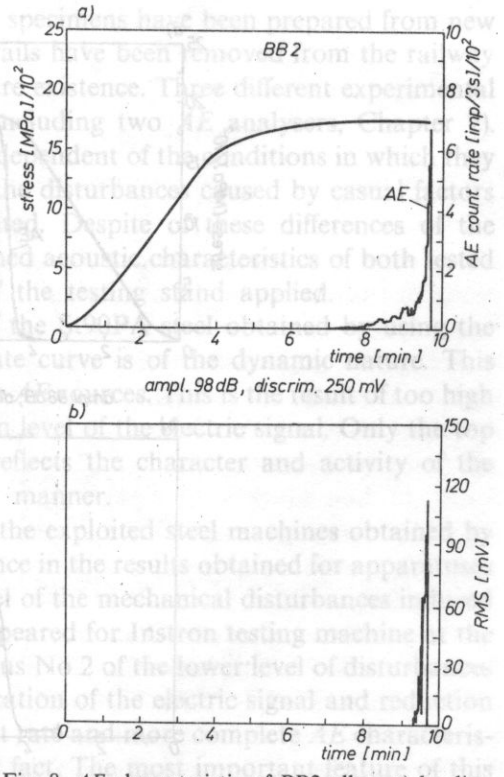

Fig. 8. *AE* characteristic of BB2 alloy: a) loading curve and *AE* count rate; b) *RMS*

5. BB2 beryllium bronze (Fig. 8) in the state after supersaturation and ageing has the most atypical *AE* characteristic of all the tested material although its tension curve is entirely typical. Acoustic effect appears only for the final phase of the specimen's tension process, just before its rupture. These is no acoustic activity in the hardening range of the material. Similarly as it was in the case of the bearing steel, also here these is no neck in the specimen and its cross area contraction is transiently small.

6. N18K9M5T maraging type alloy exhibits relatively high *AE* within all the range of plastic deformations (Fig. 9). Maximum activity coincides with the maximum point of the tension curve. Acoustic effect appears for load similar to the offset yield strength and grows monotonically within all the hardening range. In the range approximate for necking it grows small but remains perceptible to the final repture of the specimen.

7. PA2N aluminium alloy. *AE* of the PA2N alloy in the state hardened by cold working is typical (Fig. 10). Acoustic activity appears in the beginning of hardening. In the qualitative sense it can be compared with the *AE* characteristic of the 45HNMFA steel of the hardness equal 52HRC (Fig. 5). In the quantitative sense significant differences between both materials are manifested. These differences have

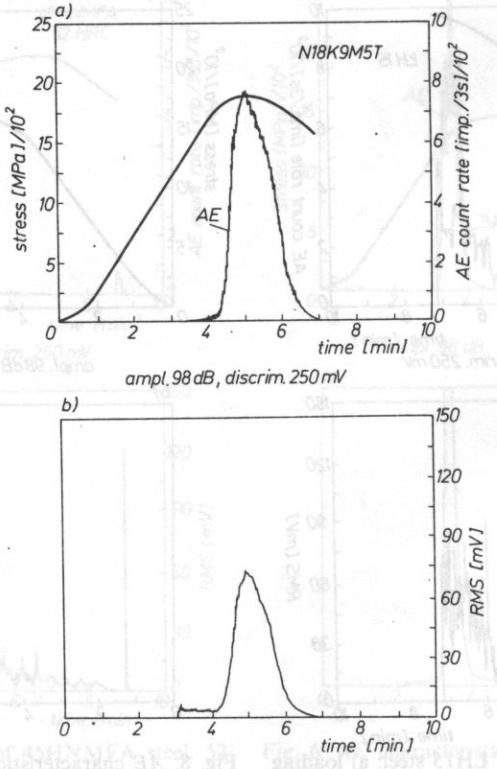

Fig. 9. *AE* characteristic of N18K9M5T alloy: a) loading curve and *AE* count rate; b) *RMS*

their reason both in different laboratory equipment used in test and in structural differences of both materials. The differences reflect in different acoustic effects for tentative loading conditions.

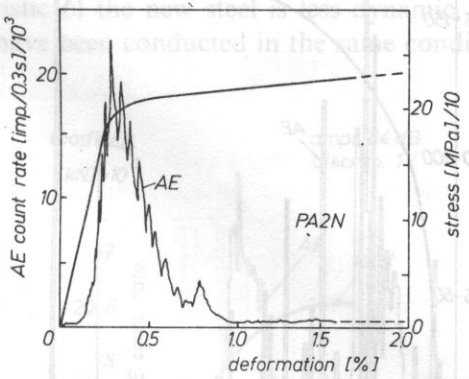

Fig. 10. *AE* characteristic of aluminium alloy PA2N after cold-working

8. St90PA carbon manganese steel has been tested in two varieties, that is non-exploited and exploited. It means that specimens have been prepared from new and 10-th years exploited rails. Exploited rails have been removed from the railway line due to the menace of the fatigue fracture existence. Three different experimental stands have been used in measurement (including two *AE* analysers, Chapter 2). Certain differences in measurement results dependent of the conditions in which they have been done, were found. Influence of the disturbances caused by casual factors on the observed differences has been stated. Despite of these differences of the quantitative nature, the shape of the obtained acoustic characteristics of both tested steel varieties has not been dependent of the testing stand applied.

Fig. 11 shows the *AE* characteristic of the St90PA steel obtained by using the apparatus No. 1 Sec. 2. The *AE* count rate curve is of the dynamic nature. This nature is not easy to justify by analysing the *AE* sources. This is the result of too high mechanical disturbances and discrimination level of the electric signal. Only the top of the *AE* curve has been registered. It reflects the character and activity of the acoustic source only in an approximated manner.

Fig. 12 shows the *AE* characteristic of the exploited steel machines obtained by using the apparatus No 2. The main difference in the results obtained for apparatuses No 1 and No 2 are due to the different level of the mechanical disturbances induced testing machines. Stronger disturbances appeared for Instron testing machine at the apparatus No 1. Application of the apparatus No 2 of the lower level of disturbances made possible the increase of total amplification of the electric signal and reduction of the discrimination level. Higher *AE* count rate and more complete *AE* characteristic of the tested material resulted from this fact. The most important feature of this characteristic is the distinctly marked shape of the area below the *AE* count rate

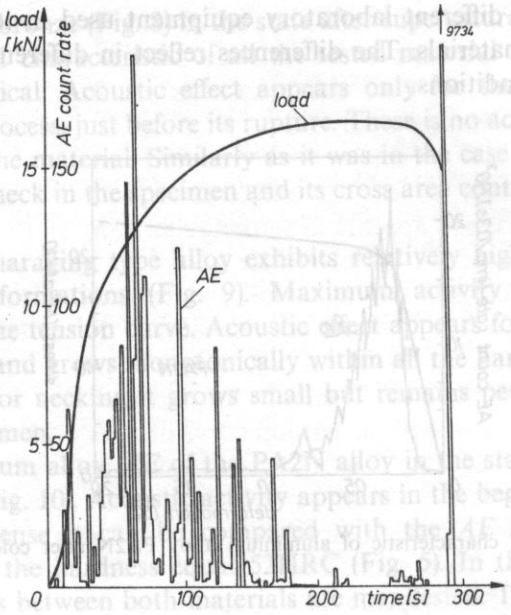

Fig. 11. *AE* characteristic of St90PA steel for tensile test on the test stand No 1. decreased amplification and increased discrimination level

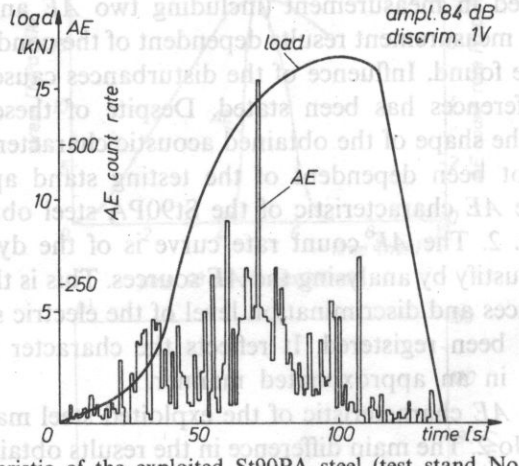

Fig. 12. *AE* characteristic of the exploited St90PA steel (test stand No 2. *AE* analyser *E*1)

curve. Evaluation of the source character is based on this shape. Initiation of the phenomenon appears when offset yield limit $\sigma_{0.2}$ is reached. For the exploited material this limit has been equal to 5 MPa and the value approximate the new material has been about 7 MPa. *AE* count rate rapidly grows and reaches maximum at the 2/3 of the hardening range. Then it grows small with the rate several times

smaller comparing to the grow rate. Acoustic effect accompanies the deformation of the specimen to its rupture. Dynamic character of the *AE* count rate well as acoustic activity existing within all the range of the plastic deformation of the material proves the existence of the strong jump internal reactions of the deforming material.

The *AE* characteristic of the new steel is less dynamic, Fig. 13. Measurements done for a new steel have been conducted in the same conditions as applied for the

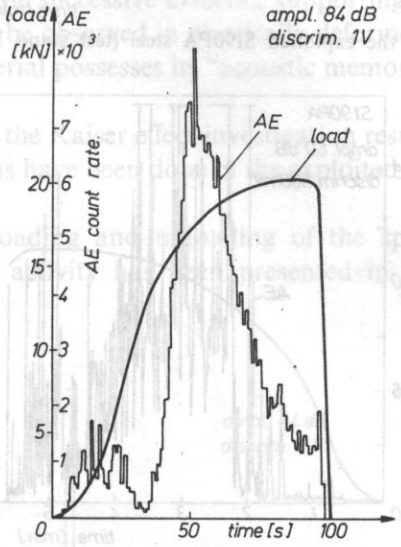

Fig. 13. *AE* characteristic of the new St90PA steel (test stand No 2. *AE* analyser *E*1)

exploited material, Fig. 12. The count rate graph is in the qualitative sense as the same the graph described above. Apparent quantitative differences consist in about 10 times greater acoustic activity, significantly marked characteristic and lower dynamic (nonhomogenity) of the *AE* count rate curve. Beginning of tension is accompanied by disturbances resulting from the arranging of the specimen ends in special catch handles and are not connected with the proper acoustic of the material.

Characteristics of the exploited and not exploited steel obtained by using the set-up No 3 with the DEMA-10 analyser are shown in Figs 14 and 15. None disturbances have been present here and the results have been registered by the *y–t* plotter. Both results have been obtained for the same measuring conditions which, in term, differ from the conditions of the set-up No 2 by the value amplification and the voltage of the discrimination level. Differences result from the requirements of the register installation. The qualitative changes of the *AE* count rate obtained by use of the two sets are nearly the same. It gives arguments for the appropriateness of the applied equipment and testing techniques. The *AE* in bending (Fig. 16) is generally similar to the characteristic obtained in tension (Fig. 13). On the other hand, determination of the peculiar points of the bending curve is more difficult. It leads to

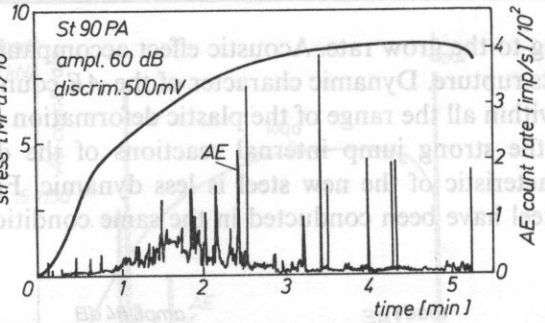

Fig. 14. *AE* characteristic of the exploited St90PA steel (test stand No 3, *AE* analyser *DEMA*-10)

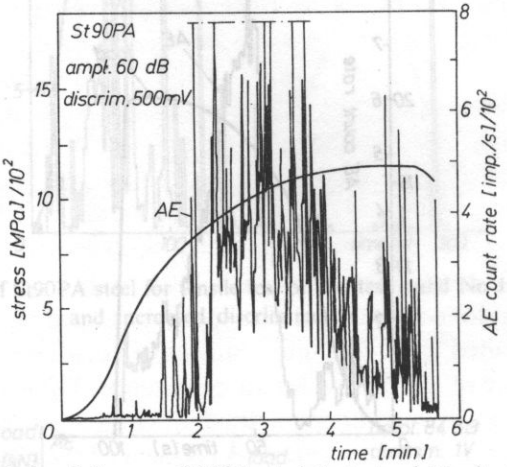

Fig. 15. *AE* characteristic of the new St90PA steel (test stand No 3, *AE* analyser *DEMA*-10)

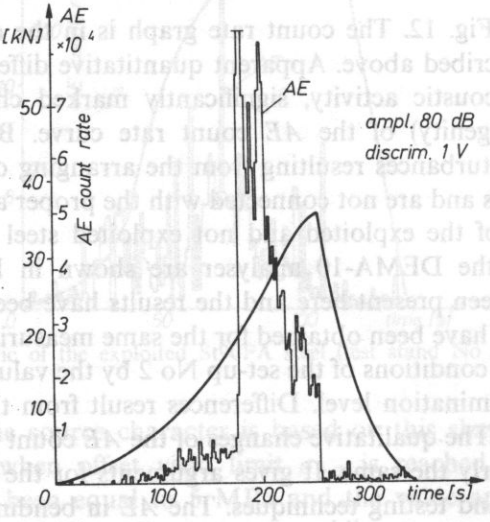

Fig. 16. *AE* characteristic of St90PA steel in bending (test stand No 1)

the certain difficulties in identification of the level of material deformation with the adequate acoustic effect. This effect is also connected with the existence of nonhomogeneous stresses inside the bended specimen that is with the simultaneous existence of compression and tensional stresses within the sample.

5. The Kaiser effect

The Kaiser effect is the successive evidence supporting the statement that certain irreversible changes can be observed in plastically deformed material. It also justifies the hypothesis that material possesses its "acoustic memory" of the loads it had been subjected in the past.

Figs 17 and 18 show the Kaiser effect investigation results obtained for specimens in tension. The specimens have been done of the exploited and non-exploited St90PA steel.

Example of triple loading and unloading of the specimen together with the accompanying acoustic activity has been presented in Fig. 19 to show that the

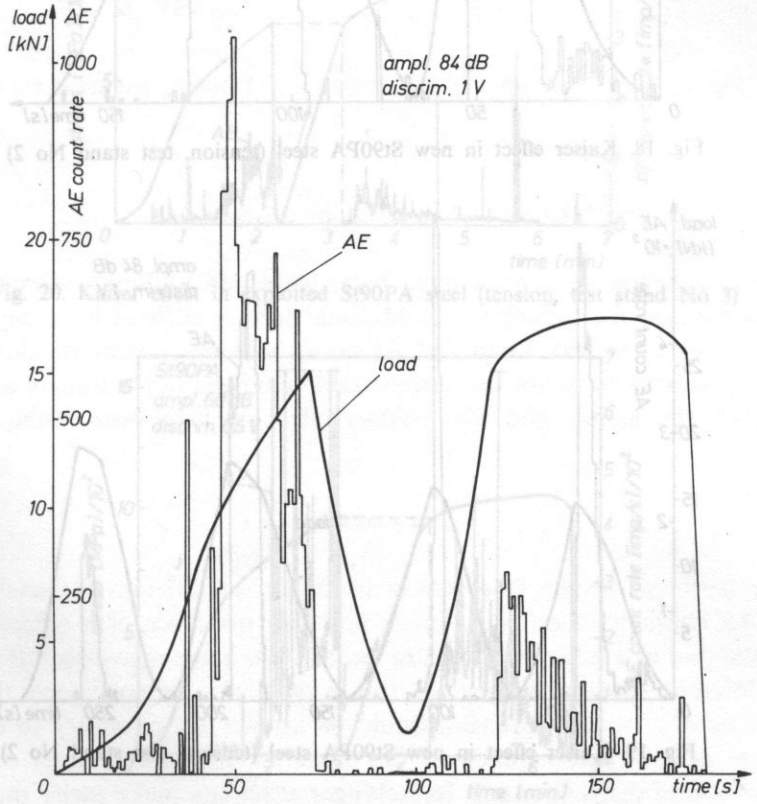

Fig. 17. Kaiser effect in exploited St90PA steel (tension, test stand No 2)

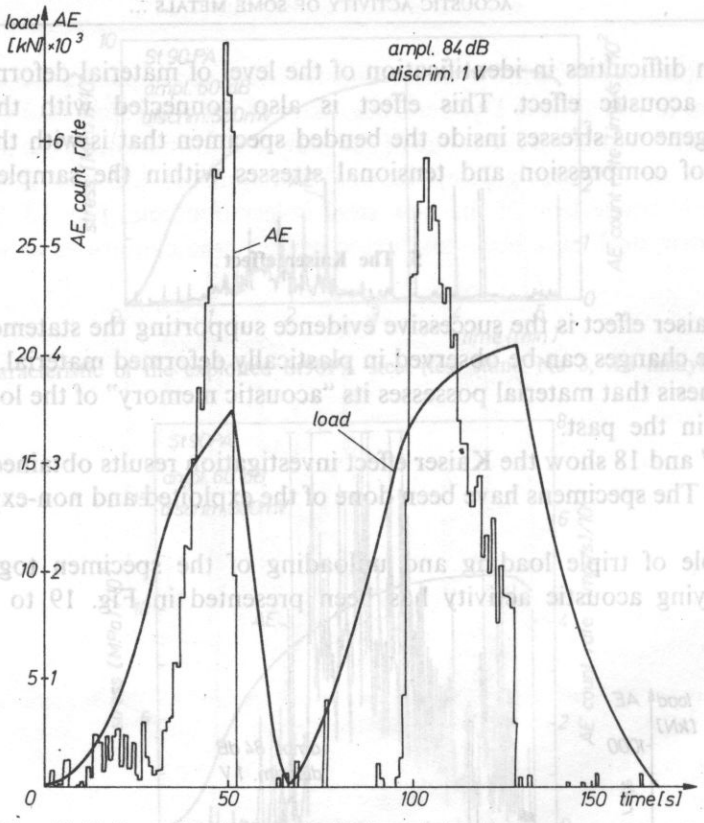

Fig. 18. Kaiser effect in new St90PA steel (tension, test stand No 2)

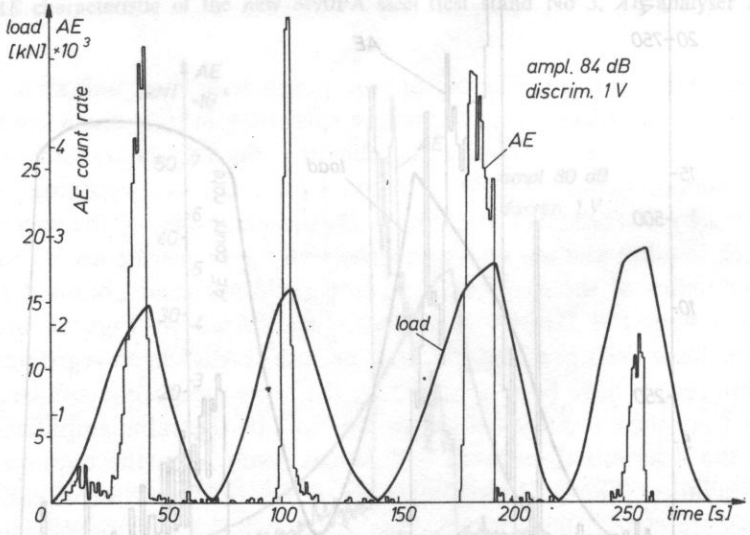

Fig. 19. Kaiser effect in new St90PA steel (tension, test stand No 2)

process does not depend on the stress value for which unloading begins and to show reliability of the material memory. We must notice that *AE* intensity reached for the moment of recovering activity in new loading is the same as it had been for the moment of unloading.

The results of the Kaiser effect measurements performed by using the set-up No. 3 are shown in Figs. 20 and 21. As before, also here they are all characterized by a very good repeatability. It can be seen that St90PA steel exhibits significant Kaiser effect for its both tested varieties. This effect establishes the certain kind of the material load memory and for this reason it makes possible the control of the loads applied in the past. It happens if the acoustic image is out disturbed by such sources of *AE* as the crack propagation or phase transitions. On the other hand, when the maximum level of the load applied is known, it forms a convenient background for controlling growth of dangerous processes leading to fracture.

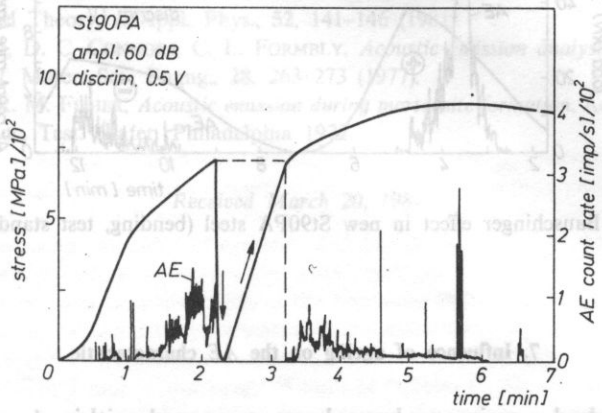

Fig. 20. Kaiser effect in exploited St90PA steel (tension, test stand No 3)

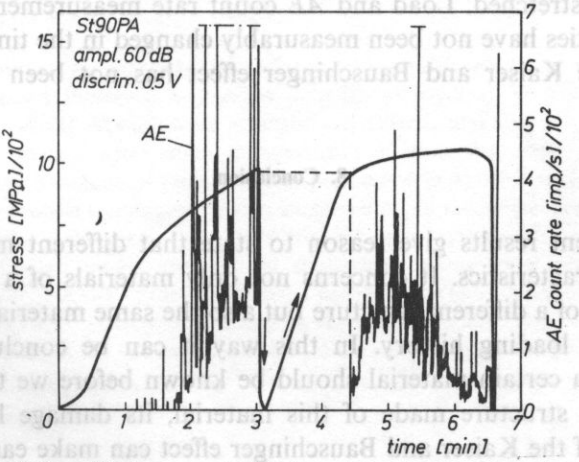

Fig. 21. Kaiser effect in new St90PA steel (tension, test stand No 3)

6. Bauschinger effect

Bauschinger effect has been confirmed much earlier than *AE* phenomenon was discovered. This effect concerns certain characteristic mechanical properties of the material. It consists in the reduction of the yield limit in metals due to their earlier plastic strain. Result of the *AE* count rate measurement in 3-point bending is shown in Fig. 22. The left-hand side of the figure (plus) concerns bending into one side whereas the right-hand side (minus) concerns bending of the same specimen but into other side. The result confirms existence of the phenomena accompanying it. The acoustic effect observed for second bending is much weaker out it is characterized by nearly constant level of activity.

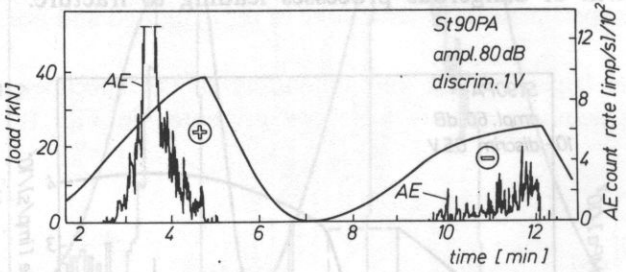

Fig. 22. Bauschinger effect in new St90PA steel (bending, test stand No 2)

7. Influence of ageing on the *AE* characteristic

Initially stretched specimens have been preserved within 1 month in natural conditions without the influence of additional factors such as humidity. Next they have been again stretched. Load and *AE* count rate measurements allow us to say that these quantities have not been measurably changed in the time of ageing. Effect of ageing on the Kaiser and Bauschinger effect has not been found also.

8. Conclusion

The experiment results give reason to state that different materials have very different *AE* characteristics. It concerns not only materials of a different chemical composition and of a different structure but also the same materials but heat treated or of a different loading history. In this way it can be concluded that the *AE* characteristic of a certain material should be known before we try to estimate the actual state of a structure made of this material, its damage level etc.

Application of the Kaiser and Bauschinger effect can make easier the estimation of maximum load that has acted on the structure in the past.

References

[1] S. PILECKI, *Wykorzystanie emisji akustycznej w badaniach własności mechanicznych i pękania ciał stałych*, Arch. Akust., **21**, 109 (1986).

[2] J. EISENBLÄTTER, J. BRECHT, P. JAX, *Werkstoffprüfung mit der Schallemissionanalyse*, Zeitsch. Werstofftechnik, 4, 306 (1973).

[3] H. JÖST, *Schallemissionsmessungen an bruchmechanischen Proben während wechselnder und zügiger Belastung*, Schallemission. DGM, München, April 1974, 149–169.

[4] C. B. SCRUBY, J. C. COLLINGWOOD, H. N. G. WADLEY, *A new technique for the measurement of acoustic emission transients and their relationship of crack propagation*, J. Appl. Phys. D., **11** (1978).

[5] F. HAMEL, J. P. BAILON, M. N. BASSIM, *Acoustic emission mechanism during high – cycle fatigue*, Eng. Fract. Mech., **14**, No 1, (1981).

[6] D. E. MACHA, D. M. CORBHY, I. W. JONES, *On the variation of fatigue crack – opening load with measurement location*, Exper. Mech., **19**, No 6 (1979).

[7] S. PILECKI, *Dislocation-diffusion mechanism of fatigue crack formation*, Fracture Vol. 2 ICF4 Waterloo, Canada, 1977, 687–693.

[8] R. A. KLINE, R. E. GREEN, C. H. PALMER, *Acoustic emission wave forms from cracking steel*, Experiment and Theory, J. Appl. Phys., **52**, 141–146 (1981).

[9] A. C. SINCLAIR, D. C. CONNORS, C. L. FORMBLY, *Acoustic emission analysis during fatigue crack growth in steel*. Mater. Sci., Engng., **28**, 263–273 (1977).

[10] G. R. SPEICH, R. M. FISHER, *Acoustic emission during martensite formation*, Acoustic Emission, STP – 505 Am. Soc. Test. Mater. Philadelphia 1972.

Received March 20, 1987

ARCHIVES OF ACOUSTICS
14, 3 4, 283 292 (1989)

ACOUSTIC PROPERTIES OF GAS BUBBLES COATED WITH MONOLAYERS OF OIL SUBSTANCE[1]

STANISŁAW J. POGORZELSKI, KHALIFA S. SAEID[2]

Environmental Laboratory of Acoustics and Spectroscopy Gdańsk University
[2]Institute of Experimental Physics
(80-950 Gdańsk, Wita Stwosza 57)

A gas bubble coated with a monolayer of oil substance, submerged in liquid, in the field of an acoustic wave is given theoretical consideration in this paper. Radial oscillations in the wave frequency band much below the resonance frequency depend mainly on the value of the monolayers modulus of elasticity and relaxation time t_r of the process of molecule reorientation which occurs in the monolayer due to its deformation. The following parameters were calculated: shift of the resonance frequency, damping constant of radial oscillations, and acoustic wave scattering and extinction cross-sections for a gas bubble in water, coated with a condensed monolayer of Extra 15 engine oil in angular frequency range $\omega \in [10^1 \div 10^5]$ rads^{-1} and range of radii of bubbles (3–50) μm. Predicted values of the damping constant and extinction cross-section in the wave frequency range $\omega < \alpha(\alpha = 2\pi/t_r)$ are by several orders of magnitude greater than those for a bubble with a clean surface. This effect is especially distinct in the case of microbubbles (with μm radii and smaller) placed at small depths (up to about 0.5 m).

Teoretycznym rozważaniom poddano pęcherzyk gazowy zanurzony w cieczy, pokryty monowarstwą substancji olejowej w polu fali akustycznej. W paśmie częstotliwości fali znacznie poniżej częstotliwości rezonansowej układu, drgania radialne zależą głównie od wartości modułu sprężystości monowarstwy i czasu relaksacji t_r procesu reorientacji molekuł zachodzącego w monowarstwie pod wpływem jej deformacji. Obliczono przesunięcie częstotliwości rezonansowej, stałą tłumienia drgań radialnych oraz przekroje czynne na rozpraszanie i ekstynkcję fali akustycznej dla pęcherzyka gazowego w wodzie pokrytego skondensowaną monowarstwą oleju silnikowego Extra 15 w przedziale częstotliwości kątowej $\omega \in [10^1\text{–}10^5]$ rads^{-1} i promieni pęcherzyków $(3 \div 50)$ μm. Przewidywane wartości stałej tłumienia i przekroju czynnego na ekstynkcję są o kilka rzędów wielkości większe od tych dla pęcherzyka o czystej powierzchni dla zakresu częstotliwości fali $\omega < \alpha(\alpha = 2\pi/t_r)$. Efekt jest szczególnie wyraźny dla mikropęcherzyków o promieniu μm i mniejszych usytuowanych na niewielkiej głębokości (do około 0.5 m).

[1] Research performed within the framework of problem CPBP 02.03 II/2.16.

1. Introduction

Physical characteristic of many hydrodynamic systems with interfaces with an adsorbed film (foams, micro- and macroemulsions, gas bubbles) greatly depend on the modulus of elasticity of the surface monolayer [6, 16, 23]. Presented considerations concerning radial oscillations of a gas bubble covered with a monolayer of surface-active substance are based on Glazman's theoretical papers [11, 12]. Previous research on this problem disregarded the influence of monolayer's visco-elastic properties. This led to incorrect estimations of the resonance frequency of the bubble's oscillations or threshold of surface wave generation [2, 4, 10, 14, 15], for example. One of the authors previously investigated properties of monolayers of oil substances with various physical properties. These monolayers were formed on water surface [20]. It was possible to determine the influence of a condensed monolayer of light engine oil Extra 15 covering a gas bubble on the resonance frequency and damping constant of radial oscillations on the basis of these investigations. Dispersed in sea water oil-derivative substances can be accumulated for example on the surface of gas bubbles formed in the conditions of intensive wavy motion. This paper is also aimed at the determination of the influence of changes of the bubble's surface properties on acoustic wave scattering and extinction, and so on quantities directly deciding about conditions of wave propagation in a medium with bubbles. Presented results of theoretical considerations can be, applied in order to create a new effective method of evaluation of the water pollution based on bubble spectrometry [17].

2. Frequency of natural oscillations and damping constant of radial oscillations of gas bubble coated with adsorbed film

The classical Rayleigh's equation for oscillations of a gas bubble in liquid has been supplemented by GLAZMAN [11] with an additional term which includes visco-elastic properties of the adsorbed monolayer. The film decreases the average radius of an oscillating bubble in comparison to a clean surface, and as a consequence increases the frequency of natural oscillations. The ratio of frequency of free oscillations of a bubble with adsorbed film, ω_p, and a bubble with a clean surface, ω_0, is given by expression [11]

$$\omega_0/\omega_p = h\{[3kh^{3k} - W(h+3\beta h^3)]/(3k-W)\}^{1/2} \tag{1}$$

where: $h = R_0/\mathbf{R}$, R_0, $\mathbf{R}$ – equilibrium and mean radius, respectively, related by expression (30) in [11], k – polytropic exponent for the gas,

$$W = 2\gamma/(P_{i.eq}R_0) \tag{2}$$

is Weber number, $P_{i,eq} = 2\gamma/R_0 + 1.013\cdot 10^5\ (1+0.1H)$ – gas pressure inside the bubble, H – depth in liquid of the bubble, γ – interfacial tension,

$$\chi = -d\gamma/d\ln\Gamma \tag{3}$$

is modulus of elasticity of the monolayer discussed more fully in the next chapter [6, 16, 23], $\beta = \chi_0/\gamma$.

The damping constant B of the bubble's radial oscillation is expressed by a real and imaginary part of complex parameters $\tilde{\mu}$ and $\tilde{v}$ in the following form [12]

$$B = \omega^{-1}(\mathrm{Re}\,\tilde{\mu} - \tfrac{1}{2}\mathrm{Im}\,\tilde{v}^2), \tag{4}$$

where ω – angular frequency of acoustic wave, $\tilde{\mu} = (4\chi_0|\varrho\mathbf{R}^3)\eta/(1+\eta^2)$, ϱ – density of liquid,

$$\tilde{v}^2 = (\varrho\mathbf{R}^2)^{-1}\left\{3kP_{i,eq} - \left(\frac{2\gamma}{R}\right)\left[1+\beta\left(3-4\frac{\eta^2}{1+\eta^2}\right)\right]\right\},$$

$$\eta = \alpha/\omega.$$

Parameter α is the angular frequency of relaxation processes of diffusion and reorientation of the surface-active substance's molecules in the monolayer due to changes of its area. The dimensionless damping constant δ (in the PROSPERETTI notation [22]) is related to the B constant in equation [8]:

$$\delta = 2\beta\omega/\omega_0^2 \tag{5}$$

It consists of three terms responsible for losses due to: viscosity of surrounding liquid, heat conduction and acoustic radiation. DEVIN [8] thoroughly discusses the share of individual physical processes in oscillation damping of a gas bubble, and their value in the entire frequency range of the acoustic wave's field can be calculated from relationships given by EULER [9], PROSPERETTI [22] and PLESSET [18].

3. Properties of adsorbed monolayers

A monolayer of surface-active substance is formed as a result of surface adsorption, described with Langmuir-Szyszkowski equations. These equations present relationships between surface pressure π and adsorption [7]

$$\pi = \gamma_0 - \gamma = RT\Gamma_\infty\left(1+\frac{c}{a}\right), \tag{6}$$

and

$$\Gamma = \Gamma_\infty\left(\frac{c}{c+a}\right), \tag{7}$$

where γ_0, γ – surface tension for the solvent (water) and solution of the surface-active substance, respectively, R – gas constant, T – absolute temperature, c – molar concentration, Γ, Γ_∞ – adsorption and saturation adsorption, respectively, a – Szyszkowski's coefficient of surface activity.

Compression and dilatation of the area occupied by the monolayer causes adsorption changes. In accordance with Gibbs law [1] a periodical moleculae exchange between the monolayer and subsurface area occurs, as well as their

reorientation in the monolayer itself (for insoluble substances). Both processes are characterized by definite relaxation times, t_r, related to parameter $\alpha(\alpha = 2\pi/t_r)$.

Limiting the problem to the diffusion process described by Fick's law, this time will have the following value [13]

$$t_r = \left[\frac{a}{\Gamma_\infty}\left(1+\frac{c}{a}\right)^2\sqrt{D}\right]^{-2}, \tag{8}$$

where D — diffusion coefficient.

Table 1 in paper [21] presents t_r values for several chosen surface-active substances present in the subsurface layer of natural waters. They greatly vary depending on the molecular structure of the substance (length of the hydrocarbon chain, type, quantity and configuration of polar groups in the molecule). The diffusional interchange between bulk and surface during area contraction and expansion causes time dependent variations of the monolayer's modulus of elasticity which has a different value from determined by surface equation of state — $\gamma(\Gamma)$ (Equation (3)).

Table 1. Values of physical quantities used in calculations
*Data taken from [20, 21]

$P_{i,eq} = 101325$ Pa	$H = 0.2$ m
$T = 293$ K	$\gamma_o = 72.5$ m Nm^{-1}
$\varrho = 0.998 \times 10^3$ kgm^{-3}	$\gamma_0 < 47.5$ m Nm^{-1}
$R_0 = 3, 5, 30, 50$ μm	$^*t_r = 0.035$ s
$k = 1$ (for $R_0 = 3$ and 5 μm)	$^*\alpha = 179.1$ rads^{-1}
$k = 7/5$ (for $R_0 = 30$ and 50 μm)	$^*\chi_0 = 136.8$ m Nm^{-1}

Now it is expressed by [16]

$$\chi = \chi_0(1+2\tau+2\tau^2)^{-1/2} \tag{9}$$

where the diffusion parameter τ is equal to [16]

$$\tau = \frac{(c/a+1)^2 a}{\Gamma_\infty}\sqrt{\frac{D}{2\omega}}, \tag{10}$$

for monolayers obeying equations (6) and (7). The second type of relaxation observed for insoluble surface-active substances [3], can not be expressed by measured in macroscale parameters of the system on the basis of existing theories. Values of the α parameter for such monolayers (also oil) are determined on the basis of experimental measurements of their dynamic properties [16].

4. Oil monolayers

The author investigated monolayers of oil-derivative substances with varying physical properties, spread on water surface [20]. Light oil fractions such as gasoline 78, kerosene, diesel oil have low surface activity and the modulus of elasticity of their

monolayers does not exceed 20 m Nm^{-1} at maximal compression ($\pi = 20$ m Nm^{-1}). While engine oils form "solid" type condensed layers, S [1]. The value of the modulus is equal to 93.6 and 136.8 m Nm^{-1} for Marinoll 111 oil and Extra 15 oil, respectively, at maximal compression of the monolayer. These values have been determined from separate physical and chemical measurements on the basis of relation $\gamma(\Gamma)$ (Equation (3)) obtained by means of Wilhelmy plate method [20]. One of the authors determined the α parameter for a monolayer of Extra 15 oil using the ultrasonic method of surface carpillary wave attenuation measurements [19]. The inflexion point of the wave attenuation coefficient versus frequency curve indicates the presence of a relaxation process at $f_r = 28.5$ Hz ($\alpha = 179.1$ s^{-1}) [21].

5. Gas bubble with oil monolayer

The knowledge of properties of oil substance monolayers on water surface [20] makes it possible to theoretically estimate their effect on oscillations of gas bubbles. Fig. 1 presents the ratio of the natural frequency of a gas bubble coated with a monolayer of Extra 15 engine oil in water, to the one of a clean bubble. It covers

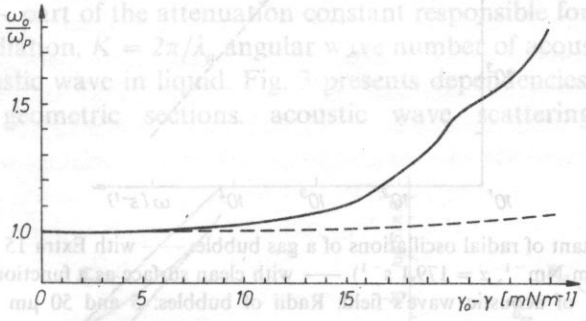

Fig. 1. Frequency shift of natural oscillations of a gas bubble coated with Extra 15 oil monolayer as a function of surface pressure of the monolayer; the bubble is placed at the depth of 0.2 m under the water surface. Bubble's radius – – – 30 μm, —— 3 μm

the entire range of surface pressures of the monolayer and was calculated from expression (1). Calculations were performed for two kinds of bubbles: $R_0 = 3$ μm (solid line) and $R_0 = 30$ μm (dashed line), placed 0.2 m under the water surface. The frequency increase effect is especially distinct for a microbubble in the range of high surface pressures. Then the modulus of elasticity takes values of about 10^2 m Nm^{-1} and the relative share of the capillary component W (Equation (2)) in the total pressure inside the bubble reaches about 0.4 at the depth up to 0.5 m. The following quantities: $\chi_0 = 136.8$ m Nm^{-1}, $\gamma = 47.5$ m Nm^{-1}, $\alpha = 179.1$, which characterize the Extra 15 oil monolayer on water surface at maximal compression ($\pi = 25$ m Nm^{-1}) have been introduced with the aid of expression (4) to the damping constant B beside quantities which characterize the liquid. Calculations (presented in

graphical form in Fig. 2) were carried out for bubbles with 5 and 50 μm radii (dashed line). Values taken by B for a clean bubble placed in water adjacent to the surface ($P_{i,eq} = 101\,325$ Pa and $T = 293$ K) have been illustrated for comparison by the solid line. The polytropic exponent was chosen equal to 1 and 7/5 for the microbubble and a larger bubble respectively, [11]. A frequency range of the acoustic wave from 10^1 to 10^5 s^{-1} was chosen. Heat conduction causes main energy losses of the gas bubble in this frequency range [5]. Dependencies for clean bubbles indicate isothermal

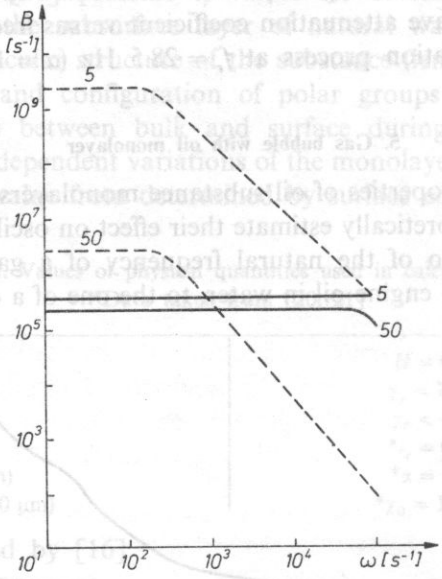

Fig. 2. Damping constant of radial oscillations of a gas bubble: --- with Extra 15 oil monolayer ($\pi = 25$ m Nm^{-1}, $\chi_0 = 136.8$ m Nm^{-1}, $\alpha = 179.1$ s^{-1}) —— with clean surface as a function of angular frequency of acoustic wave's field. Radii of bubbles: 5 and 50 μm

character of the system (curves are horizontal, attenuation constant-maximal); only the larger bubble exhibits distinctly adiabatic character (the curve begins to drop) in the kilohertz range. Dependencies for bubbles with an oil monolayer are of similar character. Hence, a certain analogy between heat dissipation of oscillation energy and energy losses created by reorientation of molecules in the oil monolayer is indicated. If the rearrangement process is quick enough in comparison with the characteristic time (period of acoustic wave) then the horizontal part of curves simulates the "isothermal" bahaviour of the system. The point of inflexion occurs at the frequency corresponding to the relaxation time of the reorientation process and to the transition of the system to "adiabatic" behaviour. At higher frequencies the oil monolayer becomes a less and less effective place of oscillation energy losses and the damping constant drops to zero. A difference of many orders of magnitude of B values between a clean bubble and a coated bubble proves that in the case of

microbubbles and in the acoustic wave's frequency range $\omega < \alpha$ the molecule reorientation process in a monolayer of oil substance decides about the energy loss of oscillations.

6. Acoustic wave scattering and extinction cross-sections

The average radius, resonance frequency and damping constant decide about propagation conditions of an acoustic wave in a bubbly medium. Dependencies for acoustic wave scattering σ_s and extinction σ_e cross-sections, respectively for gas bubbles have the following form [5]

$$\sigma_s = \frac{4\pi \mathbf{R}^2}{\left[\left(\frac{\omega_0}{\omega}\right)^2 - 1\right]^2 + \delta}, \tag{11}$$

$$\sigma_e = \frac{4\pi \mathbf{R}^2 (\delta/\delta_r)}{\left[\left(\frac{\omega_0}{\omega}\right)^2 - 1\right]^2 + \delta}, \tag{12}$$

where $\delta_r = K\mathbf{R}$ – part of the attenuation constant responsible for energy losses due to acoustic re-radiation, $K = 2\pi/\lambda_a$ angular wave number of acoustic wave in liquid, λ_a length of acoustic wave in liquid. Fig. 3 presents dependencies of calculated and normalized to geometric sections, acoustic wave scattering and extinction

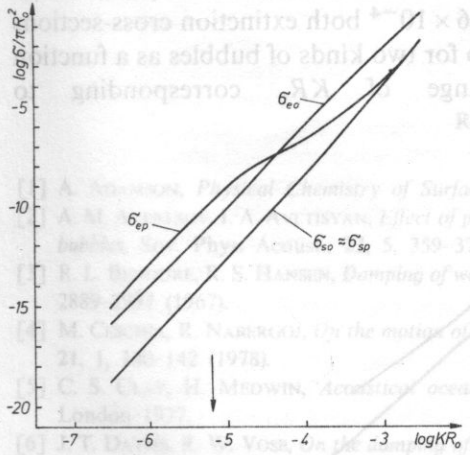

Fig. 3. Normalized acoustic wave scattering σ_s and extinction σ_e cross-sections for a bubble with clean surface "o" and a bubble with an oil monolayer "p" as a function of parameter KR_0 Bubble's radius – 50 μm. The arrow indicates the KR_0 value corresponding to acoustic wave's frequency $\omega = \alpha = 179.1\ s^{-1}$

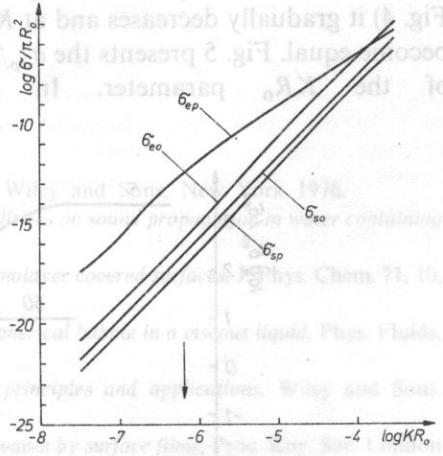

Fig. 4. Normalized acoustic wave scattering σ_s and extinction σ_e cross-sections for a bubble with clean surface "o" and a bubble with an oil monolayer "p" as a function of parameter KR_0. Bubble's radius: 5 μm. The arrow indicates the KR_0 value corresponding to acoustic wave's frequency $\omega = \alpha = 179.1\ s^{-1}$

cross-sections for bubbles with a monolayer "p" and clean ones "o" with the same equilibrium radius $R_0 = 50$ μm, in terms of parameter KR_0. Physical properties of the liquid, properties of the Extra 15 oil monolayer, localization of bubbles and the wave's frequency range are the same as in previous considerations. Curves of scattering cross-sections are characteristic for Rayleigh scattering ($KR_0 \ll 1$) and the scattering function is proportional to $(KR_0)^4$ [5]. The difference between δ_{s0} and σ_{sp} is insignificant. This result from the fact that the monolayer on a larger bubble causes only a slight frequency increase of natural oscillations (about 13%), and a greater value of the damping constant (see Fig. 2) does not effectively influence σ_s in this frequency range. The extinction cross-section of the bubble with oil layer σ_{ep} initially exceeds the analogous quantity for a clean bubble σ_{e0} but from $KR_0 = 2.6 \times 10^{-6}$ (what corresponds to $\omega = \alpha = 179.1$ s^{-1} and is marked with an arrow in Fig. 3) it gradually tends to σ_{e0}. Both cross-sections become equal at $KR_0 = 4.5 \times 10^{-5}$, above it σ_{ep} is even smaller. The $\sigma_{ep}(KR_0)$ dependence corresponds precisely with previously presented interpretation of the physical situation concerning the change of behaviour of a bubble with an adsorbed monolayer. The same quantities as in Fig. 3 but for a microbubble with radius $R_0 = 5$ μm are shown in Fig. 4. In this case the difference between σ_{sp} and σ_{s0} is much layer than before and corresponds with the difference of the target strength TS (TS $= 10 \lg \sigma_s / 4\pi$ [5]) of about 4.5 dB. This is mainly due to a significant resonance frequency increase of the coated microbubble (see Fig. 1) of about 60% in this case. Like before, the many times greater value of the damping constant has an insignificant influence on σ_{sp} in this frequency range. The extinction cross-section σ_{ep} initially exceeds δ_{e0} over 10^3 times. However, for KR_0 exceeding 6×10^{-7} (what corresponds to $\omega = \alpha = 179.1$ s^{-1} and is marked with an arrow in Fig. 4) it gradually decreases and at $KR_0 = 1.6 \times 10^{-4}$ both extinction cross-sections become equal. Fig. 5 presents the σ_{ep}/σ_{0e} ratio for two kinds of bubbles as a function of the KR_0 parameter. In the range of KR_0 corresponding to

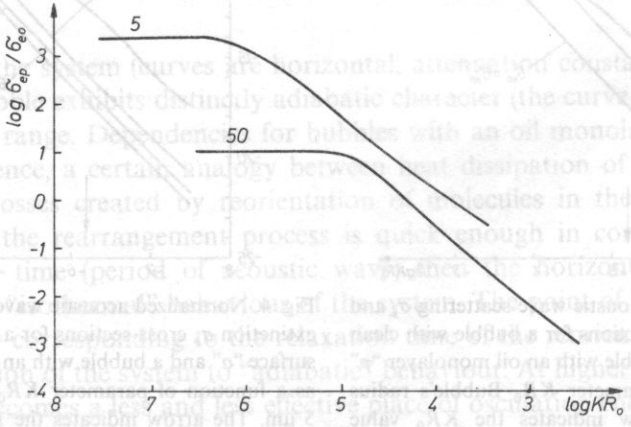

Fig. 5. Ratio of acoustic wave extinction cross-sections for bubbles with monolayer σ_{ep} and clean bubbles σ_{oe} as a function of parameter KR_0. Radii of bubbles: 5 and 50 μm

$\omega < \alpha$, the ratio is equal to 10^3 and 10 for a microbubble and larger bubble, respectively. The ratio decreases when frequency is increased and equals 10^{-1} and 10^{-3} for the highest frequency in the range under consideration. Presented relationships prove that viso-elastic properties of the adsorbed monolayer play a decisive role in the oscillation process, especially for bubbles with radii equal to several μm and localized near the surface.

7. Conclusions

The condensed monolayer of oil substance on the surface of bubbles (with radii 10^{-6} m and less) can cause a significant frequency increase of natural oscillations in comparison with bubbles with clean surfaces, especially when they are placed near the surface of the liquid (up to the depth of 0.5 m). The damping constant of radial oscillations and acoustic wave extinction cross-section by several orders of magnitude exceed analogic quantities for a clean bubble in the wave's frequency range not exceeding the characteristic frequency of the relaxation process of oil substance molecule reorientation in the monolayer. Actual values of acoustic parameters of gas bubbles coated with oil monolayer depend on quantities χ_0 and α, which are directly related to the molecular structure of the monolayer forming substance.

Measurements of parameters characterizing the acoustic wave propagation in the near-surface layers of natural waters, supplemented with data on bubble concentration and, properties of adsorbed monolayers on bubble's surfaces can be a basis for creation of a new effective method for the pollution evaluation of the sea water influenced by surface-active substances, including oil substances.

References

[1] A. ADAMSON, *Physical Chemistry of Surfaces*, John Wiley and Sons, New York 1976.

[2] A. M. AVENESOV, I. A. AVETISYAN, *Effect of polymer additives on sound propagation in water containing bubbles*, Sov. Phys. Acoust., **22**, 5, 359–370 (1976).

[3] R. L. BENDURE, R. S. HANSEN, *Damping of waves on monolayer covered surfaces*, J. Phys. Chem. **71**, 10, 2889–2997 (1967).

[4] M. CESCHIA, R. NABERGOJ, *On the motion of a nearly spherical bubble in a viscous liquid*, Phys. Fluids, **21**, 1, 140–142 (1978).

[5] C. S. CLAY, H. MEDWIN, *Acoustical oceanography, principles and applications*, Wiley and Sons, London 1977.

[6] J. T. DAVIES, R. W. VOSE, *On the damping of capillary waves by surface films*, Proc. Roy. Soc. London A **286**, 218–233 (1965).

[7] P. DE KEYSER, P. JOOS, *Desorption at constant surface pressure from slightly soluble monolayers*, J. Colloid Interface Sci. **91**, 1, 131–137 (1983).

[8] C. DEVIN, *Survey of thermal, radiation and viscous damping of pulsating air bubbles in water*, J. Acoust. Soc. Am., **31**, 5, 1654–1667 (1959).

[9] A. I. ELLER, *Subharmonic response of bubbles to underwater sound*, J. Acoust. Soc. Am., **55**, 4, 871–873 (1974).

[10] A. FRENCESCUTTO, R. NABERGOJ, *Pulsation amplitude threshold for surface waves on oscillating bubbles*, Acustica, **41**, 4, 215–220 (1978).

[11] R. E. GLAZMAN, *Effects of adsorbed films on gas bubble radial oscillations*, J. Acoust. Soc. Am., **74**, 3, 980–986 (1983).

[12] R. E. GLAZMAN, *Damping of bubble oscillations induced by transport of surfactant between the adsorbed film and the bulk solution*, J. Acoust. Soc. Am., **76**, 3, 890–896 (1984).

[13] P. JOOS, G. BLEYS, *Desorption from slightly soluble monolayer*, Colloid Polymer Sci., **261**, 12, 1038–1042 (1983).

[14] W. LAUTERBORN, E. CRAMER, *On the dynamics of acoustic cavitation noise spectra*, Acustica, **49**, 4, 280–287 (1981).

[15] S. P. LEVITSKII, *Dissipation effects with pulsations of gas bubbles in viscoelastic polymeric liquids*, J. Appl. Mech. Theor. Phys., **20**, 1, 74–79 (1979).

[16] E. H. LUCASSEN-REYNDERS, J. LUCASSEN, *Properties of capillary waves*, Advan. Colloid Interface Sci., **2**, 347–395 (1969).

[17] H. MEDWIN, *Acoustical bubble spectrometry at sea*, in: Cavitation and inhomogenities in uderwater acoustics, Proc. 1st International Conference, Springer-Verlag, Berlin 1980, pp. 187–193.

[18] M. S. PLESSET, A. PROSPERETTI, *Thermal effects in the free oscillations of gas bubbles*, Ann. Rev. Fluid Mech., **9**, 2, 145–185 (1977).

[19] S. POGORZELSKI, B. LINDE, A. ŚLIWIŃSKI, *Capillary wave attenuation on a water surface coated with monolayers of oil-derivative substances*, Acoust. Lett., **8**, 1, 5–9 (1984).

[20] S. POGORZELSKI, *Investigations of processes related to the presence of oil-like substances on water surface with the acoustic method*, Ph. D. thesis, Gdańsk University, Gdańsk 1985 (in Polish).

[21] S. POGORZELSKI, *Radial oscillations of gas bubbles coated with a monolayer of surface-active substances in the near-surface sea layer*, Oceanologia, **25**, 53–63 (1988).

[22] A. PROSPERETTI, *Thermal effects and damping mechanisms in the forced radial oscillations of gas bubbles in liquids*, J. Acoust. Soc. Am., **61**, 1, 17–27 (1977).

[23] J. D. ROBB [ed], *Microemulsions*, Plenum, New York 1980.

Received August 21, 1987.

ARCHIVES OF ACOUSTICS
14, 3 4, 293 312 (1989)

A NONINVASIVE ULTRASONIC METHOD FOR VASCULAR INPUT IMPEDANCE DETERMINATION APPLIED IN DIAGNOSIS OF THE CAROTID ARTERIES

TADEUSZ POWAŁOWSKI

Institute of Fundamental Technological Research Polish Academy of Sciences
(00-049 Warszawa, ul. Świętokrzyska 21)

In this study, a new method is presented for diagnosis of the extracranial carotid arteries, based on analysis of the vascular input impedance noninvasively determined in human common carotid arteries. The input impedance calculations were based on simultaneous measurements of the blood pressure and the blood flow using the ultrasonic Doppler and echo methods. In the analysis of the vascular input impedance a four-element model was applied, whose elements represented the vessel resistance (R_0), the peripheral resistance (R_p), the vessel compliance (C) and the inertance (L). The values of these elements were determined by computer simulation of the vascular input impedance using the input impedance of the model. The index of the optimum impedance simulation was the degree of agreement between the blood flow measured in the common carotid artery and the blood flow calculated from the input impedance of the model and the blood pressure. Preliminary clinical investigations were performed in 43 healthy persons and 9 sick patients. The obtained results indicate that the ratio between the vessel resistance (R_0) and the peripheral resistance (R_p) as determined by the proposed measurement method and analysis of the vascular input impedance can be an indicator in identification of stenosis and occlusions of the extracranial carotid arteries. The method described in the study permits identification of stenosis of the internal carotid arteries of $\geqslant 30\%$. The degree of the patency of the carotid arteries in sick persons was determined from X-ray arteriographic examinations, which were confirmed by surgical operations in 8 cases.

Key words: vascular input impedance, carotid arteries, ultrasound.

W pracy przedstawiono nową metodę diagnostyki tętnic szyjnych pozaczaszkowych na podstawie analizy wejściowej impedancji naczyniowej, wyznaczanej nieinwazyjnie, w tętnicach szyjnych wspólnych człowieka. Podstawą do obliczeń wejściowej impedancji był równoczesny pomiar ciśnienia i prędkości objętościowej krwi trzy użyciu ultradźwiękowej metody dopplerowskiej i metody echa. Do analizy wejściowej impedancji naczyniowej zastosowany został model czteroelementowy, którego elementy reprezentują opór naczyniowy (R_0), opór peryferyjny (R_p), podatność (C) i inertancję (L). Wartości tych elementów wyznaczane były na drodze symulacji komputerowej wejściowej impedancji naczyniowej za pomocą impedancji wejściowej modelu. Wskaźnikiem optymalnej symulacji był stopień zgodności pomiędzy prędkością objętościową krwi zmierzoną w tętnicy szyjnej wspólnej a prędkością krwi obliczoną na podstawie wejściowej impedancji modelu i ciśnienia krwi.

Wstępne badania kliniczne przeprowadzono u 43 osób zdrowych i 9 chorych. Uzyskane wyniki wskazują, że wyznaczony na podstawie proponowanej metody pomiaru i analizy wejściowej impedancji naczyniowej stosunek oporu naczyniowego (R_0) do peryferyjnego (R_p) może być wskaźnikiem przy wykrywaniu zwężeń i niedrożności tętnic szyjnych pozaczaszkowych. Opisana w pracy metoda pozwala na wykrywanie zwężeń tętnic szyjnych wewnętrznych $\geqslant 30\%$. Stopień drożności tętnic szyjnych u osób chorych określany był na podstawie badań arteriograficznych, które w 8 przypadkach potwierdzone zostały operacyjnie.

1. Introduction

Diagnosis of the carotid arteries is important in prevention of the brain stroke. Apart from malignant tumors and heart strokes, this serious disease is, statistically, the third cause of death. The main reason of the brain stroke is ischemia of the brain caused by atherosclerotic changes in the brain-supplying arteries, including the carotid ones.

At the present moment, the basic method in noninvasive diagnosis of the carotid arteries is the ultrasonic Doppler method. It is used to identify stenosis and occlusions of the arteries [1, 6, 7, 13, 14, 15, 22, 30, 32, 33, 34, 36, 38, 39]. The evaluation of the patency of the examined vessel is based on analysis of blood velocity in the cross-section of the vessel determined by Doppler frequency measurements [13, 15, 30, 38], or on analysis of the Doppler signal spectrum [7, 14, 16, 34, 36, 39]. However, the results of clinical examinations show that the ultrasonic Doppler method does not always permit unambiguous evaluation of pathological changes in the carotid arteries. The reason for this is very complex form of the blood flow at the point of stenosis in the vessel and beyond this point, whose evaluation from Doppler frequency measurement is little accurate. Attempts to analyze the blood velocity measured by the Doppler method before the point of stenosis [30], also failed to give the expected results [39].

An attempt at a new approach to diagnosis of the carotid arteries is the method presented in this study based on analysis of the vascular input impedance determined noninvasively in the common carotid arteries. These arteries are important paths of blood supply to the brain. Atherosclerotic changes in the bifurcation of these arteries, at the inlet of the internal carotid arteries, are the main cause of the brain stroke.

2. Method of the noninvasive measurement of the vascular input impedance in the common carotid arteries

The vascular impedance is a function of the hemodynamic properties of the vascular system at the input of which it is measured. It is determined in the frequency domain and defined as the ratio between the blood pressure and the blood flow for n succesive harmonics of the heart beat frequency according to the dependence

$$Z(n\omega_0) = p(n\omega_0)/Q(n\omega_0) = Z_{\mathrm{mod}_n} e^{j f_n} \tag{1}$$

where $\omega_0 = 2\pi f_0$; f_0 is the frequency of the heart; $n = 0, 1, 2, \ldots,$; $Z(n\omega_0)$ is the vascular input impendance, Z_{mod_n} and φ_n are the modulus and phase; $p(n\omega_0)$ and $Q(n\omega_o)$ are the spectra of the signals of the blood pressure and the blood flow.

For $n = 0$, the vascular input impedance expresses the ratio between the meain pressure p_{med} and the mean blood flow Q_{med}. Assuming that the value of the pressure at the end of the vena cava is much smaller than the pressure in the arteries in which the measurement takes place, for $n = 0$, the input vascular impendance represents the mean resistance of the examined fragment of the vascular system.

In 1956, RANDALL and STACY [31] were the first to propose the concept of the measurement of the hydraulic impedance in blood vessels called the vascular input impedance. So far, the method of investigating the properties of the vascular system by the measurement of the vascular input impedance has not been widely applied in medical diagnosis. The reason for this was the inability to measure noninvasively the instantaneous blood pressure, which is, a part from the blood volume velocity, the basic parameter in the determination of the vascular input impedance. Investigations of the vascular input impedance performed in many centres in the world are based on invasive measurement made mainly on animals. They apply above all to such vessels as the aorta [4, 10, 17, 18, 37], the femoral artery [8, 19] and the pulmonary artery [2].

The method of the noninvasive measurement of the vascular input impedance presented in this study is based on previous investigations by the author [23, 24, 25, 26, 27, 28, 29]. In this method the instantaneous course of the blood pressure is determined from ultrasonic measurement of the instantaneous vessel diameter. It is assumed here that between the vessel diameter and the blood pressure there is the logarithmic dependence of the form

$$S(p) = (1/\gamma)\ln(p/p_0), \quad \text{for } p > p_0 > 0, \tag{2}$$

where p is the blood pressure, S is the cross-section area of the vessel, and p_0 and γ are constant coefficients.

The coefficients p_0 and γ present in formula (2) can be determined from measurements of the systolic pressure p_s and the diastolic pressure p_d and the vessel cross-sections S_s and S_d for both of the pressures. Putting the two pairs of values (S_s, p_s) and (S_d, p_d) into expression (2), it is obtained that

$$p_0 = \frac{p_d}{\exp\left[\dfrac{S_d}{S_s - S_d}\ln\dfrac{p_s}{p_d}\right]}, \tag{3a}$$

$$\gamma = \frac{1}{S_s - S_d}\ln\frac{p_s}{p_d}. \tag{3b}$$

The examination carried out by the author in the common carotid arteries in healthy and sick persons aged between 9 and 64 showed that the value of the coefficient p_0 is positive and smaller than 15 mm Hg [27, 29]. The logarithmic

function described by formula 2 is applied only to the pressure range between the systolic and diastolic pressures whose physiological values are greater than 50 mm Hg. For this range the condition $p > p_0 > 0$ shown in formula (2) is met. Putting the values of p_0 and γ described by formulae (3 a and 3 b) into formula (2), it is obtained that

$$S(p) = S_d\left[1+\frac{(S_s-S_d)\ln(p/p_d)}{S_d\ln(p_s/p_d)}\right]. \tag{4}$$

It should be pointed out that the logarithmic function $S(p)$ discussed above, applies to the so-called static conditions where the blood pressure and the artery cross-section take values stationary in time. For time variable (dynamic loads), the vessel walls can show viscoelastic properties. Research by many authors [11, 20] showed that for large arterial vessels the phase shift between the blood pressure and a change in the vessel radius does not exceed 10°, permitting the viscoelastic effect to be neglected in a simplified model.

The assumptions presented here for the mutual relations between the artery cross-section and the blood pressure are the basis for the concept of noninvasive determination of the course of the blood pressure $p(t)$ in the common carotid artery from the measurement of the instantaneous diameter $d(t)$ of this artery by the ultrasonic echo method. For this purpose, from formula (4), the following dependence is applied

$$p(t) = p_d\exp\left(\frac{d^2(t)-d^2_{\min}}{d^2_{\max}-d^2_{\min}}\ln\left(\frac{p_s}{p_d}\right)\right), \tag{5}$$

where $d_{\max}$ and $d_{\min}$ are the maximum and minimum artery diameters for the systolic pressure p_s and the diastolic one p_d.

The blood pressure course $p(t)$ determined in this way in the common carotid artery is calibrated with the systolic pressure p_s and the diastolic pressure p_d, which are identifield by using a cuff method in the brachial artery, with the patient in supine position.

In assuming for the common carotid artery the value of the systolic and diastolic pressures determined in the brachial artery, account was, e.g., taken of the results of the investigations carried out in 1982 by Borow [3]. They were concerned with the comparative evaluation between the blood pressure in the brachial artery determined noninvasively by the oscillometric method and the blood pressure found using a catheter in the ascending aorta. Performed on a group of 30 persons, aged between 30 and 83, these studies showed that, for the patients, in supine position, the differences in the values of the systolic and diastolic pressures between the aorta and the brachial artery were respectively 1% and 1.7% mean values, and could, therefore, be neglected in practice. Since the common carotid artery has a diameter close to that of the brachial one, it can be believed that the assumed method of the evaluation of the systolic and diastolic pressures in the common carotid artery from measurements of these pressures in the brachial artery should not introduce any significant error.

The necessary condition for the present method of the determination of the blood pressure course is the full patency of the arterial vessels between the point of measurement of the diameter of the common carotid artery and the point of measurement of the blood pressure in the brachial artery. The presence of stenosis means that the blood pressures from the two measurements points are different.

Parallel to the measurements of the instantaneous artery diameter, in the same vessel cross-section, the instantaneous blood velocity $v_s(t)$ is measured by the noninvasive continuous wave ultrasonic Doppler method. Information on the instantaneous artery diameter, used previously to reconstruct the blood pressure course, also serves for determining the course of the instantaneous blood flow $Q(t)$, according to the dependence

$$Q(t) = v_s(t)\frac{\pi d^2(t)}{4}, \tag{6}$$

where $v_s(t)$ is the blood velocity averaged over the vessel cross-section.

The simultaneous measurement of the blood pressure and the blood flow, made in the above way, in the same cross-section of the common carotid artery, is the basis for the noninvasive determination of the vascular input impedance in this artery, from formula (2).

3. Measurement system

A schematic diagram of the measurement system is shown in Fig. 1. It was constructed by the author [27, 28] for noninvasive investigations of the vascular input impedance in the common carotid arteries. This system includes two ultrasonic probes $P1$ and $P2$ set at an angle of 30° to each other. The probe $P2$ is connected with a bi-directional continuous wave Doppler flowmeter *cwDF*, meant for blood velocity measurements. The probe $P1$, set perpendicularly to the blood vessel, is connected with the transmitter T and the receiver R of the pulsed system meant for the measurement of the instantaneous vessel diameter by the ultrasonic echo method. To gain large measurement resolution, the ultrasonic beams transmitted by the probes $P1$ and $P2$ are focused. The width of the ultrasonic beam (defined for the $-$ 20 dB acoustic pressure level relative to the maximum value on the beam axis) is 1 mm at the focus of the probe $P1$, and 2.5 mm at that of the probe $P2$. For both probes, the ultrasonic wave focusing range varies between 1 and 3 cm. The probe $P1$ and $P2$ transmit ultrasonic waves at two different frequencies. The frequency of the impulse wave transmitted by the probe $P1$ is 6.75 MHz, and the frequency of the continuous wave transmitted by the probe $P2$ is 4.5 MHz.

Information on the instantaneous vessel diameter is gained from ultrasonic measurements of the instantaneous distances between the probe $P1$ and the internal surfaces of the two vessel walls. The measurement of the internal diameter of the blood vessel requires high resolution of the ultrasonic pulsed system. For this

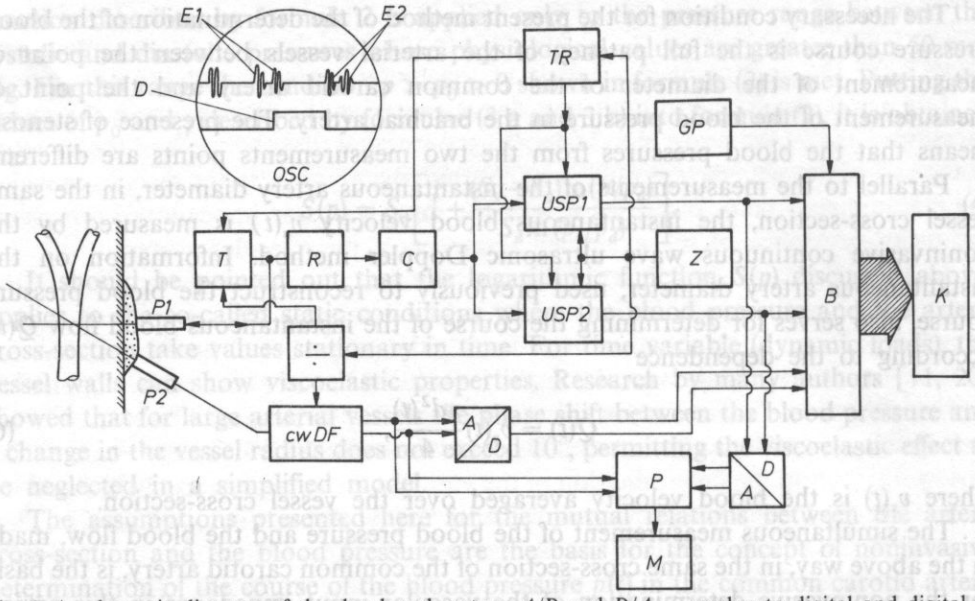

Fig. 1. A schematic diagram of the developed system: *A/D* and *D/A* – analog to digital and digital to analog converters, *B* – buffer, *C* – comparator, *cwDF* – bi-directional continuous wave Doppler flowmeter, *GP* – oscillator of impulse for copying data into the computer, *K* – computer, *M* – monitor, *OSC* – oscilloscope tube, *P* – recorder, *P*1 and *P*2 – ultrasonic probes, *T* – impulse transmitter, *R* – impulse receiver, *TR* – trigger impulse oscillator, *USP*1 and *USP*2 – digital systems for tracking and measuring the position of echos, *Z* – clock impulse oscillator

purpose, apart from the previously mentioned focusing of the probe *P*1, a narrow transmitted impulse was used in the measurements, with the duration of 0.3 μs (2 cycles of a transmitted wave) corresponding to its length in tissue equal to 0.45 mm. As a result this made it possible to obtain single echos from the external and internal surfaces of the walls of the investigated common carotid arteries. The repetition frequency of the transmitted ultrasonic wave impulses was 18 kHz. This permits the measurement range to reach 4.2 cm into the patient's body.

The echos obtained in the course of the measurement at the output of the receiver *R* are transformed into rectangular signals by the level comparator *C*. The echos thus formed are fed to two digital systems (*USP*1 and *USP*2), using which it is possible to track the displacements of chosen slopes of echos detected from the front and back walls of the blood vessel [12, 27, 28]. In these systems for every work cycle of the impulse transmitter T the time is digitally measured between the on set of the transmitted pulse and the tracked slopes of the echos from both walls of the vessel. This provides the basis for calculation, by the computer *K*, of the instantaneous distances u_1 and u_2 between the ultrasonic probe and the blood vessel surface. For the successive *n*-th measurement cycle, these distances are

$$u_1 = \frac{cN_n}{2f_z}, \quad u_2 = \frac{cM_n}{2f_z} \tag{7}$$

where N_n and M_n are the numbers of clock impulses counted in the n-th cycle of the impulse transmitter by the two channels *USP2* and *USP2* of the measurement system; f_z is the clock frequency and c is the ultrasonic wave velocity in the investigated medium.

From dependence (7), there follows the accuracy of representation of displacements of the vessel walls, which for the clock frequency used in the measurements, $f_z = 27$ MHz, was $3 \cdot 10^{-5}$ m.

11-bit data obtained at the outputs of *USP1* and *USP2* are fed to the output buffer *B* of the device, along with two 8-bit data on the frequencies f_{zc} of the Doppler signals. These frequencies are measured by the ultrasonic Doppler flowmeter cwDF for blood velocity in two directions. The frequency f_{zc} is determined by the method of "zero crossings" and is proportional to mean blood velocity v_s in the vessel cross-section, from the dependence [9, 21, 27]

$$v_s = a \frac{cf_{zc}}{2f_n \cos\theta}, \tag{8}$$

where: f_n is the frequency of the ultrasonic wave transmitted by the probe *P2* of the flowmeter *cwDF*, c is the ultrasonic wave velocity in the studied medium, θ is the angle between the direction of the transmitted and received ultrasonic wave and that of the blood flow, and a is the proportionality coefficient [9, 21, 27].

In calculating the blood velocity from the Doppler frequency f_{zc} measured by the flowmeter, it was assumed that the angle θ between the direction of the transmitted and received ultrasonic wave and the axis of the blood vessel was 60°. This resulted from the constant angle of 30° between the probes and from the assumption that the probe *P1* was set perpendicularly to the vessel axis. The gaining of the maximum amplitude of the echos from both vessel walls was assumed to indicate the perpendicular position of the probe *P1* relative to the blood vessel. These echos can be observed in the course of measurements, on the oscilloscope tube *OSC* of the system. At the same time, on the oscilloscope screen the measured diameter of the studied vessel is shown in the form of the gate *D*.

The digital data from the buffer *B* of the measurement system were fed to a MERA-60 computer (equivalent to PDP-11) and written into its memory. Along with them, the values p of the systolic and diastolic pressures, measured by using a cuff method in the brachial artery for the patient's supine position, were fed to the computer. The data set thus formed provided the basis for the determination of the instantaneous blood volume velocity $Q(t)$ and of the blood pressure $p(t)$, according to the previously given dependencies (5) and (6).

The input vessel impedance was measured from the discrete Fourier transforms of the time courses of the blood flow and blood pressure for a cardiac cycle. 64 discrete values of the blood pressure and flow, occurring for one cardiac cycle, were used in the calculations. The sampling frequency was defined by using the oscillator *GP* of the impulses for copying data from the output of the measurement system into

the computer. In the calculations, the fast Fourier transform, FFT, algorithm was applied [5]. In its final form, the vascular input impedance is represented by the modulus Z_{mod_n} and the phase φ_n (see Fig. 2).

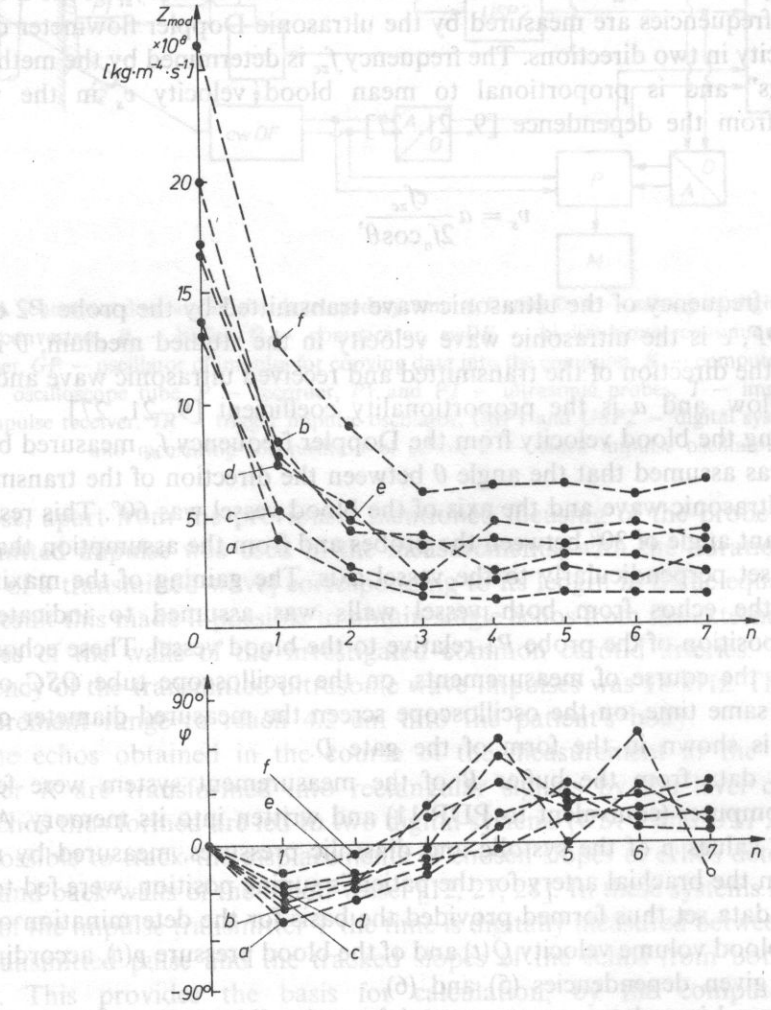

Fig. 2. The modulus Z_{mod} and phase φ of the input impedance determined noninvasively in the common carotid artery in healthy persons aged: a) 20, b) 30, c) 43, d) 52, e) 60 and in 59 year old patient in whom occlusion of the internal carotid artery was found by the X-ray arteriographic method on the studied side (f).

4. Analysis of the vascular input impedance determined noninvasively in the common carotid arteries in healthy and sick persons

The previously described method and equipment were applied is noninvasive measurements of the vascular input impedance in the common carotid arteries. The investigations were carried out, for two groups of persons. The first group (38) persons, aged between 9 and 64, did not show any pathological changes in the carotid arteries. The second group (9 persons) included patients aged between 53 and 62, in whom, using X-ray arteriography, atherosclerotic changes were found in the area of the extracranial carotid arteries in the form of stenosis or occlusions of these arteries. In 8 cases the results of the X-ray examinations were confirmed by surgical operations[1].

In all the examined persons, the measurements were performed at a distance of 2–3 cm before the bifurcation of the common carotid artery.

As an example the courses of the vascular input impedance determined for 5 healthy persons aged between 20 and 60 and for a 59-year-old patient with occlusion of the internal artery are shown in Fig. 2.

The results of the investigations of the vascular input impedance obtained for healthy and sick persons indicate the characteristic course of the modulus and phase for the first few **n** harmonics of the heart, beat frequency. The value of the modulus shows a small minimum between the second and fifth harmonics, which is accompanied by a change in the phase from negative to positive. This form of the vascular input impedance suggests that its course is affected by the compliance properties the (negative phase) and the inertia properties the (positive phase) of the studied vascular system. In older persons, in particular those with atherosclerotic changes in the area of the examined arteries, less negative phase was found compared with that for young healthy persons.

The modulus of the vascular input impedance for $n = 0$ represents the mean resistance of the vascular system supplied by the common carotid artery. This resistance was determined in kg m^{-4} s^{-1}, (u.r.).

The value of the resistance determined for the examined group of healthy persons aged between 19 and 64 fell in the interval $11.6 \cdot 10^8 - 22.9 \cdot 10^8$ u.r., whereas its mean value was $(15.8 \pm 2.6)\ 10^8$ u.r. A distinct increase in the resistance was observed in the sick in whom the critical (90%) stenosis of the internal carotid artery (1 person) and occlusion of the internal carotid artery (3 persons) were found. For these patients the resistance varied between $25.8 \cdot 10^8$ and $27.3 \cdot 10^8$ u.r., and, in one case, was $40.2 \cdot 10^8$ u.r. An arteriographic examination for this person showed the occlusion of the internal carotid artery and a stenosis in the initial section of the external carotid artery.

[1] The examinations on the group of sick persons were carried out in cooperation with the Department of General and Thoratic Surgery of the Institute of Surgery, Medical Academy of Warsaw headed by Prof. dr M. SZOSTEK.

For the others in the group of sick persons, in whom the stenosis of the internal carotid arteries, determined by the X-ray arteriographic method, were found to be vary between 30% and 70%, the values of the resistance fall in the upper range of the value internal for healthy persons, varying between $17.9 \cdot 10^8$ and $21.9 \cdot 10^8$ u.r.

Assuming the linearity of the studied vascular system, a four-element model was used in further analysis of the vascular input impedance. The electric equivalent circuit of the model is shown in Fig. 3 [24, 27].

This model includes the elements representing the inertance L, the vessel compliance C, the vessel resistance R_0 and the peripheral resistance R_p. These elements were determined through computer simulation of the input vascular impedance by means of the impedance $Z_M(\omega)$ of the model

$$Z_M(\omega) = R_0 + j\omega L + R_p/(1 + j\omega C R_p) \tag{9}$$

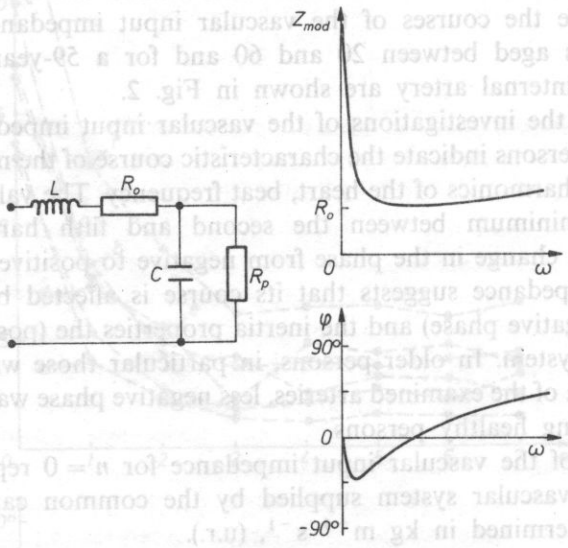

Fig. 3. The electric circuit equivalent to the model of the vascular system, and the modulus Z_{mod} and phase φ of its input impedance

In the simulation of the vascular input impedance, the following parameters were taken into account:

- the value of the modulus Z_{mod_0} of the impedance for $n = 0$,
- the real value RE_1 and the imaginary value IM_1 of the impedance for the first harmonic, and
- the frequency f_m for which the impedance phase changes its sign from negative to positive.

The frequency f_m was matched. In a general case, it cannot be determined from the course of the discrete values of the input vascular impedance. Only the internal of values where it falls, is known. The limits of this interval are defined by two

frequencies corresponding to two adjacent harmonics between which the impedance phase changes its sign for the first time (see Fig. 2).

The assumption of the first harmonic of the vascular input impedance as the basis of the simulation resulted from the fact that its value is the quotient of two components with the greatest amplitude in the spectra of the signals of the blood pressure and flow rate, therefore, it is least dependent on the noise of the measurement device.

From the above-mentioned parameters, the elements of the model were determined by solving for this purpose the following system of equations

$$\begin{aligned} R_0 + R_p &= Z_{\mathrm{mod}_0}, \\ R_0 + R_p/[1+(2\pi f_0 C R_p)^2] &= RE_1, \\ 2\pi f_0 L - 2\pi f_0 C R_p^2/[1+(2\pi f_0 C R_p)^2] &= IM_1, \\ L &= C R_p^2/[1+(2\pi f_m C R_p)^2], \end{aligned} \tag{10}$$

where L, C, R_0 and R_p are the elements of the model, f_0 is the frequency of the heart rate and f_m is the frequency for which the impedance phase changes its sign.

It follows from the above system of equations that the values of the elements L,

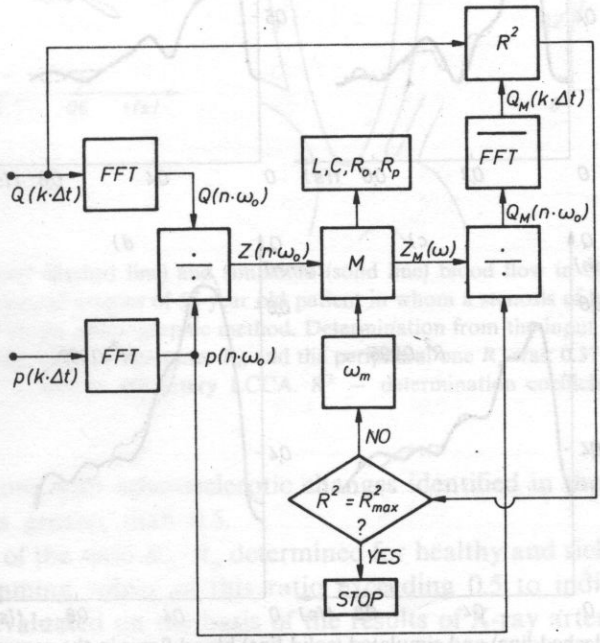

Fig. 4. The flow chart of operations in the computer analysis of the input impedance: M – model of the vascular input impedance by means of the impedance $Z_M(\omega)$ of the four-element equivalent model, FFT and $\overline{\mathrm{FFT}}$ – the algorithms of the fast Fourier transform and inverse fast Fourier transform, R^2 – the coefficient of agreement between the measured Q and simulated Q_M blood flows described by formula (11)

C, R_0 and R_p depend on f_m. This frequency is so matched as to ensure the best simulation of the input vascular impedance. The optimum simulation was indicated by the degree of agreement between the measured course of the blood flow Q and the course of the flow Q_M determined from the measured pressure and from impedance of the model $Z_M(\omega)$. The agreement between the two courses of the blood flow was compared by means of the determination coefficient R^2 given by the formula [35]:

$$R^2 = 1 - \frac{\sum_k (\tilde{y}_k - y_k)^2}{\sum_k (\bar{y} - y_k)^2}, \tag{11}$$

where y_k is the value of y measured experimentally for the independent variable

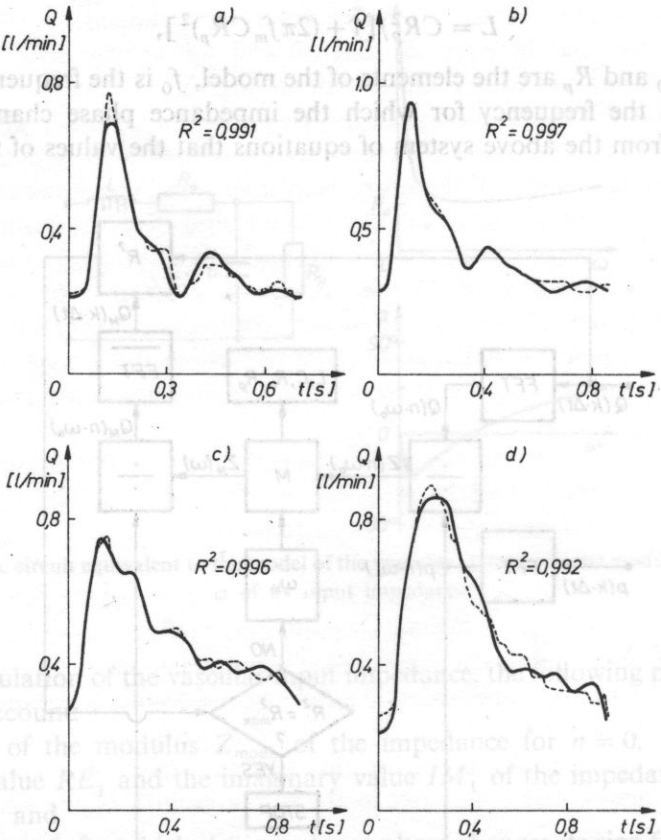

Fig. 5. The measured (dashed line) and simulated (solid line) blood flows in the common carotid artery in healthy persons aged: a) 12, b) 30, c) 52, d) 64. The simulated flow was determined from the course of the blood pressure and the input impedance of the model (see Fig. 3.). The value of the determination coefficient R^2 applied in evaluating the agreement between the simulated and measured courses (see formula 11) is marked in this figure

x equal to x_k, y is the arithmetic mean of N measurements, and $y_k = f(x_k)$, if $f(x)$ denotes the approximating function applied.

The flow chart of the operations performed in the implementation of the above computer simulation of the vascular input impedance is shown in Fig. 4.

For all the investigated cases, the value of R^2 was close to unity, falling in the interval from 0.988 to 0.998, meaning an almost ideal agreement between the compared flow courses (see Figs. 5 and 6). The elements of the model thus determined were the basis for comparative examinations of healthy and sick persons (Tables 1 and 2). It was found that the parameter which distinguished best between the sick and the healthy was the ratio between the vascular resistance R_0 and the peripheral ratio R_p. For the healthy the ratio R_0/R_p was less than 0.5, whereas for

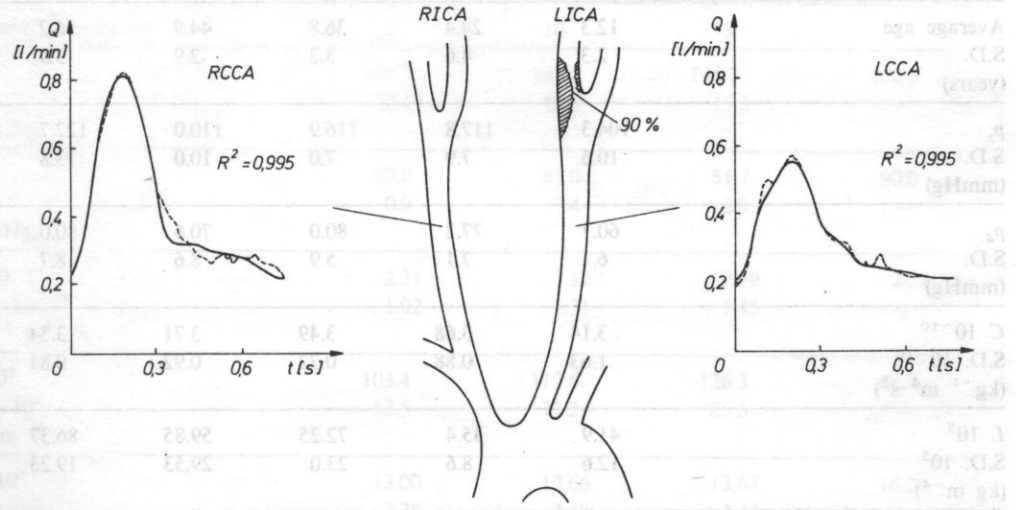

Fig. 6. The measured (dashed line) and simulated (solid line) blood flow in the left (LCCA) and right (RCCA) common carotid arteries of 58-year old patient in whom a stenosis of left internal carotid artery (LICA) was found by the arteriographic method. Determination from the input impedance of the model, the ratio between the vascular resistance R_0 and the peripheral one R_p was: 0.37 in the artery RCCA and 1.03 in the artery LCCA. R^2 – determination coefficient

most sick persons with atherosclerotic changes identified in the area of the carotid arteries, it was greater than 0.5.

The values of the ratio R_0/R_p determined for healthy and sick persons are shown in Fig. 7. Assuming values of this ratio exceeding 0.5 to indicate pathology this criterion was evaluated on the basis of the results of X-ray arteriographic examinations. It is shown in Table 3. It follows from the table that for the total number of 17 examined arteries in the sick, only in two cases a false, negative result was obtained, in terms of the X-ray arteriographic diagnosis. These cases were those of small stenosis of the internal carotid artery.

Table 1. The values of the elements L, C, R_p and R_0 of the equivalent model of the vascular system, determined from the vascular input impedance in the common carotid arteries for a group of healthy persons; p_s and p_d are the systolic and diastolic pressures in the brachial artery

Age group (years)	9–16	19–30	32–40	41–50	52–64
No. of persons	7	9	8	8	11
Average age	12.3	24.4	36.8	44.9	56.2
S.D. (years)	2.3	4.6	3.2	2.9	3.9
p_s	104.3	117.8	116.9	110.0	122.7
S.D. (mmHg)	10.6	7.9	7.0	10.0	13.8
p_d	60.7	77.2	80.0	70.6	80.0
S.D. (mmHg)	6.1	7.1	5.9	8.6	8.7
$C\ 10^{-10}$	3.14	3.68	3.49	3.71	3.34
S.D. 10^{-10} ($kg^{-1}\ m^4\ s^2$)	1.63	0.88	0.72	0.92	0.81
$L\ 10^5$	41.9	35.4	72.25	59.85	86.37
S.D. 10^5 ($kg\ m^{-4}$)	12.6	8.6	23.0	29.53	19.23
$R_p\ 10^8$	15.51	13.38	12.25	10.35	13.53
S.D. 10^8 ($kg\ m^{-4}\ s^{-1}$)	2.06	2.14	1.73	1.43	2.11
$R_0\ 10^8$	3.72	2.55	3.14	3.16	4.09
S.D. 10^8 ($kg\ m^{-4}\ s^{-1}$)	0.68	0.73	0.99	0.68	1.28
R_0/R_p	0.26	0.20	0.26	0.31	0.30
S.D.	0.06	0.06	0.09	0.07	0.08

S.D. – standard deviation

Table 2. The values of the elements L, C, R_p and R_0 of the equivalent model of the vascular system determined from the vascular input impedance in the common carotid arteries in sick patients; p_s and p_d are the systolic and diastolic pressures in the brachial artery ICA-internal carotid artery, ECA-external carotid artery

Degree of stenosis	Without stenosis	Stenosis of ICA 30–80%	Stenosis of ICA 90% (1) occlusion of ICA (2)	Occlusion of ICA and stenosis of ECA
Number of arteries	3	10	3	1
p_s	141.7	148.5	146.7	150.0
S.D. (mmHg)	16.1	19.2	15.3	–
p_d	80.0	81.0	81.7	90.0
S.D. (mmHg)	0.0	7.4	2.9	–
$C\ 10^{-10}$	2.21	3.12	2.29	2.27
S.D. 10^{-10} ($kg^{-1}\ m^4\ s^2$)	1.02	1.31	1.45	–
$L\ 10^5$	103.4	117.6	126.3	48.7
S.D. 10^5 ($kg\ m^{-4}$)	53.5	71.2	85.6	–
$R_p\ 10^8$	13.00	12.66	13.67	16.08
S.D. 10^8 ($kg\ m^{-4}\ s^{-1}$)	3.38	2.48	2.43	–
$R_0\ 10^8$	4.90	7.06	12.87	24.14
S.D. 10^8 ($kg\ m^{-4}\ s^{-1}$)	1.61	2.09	2.17	–
R_0/R_p	0.39	0.58	0.98	1.50
S.D.	0.08	0.17	0.32	–

S.D. – standard deviation

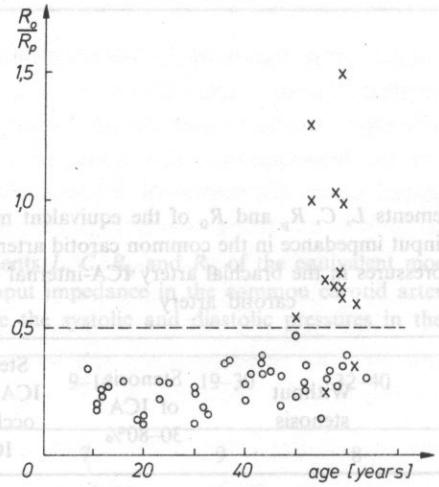

Fig. 7. The ratio between the vascular resistance R_0 and the peripheral one R_p determined from the vascular input impedance in the common carotid arteries in healthy (o) and sick (×) persons with atherosclerotic changes in the extracranial carotid arteries (see Table 3). The age of the examined persons is marked on the horizontal axis

Table 3. Evaluation of detectability of pathological changes in the carotid arteries by means of the resistance ratio compared with the X-ray arteriography results

Arteriography	Vascular input impedance		
	$R_0/R_p > 0.5$		$R_0/R_p < 0.5$
	Number of cases		
ICA occlusion	3	3	–
ICA stenosis >75%	2	2	–
ICA stenosis 50%–75%	1	1	–
ICA i CCA stenosis 40%–50%	1	1	–
ICA stenosis 30%–50%	4	3	1
ICA stenosis 30%	3	2	1
no stenosis	3	–	3
Number of arteries	17	12 true positive	3 true negative 2 false negative

ICA – internal carotid artery
CCA – external carotid artery

5. Conclusions

The method and system presented in the study for the noninvasive determination of the input impedance in the common carotid artery is a proposed of a new approach to diagnosis of human circulation system. The results of the investigations permit the following conclusions to be drawn:

a. The investigations of the vascular input impedance in the carotid artery carried out on a group of 38 healthy persons aged between 9 and 64 and a group of sick patients (17 arteries) aged between 53 and 62. indicate a characteristic course of the values of the modulus and the phase of the vascular impedance for the first 6-7 harmonics of the heart beat frequency (see Fig. 2). The value of the modulus show a slight minimum between the second and fifth harmonics, accompanied by a change in the sign of the phase from negative to positive. This form of the dependence suggests the influence of the compliance properties (the negative phase) and the inertia properties (the positive phase) in the vascular system supplied with blood by the common carotid artery.

b. Using a simple four-element equivalent model of the vascular system, it is possible to simulate the course of the vascular input impedance determined noninvasively in the common carotid artery. This is indicated by large agreement obtained for all examined persons between the measured blood flow and that determined from the impedance of the model and the blood pressure. The determination coefficient R^2 determining this agreement, fell within the interval between 0.988 and 0.998.

c. The method of analysis of the vascular input impedance elaborated by the author permits the determination of the element of the equivalent model of vascular system. These elements represent the four basic hemodynamics parameters, namely the compliance of the vascular system C the inertance L, the vessel resistance R_0 and the peripheral resistance R_p.

d. The total mean resistance of the vascular system (R_0+R_p), determined in the common carotid artery for the examined group of healthy persons aged between 19 and 64, fell in the internal $11.6 \cdot 10^8$–$22.9 \cdot 10^8$ kg m^{-4} s^{-1}. A distinct increase in the resistance was observed in the patients in whom a critical (90%) stenosis in the internal carotid artery (1 persons) or occlusion of the internal carotid artery (3 persons) were found. For these sick persons, the resistance varied between $25.8 \cdot 10^8$ and $27.3 \cdot 10^8$ kg m^{-4} s^{-1}, and, in one case, it was $40.2 \cdot 10^8$ kg m^{-4} s^{-1}. In this person, an X-ray arteriographic examination showed occlusion of the internal carotid artery and a stenosis in the initial section of the external carotid artery. For the others in the sick group, in whom, using the arteriographic method, stenosis of the interval carotid arteries were found to vary between 30% and 70%, the values of the resistance fell in the upper range of the values for the healthy. varying between $17.9 \cdot 10^8$ and $21.9 \cdot 10^8$ kg m^{-4} s^{-1}.

e. Atherosclerotic changes in the extra-cranial carotid arteries are identified from the input impedance and the adopted model of the vascular system by the ratio

between the vessel resistance R_0 and the peripheral resistance R_p. This ratio increases if stenosis or occlusions of the carotid arteries are present. Assumed by the author to indicate pathology, the ratio $R_0/R_p > 0.5$ seems to be a sufficiently sensitive criterion for identifying stenosis or occlusions. It permits the detection of 30% of stenosis of the internal carotid arteries (see Table 3).

f. The preliminary results of clinical investigations indicate that the determined resistance ratio R_0/R_p tends to increase as a function of the degree of stenosis the carotid arteries beyond the point of measurement of the vascular input impedance (see Table 2).

g. The method for detecting stenosis and occlusion of the extracranial carotid arteries proposed in this study has a few advantages over the currently used ultrasonic methods. Firstly, the measurement is performed before the point of stenosis where the blood flow is not perturbed. Secondly, the measurement is taken in the common carotid artery which is easily accessible to ultrasonic examinations. The blood flow rate measurement carried out so far in this artery does not detect so small stenosis as those in the case of the vascular input impedance. Analysis of blood flow changes based on the pulsatility index permits only the detection of critical stenosis of more than 80% [30, 33, 39].

References

[1] R. AASLID, K. F. LINDEGAARD, *Cerebral hemodynamics*, in: Transcranial Doppler sonography, [Ed.] R., Aaslid Springer Verlag, Wien and New York 1986.

[2] D. BERGEL, D. SCHULTZ, *Arterial elasticity and fluid dynamics*, Progress in biophysics and molecular biology, Pergamon Press, New York 1971.

[3] K. M. BOROW, J. W. NEWBURGER, *Noninvasive estimation of central aortic pressure using the oscillometric method for analyzing systemic artery pulsatile blood flow: Comparative study of indirect systolic, diastolic and mean brachial artery pressure with simultaneous direct ascending aortic pressure measurements*, Amer. Heart J., **103**, 879–886 (1982).

[4] Y. LE BRAS, G. FONTENIER, J. P. MERILLON, *Methods for in vivo determinations of the impedance spectrum and reflection coefficients at the human aorta input calculation of the characteristic impedance*, Med. and Biol. Eng. and Comput., **24**, 329–332 (1986).

[5] E. O. BRIGHAN, *The Fast Fourier Transform*, Prentice Hall, Inc., Englewood Cliffs, New Jersey 1974.

[6] G. R. CURRY, D.N. WHITE, *Color coded ultrasonic differentional velocity scanner (Echoflow)*, Ultrasound in Medicine and Biology, **4**, 27–35 (1978).

[7]Y. DOUVILLE, K. W. JOHNSTON, M. KASSAN, *Determination of the hemodynamic factors which influence the carotid Doppler spectral broadening*, Ultrasound in Medicine and Biology, **11**, 3, 417–423 (1985).

[8] D. J. FARRAR, G. S. MALINDZAK, G. JOHNSON, *Dynticmic pressure-flow diagrams and impedance in experimental arterial stenosis and in stenotic atherosclerosis*, Annals of Biomedical Engineering, **6**, 413–428 (1978).

[9] L. FILIPCZYŃSKI, R. HERCZYŃSKI, A. NOWICKI, T. POWAŁOWSKI, *Przepływy krwi — hemodynamika i ultradźwiękowe dopplerowski metody pomiarowe*, PWN, Warszawa 1980.

[10] J. P. GIOLNA, N. WESTERHOF, *Aortic input impedance in normal man: Relationship to pressure wave forms*, Circulation, **62**, 1 (1980).

[11] B. S. GOW, M. G. TAYLOR, *Measurements of viscoelastic properties of arteries in the living dog*, Circulation Research, **23** (1968).

[12] D. H. GROVES, T. POWAŁOWSKI, D. H. WHITE, *A digital technique for tracking moving interfaces*, Ultrasound in Med. and Biol., **8**, 2, 185–190 (1982).

[13] M. S. KASSAM, R. S. C. COBBOLD, K. W. JOHNSTON and C. M. GRAHAM, *Method for estimating the Doppler mean velocity waveform*, Ultrasound in Medicine and Biology, **8**, 537–544 (1982).

[14] Y. LANGLOIS, G. O. REODERER, A. CHAN, D. J. PHILIPS, K. W. BEACH, D. MARTIN, P. M. CHIKOS and D. E. STRANDNESS, *Evaluating carotid disease. The concordance between pulsed Doppler/spectrum analysis and angiography*, Ultrasound in Medicine and Biology, **9**, 1, 51–63 (1983).

[15] K. F. LINDEGAARD, S. J. BAKKE, A. GRIP, H. NORNES, *Pulsed Doppler techniques for measuring instantaneous maximum and mean flow velocities in carotid arteries*, Ultrasound in Medicine and Biology, **10**, 4, 419–426 (1984).

[16] T. MERODE, P. HICK, A. P. G. HOEKS, R. S. RENEMAN, *Limitations of Doppler spectral broadening in the early detection of carotid artery disease due to the size of the sample volume*, Ultrasound in Medicine and Biology, **9**, 6, 581–586 (1983).

[17] J. P. MURGO, N. WESTERHOF, J. P. GIOLMA, S. A. ALTOBELLI, *Aortic input impedance in normal man relationship to pressure wave forms*, Circulation, **62**, 1 (1980).

[18] M. F. O'ROURKE, M. G. TAYLOR, *Input impedance of the systemic circulation*, Circulation Research, **20**, 4 (1967).

[19] M. F. O'ROURKE, M. G. TAYLOR, Vascular impedance of the femoral bed, Circulation Research, **18**, (1966).

[20] D. J. PATEL, J. C. GREENFIELD, D. L. FRY, *In vivo pressure-length-radius relationship of certain blood vessels in man and dog*, Pulsatile Blood Flow Proceedings. Editor E. O. Attinger, New York 1964.

[21] T. POWAŁOWSKI, *An ultrasonic c.w. Doppler method of measurements of the blood flow velocity*, Archives of Acoustics **6**, 3, 287–306 (1981).

[22] T. POWAŁOWSKI, J. ETIENNE, L. FILIPCZYŃSKI, A. NOWICKI, M. PIECHOCKI, W. SECOMSKI, A. WLECIAŁ, M. BARAŃSKA, *Ultrasonic gray scale Doppler imaging angiography*, Archives of Acoustics, **9**, 1–2, 131–136 (1984).

[23] T. POWAŁOWSKI, B. PEŃSKO, Z. TRAWIŃSKI, L. FILIPCZYŃSKI, *An ultrasonic transcutaneous method of simultaneous evaluation of blood pressure, flow rate and pulse wave velocity in the carotid artery*, Abstracts of Satellite Symp. of the XIII-th World Congress of Neurol., Aachen, M–68 (1985).

[24] T. POWAŁOWSKI, B. PEŃSKO, *Noninvasive ultrasonic method of pressure and flow measurements for estimation of hemodynamical properties of cerebrovascular system*, Archives of Acoustics, **10**, 3, 303–314 (1985).

[25] T. POWAŁOWSKI, B. PEŃSKO, L. FILIPCZYŃSKI, A. MAŁEK, W. STASZKIEWICZ, M. SZOSTEK, *Transcutaneous ultrasonic examination of cerebro-vascular system by means of hemodynamic impedance method*, Proc. Sixth Congress of the European Federation of Societies for Ultrasound in Med. and Biol. EUROSON 87, 346–347, Helsinki (1987).

[26] T. POWAŁOWSKI, B. PEŃSKO, *Elasticite d'artere carotide de sujets normaux et pathologiques*, Colloque sur les Ultra-sons et Acoustique Physique, 63–73, Paris 1987.

[27] T. POWAŁOWSKI, *Ultradźwiękowe metody wyznaczania parametrów hemodynamicznych układu naczyniowego pod kątem diagnostyki tętnic szyjnych*, Prace IPPT, 36, Warszawa 1988.

[28] T. POWAŁOWSKI, *Ultrasonic system for noninvasive measurement of hemodynamic parameters of human arterial-vascular system*, Archives of Acoustics, **13**, 1–2, 89–108 (1988).

[29] T. POWAŁOWSKI, B. PEŃSKO, *A noninvasive ultrasonic method for the elasticity evaluation of the carotid arteries and its application in the diagnosis of the cerebro-vascular system*, Archives of Acoustics, **13**, 1–2, 109-126 (1988).

[30] L. POURCELOT, *C. W. Doppler technique in cerebral vascular disturbances*, in: Doppler ultrasound in the diagnosis of cerebrovascular disease, Ed. Reneman R. S. and Hoeks A. P. G., Research Studies Press, Chichester 1982.

[31] J. E. RANDALL, R. W. STACY, *Mechanical impedance of dog's hind leg to pulsatile blood flow*, Amer. J. Physiol., **187**, 94–98 (1956).

[32] J. M. REID, M. P. SPENCER, *Ultrasonic Doppler technique for imaging blood vesels*, Science, **176**, 1235 1236 (1972).

[33] R. S. RENEMAN and A. P. G. HOEKS, *Doppler ultrasound in the diagnosis of cerebrovascular disease*, Research Studies Press, Chichester, 1982.

[34] R. S. RENEMAN, M. P. SPENCER, *Local Doppler audio spectra in normal and stenosed carotid arteries in man*, Ultrasound in Medicine and Biology, **5**, 1, 1–11 (1979).

[35] J. T. ROSCOE, *Fundamental Research Statistics for the Behavioural Sciences*, Holt, Rinehart, Winston, New York, 1969.

[36] C. D. SHELDON, J. A. MURIE, R. O. QUIN, *Ultrasonic Doppler spectral broadening in the diagnosis internal carotid artery stenosis*, Ultrasound in Medicine and Biology, **9**, 6, 575–580 (1983).

[37] N. WESTERHOF, P. SIPKENA, G. ELZINGA, *Arterial Impedance*, in: Cardiovascular studies, Hweny, Gross, Patel, University Park Press, Baltimore 1979.

[38] J. P. WOODCOCK, *Doppler ultrasound in clinical diagnosis*, British Medical Bulletin, **36**, 3, 243–248 (1980).

[39] W. J. ZWIEBEL, *Spectrum analysis in carotid sonography*, Ultrasound in Medicine and Biology, **13**, 10, 625–636 (1987).

Received March 15, 1989.

Acknowledgements

No scientific journal could survive without the help of experts who have agreed to act as referees. It is encouraging to note that despite the conditions under which researchers work, a pure and unselfish scientific spirit is preserved by the reference who ensure the very existence of scientific communication.

Because of the large diversity of typics that *Archives of Acoustics* covers and our efforts to shorten the publication process, it is impossible for our Editorial Board members to review all the papers we are receiving.

Here we are give a list of colleagues who have kindly agreed to review manuscripts for *Archives of Acoustics* 14 volume. I would like to thank all of them for their assistance and hope that they will continue to give us the benefit of their invaluable advice.

Eugeniusz DANICKI

Editor-in-chief

J. DEPUTAT
S. ERNST
L. FILIPCZYŃSKI
S. GIBOWICZ
G. GRELOWSKA
A. JAROSZEWSKA
A. JUSZKIEWICZ
J. KACPROWSKI
E. KOZACZKA
M. ŁABOWSKI
A. MARKIEWICZ
W. MYŚLECKI
A. OPILSKI
W. PAJEWSKI
R. PŁOWIEC
R. SALAMON
M. SZUSTAKOWSKI
M. TAJCHERT
R. WYRZYKOWSKI
B. ŻÓŁTOGÓRSKI